

Microscale Wave Breaking and Its Effect on Air-Water Gas Transfer Using Infrared Imagery

by Christopher J. Zappa

Technical Report
APL-UW TR 9904
December 1999

20000224 163

*ONR Grant N00014-93-1-1326 and
NSF Grant 9633423*

DTIC QUALITY INSPECTED 4

**Microscale Wave Breaking and Its Effect on Air–Water Gas Transfer
Using Infrared Imagery**

by

Christopher Joseph Zappa

**A dissertation submitted in partial fulfillment of the
requirements for the degree of**

Doctor of Philosophy

University of Washington

1999

Program Authorized to Offer Degree: Civil and Environmental Engineering

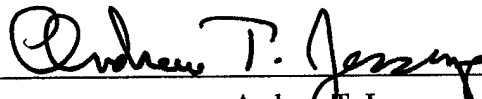
University of Washington
Graduate School

This is to certify that I have examined this copy of a doctoral dissertation by

Christopher Joseph Zappa

and have found that it is complete and satisfactory in all respects,
and that any and all revisions required by the final
examining committee have been made.

Chair of Supervisory Committee:

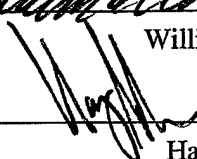


Andrew T. Jessup

Reading Committee:



William E. Asher



Harry H. Yeh

Date:

11-8-99

Doctoral Dissertation

In presenting this thesis in partial fulfillment of the requirements for the Doctoral degree at the University of Washington, I agree that the Library shall make its copies freely available for inspection. I further agree that extensive copying of the dissertation is allowable only for scholarly purposes, consistent with "fair use" as prescribed in the U.S. Copyright Law. Requests for copying or reproduction of this dissertation may be referred to Bell and Howell Information and Learning, 300 North Zeeb Road, P.O. Box 1346, Ann Arbor, MI 48106-1346, to whom the author has granted "the right to reproduce and sell (a) copies of the manuscript in microform and/or (b) printed copies of the manuscript made from microform."

Signature Christopher J. Zappa

Date 11-8-99

FOREWORD

This report is a slightly revised version of the dissertation submitted in partial fulfillment of the requirements for the Doctor of Philosophy degree at the University of Washington in November 1999. Dr. Andrew T. Jessup was the chair of the supervisory committee.

University of Washington

Abstract

MICROSCALE WAVE BREAKING AND ITS EFFECT ON
AIR-WATER GAS TRANSFER USING INFRARED IMAGERY

by Christopher Joseph Zappa

Chairperson of the Supervisory Committee:
Affiliate Assistant Professor Andrew T. Jessup
Department of Civil and Environmental Engineering

Air-sea gas exchange plays a crucial role in geochemical cycling, and a robust parameterization of the gas transfer velocity, k , is needed to improve models of global fluxes. However, the dependence of k on wind speed or wind stress has been shown to be a function of the concentration of surfactants, which are ubiquitous in nature. Laboratory measurements indicate that a wave-related mechanism regulates gas transfer because the correlation of k with wave slope is unaffected by the presence of surfactants. Microscale wave breaking has been proposed as the underlying physical process that determines k at low to moderate wind speeds. However, quantifying the effects of microscale wave breaking has been difficult because the phenomenon lacks the visible manifestation of whitecapping.

Measurements here show that microscale breaking waves produce thermal surface signatures that can be quantified by infrared imaging techniques. Simultaneous and co-located infrared and wave slope imagery of laboratory wind waves show that distinct areas of the water surface where the thermal boundary layer is disrupted occur coincidentally with waves that have a steep forward face and a dimpled bore-like crest. The measurements show that these wave-related areas of enhanced surface renewal are the turbulent wakes of microscale breaking

wave-related areas of enhanced surface renewal are the turbulent wakes of microscale breaking waves. The local k within the wakes, measured using the controlled flux technique, is on average 3.5 times greater than k outside the wakes. The fractional area coverage, A_B , of the surface affected by these renewal features is significant (0.25 – 0.40) and found to be linearly correlated with both k and the mean square wave slope, $\langle S^2 \rangle$. Microscale wave breaking is shown to directly contribute up to 75% of the transfer across the air–water interface under moderate wind speeds. The roughness features associated with microscale breaking waves are shown to contribute significantly to $\langle S^2 \rangle$ and may explain the observed correlation between k and $\langle S^2 \rangle$. The correlation between k and A_B that is insensitive to the presence of surfactants, combined with the local k and wave slope results, provides the first quantitative laboratory evidence that microscale wave breaking is the underlying physical mechanism that governs gas transfer at low to moderate wind speeds.

TABLE OF CONTENTS

List of Figures	iii
List of Tables	xiii
Chapter 1: Introduction.....	1
1.1 Importance of Air–Sea Gas Transfer	1
1.2 Theoretical Basics of Air–Water Gas Transfer	4
1.2.1 Surface Renewal Modeling	7
1.2.2 Eddy-Diffusive Models	10
1.3 Observations of Gas Transfer in the Presence of Waves	14
1.3.1 Transition from Smooth to Rough Flow	14
1.3.2 Correlating Gas Transfer with Wave Slope	16
1.3.3 Fetch Dependence of The Transfer Velocity	20
1.4 Wave Mechanisms for Gas Transfer.....	21
1.4.1 Mechanisms for Gas Transfer by Capillary Waves	21
1.4.2 Wave Breaking as a Mechanism for Gas Transfer	22
Chapter 2: The Skin Layer at the Air–Water Interface	35
2.1 Imaging the Dynamics of the Skin Layer in the Infrared.....	35
2.1.1 Infrared Signature of Large-Scale Wave Breaking	36
2.1.2 Infrared Signature of Microscale Wave Breaking	37
2.2 Characterizing Transfer Using Heat as a Tracer.....	39
2.3 Relationship Between Skin Layer Disruption and Surface Renewal.....	42
2.4 Dissertation Outline for the Presentation of Data and Discussion of Results	46
Chapter 3: Defining and Quantifying Microscale Wave Breaking Using Infrared Imagery	53
3.1 Introduction.....	53

3.2 Analysis of the Observations Made During the Preliminary CCIW/Harris Experiments	54
3.3 Comparison of Infrared and Wave Slope Imagery.....	56
3.4 Measurements of Infrared Imagery and Particle Image Velocimetry	62
3.5 Discussion.....	63
Chapter 4: Correlating Microscale Wave Breaking with Gas Transfer	82
4.1 Introduction	82
4.2 Measurements.....	82
4.3 Discussion.....	85
Chapter 5: Quantifying the Direct Effect of Microscale Wave Breaking on Gas Transfer.....	95
5.1 Introduction	96
5.2 Experimental Setup	96
5.3 Measurements of Transfer Velocity and A_B	97
5.4 Controlled Flux Technique	100
5.5 Localized Gas Transfer Within Microscale Breaking Waves.....	105
5.6 Discussion.....	108
Chapter 6: Relationship Between Microscale Wave Breaking, Wave Slope, and Gas Transfer.....	134
6.1 Introduction	134
6.2 Correlating Gas Transfer and A_B with $\langle S^2 \rangle$	135
6.3 Analysis of Infrared and Wave Slope Imagery	136
6.4 Discussion.....	139
Chapter 7: Summary and Conclusions	150
Bibliography	158
Appendix A: Determination of A_B from Infrared Imagery	169
Appendix B: Heat Flux Dependence of the Controlled Flux Technique	190
Color Plates	

LIST OF FIGURES

Number	Page
<p>Figure 1.1. Measurements of oceanic gas transfer velocity, k, referenced to CO_2 at 20°C versus wind speed, U_{10}, referenced to a measurement height of 10 m. The wind speed parameterizations of k by <i>Liss and Merlivat</i> [1986] and by <i>Wanninkhof</i> [1992] are also plotted. Data shown were measured by the deliberate dual tracer method, by the bomb ^{14}C invasion method, and by the Radon method. The data key corresponds to: A, <i>Broecker and Peng</i> [1971]; B, <i>Peng et al.</i> [1974]; C, <i>Peng et al.</i> [1979]; D, <i>Kromer and Roether</i> [1983]; E, <i>Broecker et al.</i> [1985]; F, <i>Cember</i> [1989]; G, <i>Watson et al.</i> [1991]; H, <i>Wanninkhof et al.</i> [1993]; I, <i>Wanninkhof et al.</i> [1997]; J, <i>Wanninkhof and McGillis</i> [1999].</p>	26
<p>Figure 1.2. (a) Gas transfer velocity, k_{600}, referenced to $Sc = 600$ (CO_2 at 20°C) and (b) Schmidt number exponent, n, as a function of u_*. The measurements from experiments for a carefully cleaned water surface vividly show the enhanced transfer in the presence of waves, as compared to the data for a surfactant-influenced surface. The data shown are: solid circles, surfactant-influenced water surface in the small annular wind tunnel at Heidelberg (1.57 m circumference, 0.1 m width, 0.1 m depth); open circles, cleaned water surfaces in the small annular Heidelberg facility, the large annular Heidelberg facility (11.6 m circumference, 0.3 m width, 0.4 m depth), and the large linear IMST facility, Marseilles (40 m fetch, 2.6 m width, 1 m depth). The rigid wall and the free surface, or surface renewal, models are indicated by the solid and the short dashed lines respectively. (Redrawn from <i>Coantic</i> [1986].)</p>	27
<p>Figure 1.3. Gas transfer velocity, k_{470}, for O_2 at 20°C ($Sc = 470$) as a function of u_* for a clean surface and for surfaces modified by different concentrations of Triton X-100. The solid line is a fit through the clean surface data and the dashed-dotted line is a fit through the data for $U = 9 \text{ m s}^{-1}$. The data were taken in the small annular wind tunnel at Woods Hole Oceanographic Institution (1.57 m circumference, 0.1 m width, 0.1 m depth). (Redrawn from <i>Frew et al.</i> [1995].)</p>	28
<p>Figure 1.4. (a) Gas transfer velocity, k_{600}, referenced to $Sc = 600$ (CO_2 at 20°C) as a function of mean-square capillary wave slope ($f > 14 \text{ Hz}$; $\Lambda < 1.7 \text{ cm}$), $\langle S^2 \rangle_c$. (b) Gas transfer velocity, k, as a function of total mean square wave slope, $\langle S^2 \rangle$. The data shown are: + cleaned small annular Heidelberg facility (5 cm water depth);</p>	

- ×, cleaned small annular Heidelberg facility (8 cm water depth); o, cleaned large annular Heidelberg facility; *, cleaned large linear IMST facility, Marseilles. (Redrawn from *Jähne et al.* [1984].)..... 29
- Figure 1.5. Correlation of gas transfer velocity, k_{470} , for O_2 at 20°C ($Sc = 470$) with total mean-square slope, $\langle S^2 \rangle$, for a range of wind speeds (rotor speeds ranged from 1 – 9 m s⁻¹), surface conditions, and contaminants. (Redrawn from *Frew* [1997].) 30
- Figure 1.6. Gas transfer velocity, k_{600} , determined from O_2 referenced to $Sc = 600$ as a function of various measures of the mean square slope for a clean surface and for surfaces modified by the surfactant Triton X-100. The data were taken in the small annular wind tunnel at Woods Hole Oceanographic Institution (squares) and the large annular tank in Heidelberg. Open squares, small annular wind tunnel with clean water; filled squares, small annular wind tunnel with surfactant; open diamonds, large annular wind tunnel with clean water; filled diamonds, large annular wind tunnel with surfactant. Solid line is the best fit to the observation. Mean square slope is calculated over: (a) all κ ; (b) κ below 50 rad m⁻¹; (c) κ between 50 and 200 rad m⁻¹; (d) κ above 200 rad m⁻¹. (Redrawn from *Bock et al.* [1999].)..... 31
- Figure 1.7. Dependence of k and $\langle S^2 \rangle$ on fetch, Ω . (a) Ratio of the heat transfer velocity at a given fetch to the value at 8 m fetch, $R_{\Omega/8}$, versus Ω and as a function of wind speed. (b) Mean square slope of the waves, $\langle S^2 \rangle$, versus Ω and as a function of wind speed. The symbol key for the wind speed regimes: circles, $3.2 < U < 4.2$ m s⁻¹; squares, $4.2 < U < 5.6$ m s⁻¹; diamonds, $5.6 < U < 6.7$ m s⁻¹; triangles, $6.7 < U < 7.7$ m s⁻¹. (Redrawn from *Jähne et al.* [1989].) 32
- Figure 1.8. Top: The characteristic feature of a microscale breaking wave is a bore-like crest with parasitic capillary waves riding along the forward face; U is the wind speed and C_b is the crest speed of the microscale breaking wave. (Adapted from *Ebuchi et al.* [1987].) Bottom: Video image of a microscale breaking wave with a wavelength of roughly 0.1 m..... 33
- Figure 2.1. Sequence of simultaneous, co-located video images (left) and infrared images (right) of a breaking wave in the open ocean. Image size is approximately 5 m × 10 m. The breaking wave is propagating from right to left; time increases down the page and spans 1.6 s. For reference purposes, each image includes two dashed vertical lines corresponding to roughly the same locations; the right-hand line denotes the leading edge of the breaking wave crest in the first frame. The whitecap in the video images appears as the warmest region in the infrared images. After the crest spills, a roughly circular warm patch remains (infrared image 4) which is significantly removed from the area dominated by the whitecap and foam. The infrared signature of the turbulent wake results from the

disruption of the cool skin layer by the breaking wave. For this example, the bulk-skin temperature difference was approximately 0.15°C and the wind speed was 7.7 m s^{-1} . The measurements were made aboard the research platform R/P *FLIP* off San Diego, California using an infrared imager (Agema model 880LW) operating at wavelengths of 8 to $12 \mu\text{m}$. The temperature differences between the wake and undisturbed regions of the ocean surface that were derived from the infrared imagery were consistent with independent measurements of the bulk-skin temperature difference.48

Figure 2.2. Conceptual model of disruption of the cool skin layer by a microscale breaking wave which leads to the thermal signature detectable by infrared imaging. The cool skin is disrupted and replaced by warmer bulk fluid from below. The bulk-skin temperature difference, T , across the cool skin layer of thickness, δ_T , is supported by the net heat flux, Q_N [Saunders, 1967].49

Figure 2.3. Simultaneous video images (top) and infrared images (bottom) of wind waves in the University of Washington wave tank that measured 9.1 m long, 1.2 m wide, and 0.9 m deep. Time increases from left to right in 0.16 s increments and the wind direction in the images is from top to bottom. Thermal features in the infrared images, taken with an Agema model 880 LW imager, are clearly associated with the wave crests labeled A – C in the video images and thus qualify as microscale breaking waves according to the conceptual model of Figure 2.2. Note that the crests labeled 1 and 2 have no detectable thermal signature, implying that not all waves are breaking. The bulk water temperature, T_w , was 25.8°C , the air-water temperature difference, T_{aw} , was -7.3°C , the relative humidity, RH , was 53%, the frequency of the dominant wave, f_p , was 3.44 Hz (measured at the test section), and the wind speed, U , was 6.3 m s^{-1}50

Figure 2.4. Nighttime sequences of infrared imagery demonstrating observations of microscale wave breaking aboard R/P *Flip* in September of 1995. Time increases from left to right in 0.12 s increments and the wind direction in the images is from top to bottom. The microscale breaking events within both sequences have been thresholded and outlined. These disruption events produce temperature changes of 0.1°C , which are comparable to an independently measured T . Top: Evolution of a single event labeled J followed by the inception of a second event labeled K; $U_{10} = 6.6 \text{ m s}^{-1}$, $SWH = 2.28 \text{ m}$, $f_{ps} = 0.070 \text{ Hz}$. Bottom: Example of multiple microscale breaking events; $U_{10} = 5.7 \text{ m s}^{-1}$, $SWH = 2.14 \text{ m}$, $f_{ps} = 0.074 \text{ Hz}$. In both cases, the microscale breaking occurred as the orbital motion of long waves augmented the surface drift.51

Figure 2.5. (a) Conceptual sketch (top) of the random-eddy penetration process [Harriott, 1962] occurring on the water side of the air-sea interface and a time series

(bottom) of the thermal boundary layer thickness, δ_T , at a single location (adapted from *Gulliver* [1991]). Turbulent eddies intermittently penetrate the boundary layer, forcing δ_T toward zero and allowing the underlying water to mix to the surface. (b) Idealized time series of sea surface temperature, T_s , for a cool skin layer at a single location, illustrating the distinct difference between the skin-layer recovery time, t_* , and the surface-renewal time scale, θ . Skin-layer recovery is the response to a disruptive event. As the turbulence decays, T_s returns to its original value after a time t_* . In contrast, θ is the lifetime of a turbulent eddy at the surface.....52

Figure 3.1. Example of detection technique based on the mean surface temperature, $\langle T \rangle$, and the bulk-skin temperature difference for the entire run, T . The image on the left is the same as the fifth infrared image in Figure 2.3 except that the horizontal scale is now 0.4 m. Areas with a temperature greater than the lower threshold ($\langle T \rangle + 0.20 T$) are outlined in the middle image, while the right image shows areas greater than the higher threshold ($\langle T \rangle + 0.33 T$). Note that the higher threshold identifies the three individual events labeled A – C in Figure 2.3.....69

Figure 3.2. Time series of A_B , the fractional area of microscale wave breaking, detected when using the lower (top: mean $A_B = 0.35$) and higher (bottom: mean $A_B = 0.19$) thresholds. Data were taken during an experiment at the Canada Center for Inland Waters (CCIW); $T_w = 26.8^\circ\text{C}$, $T_{aw} = -1.7^\circ\text{C}$, $RH = 65\%$, $f_p = 3.28$ Hz (measured 1 m downwind of the test section.), $U = 5.0$ m s⁻¹, and $\Omega = 6$ m.....70

Figure 3.3. Comparison of normalized power spectra of surface displacement and fractional area, A_B , for the run in Figure 3.2 using the same threshold levels. The dominant frequency of A_B provides a measure of the frequency of occurrence of microscale wave breaking and is roughly one-third the dominant wave frequency.71

Figure 3.4. Example of measurements using the infrared imager to scan a single line oriented along the tank at a rate of 2500 Hz. Top: Sequence of video images showing the location of the line scan and three individual wave crests labeled E – G propagating along the tank. Bottom: Space-time plot of surface temperature spanning the time of the video images. The scan lines corresponding to the three video images are indicated. The disruption of the skin layer by each breaking crest appears as a sloping line which corresponds to $C_b = 0.5$ m s⁻¹. The warmer temperatures above these lines indicate that the skin layer is disrupted by the breaking crests; $T_w = 25.1^\circ\text{C}$, $T_{aw} = -6.5^\circ\text{C}$, $RH = 49\%$, $f_p = 3.24$ Hz (measured at the test section), and $U = 8.1$ m s⁻¹.....72

- Figure 3.5. Examples of image slope taken at a fetch of 5.6 m as a function of wind speed and surface condition. (a) 4.2 m s^{-1} wind speed and cleaned water surface. (b) 5.5 m s^{-1} wind speed and cleaned water surface. (c) 5.6 m s^{-1} wind speed and Triton X-100 added. (d) 6.9 m s^{-1} wind speed and cleaned water surface. (e) 6.9 m s^{-1} wind speed and Triton X-100 added.73
- Figure 3.6. An example of both infrared (Top) and wave slope imagery (Bottom) at a wind speed of 6.9 m s^{-1} with a cleaned water surface depicting a microscale breaking wave; $T_w = 27.2^\circ\text{C}$, $T_{aw} = -5.6^\circ\text{C}$, $RH = 41.9\%$, $f_p = 3.20 \text{ Hz}$, and $\Omega = 5.6 \text{ m}$. The disruption of the skin layer imaged in the infrared is coincident with the appearance of a “dimpled” feature on the bore-like crest in the slope imagery. Time increases from left to right in 0.07 s increments and the wind direction in the images is from top to bottom. The first sequence of infrared images shows a box drawn to highlight the overlapping slope image area. The second infrared sequence is an expanded view of this highlighted region with an outline of the measured A_B . Likewise, only the portion below the line drawn in the slope images corresponds directly to the box (highlighted region) in the infrared images. The second wave slope sequence shows an overlay of the outline of A_B74
- Figure 3.7. An example of both infrared (Top) and wave slope imagery (Bottom) depicting a microscale breaking wave for the same conditions as in Figure 3.6. See caption in Figure 3.6 for key to description of sequences.75
- Figure 3.8. An example of both infrared (Top) and slope imagery (Bottom) depicting a wave that does not break for the same conditions as in Figure 3.6 and Figure 3.7. The wave train propagating through the slope imagery produces no detectable disruption of the thermal boundary layer in the infrared. Capillary waves dominate the slope image and no “dimpled” feature associated with a microscale breaking wave crest is evident. See caption in Figure 3.6 for key to description of sequences.76
- Figure 3.9. An example of both infrared (Top) and slope imagery (Bottom) at a wind speed of 5.5 m s^{-1} with a cleaned water surface depicting a microscale breaking wave; $T_w = 27.9^\circ\text{C}$, $T_{aw} = -5.9^\circ\text{C}$, $RH = 47.3\%$, $f_p = 3.58 \text{ Hz}$, and $\Omega = 5.6 \text{ m}$. The disruption of the skin layer imaged in the infrared is coincident with the appearance of a “dimpled” feature on the bore-like crest in the slope imagery, similar to Figure 3.6 and Figure 3.7. See caption in Figure 3.6 for key to description of sequences.77
- Figure 3.10. An example of both infrared (Top) and slope imagery (Bottom) depicting a microscale breaking wave for the same conditions as in Figure 3.9. See caption in Figure 3.6 for key to description of sequences.78

- Figure 3.11. An example of both infrared (Top) and slope imagery (Bottom) depicting a microscale breaking wave at the same wind speed of 6.9 m s^{-1} as in Figure 3.6 and Figure 3.7 only with Triton X-100 added to the water; $T_w = 28.2^\circ\text{C}$, $T_{aw} = -5.8^\circ\text{C}$, $RH = 50.8\%$, $f_p = 3.25 \text{ Hz}$, and $\Omega = 5.6 \text{ m}$. The disruption of the skin layer imaged in the infrared is coincident with the appearance of a "dimpled" feature on the bore-like crest in the slope imagery, similar to Figure 3.6, Figure 3.7, Figure 3.9, and Figure 3.10. See caption in Figure 3.6 for key to description of sequences. 79
- Figure 3.12. Example of (a) infrared imagery and (b) a vorticity plot with velocity vectors from the particle image velocimetry (PIV) depicting a microscale breaking wave. The wind direction in the infrared imagery is from top to bottom and in the PIV plot is from right to left. The vertical line in the infrared imagery corresponds to the laser sheet that intersects the water surface for the PIV measurement. The arrow in the PIV plot denotes the location of the propagating thermal front of the microscale breaking wave in the infrared imagery. Experimental conditions: $T_w = 35.1^\circ\text{C}$, $T_{aw} = -8.6^\circ\text{C}$, $RH = 45.5\%$, $f_p = 2.9 \text{ Hz}$, $U = 9.7 \text{ m s}^{-1}$, and $\Omega = 5.5 \text{ m}$ 80
- Figure 3.13. Illustration showing that not all wind waves are microscale breakers and not all microscale breaking waves produce bursts. (a) This wave is not a microscale breaker since the "roller" has not evolved into a "bore-like" crest which will disrupt the skin layer. (b) Microscale breaking produces small-scale eddies that are sufficiently energetic to bring about surface disruption. (c) Downward "bursting" motion may emerge as a result of a more intense microscale breaking event. The burst is shown for a reference frame moving with the crest. In general, no skin-layer disruption will occur for eddies incapable of inducing fluid-parcel overturning at the surface. Furthermore, not all turbulent eddies are due to microscale breaking events. 81
- Figure 4.1. Bulk gas transfer velocity, k , plotted against wind speed, U , for (a) He (k_{101} for $Sc = 101$ at 30°C) and (b) SF_6 (k_{571} for $Sc = 571$ at 30°C). Open markers correspond to data for a cleaned surface, shaded markers to data for a surface affected by biological activity, and solid markers to data for a surfactant-influenced surface. The error bars for k represent the standard error of the fit from the linear regression $-\ln[c(t)/c(0)]$ versus time. 88
- Figure 4.2. Two sequences of infrared images spanning 0.4 s at wind speeds of 6.3 m s^{-1} (Top: Experiment H1; $T_w = 31.4^\circ\text{C}$, $T_{aw} = -13.3^\circ\text{C}$, $RH = 54.4\%$, and $f_p = 3.89 \text{ Hz}$) and 8.7 m s^{-1} (Bottom: Experiment H4; $T_w = 31.7^\circ\text{C}$, $T_{aw} = -12.7^\circ\text{C}$, $RH = 45.0\%$, and $f_p = 3.19 \text{ Hz}$). Time increases left to right, the wind direction in the images is from top to bottom, and $\Omega = 5.5 \text{ m}$. The detected areas of skin-layer

disruption are programmatically outlined during the image processing algorithm and highlight distinct microscale breaking events that propagate down the tank. The along-wind and cross-wind spatial scale of the microscale wave breaking features are proportional to the corresponding dominant wavelengths of roughly 10 cm and 15 cm.89

Figure 4.3. Fractional area coverage of microscale wave breaking, A_B , measured at a fetch of 5.5 m plotted versus wind speed. Open markers correspond to data for a cleaned surface, shaded markers to data for a surface affected by biological activity, and solid markers to data for a surfactant-influenced surface. Each data point represents the average of five runs performed during one Harris I experiment that lasted between 80 and 334 minutes, depending on the wind speed. Error bars for A_B represent the standard deviation of the means calculated for each run.90

Figure 4.4. The bulk gas transfer velocity, k , versus the fractional area coverage of microscale wave breaking, A_B , for He (circles; k_{101} for $Sc = 101$ at 30°C) and SF_6 (triangles; k_{571} for $Sc = 571$ at 30°C). Open markers correspond to data for a cleaned surface, shaded markers to data for a surface affected by biological activity, and solid markers to data for a surfactant-influenced surface. The correlation between k and A_B is independent of surface cleanliness and implies that microscale wave breaking is the dominant physical process that regulates the flux of gas across the air–water interface at low to moderate wind speeds.91

Figure 4.5. The Schmidt number exponent, n , versus the fractional area coverage of microscale wave breaking, A_B . Open markers correspond to data for a cleaned surface, shaded markers to data for a surface affected by biological activity, and solid markers to data for a surfactant-influenced surface. The linear regression shown is $n = 0.855 - 1.591A_B$ with a linear coefficient of determination of 0.86.92

Figure 4.6. The bulk gas transfer velocity, k_{600} , referenced to $Sc = 600$ (CO_2 at 20°C) versus the fractional area coverage of microscale wave breaking, A_B . The gas transfer velocity referenced to CO_2 was calculated from k for He (circles) and SF_6 (triangles) using n as predicted at a particular A_B from the linear regression of the data in Figure 4.5. Open markers correspond to data for a cleaned surface, shaded markers to data for a surface affected by biological activity, and solid markers to data for a surfactant-influenced surface.93

Figure 5.1. Wind wave flume at the Air–Sea Interaction Research Facility at NASA GSFC, Wallops Flight Facility.114

Figure 5.2. Top: Experimental setup for a given fetch during the Wallops study. Bottom: Photographs showing the Amber model Radiance HS infrared camera (a) imaging the water surface with the reflection guard in place and (b) observing the SBIR model 2004S blackbody during the calibration/NUC mode. The reflection

guard ducting slides along the imager line of sight to allow the blackbody carriage to move into position for calibrating the imager and correcting the non-uniformity (NUC) of the detector (see Appendix A).....	115
Figure 5.3. Bulk gas transfer velocity, k_{600-G} , for He referenced to a $Sc = 600$ as a function of (a) wind speed, U , and (b) air-side friction velocity, u_{*a}	116
Figure 5.4. Fractional area coverage of microscale wave breaking, A_B , as a function of (a) wind speed, U , and (b) air-side friction velocity, u_{*a}	117
Figure 5.5. Schmidt number exponent, n , as a function of the fractional area coverage of microscale wave breaking, A_B	118
Figure 5.6. Bulk gas transfer velocity, k_{600-G} , for He referenced to a $Sc = 600$ versus the fractional area coverage of microscale wave breaking, A_B	119
Figure 5.7. Sequence of infrared images of the water surface heated by the CO_2 laser. The patch is tracked and used to determine the characteristic timescale for transfer across the air–water interface. Time increases from left to right in 0.1 s increments and the wind direction in the images is from top to bottom. The experiment number was W5 and the wind speed was 6.9 m s^{-1} ; $T_w = 28.2^\circ\text{C}$, $T_{aw} = -5.2^\circ\text{C}$, $RH = 42.4\%$, and $f_p = 3.17 \text{ Hz}$	120
Figure 5.8. Time series of the normalized surface temperature, T_N , of the tracked CFT patch varying as a function of wind speed.....	121
Figure 5.9. Comparison of decay curve time series determined by the CM and 3D-ST tracking algorithms.	122
Figure 5.10. Direct comparison of k_{600-H} and k_{600-G} referenced to a $Sc = 600$	123
Figure 5.11. Local heat transfer velocity, k_{600-SH} , determined by the CFT referenced to a $Sc = 600$ and scaled by the factor 0.377, compared directly to the gas transfer velocity, k_{600-G} , referenced to a $Sc = 600$	124
Figure 5.12. Local heat transfer velocity, k_{600-H} , for CFT referenced to a $Sc = 600$ as a function of (a) wind speed, U , and (b) air-side friction velocity, u_{*a}	125
Figure 5.13. Local transfer velocity of k_{600-H} for $Sc = 600$ versus A_B	126
Figure 5.14. Comparison of CFT patch decay affected directly by a microscale breaking wave (Microbreaker), one that was partially affected by a microscale breaking wave (Delayed Microbreaker), and one that was not affected at all (Background). The experiment number was W5 and the wind speed was 6.9 m s^{-1} . The experimental conditions are identical to those in Figure 5.7.	127
Figure 5.15. Time series of the CFT patch decay. Examples include decay affected directly by microscale breaking (Microbreaker), decay affected by microscale breaking after some time (Delayed Microbreaker), and decay not affected by microscale breaking (Background).	128

Figure 5.16. Local transfer velocities as determined by CFT referenced to $Sc = 600$ for decay patches affected directly by microscale breaking, k_B , and those in the background, k_{NB} as a function of A_B	129
Figure 5.17. The ratio of k_B to k_{NB} , R_{enh} , as a function of A_B	130
Figure 5.18. The ratio $R_{eff} = A_B k_B / k_m$ as a function of A_B , where $k_m = A_B k_B + (1 - A_B) k_{NB}$ according to (4.1).	131
Figure 5.19. Comparison of $k_m = A_B k_B + (1 - A_B) k_{NB}$ determined from the model in (4.1) and k_{600-H} determined from CFT directly.....	132
Figure 6.1. The local heat transfer velocity, k_{600-H} , versus the total mean square slope, $\langle S^2 \rangle$	144
Figure 6.2. The fractional area coverage of microscale wave breaking, A_B , versus the total mean square slope, $\langle S^2 \rangle$	145
Figure 6.3. Time series of $\langle S^2 \rangle_B$, $\langle S^2 \rangle_{NB}$, $\langle S^2 \rangle_{ov}$, A_B , R_{SB} , and R_{SNB} during Experiment Number W5 and including data determined from Figure 3.6, Figure 3.7 and Figure 3.8.....	146
Figure 6.4. Time series of $\langle S^2 \rangle_B$, $\langle S^2 \rangle_{NB}$, $\langle S^2 \rangle_{ov}$, A_B , R_{SB} , and R_{SNB} during Experiment Number W8 and including data determined from Figure 3.9 and Figure 3.10.....	147
Figure 6.5. Time series of $\langle S^2 \rangle_B$, $\langle S^2 \rangle_{NB}$, $\langle S^2 \rangle_{ov}$, A_B , R_{SB} , and R_{SNB} during Experiment Number W13 and including data determined from Figure 3.11.....	148
Figure 6.6. Conceptual illustration of the evolution of a capillary-gravity wave packet that eventually culminates in microscale wave breaking. The wind is from right to left and time increases down the page. The observer is moving with the waves at the phase speed, C	149
Figure A.1. Schematic diagram of the image processing algorithm used to determine A_B	180
Figure A.2. Noise equivalent temperature difference, $NETD$, for the Amber model Radiance HS camera determined using the SBIR model 2004S blackbody as a function of the target temperature, T_T	181
Figure A.3. Summary of all calibrations of the Amber model Radiance HS camera performed using the SBIR model 2004S blackbody during the Wallops study. DU is the 12-bit digital dynamic range and T_T is the blackbody target temperature. The line is a polynomial fit through the data and serves as the overall calibration for this study.....	182
Figure A.4. Time series of the mean standard deviation of surface temperature, σ_T , from an image for a given run and the mean $\Delta T'$ as determined using the mean calibrated image temperature as T_s and T_w measured by the aforementioned bulk water thermometer. Also shown are time series of T_a , T_w , T_{aw} , and RH . Each group corresponds to different imager calibration.....	183

Figure A.5. (a) The bulk-skin temperature difference, T , measured during the Harris I study and (b) $\Delta T'$ measured during the Wallops study versus the standard deviation in surface temperature, σ_T , from the infrared imagery.	184
Figure A.6. Sequence of infrared imagery with outlines of the detected regions of skin-layer disruption due to microscale wave breaking, A_B , that shows the difference between the various thresholds for $j = 3.5, 4.0$, and 4.5 . Example is taken from Figure 3.9.	185
Figure A.7. Sequence of wave slope imagery with overlays of the detected A_B in Figure A.6.....	186
Figure A.8. The gas transfer velocity, k_{600-G} , referenced to a $Sc = 600$ versus A_B for a comparison of three thresholds $j = 0.100, 0.075, 0.050$ for the Harris I study.	187
Figure A.9. The gas transfer velocity, k_{600-G} , referenced to a $Sc = 600$ versus A_B for a comparison of two thresholds defined by (a) $j = 3.5$ and (b) $j = 4.0$ for the Wallops study. Also shown are the linear fits to the data for $j = 3.5$ (solid line) and $j = 4.0$ (dashed line).	188
Figure B.1. Comparison of k_{600-H} from the Harris II study and k_{600-G} from the Harris I study discussed in Chapter 4.	195
Figure B.2. Dependence of k_H on Q_N during the Wallops and the Harris II experiments.	196
Figure B.3. Dependence of k_H on Q_L during the Wallops and the Harris II experiments.....	197
Figure B.4. Dependence of k_H on Q_S during the Wallops and the Harris II experiments.....	198

LIST OF TABLES

<i>Number</i>	<i>Page</i>
Table 1.1. Summary of the results from <i>Bock et al.</i> [1999] in Figure 1.6 giving the mean square slope notation, the wavenumber range analyzed, and the root-mean-square (RMS) error in the linear fit between k_{600} and mean square slope. $\langle S^2 \rangle$ is the total mean square slope, $\langle S^2 \rangle_{50}$ is the mean square slope integrated over wavenumbers less than 50 rad m^{-1} , $\langle S^2 \rangle_{50-200}$ is the mean square slope integrated over wavenumbers between 50 rad m^{-1} and 200 rad m^{-1} , and $\langle S^2 \rangle_{200}$ is the mean square slope integrated over wavenumbers greater than 200 rad m^{-1}	34
Table 4.1. Environmental conditions for the Harris I study. Wind speed (U), bulk-skin temperature difference (T), air-water temperature difference (T_{aw}), water temperature (T_w), relative humidity (RH), peak wave frequency (f_p), and root-mean-square surface displacement (RMS η) have been averaged for the duration of each experiment. Experiment numbers increase in chronological order and were performed over a two-month time period. The large air-water temperature differences were used to ensure a measurable infrared signal and did not affect the determination of k . Asterisks represent experiments with the surfactant Triton X-100 and daggers represent experiments with unsterilized water.	94
Table 5.1. Environmental conditions for the Wallops study. Wind speed (U), bulk-skin temperature difference (T), air-water temperature difference (T_{aw}), water temperature (T_w), relative humidity (RH), the peak wave frequency (f_p), and the root-mean-square (RMS) surface displacement (η) have been averaged for the duration of each experiment. Fetch (Ω) is measured to the top of the infrared image and experiment numbers increase in chronological order and were performed over a one-month time period. The large air-water temperature differences were used to ensure a measurable infrared signal and did not affect the determination of k . Asterisks represent experiments with the surfactant Triton X-100 and daggers represent experiments with an adventitious oily surfactant. NA denotes data that is not available.	133
Table A.1. Comparison of experimental differences between the Preliminary CCIW/Harris, the Harris I, and the Wallops studies.	189
Table B.1. Comparison of Cases 1 and 2 during the Harris II study.	199

ACKNOWLEDGMENTS

I would like to express sincere thanks to all those who have helped and supported me during the last five years in preparing this dissertation. My thesis advisor, Andy Jessup, has been a significant source of guidance, advice, and encouragement. I greatly appreciate his confidence in me and the resources that made this work possible. He provided the stimulus that made my graduate career a most rewarding experience. Harry Yeh and Bill Asher both provided crucial insights into my research and also served as trusted mentors on my supervisory committee. I would also like to thank Jim Riley for his participation on my doctoral committee and for his important observations and helpful input.

Collaboration with many colleagues has added an invaluable element to my research. In particular, I would like to thank Vahid Hesany and Roy Schiff for their assistance in early experiments. Mark Loewen provided his expertise in the PIV measurements, and I appreciate his overall helpfulness with my research. I extend thanks to Steve Long of NASA for providing access to his superior facility at the Air-Sea Interaction Research Facility. I am also grateful to Jochen Klinke of Scripps Institution of Oceanography for his timely work on the image wave slope measurements at Wallops. I thank Wade McGillis of Woods Hole Oceanographic Institution for providing friction velocity measurements from the experiments at Wallops.

The staff at the University of Washington Applied Physics Laboratory has been terrific. I would like to thank all the friends that I have made while working here at APL who made this an enjoyable experience. I especially want to thank Lisa Haugen and Dorothy Lowell for frequent assistance with posters, figures and other graphics materials.

My friends and family also deserve much credit for supporting me. Jim Turner, John Allen, and Gary Wick merit special thanks for their professional and personal insights. I would like to thank my mother and father for believing in me and giving me the faith in myself to persevere. Finally, I wish to express my deepest appreciation to my wife, Katell, who provided immeasurable support as I pursued my endeavors.

This research was sponsored by the National Science Foundation, the Office of Naval Research, and the Applied Physics Laboratory at the University of Washington.

DEDICATION

To my family and friends.

CHAPTER 1: INTRODUCTION

1.1 IMPORTANCE OF AIR-SEA GAS TRANSFER

The global carbon cycle is strongly influenced by the interaction between the ocean and the atmosphere yet we do not know sufficiently well how this cycle will respond, and with what feedbacks, in a changing climate. Questions remain as to how much carbon dioxide (CO_2) is being taken up by the oceans and whether this uptake will increase or decrease in the future. Improving our understanding of ocean mixing and air-sea exchange mechanisms will reduce the uncertainties in coupled atmosphere-ocean model estimates of the overall climate response. Coupled atmosphere-ocean climate models as yet do not explicitly incorporate oceanic uptake or release of natural and anthropogenic greenhouse gases [Weaver, 1993] that act to insulate the earth from releasing heat. The equilibration time for these gases in the ocean mixed layer is short compared to the time for advective transport through the thermocline from the surface waters to the deep ocean. Because of this, air-sea transfer is not the rate-limiting step for uptake of gases in most oceanic regions. Instead, it is vertical mixing that controls the global ocean uptake of gases. However, this does not imply that accurate knowledge of air-sea fluxes is unnecessary in modeling global uptake.

The flux of gas is determined as the product of the gas transfer velocity, k , which characterizes the resistance to gas exchange across the air-sea interface, and the air-sea concentration difference, which is the driving potential. Consequently, in areas of the ocean where strong upwelling or deep convective overturning exists, gas transfer can limit CO_2 uptake. Simulations of global ocean CO_2 uptake in ocean circulation models show that doubling k leads to substantial modifications in the regional CO_2 uptake especially where the disequilibrium

between the atmosphere and oceanic concentrations is large [Sarmiento *et al.*, 1992]. Because of the natural spatial and temporal variations of the air-sea CO_2 concentration difference, improved understanding of k is necessary for accurate estimation of the CO_2 flux in areas where upwelling or convective overturning exist. These areas cause most of the sensitivity to k in CO_2 uptake in ocean global circulation models.

Not only will a better knowledge of k improve our understanding of the spatial variability of the air-sea gas flux, but it also will be of critical importance in calibrating ocean circulation models. Ocean circulation models are typically validated by matching predicted to observed distributions of passive tracers (e.g., bomb ^{14}C and chloroflourocarbons, or CFC's). Gas transfer strongly affects the modeled tracer distributions that provide a constraint on the deep-water formation to global ocean circulation models. In particular, the CFC uptake in a global ocean circulation model has been shown to be highly sensitive to the parameterization of k [England *et al.*, 1994]. Despite the critical role of gas transfer in modeling global climate change, knowledge about many of the physical processes controlling gas transfer remains elusive.

Considerable effort has gone into determining empirical relations between k and wind speed [Liss and Merlivat, 1986; Wanninkhof, 1992], since the wind stress at the ocean surface plays a central role in the generation of turbulence through the transfer of momentum to the waves and currents. Turbulence is presumed to be the driving mechanism that decreases the resistance to the transfer of gas across that air-sea interface. The piecewise-continuous relationship of Liss and Merlivat [1986] incorporates three linear regimes delineated by processes observed in the laboratory and related to a smooth surface regime at low wind speeds, a rough surface regime at moderate wind speeds, and a bubble regime (due to air entrainment by large-scale wave breaking) at high wind speeds. The quadratic relationship between k and wind speed by Wanninkhof [1992] is based on an empirical fit to the global ocean and basin-wide estimates of natural and bomb ^{14}C data.

Figure 1.1 shows these parameterizations as well as oceanic measurements of the gas transfer velocity, k , referenced to CO_2 at 20°C , for various gases and techniques versus wind speed, U_{10} , referenced to a measurement height of 10 m. The data show that considerable scatter exists in the measurements of k at all wind speeds and is partly related to the variation in sea state and surface condition and partly related to inherent uncertainties in the measurement technique [Asher and Wanninkhof, 1998]. The difference between the empirical relationships and the scatter in the field data has led to the consideration of more than just wind forcing as a mechanism for generating near-surface turbulence—specifically, large-scale and microscale wave breaking have been proposed to contribute significantly to near-surface turbulence. This thesis will explore the role that microscale wave breaking, or the breaking of very short wind-forced waves without air entrainment, plays in air–sea gas exchange.

The main objectives of this thesis are to:

1. Investigate the characteristics and source of the infrared signature of microscale wave breaking.
2. Determine if the infrared signature of microscale wave breaking can be used to define and quantify this visually ambiguous process.
3. Determine if a parameter associated with the process of microscale wave breaking correlates with k since microscale breaking is thought to regulate gas transfer.
4. Utilize the controlled flux technique to quantify the direct effect of microscale breaking on the transfer velocity.
5. Quantify the contribution of surface roughness features associated with microscale breaking to the mean square wave slope, which has been used to infer a dependence of k on waves.

1.2 THEORETICAL BASICS OF AIR-WATER GAS TRANSFER

Gas transfer occurs across any air-water interface, where the resistance to slightly soluble gas exchange resides in a diffusion boundary layer at the water surface in which molecular processes dominate. According to Fick's law, the magnitude and direction of the gas flux, F , is proportional to the product of the concentration gradient and the molecular diffusivity of the gas, D , and is defined by

$$F = D \frac{\partial c}{\partial z} \sim D \frac{\Delta c}{\delta}, \quad (1.1)$$

where the vertical component $z = 0$ at the air-water interface and is measured positive downward, δ is a measure of the layer thickness through which diffusion occurs (diffusion length scale) assuming the concentration gradient is linear, and Δc is the concentration difference, $c_o - c_w$, where c_o is the surface concentration and c_w is the bulk concentration in the water column. The gas flux across an air-water interface historically has been characterized as the product of the gas transfer velocity, k , and Δc , and F is given as

$$F = k \Delta c, \quad (1.2)$$

where k incorporates the dependencies of gas transfer on turbulent transport and diffusivity. These transport processes are typically modeled in the form of

$$k = Sc^{-n} f(V, \ell), \quad (1.3)$$

where the Schmidt number, Sc , is defined as the ratio of the kinematic viscosity of water, ν , to D , and $f(V, \ell)$ represents the effect of near-surface hydrodynamics where V and ℓ are characteristic turbulent velocity and length scales, respectively. The Schmidt number exponent n varies between $\frac{2}{3}$ and $\frac{1}{2}$ depending on the surface boundary condition and the activity of waves [Jähne and Haußecker, 1998], and will be discussed in more detail in sections 1.2.2 and 1.3.1. Comparing (1.1) and (1.2) yields

$$k = \frac{D}{\delta}, \quad (1.4)$$

which is often referred to as a stagnant film model. Because a stagnant layer of water of constant thickness near the interface in the presence of turbulence is unrealistic, a stagnant film model cannot account for the dynamics of transfer. Rather, the magnitude of k is determined by diffusion through a thin, spatially and temporally varying concentration boundary layer, whose thickness is a function of near-surface turbulence and molecular diffusivity.

Liss [1973] considered a two-layer boundary system to develop at an air–water interface in which (1.2) is satisfied for both layers. Then

$$F = k_a(c_a - c_{sa}) = k_w(c_{sw} - c_w), \quad (1.5)$$

where k_a and k_w are the gas transfer velocities in air and water-side boundary layers, c_a and c_{sa} are the concentrations in the bulk and at the interface in the air layer, and c_w and c_{sw} are the concentrations in the bulk and at the interface in the water layer. Equilibrium between c_{sa} and c_{sw} is established by

$$c_{sw} = \phi c_{sa}, \quad (1.6)$$

where ϕ is the dimensionless Ostwald solubility. Eliminating c_{sw} and c_{sa} from (1.5) and (1.6), yields

$$F = k_{at} \left(c_a - \frac{c_w}{\phi} \right) = k_{wt} (\phi c_a - c_w), \quad (1.7)$$

where k_{at} and k_{wt} are the total transfer velocities in air and water and can be broken down into their component parts as

$$\frac{1}{k_{at}} = \frac{1}{k_a} + \frac{1}{\phi k_w}; \quad \frac{1}{k_{wt}} = \frac{1}{k_w} + \frac{\phi}{k_a}. \quad (1.8)$$

The relative importance of gas and liquid phase transfer then is given by the ratio of $\phi k_w/k_a$, which determines the boundary layer controlling the transfer process. Typically, k_w is less than k_a by at least a few orders of magnitude since the diffusion coefficients are much greater in the air than in the water. Therefore, gases which are air-side controlled (i.e., resistance to transfer is mainly in the air) generally have high values of ϕ and include H_2O , NH_3 , and SO_2 . In contrast, water-side controlled gases have low ϕ and include He , SF_6 , and CO_2 . It is usually reasonable to assume that the individual transfer velocity for the rate-controlling phase is numerically equal to the total transfer velocity. Hereafter, since this thesis concentrates on physical mechanisms relevant to water-side controlled transfer processes, k will refer to the total water-side gas transfer velocity.

1.2.1 SURFACE RENEWAL MODELING

While the simplistic model in (1.4), utilizing a stagnant film of constant thickness to characterize δ , is illustrative in developing the basic ideas of gas transfer, it does not incorporate characteristics of the turbulent flow driving the transfer. Surface-renewal models are more physically realistic and predict the gas transfer velocity, k , based on the continuous random renewal of the laminar sublayer with the bulk water due to turbulent eddies. As long as a water parcel resides at the free surface, gas will diffuse across the boundary and into the bulk according to

$$\frac{\partial c}{\partial t} = D \frac{\partial^2 c}{\partial z^2}, \quad (1.9)$$

where the concentration of the gas, c , varies with depth and time, t . For the initial condition $c(z, 0) = c_w$ and boundary condition $c(0, t) = c_{sw} = \phi c_a$, the solution is

$$\frac{c - c_w}{c_{sw} - c_w} = \operatorname{erfc} \left(\frac{z}{2\sqrt{Dt}} \right). \quad (1.10)$$

Substituting (1.10) into (1.1) results in

$$F = D \left. \frac{\partial c}{\partial z} \right|_{z=0} = (c_{sw} - c_w) \sqrt{\frac{D}{\pi t}}. \quad (1.11)$$

Higbie [1935] postulated that each eddy is exposed for the same time, τ_e , at the surface before being replaced, so that the transfer velocity is written as

$$k = 2 \sqrt{\frac{D}{\pi \tau_e}}, \quad (1.12)$$

where the factor of 2 results from the integration of (1.11) over τ_e to arrive at the mean rate of flux. *Danckwerts* [1951] assumed the ages of fluid elements occupying the surface were not identical, and that the probability of renewal of a patch of surface was independent of its age. The mean rate of fresh surface production, or the surface-renewal rate, s , will be constant and is determined from the distribution of surface element lifetimes

$$\Theta(\theta) = s e^{-s\theta}, \quad (1.13)$$

where θ is the lifetime of a particular parcel of water at the surface. Integrating the solution in (1.11) over all lifetimes, the mean rate of adsorption is

$$\bar{F} = (c_{sw} - c_w) \int_0^{\infty} s e^{-s\theta} \sqrt{\frac{D}{\pi \theta}} d\theta = (c_{sw} - c_w) \sqrt{Ds}. \quad (1.14)$$

The gas transfer velocity is then

$$k = (Ds)^{1/2} = \left(\frac{D}{\tau}\right)^{1/2}, \quad (1.15)$$

which is identical to (1.4) when a diffusion length scale is chosen as $\delta = \sqrt{D\tau}$, with $\tau = 1/s$ where τ is a characteristic timescale for surface renewal or the average lifetime of water parcels at the surface. While the dependence of k on turbulence is not explicitly represented by τ_e or s , more intense turbulence increases s (or decreases τ_e) and increases k .

Models have been developed to represent the surface-renewal parameters in terms of the physical quantities characteristic of turbulent flow. *Fortescue and Pearson* [1967] argued that surface renewal is governed by the largest-scale, energy-containing turbulent motions, such that the surface-renewal time scale is given by $\tau = \ell/V$ where ℓ is the integral turbulent length scale and V is the square root of twice the turbulent kinetic energy (divided by density). This results in

$$k \propto \left(\frac{DV}{\ell} \right)^{1/2}, \quad (1.16)$$

where V is defined as $V = (u'^2 + v'^2 + w'^2)^{1/2}$, and u' , v' , and w' are the root-mean-square turbulent velocity fluctuations in the standard x , y , and z Cartesian coordinate reference frame, respectively. *Lamont and Scott* [1970], on the other hand, modeled the surface renewal based upon eddies with the smallest time scale. Estimating τ by the Kolmogorov, or dissipative, timescale, $(\nu/\epsilon)^{1/2}$, the gas transfer velocity becomes

$$k \propto (\epsilon \nu)^{1/4} Sc^{-1/2}, \quad (1.17)$$

where ϵ is the turbulent kinetic energy dissipation rate and can be estimated as $\epsilon \propto V^3/\ell$. Both models allow the determination of the transfer velocity from parameters which can be measured in the laboratory, and (1.17) shows that increasing turbulence intensity (i.e., increasing ϵ) will enhance k . Neither model has been shown conclusively to be more appropriate for either grid-generated turbulence experiments or wind-wave studies [*Asher and Pankow*, 1986; *Komori et al.*, 1989; *Komori et al.*, 1993]. This implies that the choice of the two models is arbitrary. *Brumley*

and Jirka [1988] argue that turbulence is a multiscale phenomenon, and eddies with scales over a wide range impinge upon the boundary layer rather than eddies of a single size.

1.2.2 EDDY-DIFFUSIVE MODELS

Based on the analogy between momentum and mass flux, eddy-diffusive models of the gas transfer velocity [Deacon, 1977; Jähne *et al.*, 1979] have evolved into a consistent semi-empirical formulation that may be expressed as

$$k = \beta u_* Sc^{-n}, \quad (1.18)$$

where β is a dimensionless constant and u_* is the water-side friction velocity. The friction velocity is a velocity scale related to the constant momentum flux condition at the interface and is defined as $u_* = (\Gamma/\rho)^{1/2}$, where Γ is the sum of the turbulent and viscous stresses at the surface and ρ is the density of water. Deacon [1977] used empirical results for eddy-diffusive transport in turbulent boundary layers near smooth solid walls to predict an exponent of $n = 2/3$ and $\beta = 1/12$. He found this result to agree with the observed rates of transfer in laboratory experiments over smooth water at low wind speed (smooth flow implies that no waves were present). However, measurements of the transfer velocity at moderate wind speeds exceeded the k predicted from Deacon's [1977] model by a factor of 2 following the transition from smooth to rough flow that occurred at a wind speed of approximately 5 m s^{-1} (rough flow implies that waves were present). The model breaks down when waves are present since the characteristic velocity profile depends on roughness.

The model proposed by Deacon [1977] in (1.18) with $n = 2/3$ and $\beta = 1/12$ assumes both that the air-water interface is smooth and that the interface behaves as a solid, or rigid, wall.

The air–water interface, however, is not a rigid wall, but rather a free surface. In the discussion that follows, only a smooth surface will be considered in order to highlight the difference in boundary condition between a rigid and free surface. All velocity components at a rigid wall surface are zero according to the no-slip condition. In contrast, a tangential velocity may exist at a free surface even though the vertical velocity component must be zero. In order to demonstrate the effect that the rigid wall and free surface boundary conditions have on k , *Ledwell* [1984] modified (1.1) to incorporate an eddy diffusivity, D_e , for transport between a reference depth, H , where the water is well mixed, and the surface, resulting in

$$F = (D + D_e) \frac{\partial c}{\partial z}. \quad (1.19)$$

Integrating (1.19) to determine the mean concentration profile between H and the surface, and comparing this mean concentration profile with (1.2), the transfer velocity is given in the form of

$$k^{-1} = \int_0^H [D + D_e(z)]^{-1} dz. \quad (1.20)$$

The eddy diffusivity is modeled as the product of a mixing velocity, V_m , and length scale, ℓ_m , resulting in

$$D_e(z) = V_m(z) \ell_m(z). \quad (1.21)$$

The length scale is taken to vary with z and the velocity scale is taken as the turbulent velocity fluctuation normal to the interface, $w'(z)$, since these motions transport mass toward the interface. Continuity stipulates that

$$\frac{\partial w'}{\partial z} = -\left(\frac{\partial u'}{\partial x} + \frac{\partial v'}{\partial y}\right) = -\nabla \cdot V_H, \quad (1.22)$$

where $\nabla \cdot V_H$ is the divergence in a plane locally tangent to the interface. Expanding $w'(z)$ in a Taylor series about the interface ($z = 0$) results in

$$w'(z) = -\nabla \cdot V_H|_{z=0} z - \frac{\partial}{\partial z}(\nabla \cdot V_H)|_{z=0} z^2 + \dots \quad (1.23)$$

Since all velocity fluctuations vanish at a rigid surface, the first term in (1.23) goes to zero. Only the second term of the Taylor series expansion of the vertical turbulent velocity component in (1.23) is retained for describing the eddy, or turbulent, diffusivity such that $w'(z) \sim z^2$ results in $D_e \sim z^3$ from (1.21). From (1.20), k for a rigid surface is found to be proportional to $D^{3/2}$, which is consistent with the smooth, rigid-wall model of *Deacon* [1977]. However, tangential velocities at the free surface result in non-zero horizontal velocity divergence, $\partial w'/\partial z = -\nabla \cdot V_H \neq 0$. The implementation of this free surface boundary condition retains the finite first term of the Taylor expansion in (1.23) for use in scaling the turbulent diffusivity, which now decays more gradually as the free surface is approached from below, so that $w'(z) \sim z$ results in $D_e \sim z^2$ from (1.21). From (1.20), k for a free surface is found to be proportional to $D^{1/2}$, which is consistent with the classical surface-renewal theory result in (1.15). Therefore, the difference in n between surface-renewal models and smooth rigid-wall models lies in the treatment of the boundary condition.

The difference in the Schmidt number dependence of k produced by the rigid and free surface boundary conditions has important implications for cleaned and surfactant-influenced surfaces. Since the first derivative of the normal velocity component is non-zero at a cleaned water surface, tangential flow produces convergence and divergence zones according to (1.22), resulting in $k \sim Sc^{-1/2}$. However, a surfactant-influenced interface changes the free surface boundary condition to create opposing stresses that work to suppress horizontal motions and therefore near-surface turbulence. At a rigid wall, all velocity components are zero because of the no-slip condition. At a surfactant-influenced surface, stresses due to the surfactant film act to diminish velocity fluctuations, and hence the derivative of the vertical turbulent velocity component goes to zero, resulting in no divergence, or $\partial w' / \partial z = -\nabla \cdot \mathbf{v}' = 0$. Thus, a surfactant-influenced surface behaves similarly to a rigid surface and $k \sim Sc^{-2/3}$. The air-water interface will behave like a rigid surface if the surface stress is too weak to overcome the restoring forces of the surfactant film. If the stress becomes stronger, local instances of convergence or divergence will occur, more turbulence will affect the diffusive boundary layer that restricts gas transfer, and n will approach $1/2$. The air-water interface, then, may behave as either a free or rigid surface depending upon the cleanliness of the interface.

A wind-blown air-water interface, however, is rarely smooth, and its roughness must be considered since short wind waves develop even at low wind speeds. While parameterizations of the exchange of gas using surface-renewal theory and eddy-diffusive concepts have had some success [Jähne *et al.*, 1987], fundamental differences between these classical ideas and the influence of waves and surfactants remain to be reconciled in modeling the air-sea gas flux. The dependence of k on clean and surfactant-influenced surfaces will now be considered in the context of experimental observations of the influence of waves on gas exchange.

1.3 OBSERVATIONS OF GAS TRANSFER IN THE PRESENCE OF WAVES

1.3.1 TRANSITION FROM SMOOTH TO ROUGH FLOW

One of the original studies of the effect of waves on gas exchange was performed by *Kanwisher* [1963], who found that beyond a critical wind speed when capillary waves commence, the gas exchange increases dramatically. The work of *Jähne* and co-workers [*Jähne et al.*, 1979; *Jähne et al.*, 1984; *Jähne et al.*, 1985] has demonstrated that the rigid wall model is only valid in the absence of capillary waves or when the surface is heavily affected by surfactant. Transfer velocities higher than predicted by the rigid wall model were observed to occur for cleaned surfaces in the presence of capillary waves. Figure 1.2 shows (a) the gas transfer velocity, k_{600} , referenced to $Sc = 600$ (representative of CO_2 at $20^\circ C$) versus u_* and (b) the Schmidt number exponent, n , versus u_* . The data denoted as solid circles were taken in a small annular wind tunnel at the University of Heidelberg for a smooth surface flow by *Jähne et al.* [1979]. They concluded that the data from this experiment had been affected by surfactant material, since the water was not skimmed. The data denoted as open circles in Figure 1.2 were measured by *Jähne et al.* [1984, 1985, 1987] for carefully cleaned water surfaces during three laboratory experiments—one each in the small and large annular wind tunnels at Heidelberg, and the third in the large linear tank at the Institut de Mécanique Statistique de la Turbulence (IMST) in Marseille. The solid line in Figure 1.2a is the rigid wall model ($\beta = 1/12$, $n = 2/3$ from *Deacon* [1977]) and the dashed line is the free surface model ($\beta = 1/16$, $n = 1/2$ from *Jähne et al.* [1979] or *Ledwell* [1984]), both based upon (1.18). The horizontal lines in Figure 1.2b correspond to $n = 1/2$ (dashed line) and $n = 2/3$ (solid line).

Figure 1.2a shows that the measured k_{600} values for the surfactant-influenced surface with no waves present are described well by the smooth rigid-wall model of *Deacon* [1977]. The surfactant-influenced surface is able to maintain the smooth regime relationship by

inhibiting capillary waves up to $u_* = 1.5 \text{ cm s}^{-1}$. The values of n , determined from the tracers CO_2 and heat (the heat transfer velocity is discussed in detail in section 2.2), closely match the predicted limit of $\frac{2}{3}$ for the rigid wall model. However, the transfer velocities from the three wind-wave tunnel experiments with cleaned water surfaces show that k was 3 to 5 times greater in the presence of waves than for a smooth surface. The values for k for the cleaned surface experiments showed no large differences among the data from the tanks of very different scale. In conjunction with the enhanced transfer velocities in the presence of waves, the Sc dependence was observed to gradually decrease from $n = \frac{2}{3}$ to $n = \frac{1}{2}$. The enhanced transfer velocities in the presence of waves were observed for u_* as low as 0.35 cm s^{-1} and for $n = \frac{2}{3}$. For cases at low u_* when the rigid wall model ($n = \frac{2}{3}$) is applicable, the model underestimated the measured values of k for clean surfaces in the presence of waves. Likewise, for the cases when the free surface model is applicable ($n = \frac{1}{2}$), the model underestimated the measured values of k for cleaned surfaces when waves were present. In both cases, the results suggest that the turbulent diffusivity was not adequately modeled, or that a wave-related mechanism generated an additional source of enhanced transfer. Data from various other linear wind tunnel studies (summarized in *Jähne et al.* [1985]) show comparable enhanced rates of transfer in the presence of waves for tanks of widely varying scale. The direct comparison of k at the same u_* in the smooth and rough regimes demonstrates the distinct change of the transfer process in the presence of waves.

As shown in theoretical [*Lucassen*, 1982] and experimental [*Alpers and Hühnerfuss*, 1989] analyses, surfactants have long been known to damp capillary-gravity waves, as well as inhibit their generation and amplification. During the transition from smooth to rough flow at a critical wind speed, the observed change in the relationship between k and wind speed or friction velocity with the onset of waves [*Kanwisher*, 1963; *Jähne et al.*, 1979] has been attributed to the existence of surfactants [*Jähne et al.*, 1984]. Most natural surfaces are likely influenced by surfactants to some degree, and the critical wind speed has been observed in the

laboratory to increase with the level of surfactant concentration [Frew *et al.*, 1995; Frew, 1997]. Figure 1.3 from Frew *et al.* [1995] shows that the gas transfer velocity for a perfectly clean surface has a continuous linear relationship with friction velocity. Furthermore, the relationship between k and u_* becomes increasingly nonlinear with increasing surfactant concentration, qualitatively similar to the transition from smooth to rough regime observed at a critical wind speed. A critical wind speed marking the transition in roughness regimes is consistent with a change in the Schmidt number dependency and may be associated with a modification in the behavior of the boundary condition at the air–water interface.

Surfactants not only directly affect the wave field through damping, but also have been shown to modify the surface boundary condition [Hirsa and Willmarth, 1994; Sarpkaya, 1996]. Jähne and Haußecker [1998] have recently confirmed the result shown in Figure 1.2b that n gradually decreased with increasing u_* from $\frac{2}{3}$ to approach the theoretical limit of $\frac{1}{2}$ in the presence of waves. The fact that waves are present even in cases when $n = \frac{2}{3}$ suggests that the behavior of the boundary condition described by n is not affected directly by the wave field. A transition of n from $\frac{2}{3}$ to $\frac{1}{2}$ implies a transition in the boundary condition from a rigid surface to a free surface. Likewise, this transition of n from $\frac{2}{3}$ to $\frac{1}{2}$ could imply a transition from a surfactant-influenced surface to a clean surface. However, this transition does not necessarily mark the transition from a smooth to a rough flow, since waves have been observed for cases where $n = \frac{2}{3}$. This implies that a surface may behave locally as a rigid surface in the presence of surfactants, if capillary waves are damped by the surfactant while the dominant gravity waves survive.

1.3.2 CORRELATING GAS TRANSFER WITH WAVE SLOPE

Wave-related parameters such as mean square slope, $\langle S^2 \rangle$, have become a primary research focus in explaining the observed discrepancies in comparisons among

laboratory results of k at similar wind speeds [Jähne *et al.*, 1984; Jähne *et al.*, 1987; Bock *et al.*, 1999] and the significant variability observed in field measurements of k (see Figure 1.1). The one-dimensional mean square slope is defined as

$$\langle S^2 \rangle = \overline{\left| \frac{\partial \eta}{\partial x} \right|^2}, \quad (1.24)$$

where the overbar denotes a spatial and temporal average, and the expression for surface displacement, $\eta(x, t)$, of a linear, one-dimensional, progressive wave is given by

$$\eta(x, t) = a \cos(\kappa x - \omega t), \quad (1.25)$$

where a is the amplitude, κ is the wavenumber ($\kappa = 2\pi/\Lambda$ where Λ is the wavelength) and ω is the radian frequency ($\omega = 2\pi f$ where f is the wave frequency). The relationship between ω and κ is defined by the dispersion relation for linear deep water waves

$$\omega^2 = g\kappa + \frac{\gamma\kappa^3}{\rho}, \quad (1.26)$$

where ρ is the density of water, γ is the surface tension at the air–water interface and g is the acceleration due to gravity.

Support for the idea that small-scale gravity-capillary waves are important in gas transfer is given by Jähne *et al.* [1987], who reported that k may be best parameterized by the total mean-square wave slope, $\langle S^2 \rangle$. In Figure 1.4 from [Jähne *et al.*, 1984], gas transfer and wave slope data were compared from the small and large annular facilities in Heidelberg and the

large linear IMST facility in Marseilles. Figure 1.4a highlights the comparison by plotting k_{600} versus the mean-square capillary wave slope ($f > 14$ Hz; $\Lambda < 1.7$ cm), $\langle S^2 \rangle_c$. For a given transfer velocity, $\langle S^2 \rangle_c$ decreased as the size of the facility increased. However, in Figure 1.4b, k_{600} and the total mean-square wave slope, $\langle S^2 \rangle$, were similarly correlated for all three facilities, suggesting that the capillary waves did not dominate the gas transfer process. This comparison showed that k was not parameterized best by the mean-square capillary wave slope, since $\langle S^2 \rangle_c$ was considerably lower in the linear IMST facility than the small annular facility even though the gas transfer velocities were similar. At short fetches and low wind speeds in the IMST facility, $\langle S^2 \rangle_c$ showed considerable variation, while $\langle S^2 \rangle$ was fetch independent (for fetches of 4.6 m, 9.4 m, 21 m, and 30.9 m). Furthermore, the values and trends of both $\langle S^2 \rangle$ and k_{600} were well matched in all three facilities. This is notable since the wave behavior was very different in the three wind-wave tunnels. While the linear facility was characterized by a dominant gravity wave, the smaller facilities showed much more widely distributed wave frequencies. Momentum is added to the wave field by the wind stress and the energy is transferred to waves of all scale through nonlinear wave-wave interactions and dispersion. Therefore, Jähne *et al.* [1987] suggested that waves of all scales contribute to an energy cascade that eventually produces near-surface turbulence, thus enhancing k .

Figure 1.5 from Frew [1997] shows that the correlation between the gas transfer velocity, k_{470} , for O_2 at 20°C ($Sc = 470$) and $\langle S^2 \rangle$ is robust over a wide range of wind speeds, supporting the contention made by Jähne *et al.* [1987] that k is parameterized best by $\langle S^2 \rangle$. Moreover, the results in Figure 1.5 are independent of surfactant concentration, suggesting that wave-related parameters are able to integrate the effects of surfactant on gas transfer. Bock *et al.* [1999] performed careful experiments of wind-waves on clean and surfactant-influenced water surfaces in two annular wave tanks of very different scale. Figure 1.6 shows the dependence of the transfer velocity, k_{600} , determined from O_2 referenced to $Sc = 600$, on the mean square slope

of the waves for different wavenumber ranges, for both tanks and all surface conditions. Table 1.1 gives the notation for the mean square slope for the various wavenumber ranges, the wavenumber ranges, and the root-mean-square (RMS) error in the linear fits between k_{600} and the mean square slope for the particular wavenumber range shown in Figure 1.6. The gas transfer velocity showed the best correlation with $\langle S^2 \rangle$ in Figure 1.6a based upon the RMS error, and this correlation is independent of surfactant concentration, consistent with the results of *Frew* [1997] in Figure 1.5. Among particular wavenumber ranges, k_{600} showed a correlation with $\langle S^2 \rangle_{200}$ (shortest wind waves) in Figure 1.6d that was almost as good as with $\langle S^2 \rangle$ in Figure 1.6a, and showed the worst correlation with $\langle S^2 \rangle_{50}$ (longer wind waves) in Figure 1.6b. Therefore, *Bock et al.* [1999] suggested that both surfactants and the shorter capillary waves play an important role in gas transfer processes, and that the longer waves are not directly related to gas transfer.

Waves are damped by surfactants to varying degree depending on the wavelength and the level of surface contamination [*Lucassen*, 1982]. The magnitude of maximum damping and the wavelength at which this maximum occurs are known to decrease with decreasing surface dilational modulus. The surface dilational modulus describes the resistance of the surface to a change in surface area and is a function of the film pressure, or the difference between the surface tension of a clean and surfactant-influenced surface. *Bock et al.* [1999] observed that the degree of saturation (slope spectrum times κ^2) would drop up to 3 orders of magnitude for high wavenumbers ($\kappa > 200 \text{ rad m}^{-1}$) depending on the concentration of surfactant and the friction velocity, while the clean surface values remained high for all κ . Therefore, the high correlation between k and $\langle S^2 \rangle_{200}$ regardless of surfactant concentration observed by *Bock et al.* [1999] suggests that by measuring the shorter wave components, the influence of surfactants on the surface boundary condition is monitored.

1.3.3 FETCH DEPENDENCE OF THE TRANSFER VELOCITY

In the linear IMST wind-wave facility, Jähne *et al.* [1987] observed a significant fetch dependence of $\langle S^2 \rangle_c$ at short fetch, even though $\langle S^2 \rangle$ was fetch independent. Since the gas transfer velocity is hypothesized to be linked to the wave field and k correlates well with the mean square slope, Jähne *et al.* [1989] investigated the fetch dependence of k and its relationship to $\langle S^2 \rangle$ in the linear wind-wave facility at the University of Karlsruhe. For four different wind speed regimes, Figure 1.7 shows (a) the ratio of the transfer velocity at a given fetch, Ω , to that at 8 m fetch, $R_{\Omega/8}$, versus fetch and (b) $\langle S^2 \rangle$ versus Ω . The fetch was effectively varied between 2 m and 8 m by leaving the instrumentation in place while covering the appropriate amount of water surface area from the entrance of the wind into the flume. Figure 1.7a shows that at the highest wind speed, no significant change is observed in R_{Ω} . As the wind speed decreased, the reduction in $R_{\Omega/8}$ for decreasing fetch became more pronounced. The maximum reduction in gas transfer occurred at the shortest fetch (2 m) with a decrease in $R_{\Omega/8}$ of nearly 35% for the lowest wind speed. However, for the fetch of 6 m relative to 8 m, only a 10% to 15% decrease in k was observed. Figure 1.7b shows that the behavior of $\langle S^2 \rangle$ as a function fetch and wind speed is similar to k . Overall, as the wind speed increased, less dependence of $\langle S^2 \rangle$ on fetch was observed. From $\Omega = 2$ m to $\Omega = 6$ m the $\langle S^2 \rangle$ increased with fetch. However, Figure 1.7b shows negligible change in $\langle S^2 \rangle$ between 6 m and 8 m, consistent with the observation of Jähne *et al.* [1987] that $\langle S^2 \rangle$ was independent of fetch in the IMST facility at Ω greater than 4.6 m. The fetch dependence of k in Figure 1.7 appeared to be related to the development of the wave field. Therefore, the dependence of k on fetch was restricted to short fetches and low wind speeds. These results, coupled with the observations from the IMST facility, suggest that at longer fetch the dependence of k on fetch is negligible if the change in $\langle S^2 \rangle$ is negligible.

Though inconclusive as to whether $\langle S^2 \rangle$ or $\langle S^2 \rangle_c$ is a better correlate for k , the studies surveyed in section 1.3 suggest that considering wave-related parameters may lead to

improved gas transfer models. Moreover, discrepancies among laboratory and field results may be overcome by correlating k with the appropriate wave-related parameters instead of wind speed. However, as pointed out by *Back and McCready* [1988], a primary problem with attempting to directly correlate k with wave spectral scales (i.e., capillary or total wave slope) is that the velocity spectrum may not possess the same amplitude-frequency characteristics as the wave spectrum. Since it is the velocity fluctuations normal to the interface which are important to gas transfer, this correlative attempt may not be appropriate. A more fundamental approach is to determine the mechanism responsible for the observed enhanced gas transfer in the presence of waves.

1.4 WAVE MECHANISMS FOR GAS TRANSFER

1.4.1 MECHANISMS FOR GAS TRANSFER BY CAPILLARY WAVES

Mechanisms for the enhancement of gas transfer by waves span the scales from capillary wave effects to turbulence and bubbles generated by large-scale wave breaking. Modulation of the diffusive boundary layer by capillary waves [*Witting*, 1971] and their subsequent interaction with near-surface turbulence (modeled as surface renewal) [*Szeri*, 1997] has been shown theoretically to significantly enhance gas transfer. Experiments on standing capillary waves of wavelengths ranging from 2.26 – 3.96 mm, isolated from any obscuring effects, have shown transfer rates to increase by two orders of magnitude over the case without waves [*Saylor and Handler*, 1997]. The transfer velocity increases rapidly with increasing wave slope and with decreasing wavelength, and k is shown to be comparable to results from larger wind-wave facilities with waves from a broader spectrum of scales. Capillary waves also have been postulated to produce large turbulent vertical velocities by a wave-induced shear variation mechanism, resulting from the nonlinear interaction between the orbital motions of capillary waves and the drift shear current [*Coantic*, 1986; *Back and McCready*, 1988]. These results

indicate that capillary waves have the potential to transport significant amounts of gas locally. *Donelan* [1995], however, suggests that the dominant scales for waves effective in gas transfer range from 1 – 10 Hz frequencies (1.56 – 0.024 m wavelengths) according to the spectral distribution of the kinetic energy dissipation and that wave breaking is the likely source for this distribution.

1.4.2 WAVE BREAKING AS A MECHANISM FOR GAS TRANSFER

The role of deep-water wave breaking in limiting wave growth and as a source of turbulent mixing has motivated a rich and continuing history of research on the importance of breaking waves in air–sea interaction [*Banner and Phillips*, 1974; *Thorpe*, 1995; *Melville*, 1996]. In general, wave breaking is the process by which water particles near the wave crest develop a horizontal velocity that exceeds the speed of the crest and overtake the form of the wave. According to this kinematic criterion, the portion of the fluid near the crest becomes turbulent as it spills down the forward slope thereby losing its potential energy, and ultimately leaves behind a decaying turbulent wake [*Banner and Peregrine*, 1993]. In this context, breaking waves that entrain air and thereby produce whitecaps are simply the most intense and visibly obvious type of a phenomenon that occurs over a wide range of scales. *Banner and Phillips* [1974] coined the term "micro-breaking" to describe the breaking of very short gravity waves without air entrainment, noting that micro-breaking, or microscale breaking, is far more widespread than whitecapping. The widespread occurrence of microscale wave breaking suggests that its cumulative effect on the fluxes of heat and gas across the air–sea interface may be significant, especially for moderate wind speeds [*Banner and Peregrine*, 1993; *Donelan*, 1995; *Melville*, 1996].

Since breaking waves of all scales disrupt the diffusive sublayer that regulates the flux of gas across the air–sea interface, near-surface turbulence generated by wave breaking has

been proposed as a significant mechanism for air–water gas transfer. *Kitaigorodskii* [1984] submitted that the gas transfer rate is determined primarily by large-scale breaking waves that produce whitecaps. *Kitaigorodskii* [1984] proposed a model for the gas exchange similar to (1.17) that includes turbulent patches generated by large-scale breaking waves as the main source for near-surface turbulence at high wind speeds. The inclusion of dissipation due to wave breaking as the mechanism for turbulent kinetic energy dissipation demonstrated a corresponding increase in the rate of gas transport. Although no direct link has yet been established, measurements of the near-surface layer show very high rates of kinetic energy dissipation, up to two orders of magnitude greater than the law-of-the-wall scaling, beneath strongly forced and breaking wind-generated waves [*Kitaigorodskii et al.*, 1983; *Agrawal et al.*, 1992; *Terray et al.*, 1996]. Furthermore, bubble plumes produced by air entrainment generated by large-scale breaking waves accompany these local patches of intense turbulence and have been suggested to significantly enhance air–sea gas fluxes at higher wind speeds [*Wallace and Wirick*, 1992; *Farmer et al.*, 1993]. The enhancement of the air–water gas flux due to bubble plumes above 12 m s⁻¹ wind speeds [*Thorpe*, 1982] may exceed the effect of turbulence patches as modeled by *Kitaigorodskii* [1984]. However, a distinct enhancement of gas transfer also occurs well before the onset of breaking waves that produce bubbles, leading *Jähne et al.* [1987] to suggest that all scales of waves act as an additional source for near-surface turbulence. Microscale wave breaking is a likely candidate for the transfer of energy from the wave field to near-surface turbulence at low to moderate wind speeds and consequently the enhanced air–sea gas exchange.

Low visual contrast due to the absence of air entrainment makes microscale breaking waves difficult to identify, while their small scale makes quantitative measurements especially challenging. The diagram and video image in Figure 1.8 illustrate the typical features of microscale breaking waves. The defining characteristic of microscale wave breaking is a bore-like crest accompanied by parasitic capillary waves distributed along the forward face.

Microscale breaking waves are typically described as $O(10^{-1} - 1 \text{ m})$ in length and a few centimeters in amplitude. In laboratory wind-wave studies, *Okuda* [1982] and *Ebuchi et al.* [1987] identified a "high-vorticity region" near the crests of gravity waves with capillary ripples generated ahead of the crests. The origin of vorticity within this surface "roller" has been identified by *Longuet-Higgins* [1992] as the accompanying parasitic capillary waves, which themselves generate fluid rotation (i.e., vorticity) via the surface-tension effect [*Yeh*, 1992; *Yeh*, 1995]. Rollers [*Longuet-Higgins*, 1992], breaking wavelets [*Csanady*, 1990], and steep wind waves accompanied by a high-vorticity layer near the crest [*Okuda*, 1982] are all descriptions of phenomena which are identified with the "micro-breaking" described by *Banner and Phillips* [1974]. For consistency and convenience, the general description of breaking offered above is adopted and "microscale breaking waves" is used to describe very short, wind-generated gravity waves that break without entraining air.

The established importance of waves to gas transfer, combined with the ability of wave breaking to generate near-surface turbulence, implies that microscale wave breaking may indeed be a likely mechanism for enhancing k . Furthermore, the steep slopes associated with microscale wave breaking in Figure 1.8 suggest that this mechanism may provide the link between the relationship of k with wave slope. Under moderate wind speed conditions, *Csanady* [1990] proposed that microscale wave breaking, or the breaking of very short gravity wind waves without air entrainment, controls air-water gas transfer. The specific manner by which microscale wave breaking controls k has been theorized to be the thinning of the concentration boundary layer by the intense surface divergence generated during the breaking process [*Csanady*, 1990]. The work by *Csanady* [1990] to model the effect of microscale wave breaking on gas flux resulted in

$$k = \phi \beta u_* Sc^{-1/2}, \quad (1.27)$$

where β is a dimensionless constant and ϕ is the fractional surface area covered by wave-induced divergence, that is, where the diffusion boundary layer becomes thin due to microscale breaking waves. This is similar to the result in (1.18) with an $n = 1/2$. *Csanady* [1990] estimated a value of at least 0.20 for ϕ based on measurements reported by *Jähne et al.* [1987]. The difficulty in substantiating this hypothesis lies in the detection and quantification of microscale wave breaking because the phenomenon lacks the visible manifestation of whitecapping. Previous infrared measurements of turbulent disruptions of the thermal boundary layer, or skin layer, at the air–water interface suggest that microscale wave breaking events can be detected by using infrared imagery.

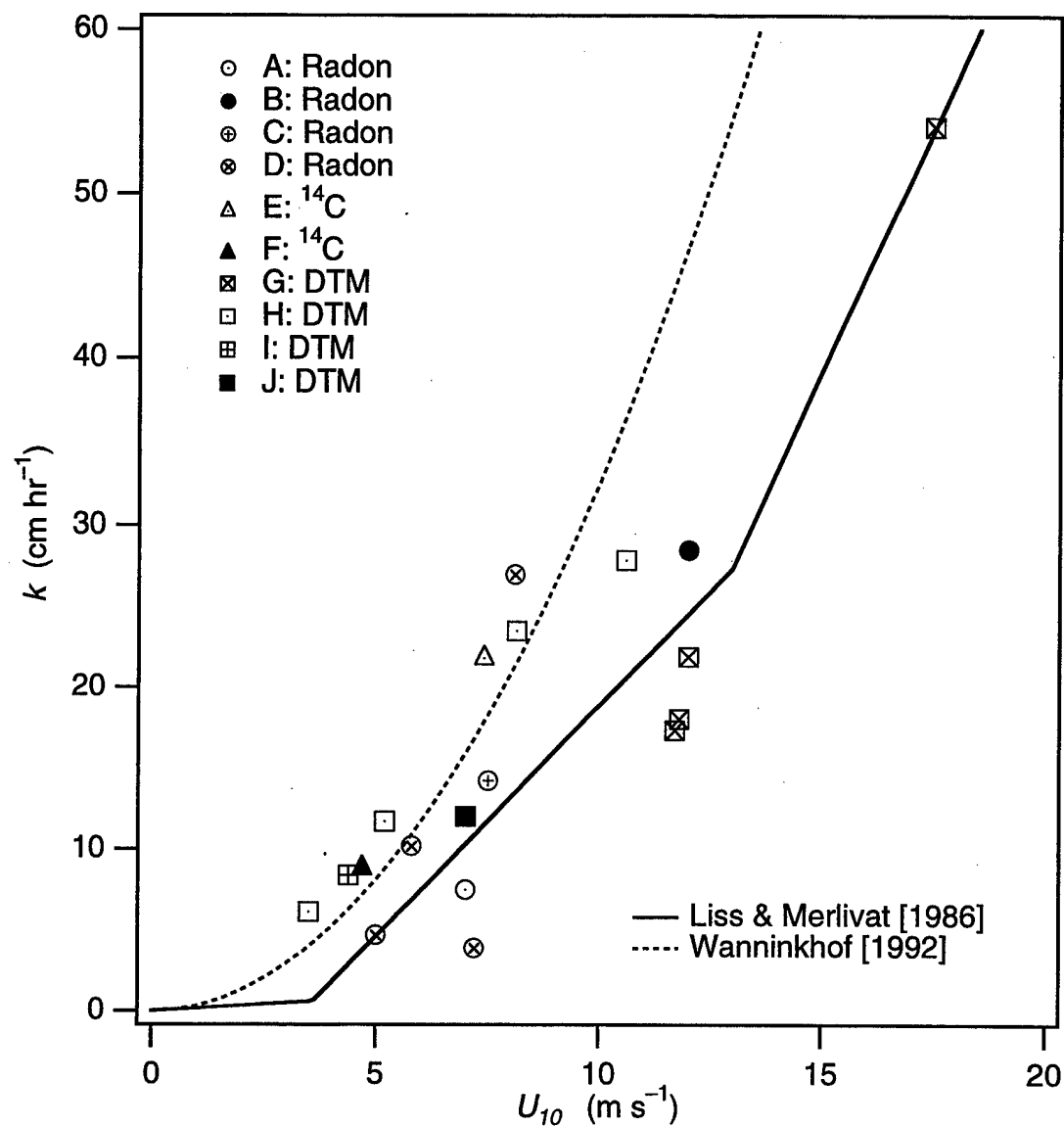


Figure 1.1. Measurements of oceanic gas transfer velocity, k , referenced to CO_2 at 20°C versus wind speed, U_{10} , referenced to a measurement height of 10 m. The wind speed parameterizations of k by Liss and Merlivat [1986] and by Wanninkhof [1992] are also plotted. Data shown were measured by the deliberate dual tracer method, by the bomb ^{14}C invasion method, and by the Radon method. The data key corresponds to: A, Broecker and Peng [1971]; B, Peng *et al.* [1974]; C, Peng *et al.* [1979]; D, Kromer and Roether [1983]; E, Broecker *et al.* [1985]; F, Cember [1989]; G, Watson *et al.* [1991]; H, Wanninkhof *et al.* [1993]; I, Wanninkhof *et al.* [1997]; J, Wanninkhof and McGillis [1999].

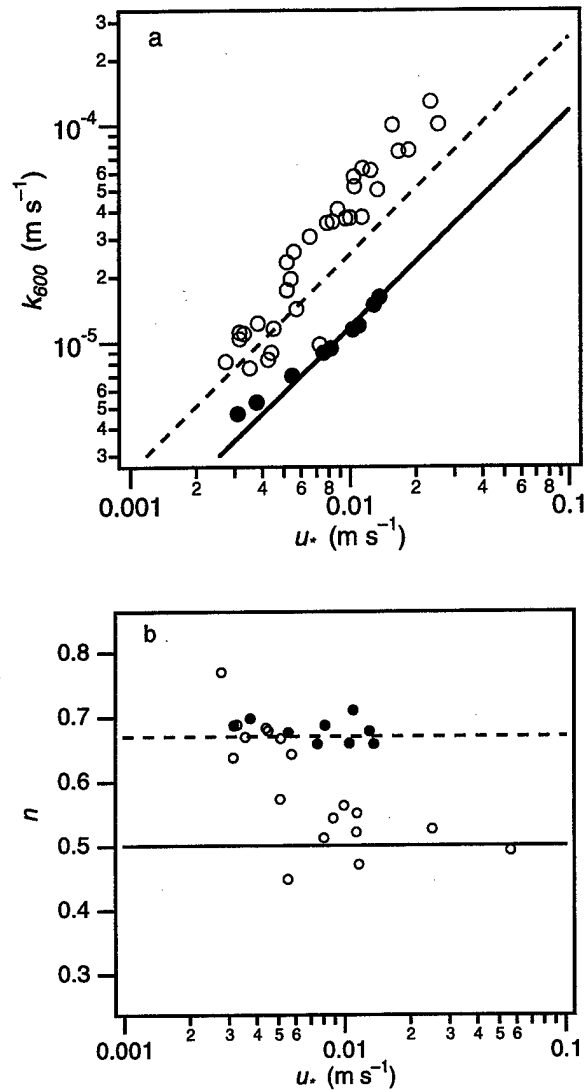


Figure 1.2. (a) Gas transfer velocity, k_{600} , referenced to $Sc = 600$ (CO_2 at 20°C) and (b) Schmidt number exponent, n , as a function of u_* . The measurements from experiments for a carefully cleaned water surface vividly show the enhanced transfer in the presence of waves, as compared to the data for a surfactant-influenced surface. The data shown are: solid circles, surfactant-influenced water surface in the small annular wind tunnel at Heidelberg (1.57 m circumference, 0.1 m width, 0.1 m depth); open circles, cleaned water surfaces in the small annular Heidelberg facility, the large annular Heidelberg facility (11.6 m circumference, 0.3 m width, 0.4 m depth), and the large linear IMST facility, Marseilles (40 m fetch, 2.6 m width, 1 m depth). The rigid wall and the free surface, or surface renewal, models are indicated by the solid and the short dashed lines respectively. (Redrawn from *Coantic* [1986].)

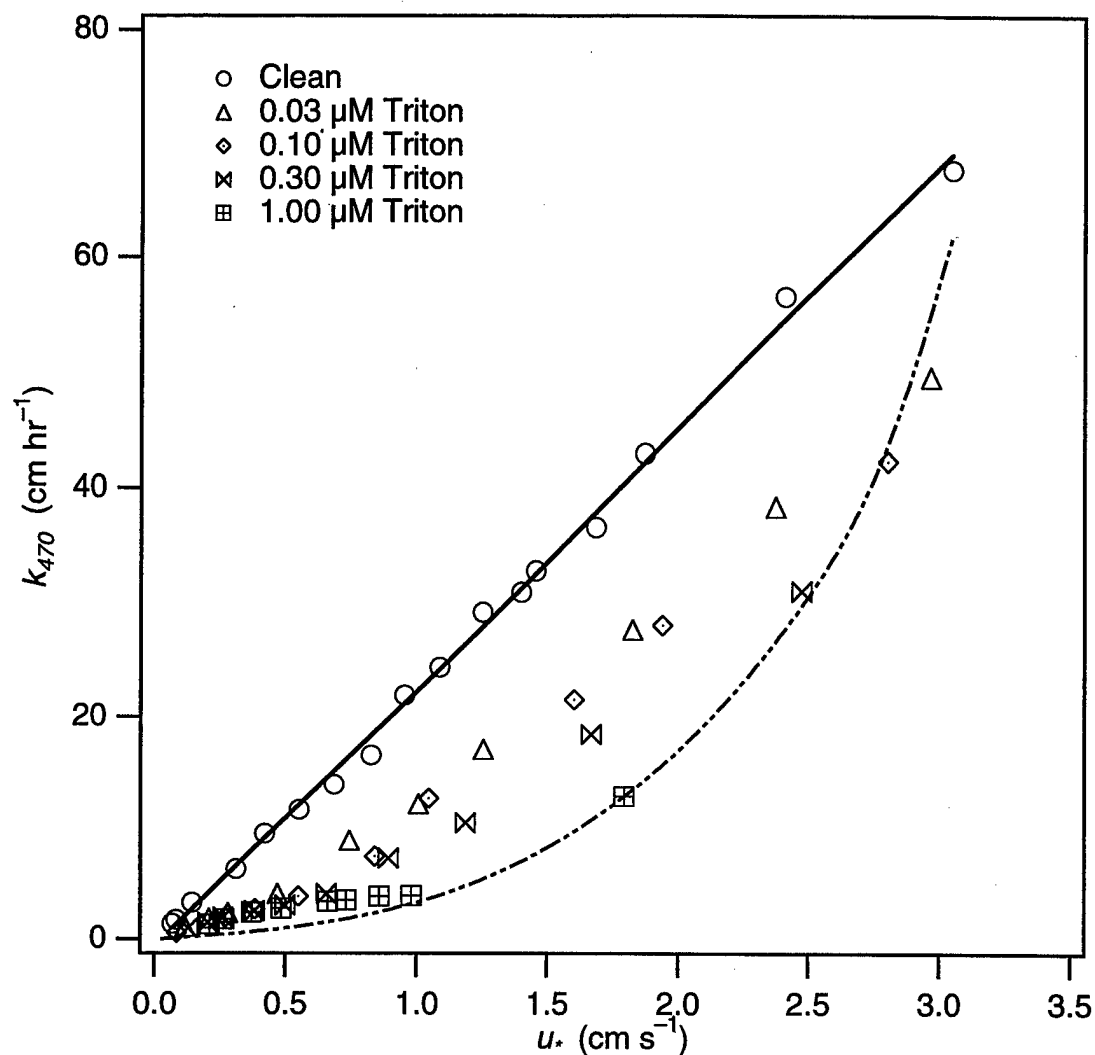


Figure 1.3. Gas transfer velocity, k_{470} , for O_2 at 20°C ($Sc = 470$) as a function of u_* for a clean surface and for surfaces modified by different concentrations of Triton X-100. The solid line is a fit through the clean surface data and the dashed-dotted line is a fit through the data for $U = 9 \text{ m s}^{-1}$. The data were taken in the small annular wind tunnel at Woods Hole Oceanographic Institution (1.57 m circumference, 0.1 m width, 0.1 m depth). (Redrawn from *Frew et al.* [1995].)

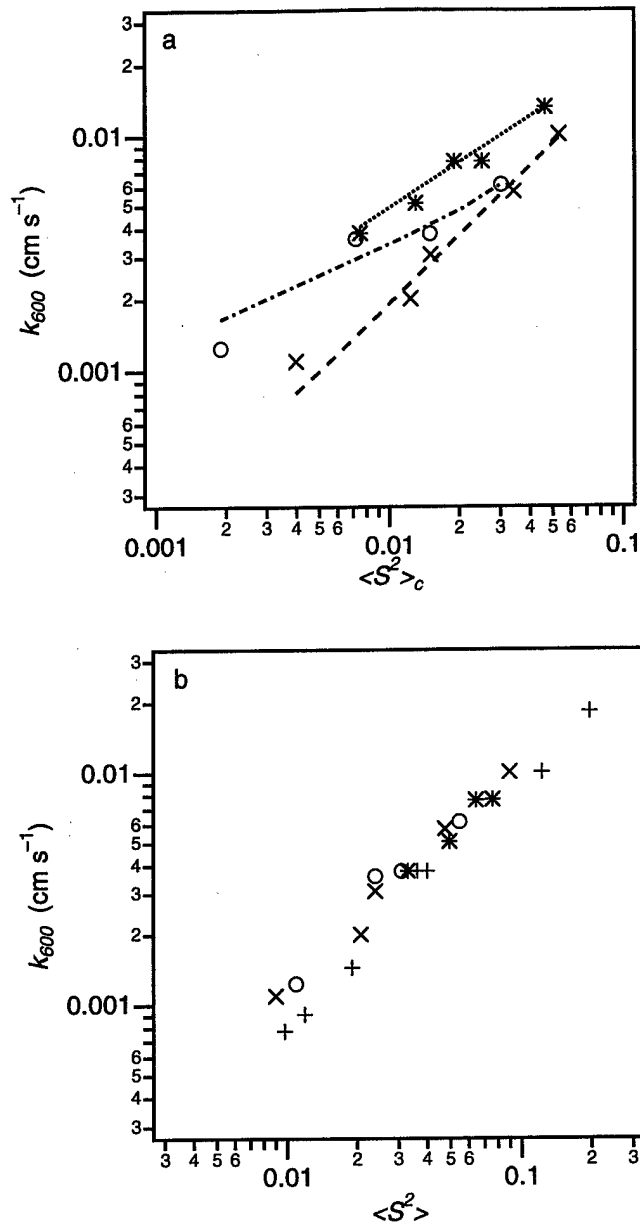


Figure 1.4. (a) Gas transfer velocity, k_{600} , referenced to $Sc = 600$ (CO_2 at 20°C) as a function of mean-square capillary wave slope ($f > 14$ Hz; $\Lambda < 1.7$ cm), $\langle S^2 \rangle_c$. (b) Gas transfer velocity, k , as a function of total mean square wave slope, $\langle S^2 \rangle$. The data shown are: + cleaned small annular Heidelberg facility (5 cm water depth); x, cleaned small annular Heidelberg facility (8 cm water depth); o, cleaned large annular Heidelberg facility; *, cleaned large linear IMST facility, Marseilles. (Redrawn from Jähne *et al.* [1984].)

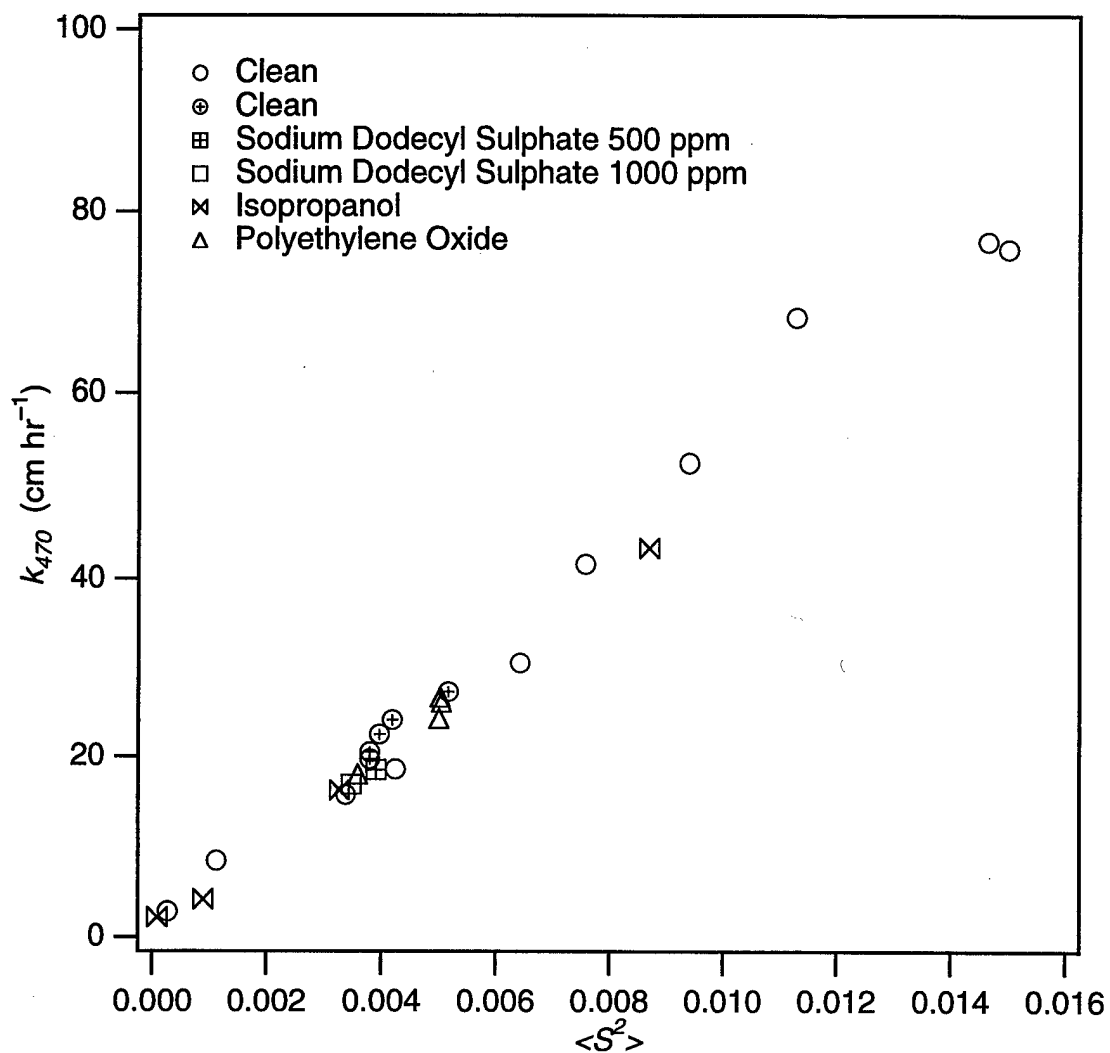


Figure 1.5. Correlation of gas transfer velocity, k_{470} for O_2 at 20°C ($Sc = 470$) with total mean-square slope, $\langle S^2 \rangle$, for a range of wind speeds (rotor speeds ranged from $1 - 9 \text{ m s}^{-1}$), surface conditions, and contaminants. (Redrawn from Frew [1997].)

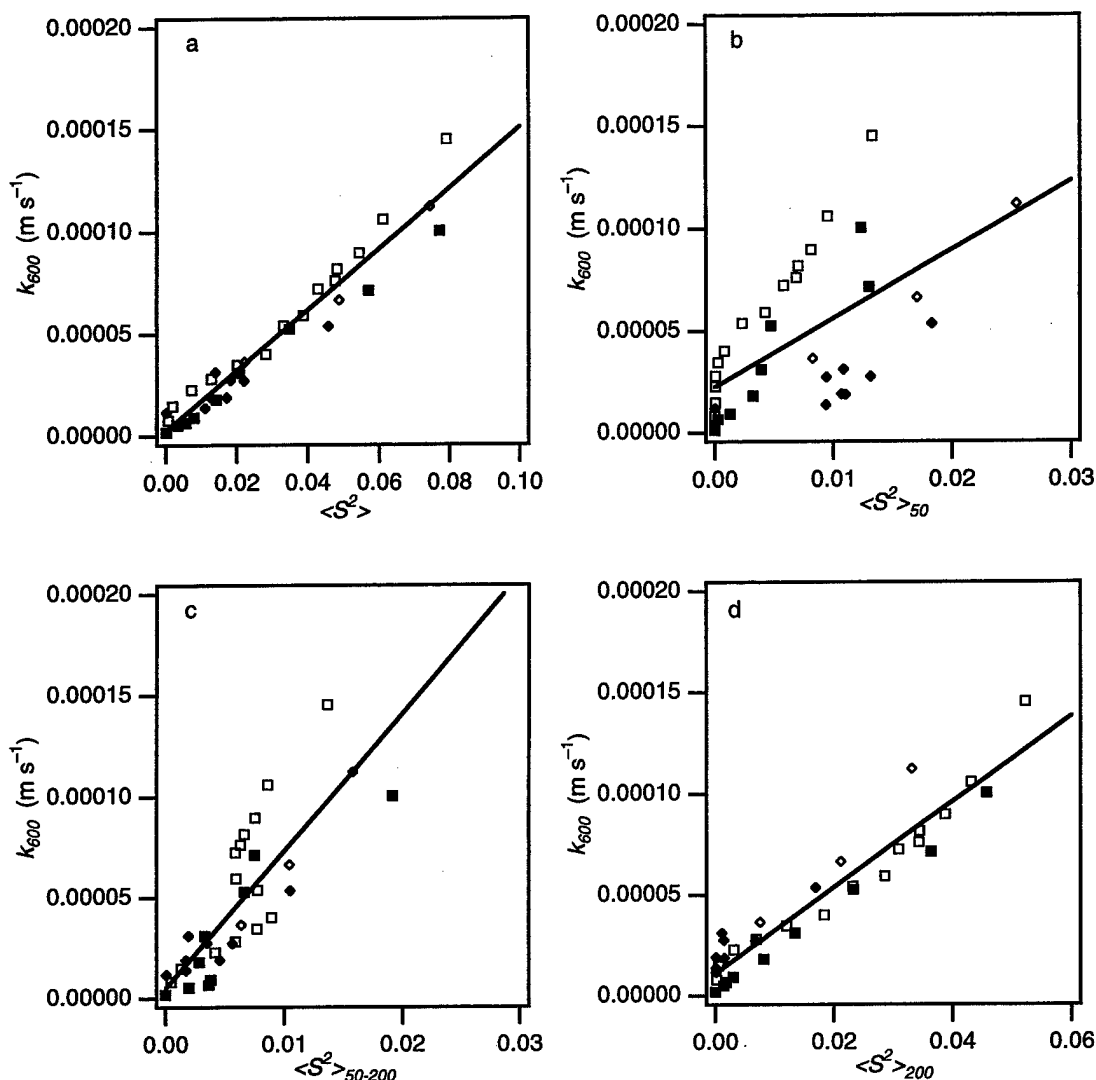


Figure 1.6. Gas transfer velocity, k_{600} , determined from O_2 referenced to $Sc = 600$ as a function of various measures of the mean square slope for a clean surface and for surfaces modified by the surfactant Triton X-100. The data were taken in the small annular wind tunnel at Woods Hole Oceanographic Institution (squares) and the large annular tank in Heidelberg. Open squares, small annular wind tunnel with clean water; filled squares, small annular wind tunnel with surfactant; open diamonds, large annular wind tunnel with clean water; filled diamonds, large annular wind tunnel with surfactant. Solid line is the best fit to the observation. Mean square slope is calculated over: (a) all κ ; (b) κ below 50 rad m^{-1} ; (c) κ between 50 and 200 rad m^{-1} ; (d) κ above 200 rad m^{-1} . (Redrawn from Bock *et al.* [1999].)

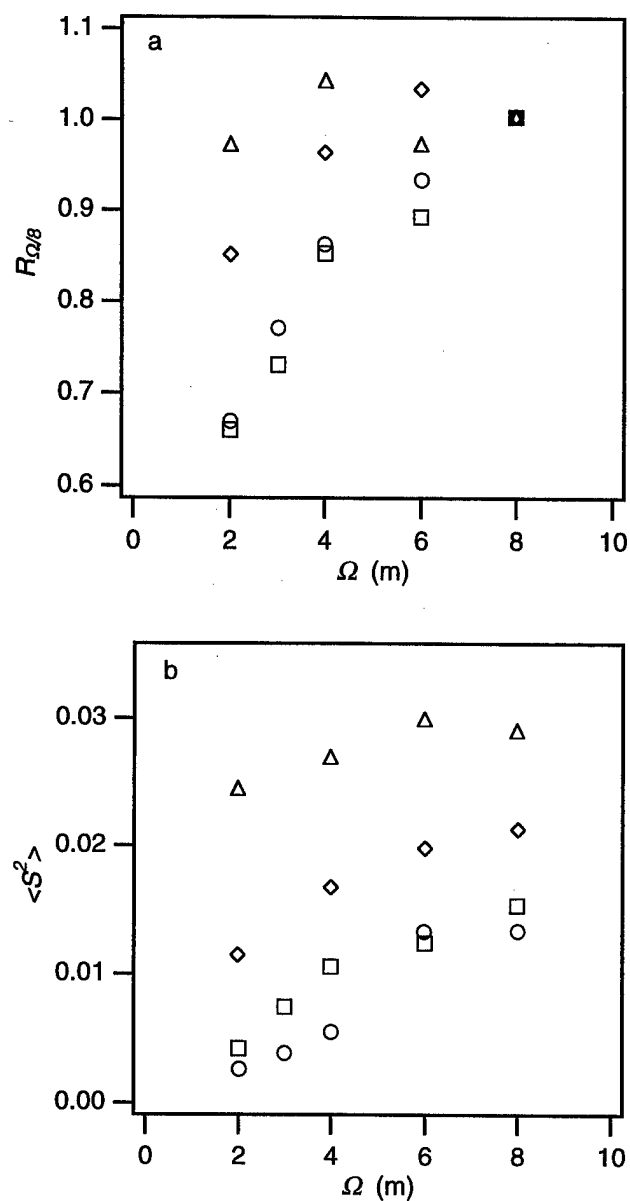


Figure 1.7. Dependence of k and $\langle S^2 \rangle$ on fetch, Ω . (a) Ratio of the heat transfer velocity at a given fetch to the value at 8 m fetch, $R_{\Omega/8}$, versus Ω and as a function of wind speed. (b) Mean square slope of the waves, $\langle S^2 \rangle$, versus Ω and as a function of wind speed. The symbol key for the wind speed regimes: circles, $3.2 < U < 4.2 \text{ m s}^{-1}$; squares, $4.2 < U < 5.6 \text{ m s}^{-1}$; diamonds, $5.6 < U < 6.7 \text{ m s}^{-1}$; triangles, $6.7 < U < 7.7 \text{ m s}^{-1}$. (Redrawn from Jähne *et al.* [1989].)

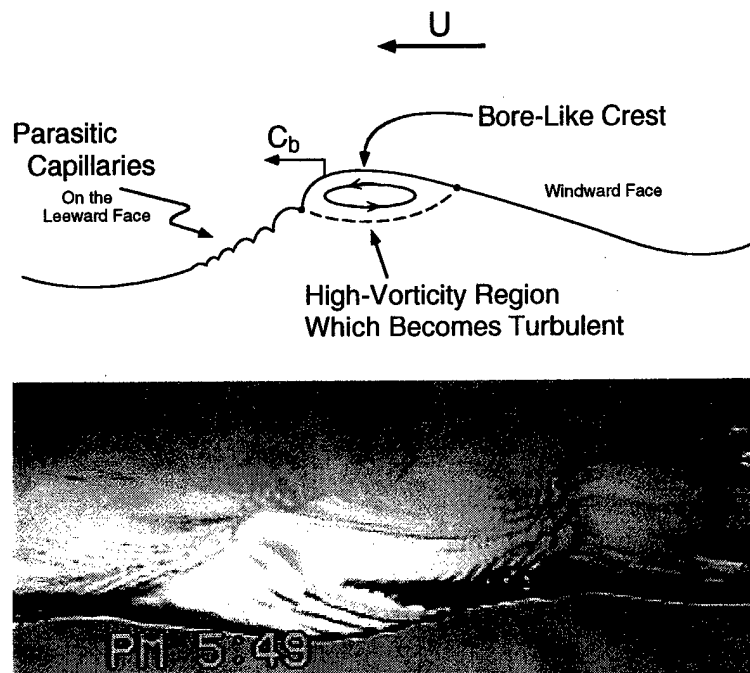


Figure 1.8. Top: The characteristic feature of a microscale breaking wave is a bore-like crest with parasitic capillary waves riding along the forward face; U is the wind speed and C_b is the crest speed of the microscale breaking wave. (Adapted from *Ebuchi et al.* [1987].) Bottom: Video image of a microscale breaking wave with a wavelength of roughly 0.1 m.

Table 1.1. Summary of the results from *Bock et al.* [1999] in Figure 1.6 giving the mean square slope notation, the wavenumber range analyzed, and the root-mean-square (RMS) error in the linear fit between k_{600} and mean square slope. $\langle S^2 \rangle$ is the total mean square slope, $\langle S^2 \rangle_{50}$ is the mean square slope integrated over wavenumbers less than 50 rad m⁻¹, $\langle S^2 \rangle_{50-200}$ is the mean square slope integrated over wavenumbers between 50 rad m⁻¹ and 200 rad m⁻¹, and $\langle S^2 \rangle_{200}$ is the mean square slope integrated over wavenumbers greater than 200 rad m⁻¹.

Mean Square Slope	Range of κ (rad m ⁻¹)	Range of Λ (cm)	RMS Error of the Fit
$\langle S^2 \rangle$	All measured	All measured	8.6×10^{-6}
$\langle S^2 \rangle_{50}$	< 50	> 12.56	2.8×10^{-5}
$\langle S^2 \rangle_{50-200}$	50 to 200	12.56 to 3.14	2.0×10^{-5}
$\langle S^2 \rangle_{200}$	> 200	< 3.14	1.0×10^{-5}

CHAPTER 2: THE SKIN LAYER AT THE AIR-WATER INTERFACE

2.1 IMAGING THE DYNAMICS OF THE SKIN LAYER IN THE INFRARED

Under most circumstances, a net upward heat flux, Q_N , from the ocean to the atmosphere occurs primarily by molecular conduction through a thermal boundary layer, or skin layer, at the ocean surface. As a result, the "skin temperature", T_s , at the top of this layer is typically of $O(10^{-1} \text{ }^\circ\text{C})$ cooler than the bulk water temperature, T_w , immediately below the skin layer [Katsaros, 1980; Robinson *et al.*, 1984]. This observed temperature difference across the thermal boundary layer at the ocean surface is defined as the bulk-skin temperature difference, $\Delta T = T_w - T_s$. An infrared radiometer is ideally suited for remotely measuring the skin temperature since the optical depth of $O(10^{-5} \text{ m})$ [McAlister, 1964; McAlister and McLeish, 1965] is much less than the skin-layer thickness, δ_T , of $O(10^{-3} \text{ m})$ [McAlister and McLeish, 1969; Wu, 1971; Hill, 1972]. Convincing evidence for the existence of the skin layer and T at the ocean surface was first provided by Ewing and McAlister [1960], who made infrared skin temperature measurements of the thermal recovery of surface disruptions produced by a pump and by breaking waves. Ewing and McAlister [1960] reported a range of skin-layer recovery times, t_* , from 5 to 40 s and that "a remarkable finding was that less intense disturbance of the water failed to produce measurable effects." This early insight, that the level of turbulence that disrupts the skin layer plays a significant role in the recovery process, is supported by the results of Jessup *et al.* [1997a].

2.1.1 INFRARED SIGNATURE OF LARGE-SCALE WAVE BREAKING

Disturbances of the skin layer by breaking waves have previously been observed with narrow field-of-view infrared radiometers [Ewing and McAlister, 1960; Gasparovic *et al.*, 1974; Simpson and Paulson, 1980]. Jessup *et al.* [1997a] presented a method for remotely quantifying the dynamics of surface-wave breaking, which uses an infrared imager to measure the temperature changes associated with the disruption and recovery of the skin layer. An infrared imager provides a time series of two-dimensional images of the skin temperature as inferred from the infrared radiance. Figure 2.1 shows a sequence of simultaneous infrared and video images of a breaking wave that was taken in the open ocean. The first three video images show the breaking wave propagating from right to left as it evolves from a narrow, curved ridge to an actively breaking crest, or whitecap. The first three infrared images show features of increased temperature that clearly correspond to the whitecap, which can be up to 0.1°C warmer than its wake. Part of the whitecap signature is probably an apparent temperature increase due to increased emissivity associated with surface roughness and bubbles [Eisner *et al.*, 1962]. Of primary interest here is the portion of the wake where the temperature changes are associated with the skin-layer disruption due to breaking-generated turbulence. In the fourth infrared image, a roughly circular region of increased temperature extends significantly beyond the area covered by the whitecap and residual foam in the corresponding video image. The extent and location of this warm patch imply that it corresponds to the turbulent wake of the breaking wave. Jessup *et al.* [1997a] reported open-ocean t_* values of $O(10^{-1} \text{ s})$ for decaying turbulent wakes of breaking waves similar to those in Figure 2.1. These t_* values increased linearly with the breaking crest speed, demonstrating that faster-moving waves dissipate more energy and produce more turbulence, resulting in longer skin-layer recovery times. Furthermore, they found that the skin-layer recovery rate in the wakes of breaking waves was correlated with a measure of the energy dissipation rate due to breaking.

2.1.2 INFRARED SIGNATURE OF MICROSCALE WAVE BREAKING

Similar to the skin-layer disruption by large-scale breaking waves that produce whitecaps, the infrared signature of the skin-layer disruption caused by microscale wave breaking may serve to define and characterize this visually ambiguous process. In this section, a brief overview of the infrared signature of microscale wave breaking is given. Chapter 3 is devoted to the details of defining and quantifying microscale wave breaking using infrared imagery. The conceptual model in Figure 2.2 portrays the disruption of this cool skin layer by a microscale breaking wave. Turbulence generated by the breaking process momentarily disrupts the skin layer and transports warmer water from below to the free surface such that the skin temperature within the resulting turbulent wake is approximately equal to the bulk temperature. As the turbulent wake subsides, the surface cools, and the skin temperature returns to its original value at a rate which increases with increasing ambient heat flux [Jessup *et al.*, 1995; Zappa *et al.*, 1998]. An infrared imager, therefore, is ideally suited to detect and quantify the renewal of surface water by individual microscale breaking events. This conceptual model suggests that thermal detection of microscale wave breaking may serve as a *de facto* definition of the phenomenon itself.

Figure 2.3 shows a sequence of simultaneous, co-located video and infrared images of wind waves taken at the wind-wave tank at the Harris Hydraulics Laboratory (Harris) at the University of Washington (UW). The sensors were directed at the surface at an incidence angle of 30° , the image size is roughly $0.6 \text{ m} \times 0.3 \text{ m}$, and the time between images is 0.16 s. The wind speed was 6.3 m s^{-1} at a fetch of 5 m, and the wind direction in Figure 2.3 is from top to bottom. Wave crests appear as dark, roughly horizontal lines in the video image. A crescent-shaped patch of higher temperature appears at the top of the first infrared image; this patch corresponds to the wave front labeled A in the first video image. This patch grows and propagates down the tank as wave-front A continues to disrupt the thermal boundary layer. Fainter warm patches corresponding to the crests that follow A in the video images (labeled B

and C) are also evident in the infrared images. These signatures are typical of the infrared manifestations of microscale breaking that were observed here. As in this example, it has been noticed that successive crests tend to break periodically in a manner suggestive of wave breaking in groups [Donelan *et al.*, 1972]. Note that the individual crests labeled 1 and 2 in the video images do not show a corresponding thermal signature, implying that only a portion of the waves qualify as microscale breaking events. This observation suggests that the infrared signature of wave-induced skin-layer disruptions may be used to define microscale wave breaking. Also apparent in the bottom of the infrared images are dark streaks aligned with the wind direction. These features generally persist much longer than the wave period and may be an indication of secondary circulation related to the waves [Gemmrich and Hasse, 1992; Melville *et al.*, 1998].

Measurements by Jessup *et al.* [1997a] aboard R/P *Flip* provided an opportunity to observe microscale wave breaking in a field setting. Figure 2.4 shows two nighttime sequences of infrared images depicting examples of the disruption of the thermal boundary layer by microscale wave breaking. These disruptions produced temperature changes of 0.1°C , which were comparable to T measured independently. The imager was mounted 8 m above the mean-water level and directed toward the surface at an incidence angle of 30° . The image size is roughly $1\text{ m} \times 0.75\text{ m}$, and the time between images is 0.12 s. The wind speed measured at a height of 10 m, U_{10} , was roughly 6.6 m s^{-1} during the top sequence and 5.7 m s^{-1} during the bottom; the wind direction in the images for both sequences is from top to bottom. The significant wave height (SWH) measured 2.28 m in the top sequence and 2.14 m in the bottom, with peak swell frequencies, f_{ps} , of 0.070 Hz and 0.074 Hz respectively. The microscale breaking events have been thresholded and outlined in a manner similar to that used in Figure 3.1, described in Chapter 3. The top sequence depicts the evolution of a single event labeled J followed by the inception of a second event labeled K, while the bottom sequence shows multiple events throughout. In both cases, the microscale breaking appeared to occur as the orbital motion

of long waves augmented the surface drift. This description is suggestive of the mechanism proposed and measured in the laboratory [Phillips and Banner, 1974] in which the increased surface drift due to longer waves leads to microscale wave breaking.

2.2 CHARACTERIZING TRANSFER USING HEAT AS A TRACER

In an attempt to provide reliable field measurements of air-sea gas transfer velocity with high spatial resolution and short response time, Jähne and co-workers have developed two distinct techniques to infer gas transfer using heat as a proxy tracer [Haußecker and Jähne, 1995; Haußecker *et al.*, 1995; Jähne and Haußecker, 1998]. The first actively heats the water surface using a remote external source to produce measurable temperature differences and is known as the controlled flux technique (CFT). The second is a passive technique that utilizes the naturally occurring horizontal spatial variability of skin layer temperature as a result of surface renewal by near-surface turbulence, and is known as the spatio-temporal temperature fluctuation technique (STTFT). Both techniques use an infrared imager to measure either the imposed (CFT) or existing (STTFT) temperature differences, and the magnitude or the rate of change of these temperature differences is used to infer k according to (1.2) or (1.15).

The controlled flux technique (CFT) was developed by Jähne *et al.* [1989] as a method to determine the local k with fast response times and high spatial resolution. In this technique, the transfer is assumed to be controlled by water-side processes and the heat flux across the air-water interface is assumed to be minimal [Jähne *et al.*, 1989]. Using a heat lamp or a CO₂ laser, a known flux density of heat is applied to the surface over an extended area. The change in steady-state temperature is measured by an infrared imager or radiometer to determine $\Delta c = \rho C_p \Delta T$ directly, where ρ and C_p are the density and specific heat of water, respectively. The heat transfer velocity is determined directly from (1.2). Models and experiments outlined in Chapter 1 have shown that the dependence of k on diffusivity can be expressed as the Schmidt

number of the gas raised to the power $-n$. This relationship expressed in (1.3) implies that if k is measured for a particular gas and the value of n is known, k for any other gas may be estimated using

$$k_1 = k_2 \left(\frac{Sc_1}{Sc_2} \right)^{-n}, \quad (2.1)$$

where the subscripts 1 and 2 represent the tracer species. Since both heat and gas are scalar tracers, *Jähne et al.* [1987, 1989] have asserted that the transfer velocity of heat should extrapolate directly to gases using (2.1). In this case, k_1 is the gas transfer velocity, k_2 is the heat transfer velocity, Sc_1 is the Schmidt of the gas and Sc_2 is the Prandtl number, $Pr = \nu/\alpha$, where α is the thermal diffusivity. Therefore, k_{600} determined from a gas, k_{600-G} , should equal k_{600} determined from heat, k_{600-H} , in this case the CFT (unless specified, the subsequent notation $k_{\#}$ refers to the transfer velocity determined from a gas and referenced to $Sc = \#$).

CFT also provides another estimate for k based upon the time scale of the transport processes, τ . Using a CO_2 laser in conjunction with an infrared imager, a locally heated spot on the water surface can be tracked within a sequence of infrared images. Following termination of the applied flux, τ is the time required for the temperature to reach equilibrium with the surrounding surface water. Specifically, the surface renewal rate is estimated from the decay curve of the heated spot as predicted from a simple surface renewal model [*Haußecker et al.*, 1995], and the heat transfer velocity is determined directly from (1.15). Details on the CFT will be given in section 5.4 and the CFT will be used in section 5.5 to quantify the transfer velocity inside and outside the wake of a microscale breaking wave.

Rather than impose a known applied flux to the water surface, *Haußecker* [1996] developed the spatio-temporal temperature fluctuation technique (STTFT), which exploits the

existing net heat flux across the air–water interface to estimate k . This technique assumes that the variability in the temperature distribution within an infrared image is produced by a vertical mixing process described by surface renewal. Based on the result from *Liu and Businger* [1975] that follows from the analogous thermal equations for surface renewal in (1.9), (1.10), and (1.14), the temperature difference as it grows between surface renewal events, $T(t)$, is given as

$$\Delta T(t) \propto -\frac{Q_N}{\rho C_p} \left(\frac{t}{\alpha} \right)^{1/2}, \quad (2.2)$$

where α is the thermal diffusivity. *Haußecker* [1996] developed a relationship between the expected value for $T(t)$, $E\{T\}$, and the standard deviation of the temperature distribution within an infrared image, σ_T . Therefore, the heat transfer velocity can be estimated by

$$k_H = -R_T \frac{Q_N}{\sigma_T \rho C_p}, \quad (2.3)$$

where R_T is defined as the ratio between $E\{T\}$ and σ_T , and has a value of 2.022 for a log-normal distribution of surface-renewal timescales that is independent of the surface renewal rate and Q_N [*Haußecker*, 1996]. The modeled surface temperature distribution determined using the log-normal distribution of surface-renewal timescales was shown to fit the data better than surface temperature distributions modeled from the exponential distribution of *Danckwerts* [1951] or the delta function of *Higbie* [1935]. While the STTFT has shown promise estimating k in the field [*Haußecker and Jähne*, 1995; *Haußecker*, 1996; *Jähne and Haußecker*, 1998], the method requires an accurate knowledge of the air–water heat flux, which is difficult to measure reliably on the open ocean [*Fairall et al.*, 1996].

Infrared cameras have also been utilized to remotely map the air-sea heat flux directly [McKeown and Leighton, 1999]. The mapping of heat flux capitalizes on the variation in the optical depth of water, which is inversely proportional to the absorption coefficient, as a function of wavelength of radiation [McAlister and McLeish, 1970; McAlister *et al.*, 1971]. Radiation at a wavelength with high absorption originates closer to the interface, as opposed to a wavelength with a lower absorption coefficient. Since Q_N is directly related to the thermal gradient across the skin layer, the differential radiation emitted from the water surface between two distinct wavelengths detected by the infrared imager produces a map of T , from which the heat flux can be inferred. McKeown and Leighton [1999] have implemented this technique successfully in the laboratory by calibrating the difference in radiation observed between two wavelengths using calorimetry data. In separate experiments, they observed heat flux variations on the order of 3 W m^{-2} due to 10-cm wavelength waves. They described the slow overturning surface renewal motions to be associated with increases in the heat flux behind the wave crests, suggesting that the surface had been thinned by some disturbance of the skin layer.

2.3 RELATIONSHIP BETWEEN SKIN LAYER DISRUPTION AND SURFACE RENEWAL

Hasse [1990] proposed that the thermal recovery time of the skin layer, t_* , may be used to estimate the characteristic surface-renewal time scale, τ , which forms the basis for surface-renewal bulk-flux models. Hasse's [1990] estimate of $\tau \approx 10 \text{ s}$, derived from typical ocean values of net heat flux and bulk-skin temperature difference, is comparable to the skin-layer recovery times measured by Ewing and McAlister [1960] and by Katsaros [1977], as well as to the air-sea exchange time scales inferred by Jähne *et al.* [1989]. However, Hasse's [1990] estimate for τ was significantly greater than t_* values measured by Jessup *et al.* [1997a] in the wakes of large-scale breaking waves on the open ocean, suggesting that large-scale turbulent

events may cause local increases in the surface renewal rate and that a fundamental difference exists between τ and t_* .

Classical surface-renewal theory used in models for the flux of gas [Danckwerts, 1951] and heat [Liu *et al.*, 1979] is based on the continuous random renewal of the surface by turbulent eddies from below. The idealized renewal process is one in which disruption is complete and instantaneous, and recovery begins immediately. The average age of fluid elements occupying the surface is taken as the characteristic time scale for surface renewal, τ , which also is interpreted as the mean time between successive surface-renewal events. In reality, a distribution of surface-renewal time scales, θ , exists for a turbulent interface based upon the surface renewal rate as modeled originally by Danckwerts [1951] in (1.13). Furthermore, not all renewal eddies produce fluid-parcel overturning at the surface as illustrated in Figure 2.5a and as described in random-eddy penetration models [Harriott, 1962]. Accordingly, the thickness of the skin layer, δ_T , varies over space and time as eddies intermittently penetrate the layer.

In contrast to the surface-renewal time scale, θ , the skin-layer recovery time, t_* , characterizes the diffusive process following disruption of the surface by a renewal eddy or other turbulent event. For a cool skin layer, Figure 2.5b illustrates how warmer bulk water mixes to the surface, so that immediately after a disruption the skin temperature, T_s , is approximately equal to the bulk temperature, T_w . As the turbulence gradually decays, T_s returns to its original value after a time t_* . At times, multiple renewal events successively disrupt the skin layer before the initial disturbance has had a chance to recover fully. Also, a sufficiently energetic and enduring disruption may delay the onset of recovery for a finite time. As the strength of the disturbance increases, the resulting increase in turbulence will force a longer t_* . While both the skin-layer recovery time and surface-renewal timescale are undoubtedly affected by turbulence, Figure 2.5b emphasizes the distinct difference between these two quantities. Whereas t_* represents a

response to a disruptive event and the decay of turbulence, θ reflects the timescale for physical replacement of surface water by turbulent eddies.

For shear-driven turbulence, δ_T can be related to the friction velocity in the water, u_* , through dimensional analysis by

$$\delta_T \propto \frac{\nu}{u_*}, \quad (2.4)$$

where ν is the kinematic viscosity and δ_T is assumed to be of the same order as the momentum boundary layer thickness. *Saunders* [1967] asserted that the average bulk-skin temperature difference, $\Delta T = T_b - T_s$, can be described by

$$\Delta T \propto -\frac{Q_N \delta_T}{K_T}, \quad (2.5)$$

where K_T is the thermal conductivity, and Q_N is the net heat flux across the skin layer (positive into the ocean). For a given Q_N , δ_T defines ΔT and is controlled by the near-surface turbulence intensity in the water. This interpretation of the dependence of ΔT on δ_T is consistent with the idea that the recovery of the skin layer is directly related to the decay of turbulence as observed by *Ewing and McAlister* [1960] and demonstrated by *Jessup et al.* [1997a]. *Zappa et al.* [1998] made measurements of the skin-layer recovery of free-surface wakes and breaking waves in the field and in the laboratory under conditions of varying Q_N and u_* . Their results show that the skin-layer recovery process depends not only on the strength of the disruption, but also on the net heat flux and the intensity of the background turbulence, as (2.4) and (2.5) imply.

Wick et al. [1996] have shown the similarity among theoretical models for ΔT when τ and δ_T are represented by the Kolmogorov time and length microscales as derived from the turbulent dissipation rate. Since τ , as well as δ and δ_T , is not constant as the nature of turbulence changes, *Soloviev and Schlüssel* [1994] proposed models for k and T based on a variable time scale for the surface-renewal process to account for the difference between turbulence generated in the free-convective [*Foster*, 1971] and shear-driven [*Csanady*, 1990] regimes. *Zappa et al.* [1998] have shown that while t_* values measured during free-convection conditions were comparable to the modeled τ , t_* did not describe the modeled τ well under shear-driven conditions. *Zappa et al.* [1998] suggested that for the shear-driven regime, energetic turbulent events such as breaking waves may enhance the surface-renewal rate within the wake of a skin-layer disruption. Resolution of this issue requires the study of the mechanisms responsible for the enhancement of surface renewal such as microscale and large-scale wave breaking in future modeling of s or τ , which are used to determine k .

Skin-layer disruptions associated with microscale wave breaking can be viewed as regions where the replacement of fluid within the concentration boundary layer is enhanced. It is this area of enhanced turbulence generated in the wake of a microscale wave that regulates the transfer of gas across the air-water interface. *Csanady's* [1990] instructive modeling work in (1.27) provides a point of reference for developing models of gas transfer that incorporate microscale wave breaking. In this dissertation, a model is suggested based upon the partitioning of k into two separate transfer velocities, one within the skin-layer disruptions in the wakes of microscale breaking waves and one outside the wakes in the background. The modeled transfer velocity based on this partitioning is given by

$$k_m = \phi k_B + (1 - \phi) k_{NB}, \quad (2.6)$$

where k_B is the transfer velocity in the wake of a microscale breaking wave, and k_{NB} is the transfer velocity in the background. This model requires the implementation of the CFT method to quantify the local k on short time scales inside and outside of the turbulent patches produced by skin-layer disruptions.

2.4 DISSERTATION OUTLINE FOR THE PRESENTATION OF DATA AND DISCUSSION OF RESULTS

This examination of gas transfer measurements and modeling has led to the hypothesis that microscale wave breaking, by generating near-surface turbulence, is a likely mechanism for enhancing k . The recently developed infrared imaging techniques first used to study large-scale wave breaking [Jessup *et al.*, 1997a] will be applied to quantify microscale wave breaking in Chapter 3. Two preliminary experiments were performed, one at the Canada Centre for Inland Waters (CCIW) wind-wave tank and one at the Harris wind-wave tank with a subsequent series of extensive measurements made at the Air-Sea Interaction Research Facility at NASA GSFC/Wallops Flight Facility (Wallops). The development of the infrared technique as it is applied to microscale wave breaking is discussed in Chapter 3, portions of which were excerpted from Jessup *et al.* [1997b]. Simultaneous and co-located infrared and slope imagery of laboratory wind waves are used to investigate if the disruption of the thermal boundary layer, or skin layer, occurs coincidentally with waves that have a steep forward face and a dimpled bore-like crest. The technique is used to detect the fraction of surface area, A_B , in which the thermal boundary layer is thinned and disrupted by microscale breaking waves. Preliminary measurements of near-surface coherent structures using particle image velocimetry are used to see if strong vortical structures near the crests of waves are associated with microscale breaking. Measurement of bulk gas transfer and A_B are discussed in Chapter 4 during the Harris I experiment. The bulk gas transfer velocity was correlated with A_B for varying degrees of surface

contamination. Chapter 5 discusses extensive measurements of bulk gas transfer, CFT-determined k , and A_B taken during the Wallops experiment and Chapter 6 discusses the measurements of wave slope. The CFT is used to investigate the role microscale wave breaking plays in directly enhancing k . Furthermore, the wave slope measurements were used to investigate the role that microscale wave breaking plays in the observed correlation of k with $\langle S^2 \rangle$. Conclusions are given in Chapter 7.

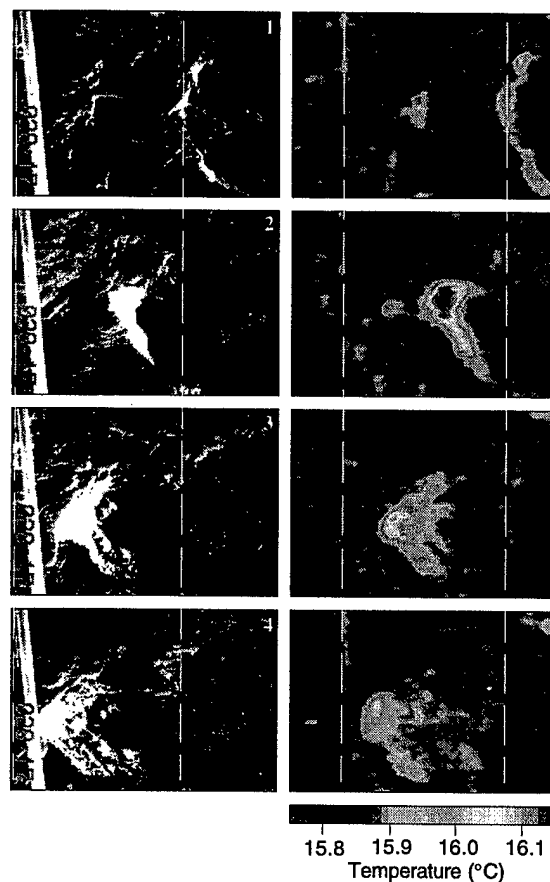


Figure 2.1. Sequence of simultaneous, co-located video images (left) and infrared images (right) of a breaking wave in the open ocean. Image size is approximately $5 \text{ m} \times 10 \text{ m}$. The breaking wave is propagating from right to left; time increases down the page and spans 1.6 s. For reference purposes, each image includes two dashed vertical lines corresponding to roughly the same locations; the right-hand line denotes the leading edge of the breaking wave crest in the first frame. The whitecap in the video images appears as the warmest region in the infrared images. After the crest spills, a roughly circular warm patch remains (infrared image 4) which is significantly removed from the area dominated by the whitecap and foam. The infrared signature of the turbulent wake results from the disruption of the cool skin layer by the breaking wave. For this example, the bulk-skin temperature difference was approximately 0.15°C and the wind speed was 7.7 m s^{-1} . The measurements were made aboard the research platform R/P *FLIP* off San Diego, California, using an infrared imager (Agema model 880LW) operating at wavelengths of 8 to $12 \text{ }\mu\text{m}$. The temperature differences between the wake and undisturbed regions of the ocean surface that were derived from the infrared imagery were consistent with independent measurements of the bulk-skin temperature difference.

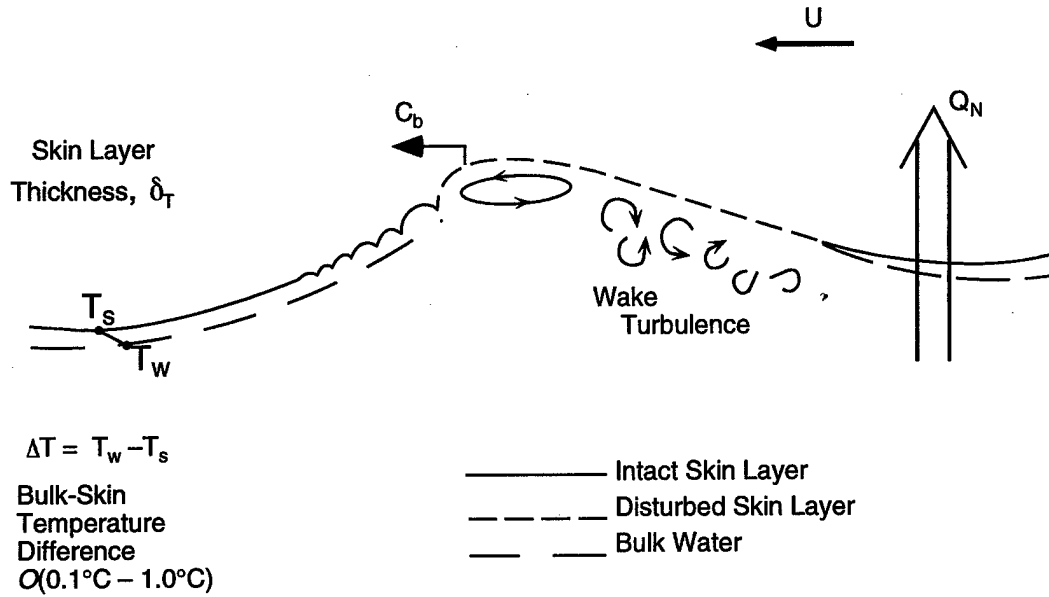


Figure 2.2. Conceptual model of disruption of the cool skin layer by a microscale breaking wave which leads to the thermal signature detectable by infrared imaging. The cool skin is disrupted and replaced by warmer bulk fluid from below. The bulk-skin temperature difference, T , across the cool skin layer of thickness, δ_T , is supported by the net heat flux, Q_N [Saunders, 1967].

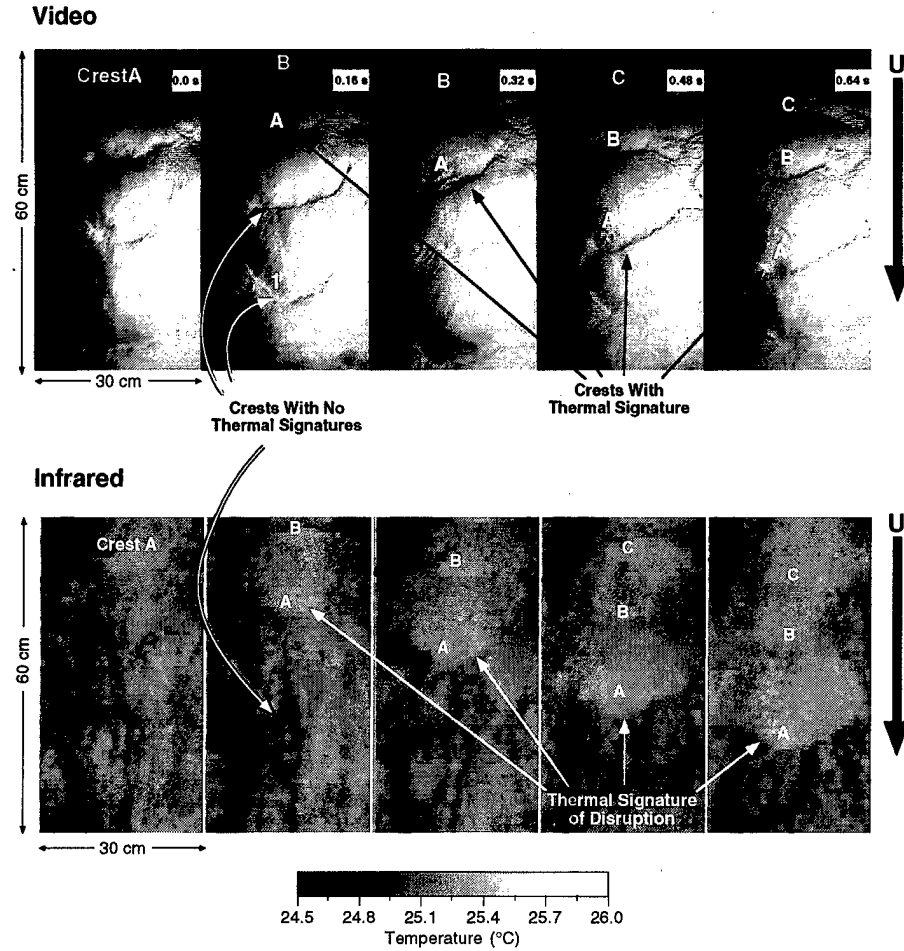


Figure 2.3. Simultaneous video images (top) and infrared images (bottom) of wind waves in the University of Washington wave tank that measured 9.1 m long, 1.2 m wide, and 0.9 m deep. Time increases from left to right in 0.16 s increments and the wind direction in the images is from top to bottom. Thermal features in the infrared images, taken with an Agema model 880 LW imager, are clearly associated with the wave crests labeled A – C in the video images and thus qualify as microscale breaking waves according to the conceptual model of Figure 2.2. Note that the crests labeled 1 and 2 have no detectable thermal signature, implying that not all waves are breaking. The bulk water temperature, T_w , was 25.8°C, the air–water temperature difference, ΔT_{aw} , was –7.3°C, the relative humidity, RH , was 53%, the frequency of the dominant wave, f_p , was 3.44 Hz (measured at the test section), the wind speed, U , was 6.3 m s^{–1}, and the fetch, Ω , was 5 m.

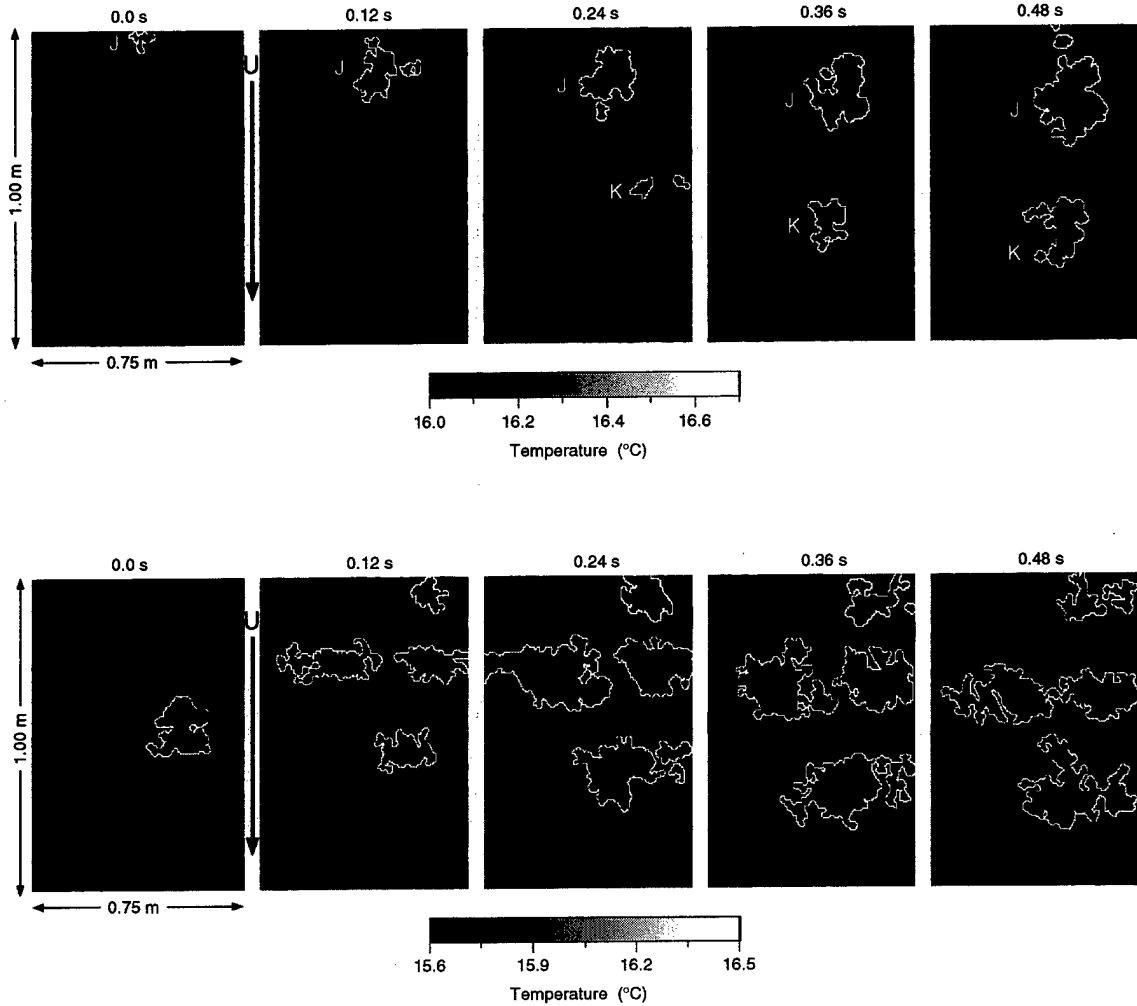


Figure 2.4. Nighttime sequences of infrared imagery demonstrating observations of microscale wave breaking aboard R/P *Flip* in September of 1995. Time increases from left to right in 0.12 s increments and the wind direction in the images is from top to bottom. The microscale breaking events within both sequences have been thresholded and outlined. These disruption events produce temperature changes of 0.1°C , which are comparable to an independently measured ΔT . Top: Evolution of a single event labeled J followed by the inception of a second event labeled K; $U_{10} = 6.6 \text{ m s}^{-1}$, $SWH = 2.28 \text{ m}$, $f_{ps} = 0.070 \text{ Hz}$. Bottom: Example of multiple microscale breaking events; $U_{10} = 5.7 \text{ m s}^{-1}$, $SWH = 2.14 \text{ m}$, $f_{ps} = 0.074 \text{ Hz}$. In both cases, the microscale breaking occurred as the orbital motion of long waves augmented the surface drift.

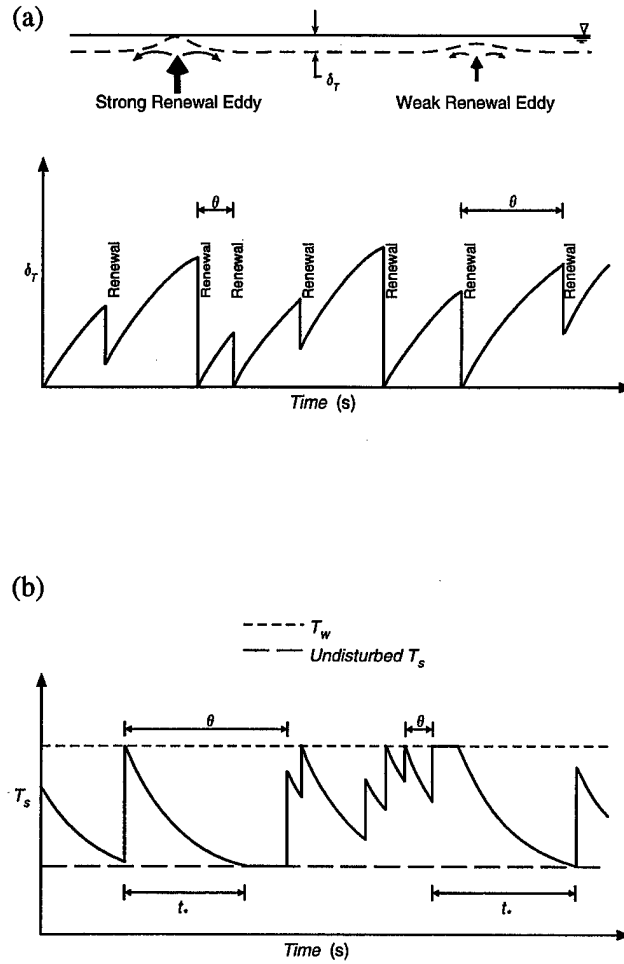


Figure 2.5. (a) Conceptual sketch (top) of the random-eddy penetration process [Harriott, 1962] occurring on the water side of the air-sea interface and a time series (bottom) of the thermal boundary layer thickness, δ_T , at a single location (adapted from Gulliver [1991]). Turbulent eddies intermittently penetrate the boundary layer, forcing δ_T toward zero and allowing the underlying water to mix to the surface. (b) Idealized time series of sea surface temperature, T_s , for a cool skin layer at a single location, illustrating the distinct difference between the skin-layer recovery time, t_* , and the surface-renewal time scale, θ . Skin-layer recovery is the response to a disruptive event. As the turbulence decays, T_s returns to its original value after a time t_* . In contrast, θ is the lifetime of a turbulent eddy at the surface.

CHAPTER 3: DEFINING AND QUANTIFYING MICROSCALE WAVE BREAKING USING INFRARED IMAGERY

3.1 INTRODUCTION

Measurements are presented during the Preliminary CCIW/Harris and Wallops experiments showing that microscale breaking waves produce thermal surface signatures that are consistently detected by infrared imaging techniques. Evidence from the literature suggests that the microscale breaking waves responsible for these thermal events are the source of the turbulent "bursting" structures observed beneath laboratory wind waves. The conceptual model presented in Figure 2.2, which explains the infrared observations, suggests that thermal detection of microscale wave breaking may serve as a de facto definition of the phenomenon itself. The results demonstrate that infrared techniques can provide the information necessary to quantify microscale breaking in order to determine its role in the exchange of heat and gas across the air-sea interface. Furthermore, infrared techniques should provide unprecedented details on the origin and evolution of microscale wave breaking.

In the course of the measurements at CCIW, which were focussed on large-scale breaking [Jessup *et al.*, 1995; Jessup *et al.*, 1997a], limited measurements of wind-generated waves (in the absence of large-scale breaking) revealed the infrared signature of microscale breaking waves. Because this experiment at the Canada Centre for Inland Waters (CCIW) in Burlington, Ontario, was not specifically designed to study microscale wave breaking, the quantitative measurements available at the time were for a narrow range of conditions. Furthermore, the video recordings of the water surface made at CCIW were inadequate to present visual details of the microscale breaking process. To provide quality flow visualization, the

CCIW measurements have been supplemented with video and infrared measurements taken under comparable conditions in a wind-wave tank at the Harris Hydraulics Laboratory (Harris) at the University of Washington (UW). As further support, extensive wave slope and infrared imagery were taken during a the study on the processes affecting air–water gas transfer at the Wallops Flight Facility (Wallops). The CCIW wave tank measured 10 m long, 0.3 m wide, and 0.4 m deep, the Harris tank measured 9.1 m \times 1.2 m \times 0.9 m, and the Wallops tank measured 18.29 m \times 0.9 m \times 0.75 m.

3.2 ANALYSIS OF THE OBSERVATIONS MADE DURING THE PRELIMINARY CCIW/HARRIS EXPERIMENTS

A simple thresholding analysis demonstrated the capability of infrared techniques to quantify the fraction of surface area affected by these microscale breaking events (see Appendix A). The preliminary analysis was performed on infrared imagery similar to that in Figure 2.3 but taken in the wind-wave facility at CCIW. The four runs of experimental data analyzed here consist of images taken at a rate of 25 Hz for a period of 300 s each. The wind speed was constant at approximately 5 m s⁻¹ at a fetch of 6 m. The heat flux was varied by controlling the air–water temperature difference while the relative humidity remained constant at 64%. Temperature thresholds based on the mean surface temperature, $\langle T \rangle$, and the bulk–skin temperature difference, T , were used to identify the disrupted area (taking into account the slow decrease in $\langle T \rangle$ over the course of the run due to cooling). The mean bulk–skin temperature difference, T , was computed as the mean difference between the maximum and mean temperatures within the images over the course of the run. For this analysis, thresholds of 0.20 T and 0.33 T above the mean were chosen to outline the features that correspond to areas of skin-layer disruption due to microscale breaking events.

After a series of standard morphological operations to reduce noise effects (see Appendix A), a time series of the fraction of the area affected by microscale breaking, A_B , was computed from the sequence of individual images; A_B denotes the fraction of the image whose temperature was above the specified threshold. Figure 3.1 shows the results when applying the two thresholds to the fifth infrared image of Figure 2.3. The lower threshold ($\langle T \rangle + 0.20 T$) detects one large event, whereas the higher threshold ($\langle T \rangle + 0.33 T$) successfully separates three events identified with the three individual crests in Figure 2.3. Although this simple definition of fractional area averages out the effect of multiple events in various stages of development within a single image, A_B nonetheless provides a measure of the area extent of microscale breaking.

Figure 3.2 shows time series of A_B computed using the chosen thresholds for one run measured during the CCIW laboratory experiment. Both time series show large, rapid fluctuations, as well as more slowly varying features. The frequency of the fluctuations depends on the recovery rate of the skin layer, the occurrence of multiple breaking events within the image, and the time between the events. For the run shown in Figure 3.2, the mean fraction of disrupted area is 0.35 for the lower threshold and 0.19 for the higher threshold, indicating that a significant fraction of the surface is disrupted on a continuous basis. For the four runs at constant wind speed and relative humidity considered here, the average A_B did not change (within ± 0.01) as the air-water temperature difference was varied from -1.7°C to -9.1°C (corresponding to an increase in T from 0.16°C to 0.36°C).

In order to evaluate how often the detected events occurred, power spectra were computed from the time series of A_B derived from the threshold analysis described above. The dominant frequency of A_B provides a measure of the frequency of occurrence of the disturbances due to microscale breaking, even though multiple events may be detected in a single image. Figure 3.3 compares the normalized power spectra of A_B with the normalized spectrum of the

surface displacement measured 1 m downwind of the imaged area. The dominant frequency of A_p is roughly one-third of the dominant wave frequency for all four runs at this wind speed of 5 m s^{-1} . Similarly, power spectra of the surface temperature for a single point at random locations also show a frequency roughly one-third of the wave frequency, implying that one out of three waves break.

Details on the origin and evolution of the surface disruption near the crest of microscale breaking waves are revealed by operating the imager in a "line-scan" mode which provides a scan along the same line at a rate of 2500 Hz. An example of the high temporal and spatial resolution available using this rapid sampling capability is shown in the infrared space-time plot in Figure 3.4, which also shows corresponding video images. The vertical axis is the distance along the tank over which the imager scans, and the white line in each video frame corresponds to the location of the scan line. The horizontal axis in the space-time plot spans a duration of 0.9 s, with each vertical line denoting the time of a video frame. The propagation down the tank of the microscale breaking crests labeled E and F in the video images corresponds to the light-colored, steeply sloping bands labeled E and F in the infrared space-time plot. The slopes of these bands determine the speed of the thermal features which, at 0.5 m s^{-1} , matches the phase speed of the dominant wave. Fine streaky signatures of surface-drift features move at a much slower velocity (3% to 4% of the wind speed, U) and correspond to the motion of the patchy features near the bottom of the infrared images in Figure 2.3. Note that the slope of the surface-drift features tends toward zero just ahead of the sloped line corresponding to breaking crest E, indicating the occurrence of a region of very small or no drift.

3.3 COMPARISON OF INFRARED AND WAVE SLOPE IMAGERY

As part of the Wallops experiment discussed in Chapters 5 and 6 studying the processes affecting gas transfer, simultaneous and co-located measurements of infrared and wave

slope imagery were made to provide indisputable evidence that the propagating disruptions observed in the infrared imagery are produced by steep wind waves with bore-like crests. Measurements of the wave slope were made by J. Klinke of Scripps Institution of Oceanography (SIO) using a one-dimensional wave slope imaging system based on the refractive light techniques developed by *Keller and Gotwols* [1983] and modernized by *Jähne et al.* [1994]. The amount of angular refraction is uniquely related to the local slope of the free surface by applying Snell's law. The technique results in gray-scale images of the surface in which the image intensity is proportional to the surface slope.

The experimental setup of the image slope system at Wallops is shown in Figure 5.2 of section 5.2. A 34" \times 40" light box at the bottom of the tank contained twenty four 36"-long fluorescent lamps ballast-modulated to roughly 40 kHz. The light box was covered by an intensity absorption screen with a linear gradient in the along-tank direction. A Sony XC-75 CCD camera shuttered at 1 ms imaged the water surface from above the tank through a glass window. The images were digitized at a frequency of 15 Hz (matching that of the Radiance HS imager) with a spatial resolution of 240 by 640 pixels per video field from the CCD camera. A mirror was used to place the camera at a distance of 3 m from the water surface so as to image an area of 18 by 24 cm with a wavenumber resolution of greater than 1000 rad m⁻¹. For still water and prior to calibration, the camera imaged a gradient in intensity from low to high in the downwind direction. Since the intensity gradient is against the wind direction, wave slope is measured only in the along-tank axis. Each pixel in the image is calibrated for 11 known slopes to give a full range of intensity corresponding to the range of known slopes. Calibration of the imagery allows for the determination of the slope based upon the intensity of light with limiting values of at least ± 1 at every pixel. The slope images give a direct measure of $\langle S^2 \rangle$ simply by squaring the value for slope at each pixel and taking the mean of this quantity for the whole

image. This image slope measurement provided the spatial resolution necessary to study the nonlinear wave characteristics that affect the processes of gas transfer.

Figure 3.5 shows examples of slope images at different wind speeds at 5.6 m fetch. Each pair of randomly selected images corresponds to a different wind speed or surface condition as follows: (a) $U = 4.2 \text{ m s}^{-1}$ and a cleaned surface; (b) $U = 5.5 \text{ m s}^{-1}$ and a cleaned surface; (c) $U = 5.6 \text{ m s}^{-1}$ and Triton X-100 added; (d) $U = 6.9 \text{ m s}^{-1}$ and a cleaned surface; (e) $U = 6.9 \text{ m s}^{-1}$ and Triton X-100 added. Areas of bright intensity denote steep leeward (front face of a wave) slope and areas of dark intensity denote steep windward (back face of a wave) slope. In general, waves in the imagery appear as oscillations in intensity between light and dark shades of gray. Gravity waves show longer oscillation, and the crest is characterized by the transition from light intensity on the leeward face to dark intensity on the windward face, with short fine-scale oscillations on the forward face corresponding to capillary waves. Changes in gross surface features are observed from trains of capillary-gravity waves that appear ordered and one dimensional at low wind speed in Figure 3.5a to a chaotic, highly two-dimensional wave field with larger slopes at higher wind speed in Figure 3.5d. Also note the apparent decreased range of slopes in the surfactant cases in Figure 3.5c and e, where the capillary waves have been suppressed relative to the corresponding cleaned cases at the same wind speed.

A comparison of co-located and simultaneous slope and infrared imagery illustrates that capillary-gravity wave packets evolve into microscale breaking waves that disrupt the diffusive boundary layers. Figure 3.6 and Figure 3.7 show two such sequences of infrared and slope images for Experiment W5 ($U = 6.9 \text{ m s}^{-1}$; cleaned surface). The wave slope and infrared imagery were synchronized with a 15 Hz TTL pulse from a Stanford Research Systems (SRS) model DG535 digital delay/pulse generator (Stanford Research Systems Inc., Sunnyvale, CA). The co-location of wave slope and infrared imagery was achieved by placing three definable objects in the overlapping fields-of-view that serve as reference points for both images.

The infrared imagery is spatially calibrated using a grid with spacings of known distance and was carefully overlayed on the slope imagery to within ± 5 mm. The top sequence shows infrared imagery with a box drawn to highlight the overlapping slope image area. The second sequence shows an enlarged view of the highlighted region in the infrared with an outline of the measured A_B . The third sequence shows the slope imagery, and only the portion below the line drawn in the slope image corresponds directly to the highlighted region in the infrared images. The final sequence shows the outline of A_B overlayed on the image slope.

As discussed in section 3.2, the characteristic signature of a microscale breaking wave in the infrared imagery consists of an abrupt front of increased temperature that propagates through the image in the direction of the wind at roughly the phase speed of the dominant wave. This distinct propagating front disrupts the surface, leaving behind a decaying turbulent wake of warmer water. As the wake turbulence decays, the skin layer recovers back to its original state as a function of the heat flux and the initial background turbulence [Zappa *et al.*, 1998]. Therefore, the scallop-shaped wakes left behind by microscale breaking waves vary in size and intensity. Smaller-scale structures observed in the imagery are most likely associated with background eddies generated by shear, buoyancy (due to the high heat flux), and/or turbulence input to the near surface by microscale breaking waves.

As the capillary-gravity wave packets propagate down the slope image, the distinct warm feature of a microscale breaking wave appears in the infrared. The infrared images show the bulk water that is mixed up to the surface following the disruption of the thermal boundary layer. The image slope shows the very front of the curved bore-like crest to have the steepest slope, and this steep slope corresponds directly to the leading edge of the propagating thermal front of the microscale breaking signature in the infrared. The mixing that produces the infrared signature is the direct consequence of the near-surface turbulence generated by the bore-like crest of the microscale breaking wave. The slope image also shows only extremely short

capillary waves riding on the forward face at the initial moment of disruption that are barely visible and nearly disappear. However, the bore-like crest and the region behind it appear distinctly "dimpled," suggesting that an energetic process occurs right at the crest. This highly three-dimensional dimpled characteristic of the bore-like crest and of the wake diminishes in subsequent slope images, but the microscale breaker is shown in the infrared imagery to continue to disrupt the surface as it dissipates energy to smaller scales. As the dimpled features diminish, short steeper capillary waves begin to emerge on the forward face of the front of the bore-like crest and continue to grow in wavelength as the microscale breaking event evolves toward completion. These simultaneous, co-located infrared and slope observations confirm that the distinct scalloped features of skin layer disruption are produced by the propagating bore-like crests of microscale breaking waves.

The distinct infrared signature of a propagating thermal front and warm turbulent wake produced by a bore-like crest defines and quantifies the breaking process directly. However, not all steep gravity wave crests accompanied by capillary waves that propagate through the imagery are microscale breaking waves. Figure 3.8 shows a wind-wave crest propagating through the slope images that does not produce an infrared signature characteristic of microscale wave breaking. In this case, the crest is accompanied by capillary waves on its forward face that are not present in the slope images during the microscale breaking event in Figure 3.6. In addition, there is no distinct dimpled feature on the crest of the wave, suggesting that it is not generating intense turbulence like a propagating bore-like crest.

The slope image features described above that are associated with actively breaking crests were observed over all wind speeds and surface conditions investigated. Figure 3.9 and Figure 3.10 show two examples of microscale breaking waves as they overtake a group of shorter capillary waves during Experiment W8 ($U = 5.5 \text{ m s}^{-1}$; cleaned surface). The microscale breaking waves have similar features to those shown in Figure 3.6 and Figure 3.7, but are for a

lower wind speed. Again, the microscale breaking wave exhibits the steep forward face coincident with the propagating thermal front and the "dimpled" features on the bore-like crest that coincide with the decaying turbulent wake. Only extremely short capillary waves are observed on the forward face of the breaking crest during the initial stages of breaking that nearly disappear, but longer steep capillary waves do emerge at a later time. Figure 3.11 shows an example of microscale breaking waves from Experiment W13 ($U = 6.9 \text{ m s}^{-1}$; Triton X-100) which was at the same wind speed as the data from Experiment W5 ($U = 6.9 \text{ m s}^{-1}$; cleaned surface) in Figure 3.6, Figure 3.7, and Figure 3.8, only here the surfactant Triton X-100 was added to the water. In comparison to the cleaned surface data in Figure 3.6 and Figure 3.7, the infrared images taken with surfactant present have a much smoother appearance. The small-scale temperature variation due to the background turbulence interacting with the free surface is damped by the surfactant, and fewer eddies strong enough to disrupt the skin layer are observed in the infrared imagery. For the cleaned cases, the surface is disrupted more easily by eddies produced by microscale breaking waves, as well as background turbulent eddies, as a consequence of the free surface boundary condition. Therefore, microscale breaking waves appear more distinctly in the surfactant-influenced surface cases than the cleaned cases because fewer skin-layer disruptions by turbulent eddies clutter the background. As expected, the slope imagery shows much less capillary wave activity as compared to the cleaned case at the same wind speed since the surfactant damps these waves. However, the typical dimpled bore-like crest of a microscale breaker and minimal existence of capillary waves riding on the forward face are still observed. The damping of waves by surfactant is not strong enough to inhibit the microscale breaking process. More importantly, the surfactant is not strong enough to inhibit the turbulence generated by microscale breaking that is thought to increase the gas transfer.

3.4 MEASUREMENTS OF INFRARED IMAGERY AND PARTICLE IMAGE VELOCIMETRY

Coherent structures frequently observed beneath wind waves have been described as bursts [Komori *et al.*, 1993], rollers [Longuet-Higgins, 1992], or high-vorticity regions [Okuda, 1982; Ebuchi *et al.*, 1987]. Smaller-scale surface-renewal eddies [Komori *et al.*, 1993] have also been observed, but neither structure has been linked directly to microscale breaking waves. To observe the coherent structures beneath microscale breaking waves, a particle image velocimetry (PIV) system was implemented at Wallops by M. Loewen (University of Alberta). PIV provides accurate velocity measurements very close to the free surface with high spatial coverage and resolution in two dimensions. In general, the water is seeded with neutrally buoyant reflective tracer particles that are illuminated by a thin laser sheet. The position of the particles is measured with a digital camera and the velocity field is determined from the distance traveled by the illuminated tracer particles between two images spaced very closely in time ($O(10^{-3}$ s) apart). Previous measurements using PIV beneath wind-generated waves [Peirson, 1997; Banner and Peirson, 1998] determined the surface tangential stress due to microscale breaking waves. Here, the interest was to show the gross spatial and velocity scales of the coherent structures and small-scale eddies beneath wind waves. The PIV laser sheet was directed from below towards the water surface at an oblique angle in the vertical along-tank plane. This produced surface reflections that resulted in ambiguous estimates of the water surface profile. Therefore, PIV measurements made at Wallops were unable to resolve the water velocities near the crests of individual waves. In July 1999, M. Loewen and M. Siddiqui collected a comprehensive data set of the measurements of PIV beneath wind waves in the Harris tank [Siddiqui *et al.*, to appear], where the PIV laser sheet was directed perpendicular to the plane of the water surface, parallel to the vertical along-tank plane. In this case, reflections were minimized and a second video camera was used to record the surface profile outlined by the intersection of the laser sheet with the airwater interface. Although the data are in the preliminary

stages of analysis, the results show that a region of high positive vorticity occurs at the crests of microscale breaking waves in the infrared images.

Figure 3.12 shows (a) a plan view of an infrared image of the water surface and (b) an along-tank slice of the water-side image produced by the PIV system (see *Siddiqui et al.* [to appear]) at a wind speed of 6 m s^{-1} . The PIV image in Figure 3.12b shows both velocity vectors and an intensity plot of the cross-tank component of vorticity, Ψ , defined as $\partial u/\partial z - \partial w/\partial x$. The location of the PIV laser sheet within the infrared imager field-of-view is indicated by the line in the infrared image in Figure 3.12a. Comparisons of the PIV and infrared imagery show a distinct breaking wave coincident with positive and negative vortical eddies in the PIV that correspond to the disruption. While not all of the smaller-scale eddies are associated with the microscale breaking event, distinct vortical structures can be directly related to microscale breaking. The example shows strong large vortical structures directly related to microscale wave breaking as well as weaker smaller-scale structures both related and unrelated to the microscale breaking event. The arrow in the PIV image coincides with the location of the front of the propagating bore-like crest in the infrared image. Strong complementary positive and negative vortical eddies appear just behind the propagating bore. Figure 3.12 highlights the promise of future work with simultaneous PIV and infrared measurements to determine both the range of conditions that distinguish bursts from smaller-scale surface renewal (due to microscale breaking and non-breaking waves) as well as the decomposed turbulent velocities. The example also supports the suggestion of *Jessup et al.* [1997b] that infrared imagery reliably defines and quantifies the microscale breaking process.

3.5 DISCUSSION

Organized, turbulent structures, or bursts, in the air and water associated with wind waves which do not produce air entrainment have been documented in a variety of

laboratory studies over the past two decades. *Toba et al.* [1975] described a downward, subsurface flow associated with the surface convergence near the bore-like crests of steep wind waves. These downward bursts have been related to flow separation and reattachment in the air that occur near the wave [*Kawamura and Toba*, 1988]. *Okuda* [1982] found a water-side region of high vorticity near crests that were occasionally accompanied by downward, subsurface bursts on the forward face.

Yoshikawa et al. [1988] used temperature as a passive tracer to detect these downward flows of water originating from the surface by combining fast-response temperature measurements (at depths of 0.015, 0.035, and 0.072 m) and velocity measurements (at 0.072 m) in the near surface layer under wind waves. The source of the tracer for the detection of downward flows was the cool skin layer, which was present owing to a net upward heat flux dominated by evaporation. Event-like temperature fluctuations of several millidegrees were coincident at all depths and occurred at intervals on the order of 10 s. These thermal intrusions were characterized by a rapid decrease in temperature followed by a more gradual recovery. The lifetime of roughly 10 s for the thermal events was much longer than the dominant wave period, which ranged from 0.24 to 0.36 s. The thermal events were correlated with increased downward and downwind velocity fluctuations which persisted for a similar duration. *Yoshikawa et al.* [1988] asserted that these low-frequency, large-scale features were due to downward bursts associated with individual wind waves, but the specific mechanism remained unresolved. These features may be attributed to small-scale Langmuir circulation, which has been observed in the top few centimeters (< 4 cm) of water in laboratory wind-wave initiation studies by *Melville et al.* [1998]. The shallower thermistors showed far more rapid fluctuations, which suggests that the large-scale features detected by the deepest thermistor and the velocity sensor might be due to larger breaking events, or perhaps due to the additive effect of wave breaking in groups. These

laboratory measurements provide direct evidence that fluid within the thermal sublayer is renewed by a turbulent process observed beneath wind waves.

The downward bursts reported by *Yoshikawa et al.* [1988] were associated with individual waves and in all likelihood were produced by microscale wave breaking. While the infrared observations indicate that not all waves are microscale breakers (as illustrated in Figure 3.13a), the frequency of microscale breaking measured here (about one-third the dominant wind-wave frequency) is significantly greater than the frequency of large-scale temperature intrusions reported by *Yoshikawa et al.* [1988]. The skin-layer disruptions detected by the infrared imager represent renewal of the surface in the sense that the fluid parcels within 10 μm of the water surface overturn and are replaced by fluid parcels from below. Microscale wave breaking, for example, likely produces small-scale eddies that are sufficiently energetic to bring about surface disruption, as illustrated in Figure 3.13b. At times, however, a downward "bursting" motion may emerge as a result of a more intense microscale breaking event, as depicted in Figure 3.13c. It is concluded that the reason for the difference between the results of this study and those of *Yoshikawa et al.* [1988] is that not every microscale breaking wave produces a strong downward burst.

Komori et al. [1993] combined near-surface velocity measurements in both the air and water with gas flux measurements to investigate whether the shear-induced turbulence under wind waves is the primary surface-renewal mechanism for gas transfer. Subsurface bursts near the wind-wave crests, as well as more frequent "surface-renewal motions," were observed to coincide with organized motions in the air. *Komori et al.* [1993] computed the surface-renewal rate based on the frequency of thresholded velocity fluctuations near the water surface, resulting in a surface-renewal rate that was an order of magnitude greater than the wave frequency.

The velocity fluctuations that *Komori et al.* [1993] measured likely represent small-scale eddy motions produced primarily by microscale breaking waves. However, the measured frequency of microscale breaking is an order of magnitude less than the frequency of "surface-renewal motions" they used to estimate s . The length scale for the eddies measured by *Komori et al.* [1993] was of $O(10^{-2} \text{ m})$ compared to the length scale of $O(10^{-1} \text{ m})$ for the turbulent wakes of microscale breaking waves that was detected here. Therefore, a probable reason for the difference between s measured by *Komori et al.* [1993] and the frequency of microscale breaking is the presence of multiple small-scale eddies within the turbulent wake of a single microscale breaking event. Another potential contributing factor is that not all small-scale eddies near the surface correspond directly to microscale breaking events. The line scan measurements, like those in Figure 3.4, do not show high-frequency skin-layer disruptions in areas unaffected by microscale breaking. In all likelihood, not all of the eddies in these areas were capable of producing skin-layer disruption by fluid-parcel overturning at the surface because of the suppression of vertical motion by the density discontinuity at the air-water interface. The findings highlight that the frequency of microscale breaking is distinctly different from the surface renewal rate used in traditional surface-renewal models that are based on shear-induced turbulence.

While models of the exchange of heat [*Wick et al.*, 1996] and gas [*Jähne et al.*, 1987] using surface-renewal theory have had some success, fundamental differences between the classical idea of surface renewal and the influence of waves remain to be reconciled in modeling these air-sea fluxes. *Csanady's* [1990] model in (1.27) and the model developed here in (2.6) suggest that the thinning of the concentration boundary layer by microscale wave breaking enhances gas transfer. For the model given in (2.6), k scales with the fraction of surface area covered by wave-induced divergence, ϕ , and can be non-zero as ϕ approaches zero. The optical depth of the detected infrared radiation, $O(10^{-5} \text{ m})$, is on the order of the mean thickness of the

concentration boundary layer. Therefore, fraction of surface area, A_B , in which the thermal boundary layer is thinned and disrupted by microscale breaking waves serves as an estimate of the surface density of breaking-induced divergence, ϕ , in (1.27) and (2.6). *Csanady* [1990] estimated a value of at least 0.20 for ϕ based on measurements reported by *Jähne et al.* [1987]. While the values of A_B in Figure 3.2 are consistent with *Csanady's* [1990] estimate for ϕ , a meaningful comparison will require measurements over a wide range of wind speeds at varying fetch. Such a data set is presented in Chapters 4 and 5. In addition to A_B , one might expect k to depend on other parameters measured by infrared imagery that characterize microscale breaking, such as the rate of recovery of the affected area and the size and intensity distribution of surface disruptions produced by breaking-generated turbulence.

Microscale wave breaking, and the near-surface turbulence it generates, is hypothesized to enhance gas transfer. In the infrared imagery, the microscale breaking process is observed to disrupt the thermal boundary layer, producing fine-scale surface thermal structures within the bore-like crest and in its wake. In the slope imagery, microscale breaking also generates the three-dimensional dimpled features. Therefore, if near-surface turbulence is the source of these observations, the spatial scales of the vortical eddy structures within the bore-like crest and determined from the PIV data should be comparable to the spatial scales of both the dimpled features and the thermal structures.

The spatial scales of the fine-scale thermal structures, the three-dimensional roughness features, and the vortical eddies were all observed to be of $O(10^{-2} \text{ m})$. Furthermore, the dimpled roughness features of the bore-like crest correspond directly to the warmest fine-scale features of the skin-layer disruption by microbreaking. Additionally, the highest vorticity is observed within the actively breaking bore-like crest. The implication is that the fine-scale thermal structures and the dimpled roughness features are directly related to the turbulence

generated at the bore-like crest. Since near-surface turbulence increases k , microscale breaking waves should prove to be the mechanism that enhances heat and mass transfer.

The observations of the characteristic features of the wave field in the slope imagery, both during the breaking process and for non-breaking waves, have importance not only to the discipline of gas transfer but also to remote sensing. Details of the formation and evolution of a breaking wave crest have recently emerged both in theory [Longuet-Higgins, 1992; Longuet-Higgins, 1994; Longuet-Higgins and Cleaver, 1994] and experiment [Duncan *et al.*, 1994; Duncan *et al.*, 1999]. The results and techniques presented here indicate that the present infrared capabilities provide unprecedented details of the microscale breaking process, such as the exact location of initial surface disruption. The images in Figure 2.4 of microscale breaking in the presence of swell show that infrared techniques can be used to detect enhanced microscale breaking due to long-wave/short-wave interaction. Preferential breaking of very short gravity waves along the phase of long waves has been suggested as the mechanism responsible for modulation of the skin temperature by swell waves [Jessup and Hesany, 1996; Wick and Jessup, 1998]. In the context of microwave remote sensing, these features of microscale breaking waves have been shown to be important in deciphering radar backscatter results. Trains of bound, tilted capillary-gravity waves produced by microscale breaking on the forward faces of longer gravity waves have been suggested as a necessary contributor to Bragg scattering in a multi-scale model for microwave Doppler sea return at high incidence angles [Plant, 1997; Plant *et al.*, 1999]. Furthermore, the microscale breaker itself is suggested to be the origin of a multiple scattering effect at grazing angles [Trizna and Carlson, 1996] because the steep slopes observed in the slope imagery at the bore-like crest may act as a corner reflector.

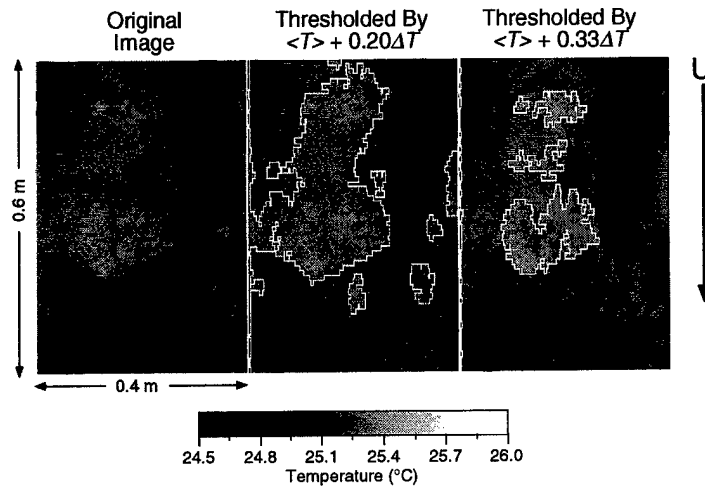


Figure 3.1. Example of detection technique based on the mean surface temperature, $\langle T \rangle$, and the bulk-skin temperature difference for the entire run, ΔT . The image on the left is the same as the fifth infrared image in Figure 2.3 except that the horizontal scale is now 0.4 m. Areas with a temperature greater than the lower threshold ($\langle T \rangle + 0.20\Delta T$) are outlined in the middle image, while the right image shows areas greater than the higher threshold ($\langle T \rangle + 0.33\Delta T$). Note that the higher threshold identifies the three individual events labeled A – C in Figure 2.3.

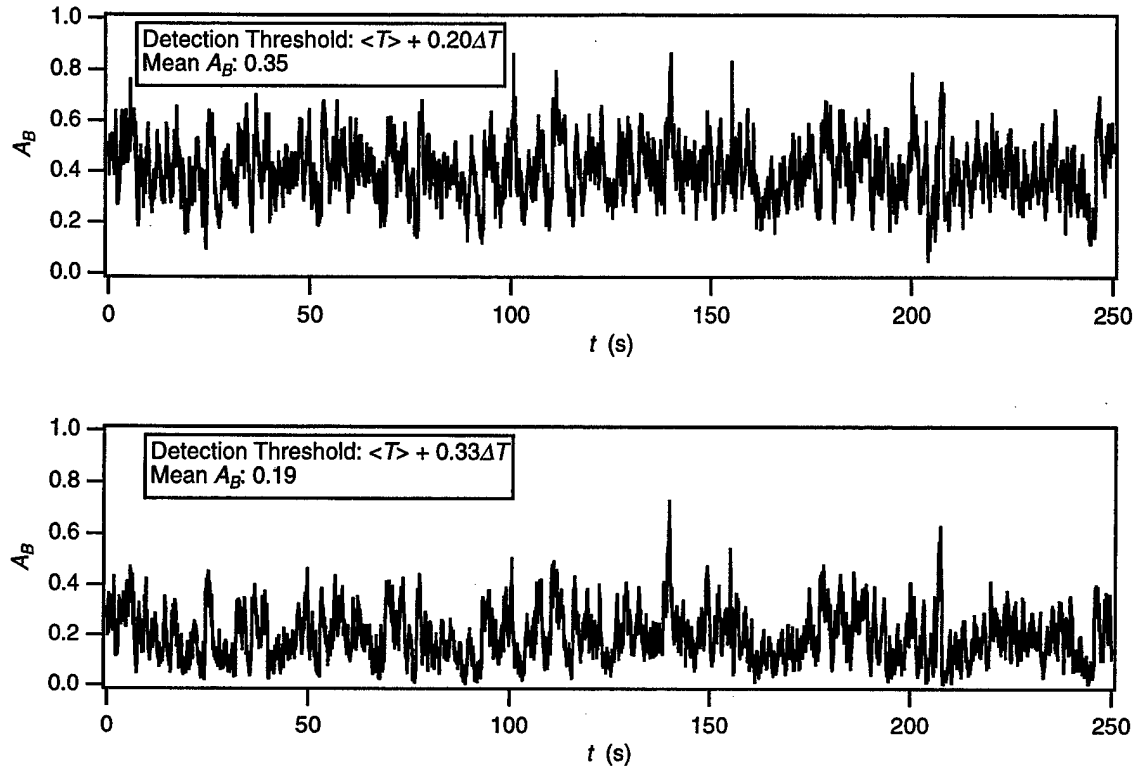


Figure 3.2. Time series of A_B , the fractional area of microscale wave breaking, detected when using the lower (Top: mean $A_B = 0.35$) and higher (Bottom: mean $A_B = 0.19$) thresholds. Data were taken during an experiment at the Canada Center for Inland Waters (CCIW); $T_w = 26.8^\circ\text{C}$, $T_{aw} = -1.7^\circ\text{C}$, $RH = 65\%$, $f_p = 3.28$ Hz (measured 1 m downwind of the test section.), $U = 5.0$ m s^{-1} , and $\Omega = 6$ m.

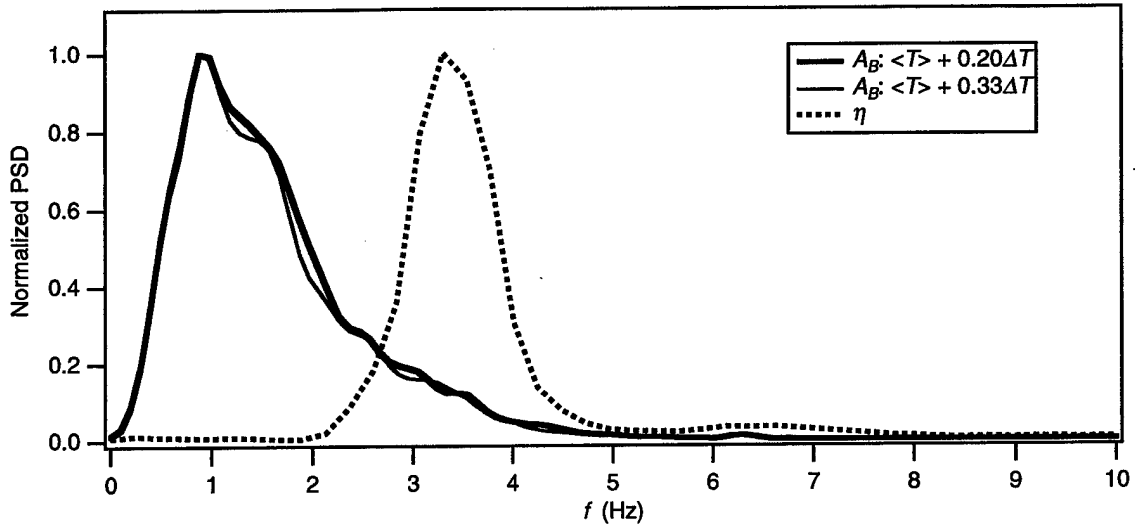


Figure 3.3. Comparison of normalized power spectra of surface displacement and fractional area, A_B , for the run in Figure 3.2 using the same threshold levels. The dominant frequency of A_B provides a measure of the frequency of occurrence of microscale wave breaking and is roughly one-third the dominant wave frequency.

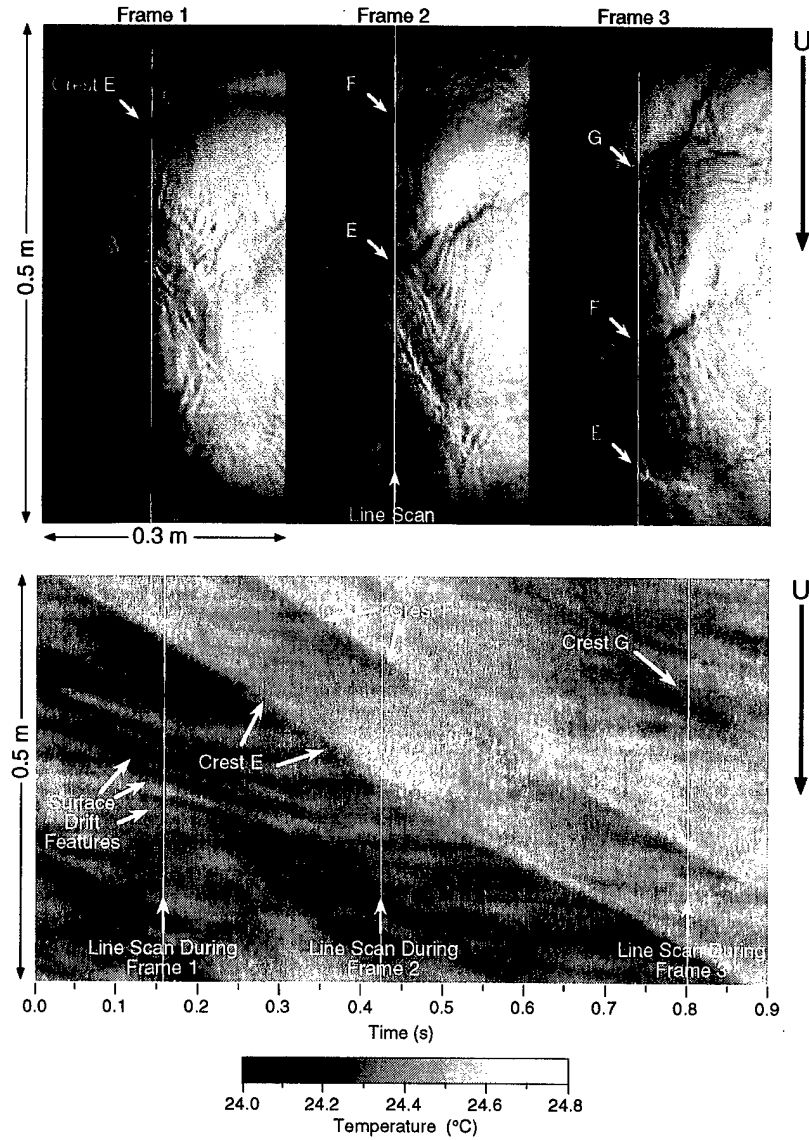


Figure 3.4. Example of measurements using the infrared imager to scan a single line oriented along the tank at a rate of 2500 Hz. Top: Sequence of video images showing the location of the line scan and three individual wave crests labeled E – G propagating along the tank. Bottom: Space–time plot of surface temperature spanning the time of the video images. The scan lines corresponding to the three video images are indicated. The disruption of the skin layer by each breaking crest appears as a sloping line which corresponds to $C_b = 0.5 \text{ m s}^{-1}$. The warmer temperatures above these lines indicate that the skin layer is disrupted by the breaking crests; $T_w = 25.1^\circ\text{C}$, $\Delta T_{aw} = -6.5^\circ\text{C}$, $RH = 49\%$, $f_p = 3.24 \text{ Hz}$ (measured at the test section), $U = 8.1 \text{ m s}^{-1}$, and $\Omega = 5 \text{ m}$.

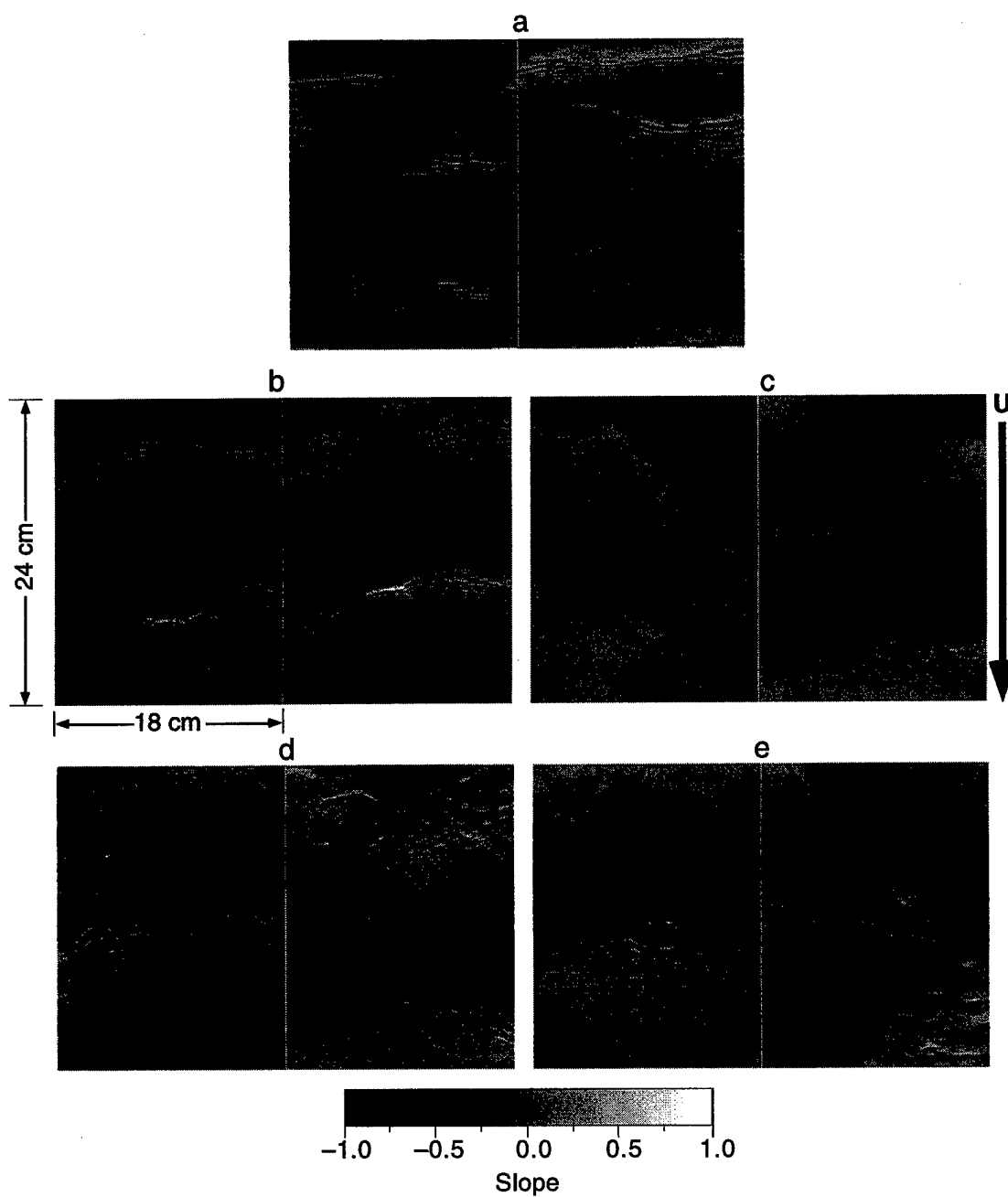
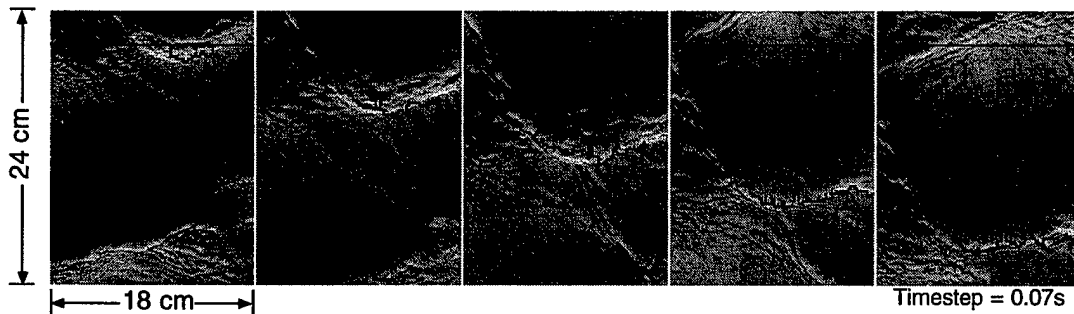
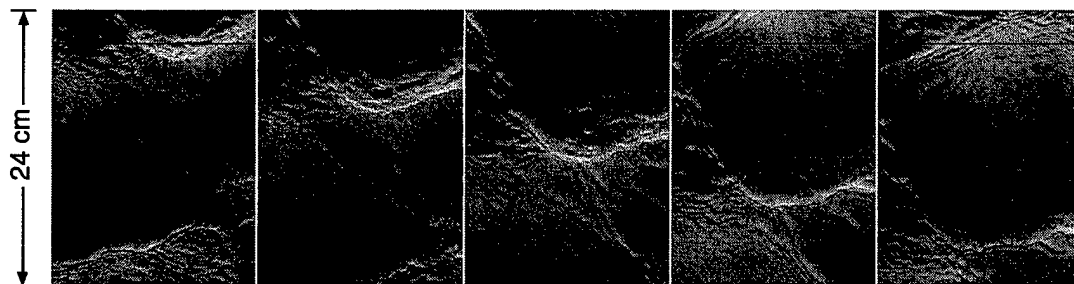
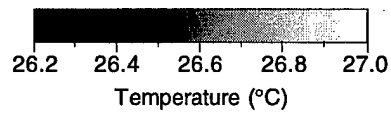
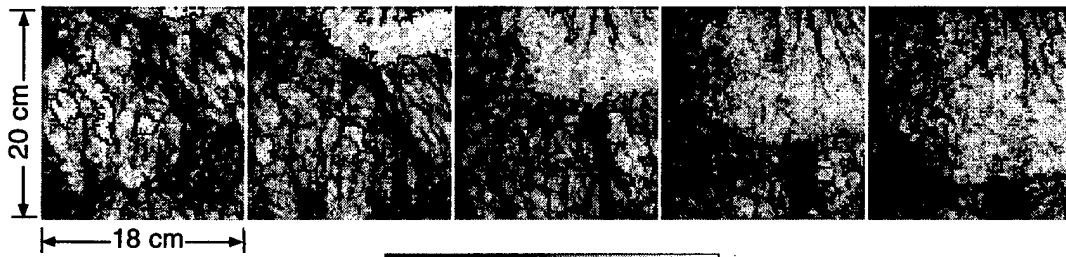
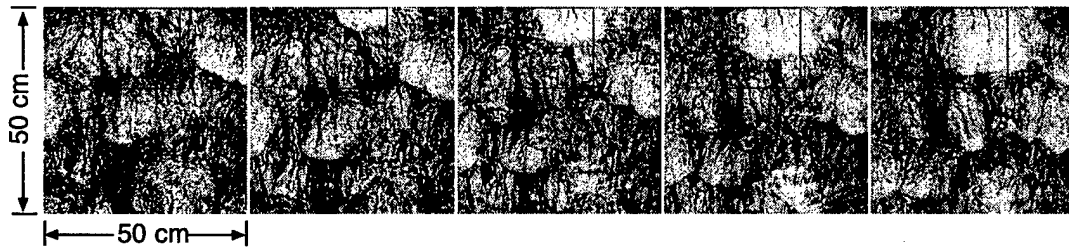
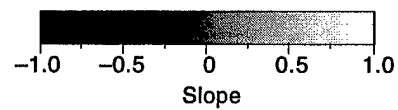


Figure 3.5. Examples of image slope taken at a fetch of 5.6 m as a function of wind speed and surface condition. (a) 4.2 m s^{-1} wind speed and cleaned water surface. (b) 5.5 m s^{-1} wind speed and cleaned water surface. (c) 5.6 m s^{-1} wind speed and Triton X-100 added. (d) 6.9 m s^{-1} wind speed and cleaned water surface. (e) 6.9 m s^{-1} wind speed and Triton X-100 added.



Timestep = 0.07s



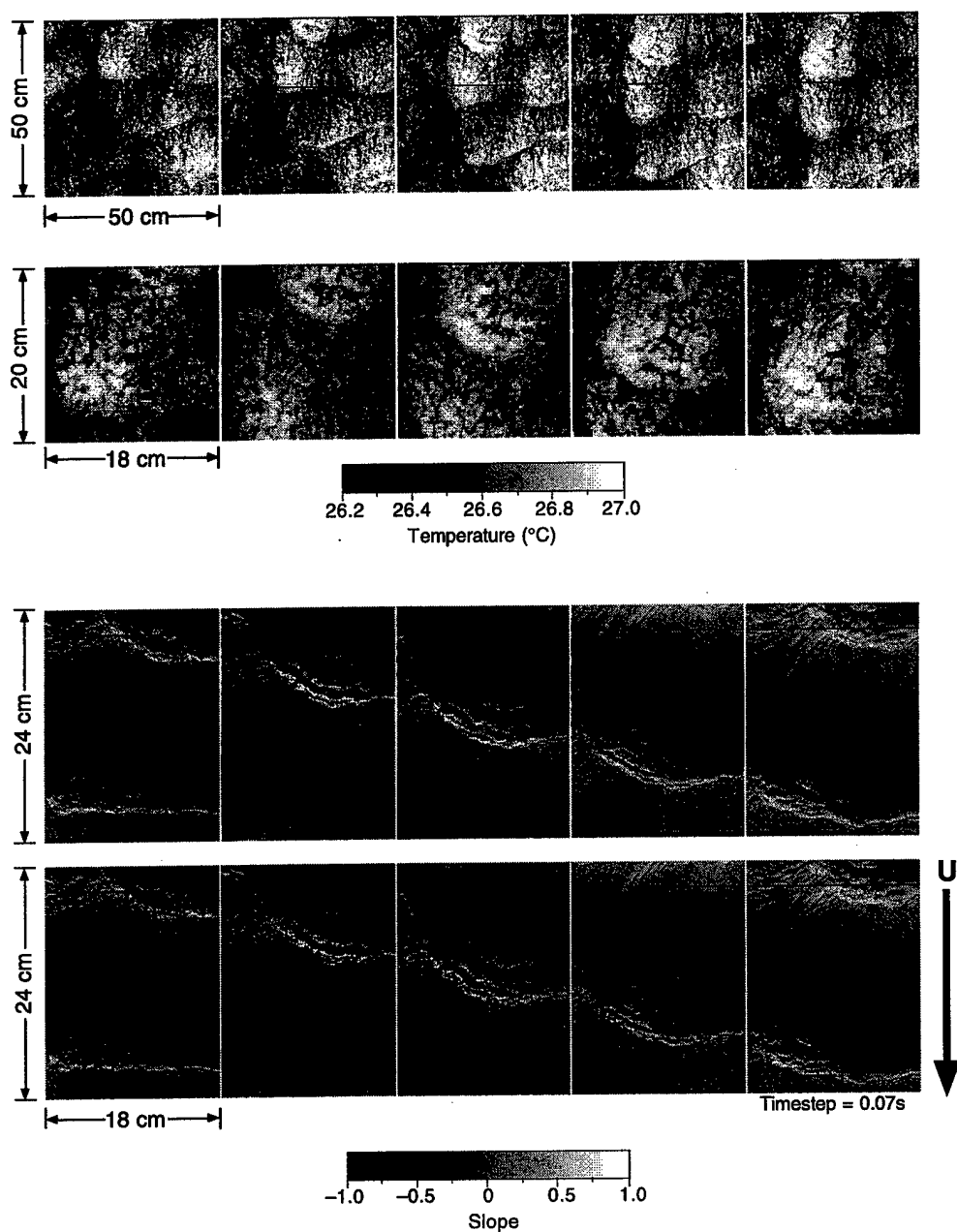


Figure 3.7. An example of both infrared (Top) and wave slope imagery (Bottom) depicting a microscale breaking wave for the same conditions as in Figure 3.6. See caption in Figure 3.6 for key to description of sequences.

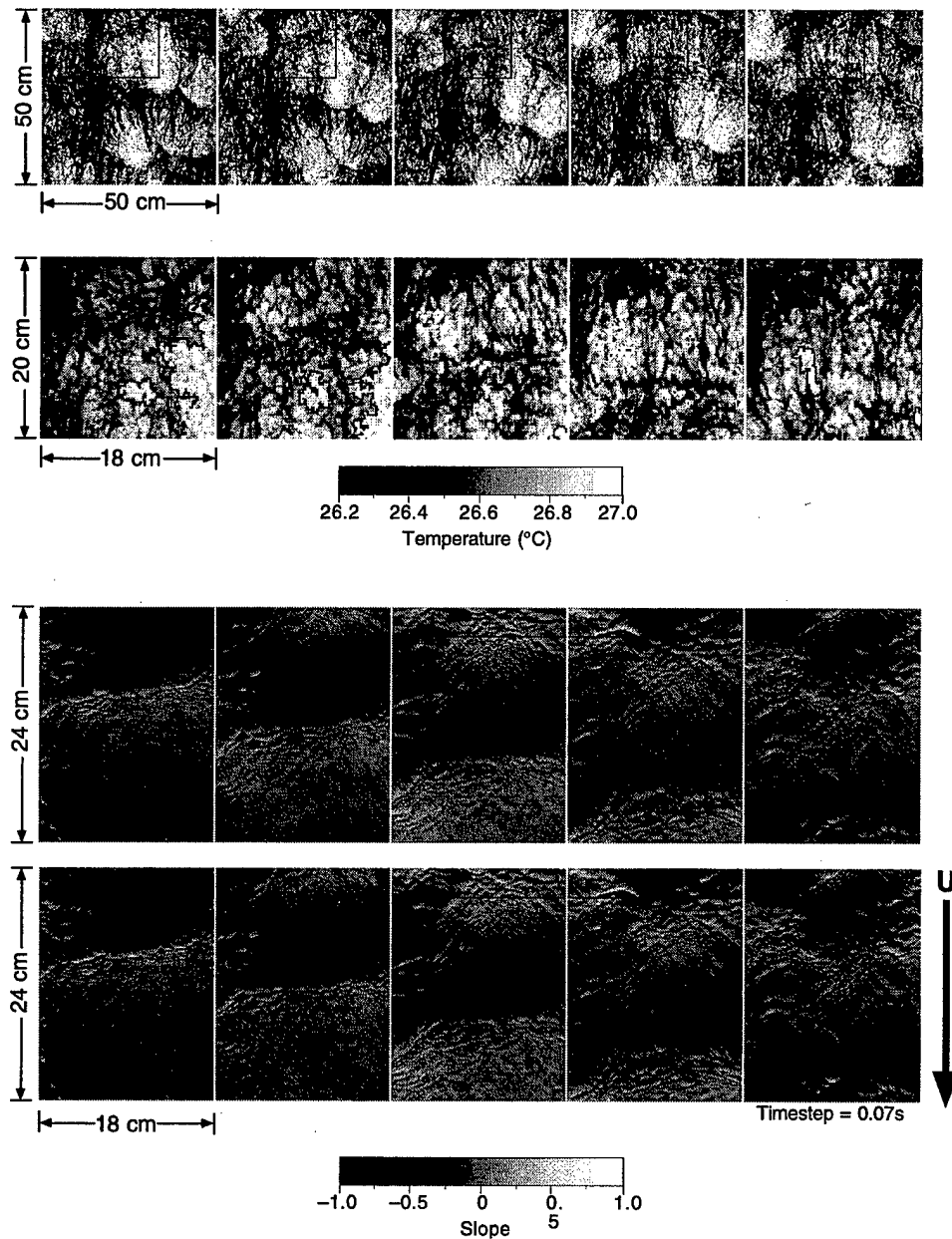


Figure 3.8. An example of both infrared (Top) and slope imagery (Bottom) depicting a wave that does not break for the same conditions as in Figure 3.6 and Figure 3.7. The wave train propagating through the slope imagery produces no detectable disruption of the thermal boundary layer in the infrared. Capillary waves dominate the slope image and no “dimpled” feature associated with a microscale breaking wave crest is evident. See caption in Figure 3.6 for key to description of sequences.

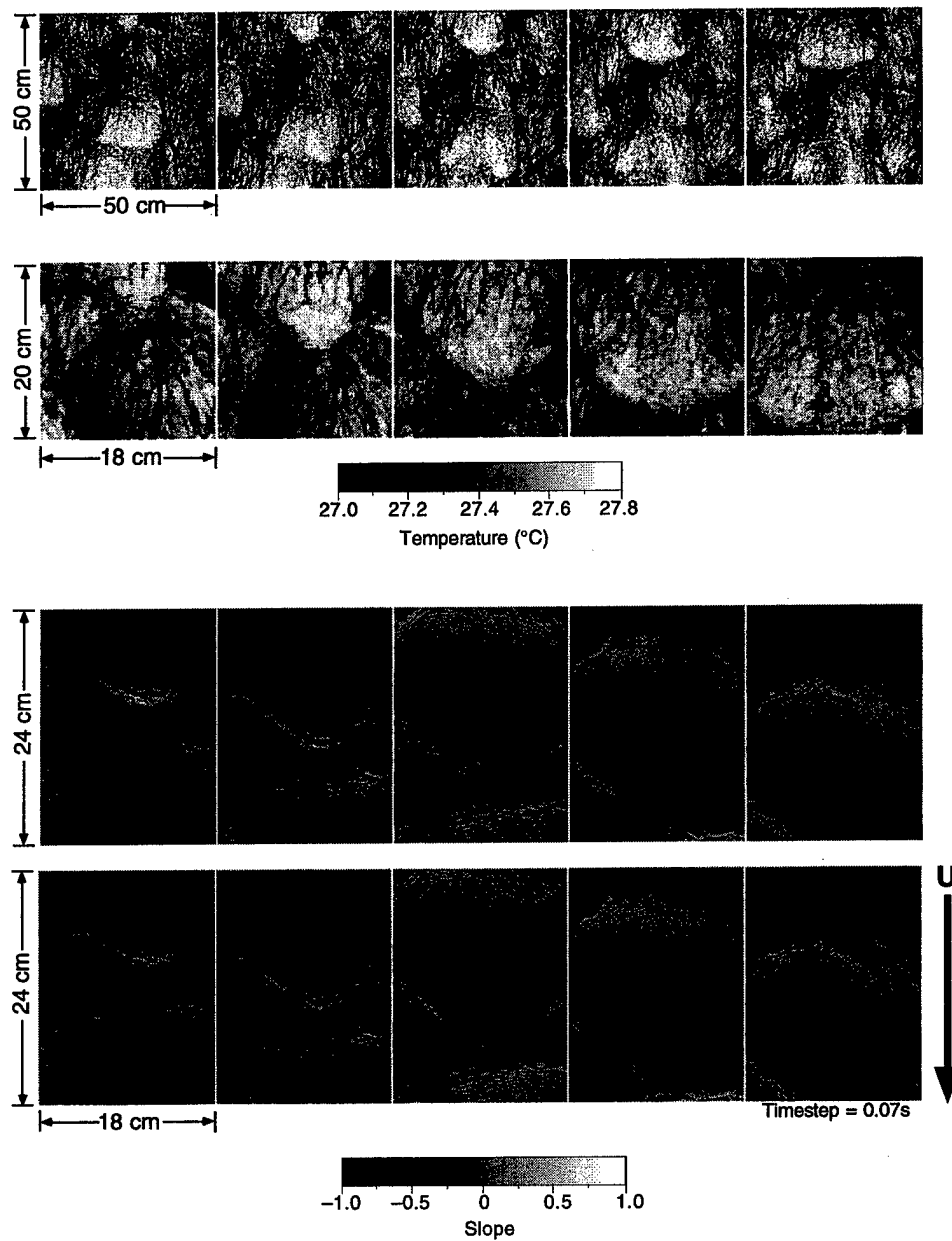


Figure 3.9. An example of both infrared (Top) and slope imagery (Bottom) at a wind speed of 5.5 m s^{-1} with a cleaned water surface depicting a microscale breaking wave; $T_w = 27.9^\circ\text{C}$, $T_{aw} = -5.9^\circ\text{C}$, $RH = 47.3\%$, $f_p = 3.58 \text{ Hz}$, and $\Omega = 5.6 \text{ m}$. The disruption of the skin layer imaged in the infrared is coincident with the appearance of a “dimpled” feature on the bore-like crest in the slope imagery, similar to Figure 3.6 and Figure 3.7. See caption in Figure 3.6 for key to description of sequences.

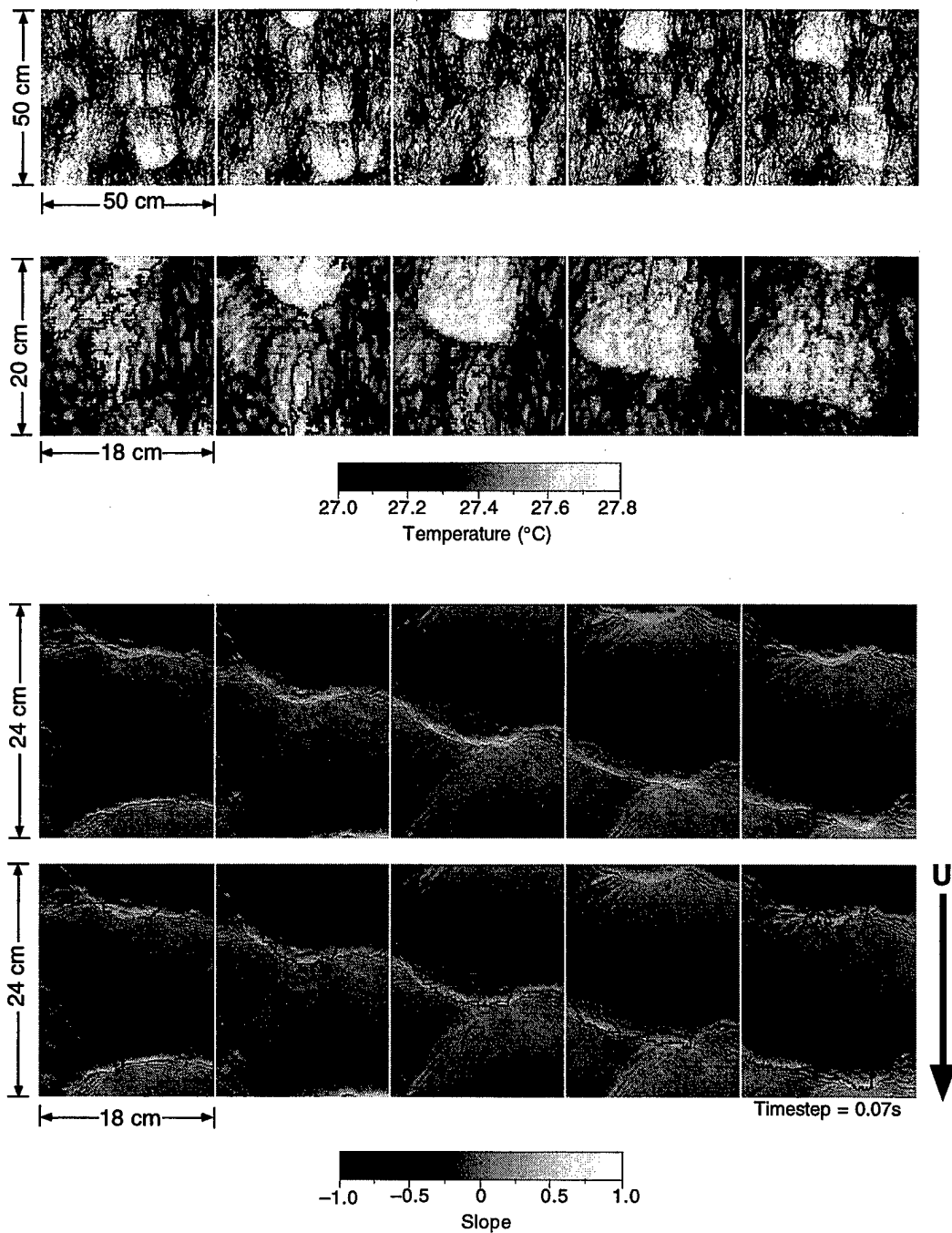


Figure 3.10. An example of both infrared (Top) and slope imagery (Bottom) depicting a microscale breaking wave for the same conditions as in Figure 3.9. See caption in Figure 3.6 for key to description of sequences.

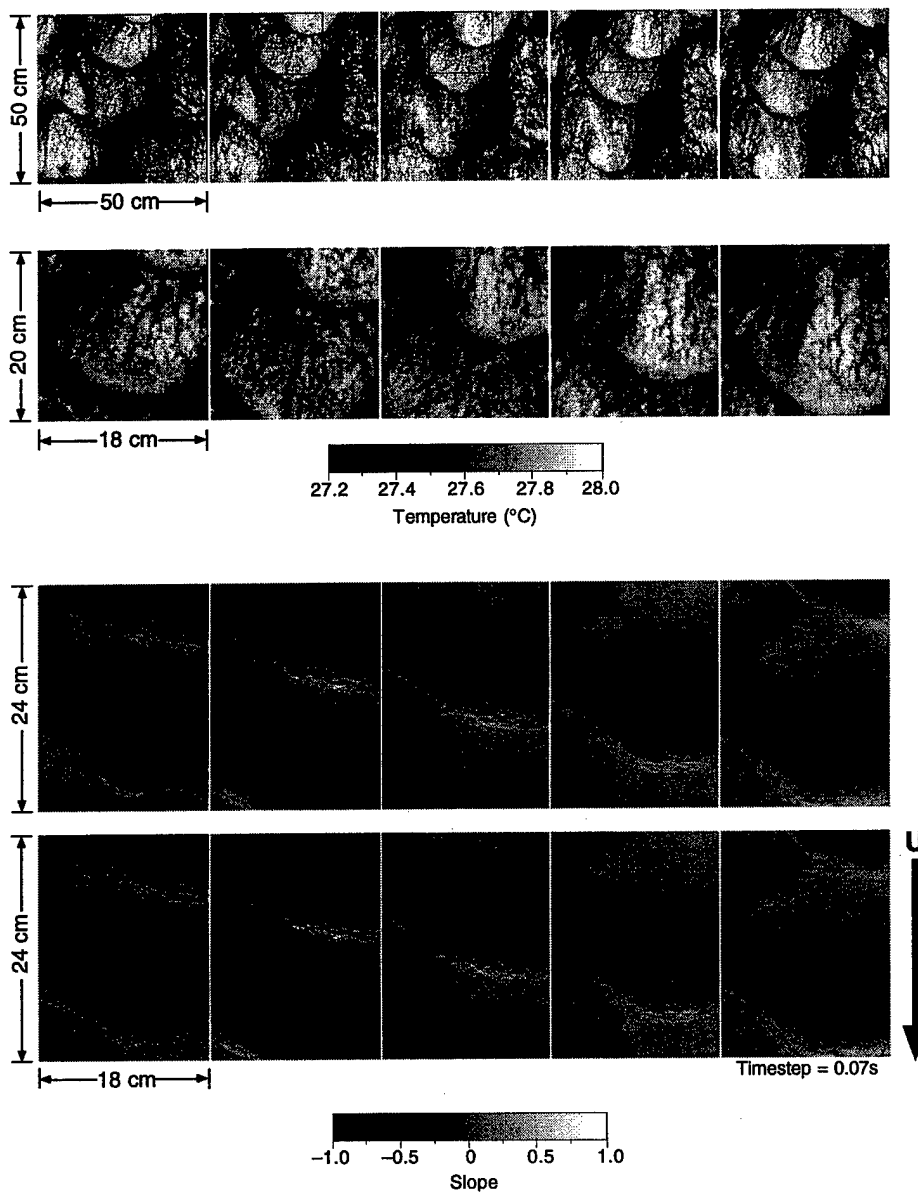


Figure 3.11. An example of both infrared (Top) and slope imagery (Bottom) depicting a microscale breaking wave at the same wind speed of 6.9 m s^{-1} as in Figure 3.6 and Figure 3.7 only with Triton X-100 added to the water; $T_w = 28.2^\circ\text{C}$, $T_{aw} = -5.8^\circ\text{C}$, $RH = 50.8\%$, $f_p = 3.25 \text{ Hz}$, and $\Omega = 5.6 \text{ m}$. The disruption of the skin layer imaged in the infrared is coincident with the appearance of a “dimpled” feature on the bore-like crest in the slope imagery, similar to Figure 3.6, Figure 3.7, Figure 3.9, and Figure 3.10. See caption in Figure 3.6 for key to description of sequences.

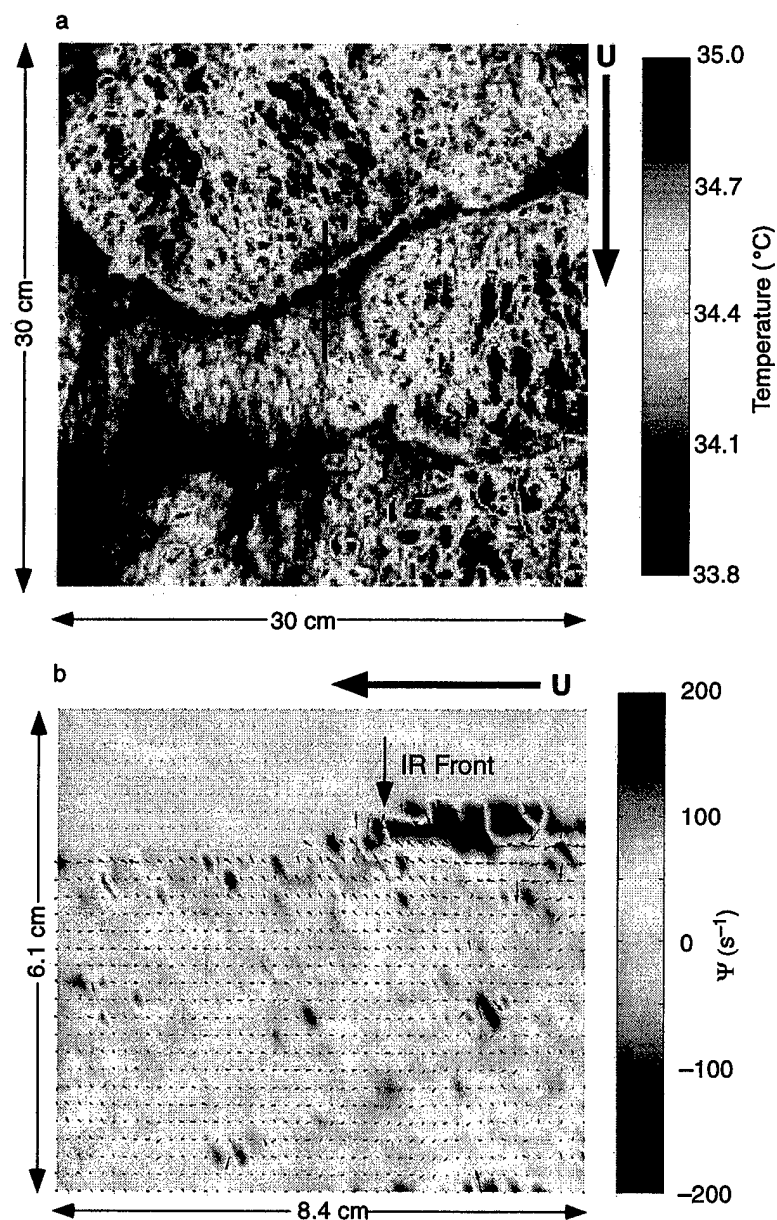


Figure 3.12. Example of (a) infrared imagery and (b) a vorticity plot with velocity vectors from the particle image velocimetry (PIV) depicting a microscale breaking wave. The wind direction in the infrared imagery is from top to bottom and in the PIV plot is from right to left. The vertical line in the infrared imagery corresponds to the laser sheet that intersects the water surface for the PIV measurement. The arrow in the PIV plot denotes the location of the propagating thermal front of the microscale breaking wave in the infrared imagery. Experimental conditions: $T_w = 35.1^\circ\text{C}$, $T_{aw} = -8.6^\circ\text{C}$, $RH = 45.5\%$, $f_p = 2.9\text{ Hz}$, $U = 9.7\text{ m s}^{-1}$, and $\Omega = 5.5\text{ m}$.

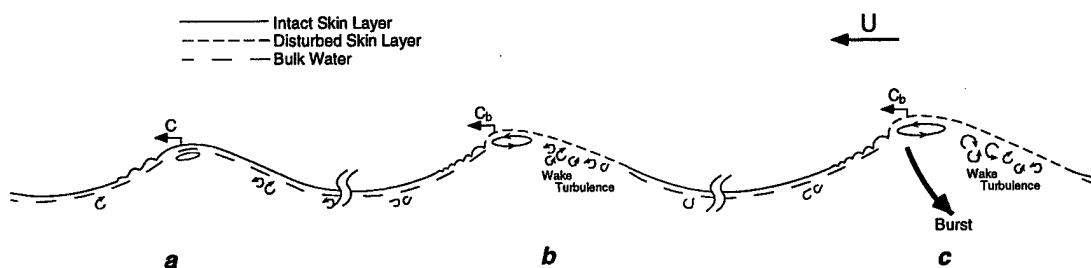


Figure 3.13. Illustration showing that not all wind waves are microscale breakers and not all microscale breaking waves produce bursts. (a) This wave is not a microscale breaker since the "roller" has not evolved into a "bore-like" crest which will disrupt the skin layer. (b) Microscale breaking produces small-scale eddies that are sufficiently energetic to bring about surface disruption. (c) Downward "bursting" motion may emerge as a result of a more intense microscale breaking event. The burst is shown for a reference frame moving with the crest. In general, no skin-layer disruption will occur for eddies incapable of inducing fluid-parcel overturning at the surface. Furthermore, not all turbulent eddies are due to microscale breaking events.

CHAPTER 4: CORRELATING MICROSCALE WAVE BREAKING WITH GAS TRANSFER

4.1 INTRODUCTION

The dependence of the transfer velocity on wind speed or wind stress has been shown to be a function of the concentration of surfactants [Frew, 1997], which are present in nature to varying degree. Laboratory measurements indicate that a wave-related mechanism may regulate gas transfer because the correlation of the transfer velocity with wave slope [Jähne *et al.*, 1984; Jähne *et al.*, 1987] is unaffected by the presence of surfactants [Frew, 1997]. Microscale wave breaking [Banner and Phillips, 1974] has been proposed as the underlying physical process that determines the transfer velocity at low to moderate wind speeds [Jähne *et al.*, 1987; Csanady, 1990]. Here in the Harris I study, the infrared imaging technique discussed in Chapter 3 is used to detect the fraction of surface area, A_B , in which the thermal boundary layer, or skin layer, is thinned and disrupted by microscale breaking waves. Measurements of the gas transfer velocity were correlated with the fraction of surface area affected by microscale breaking waves, for varying amounts of surfactant concentration.

4.2 MEASUREMENTS

In order to determine the correlation of microscale wave breaking with gas transfer, A_B and k were measured as a function of wind speed in the wind-wave tank at the University of Washington's Harris Hydraulics Laboratory (Harris). The tank measures 9.1 m long, 1.2 m wide, and 0.9 m deep and is equipped with a wind flume, a water-wave-absorbing "beach" made of rubberized horse hair, and a water heating/circulation system. The facility is instrumented to measure gas transfer, skin temperature, bulk water temperature profiles, air

temperature, relative humidity, wind speed, and surface displacement. Table 4.1 summarizes the conditions during the 13 experiments conducted for this study. The water in the tank was filtered tapwater, and the surface was vacuumed before each experiment to remove accumulated surface contaminants. Biological activity was minimized in all but two experiments by adding 0.5 kg of sodium hypochlorite to the water. As a further precaution, the tank was drained, cleaned, and refilled on a weekly basis. For controlled surfactant-influenced runs, 1 g m^{-3} of the soluble surfactant Triton X-100 was added to the water.

Bulk gas transfer velocities were determined for He ($Sc = 101$ at 30°C) and SF_6 ($Sc = 571$ at 30°) by supersaturating the water with the gases and measuring the decrease in their concentration over time [Asher *et al.*, 1996]. The concentration measurements made as a function of fetch and depth verified that the tank was well mixed with respect to the time scales of gas transfer. At each sampling time, a tank-averaged concentration, $c(t)$, was calculated from the individual concentrations at the five sampling locations. An average k was calculated as the slope of the line given by plotting $-d \ln[c(t)/c(0)]$ versus time, where $c(0)$ is the tank-averaged initial concentration in the water and d is the tank depth. Three samples were drawn at evenly spaced depths at the test section located at 5.5 m as well as a mid-depth sample 4 m upstream and a mid-depth sample 3.5 m downstream of the test section. Figure 4.1 shows the bulk transfer velocity, k , for He and SF_6 plotted versus wind speed, U . As expected, k was lower for a given wind speed for the controlled surfactant-influenced experiments compared to the cleaned surface cases, consistent with previous results in wind-wave flumes [Frew, 1997]. The two experiments conducted using unsterilized water (Nos. H3 and H7) also resulted in decreased values for k , suggesting the presence of surface-active material produced by biological activity. The data in Figure 4.1 verify the inadequacy of using wind speed to parameterize gas exchange since k can vary at a particular wind speed, depending on surface cleanliness.

As shown in Chapter 3, the infrared signature of the skin layer disruption caused by microscale wave breaking can serve to define and characterize this visually ambiguous process. Figure 4.2 shows two sequences of infrared images of the water surface in the wind-wave tank at different wind speeds that illustrate the detection technique. The measurements were made using an Amber model Radiance HS infrared imager (Amber Engineering, Goleta, CA) with a 256 by 256 element InSb focal-plane array that measured infrared radiation over the wavelength range of 3–5 μm . The imager viewed a 30 cm by 30 cm surface area at a range of 1 m and an incidence angle of 20° , and the skin temperature was inferred from the measured infrared radiance. Laboratory tests of the imager show a noise-equivalent temperature difference of less than 0.025°C (see Appendix A). A non-uniformity correction was performed before each run during the experiment and care was taken to minimize reflection effects. A_B was computed by applying a standard morphological image processing algorithm to thresholded infrared images (see Appendix A). The threshold is the mean temperature of each image plus 10% of the bulk–skin temperature difference, the latter being measured directly using bulk thermistors and calibrated infrared radiometers. As microscale breaking waves propagate down the tank, they disrupt the skin layer and mix warmer water from below to the surface, producing discrete quantifiable features within the images. The regions highlighted in Figure 4.2 correspond to areas of the skin layer disrupted by the turbulence generated by the breaking process. The ratio of the total area of the outlined regions to the total area of the image is the measure of A_B . The algorithm spatially filters out the small-scale surface renewal features of $O(10^{-2} \text{ m})$ as observed by Komori *et al.* [1993], such that A_B predominantly represents features produced by microscale breaking waves. The along-wind and cross-wind spatial scale of individual events were proportional to the dominant wavelength, and increased with wind speed as the dominant wavelength increased from roughly 10 cm to 15 cm. Furthermore, the variability in size and intensity of the fine-scale structures within the wakes suggests that the interaction of breaking-

induced turbulence with the free surface is influenced by the net heat flux and background turbulence [Zappa *et al.*, 1998].

Figure 4.3 shows A_B as a function of wind speed for all 13 Harris I experiments. For the cleaned surface cases, A_B increased from 0.10 to 0.25 as the wind speed increased from 4.5 to 11 m s⁻¹. With the addition of the surfactant Triton X-100, and in the presence of biological activity, A_B was significantly lower at a given wind speed, consistent with the known ability of surfactants to damp capillary-gravity waves [Lucassen, 1982; Alpers and Hühnerfuss, 1989]. These measurements of A_B are the first to cover a wide range of conditions, and the values determined here are comparable to previous estimates [Csanady, 1990; Jessup *et al.*, 1997b].

Figure 4.4 shows k versus A_B for He ($Sc = 101$ at 30°C) and SF₆ ($Sc = 571$ at 30°C). In contrast to the scatter with surface condition shown in Figure 4.1, the transfer velocity for each gas is linearly correlated with A_B . The correlation is independent of surface cleanliness and the linear coefficient of determination between k and A_B was 0.98 for He and 0.97 for SF₆ for wind speeds between 4.5 and 11 m s⁻¹. The correlation between k and A_B does not change with a variation of the threshold to determine A_B (see Appendix A).

4.3 DISCUSSION

The skin-layer disruptions associated with microscale wave breaking events can be viewed as regions where the replacement of fluid within the concentration boundary layer is enhanced. Since the wakes of microscale breaking waves are the warmest features in the infrared imagery, the renewal within the wakes appears more intense than the renewal in the background. It is this area of enhanced turbulence generated in the wake of a microscale breaking wave that dominates the transfer of gas across the air–water interface. Thus, it is likely that the gas transfer velocity could be modeled according to (2.6) as

$$k_m = A_B k_B + (1 - A_B) k_{NB}, \quad (4.1)$$

where A_B serves as an estimate for ϕ , k_B is the transfer velocity within A_B and k_{NB} is the transfer velocity outside of A_B . If $k_B \gg k_{NB}$, microscale wave breaking will contribute significantly to gas transfer and k should scale directly with A_B as found in Figure 4.4. The linear relationship between k and A_B shown in Figure 4.4 indicates that enhanced near-surface turbulence due to microscale wave breaking may be the underlying mechanism responsible for a significant fraction of the increase in k with wind speed.

Laboratory measurements have indicated that statistical increases in the local wave slope are associated with microscale breaking waves [Banner, 1990]. The simultaneous infrared and wave slope imagery presented in section 3.3 indicates significant increases in local wave slope associated with the actively breaking waves. Therefore, the data in Figure 4.4 may explain why wave slope has been observed to correlate with k for a range of surfactant-influenced surface conditions [Frew, 1997]. This point will be discussed in more detail in Chapter 6.

Models and experiments have shown that if k is measured for a particular gas and the value of n is known, k for any other gas may be estimated by multiplying the known transfer velocity by the ratio of the corresponding Schmidt numbers raised to the power $-n$, as expressed in (2.1). The Schmidt number exponent, n , theoretically ranges from $\frac{1}{2}$ for a perfectly clean surface that would be described by the free surface boundary condition to $\frac{2}{3}$ for a surface that is affected by surfactants and approaches the rigid boundary condition. In the case of the data in Figure 4.4, however, it is unclear that there is a unique value for n at a particular value of A_B because the cleaned and surfactant-influenced points are interspersed. If n is a multi-valued function of A_B , the linear correlation of k with A_B is of little practical use, since measuring A_B alone would provide no information concerning the value of n necessary for estimating transfer

velocities. Therefore, the dependence of n on A_B is of equal importance to the dependence of k on A_B .

In Figure 4.5, n for each experiment is plotted versus A_B . The value of n for a particular experiment was calculated from the measured k values and the Schmidt numbers for He and SF₆ using

$$n = \ln[k_1/k_2] / \ln[Sc_2/Sc_1], \quad (4.2)$$

where the subscripts 1 and 2 correspond to He and SF₆, respectively. The data show that n decreases linearly from $\frac{2}{3}$ to $\frac{1}{2}$ as A_B increases from 0.10 to 0.25. This behavior of n with respect to A_B is significant because it indicates that at a particular A_B , k for He and SF₆ can be related to k for any other gas by using the Sc^{-n} scaling. Figure 4.6 shows the gas transfer velocity, k_{600} , referenced to $Sc = 600$ (CO₂ at 20°C) calculated from k for He and SF₆ using n as predicted from the linear fit of the data in Figure 4.5. This demonstrates that k for He and SF₆ in Figure 4.4 collapses to a common linear relationship as a function of A_B that is unaffected by the presence of surfactants. The result suggests that microscale wave breaking is the wave-related mechanism that regulates the gas transfer velocity at low to moderate wind speeds.

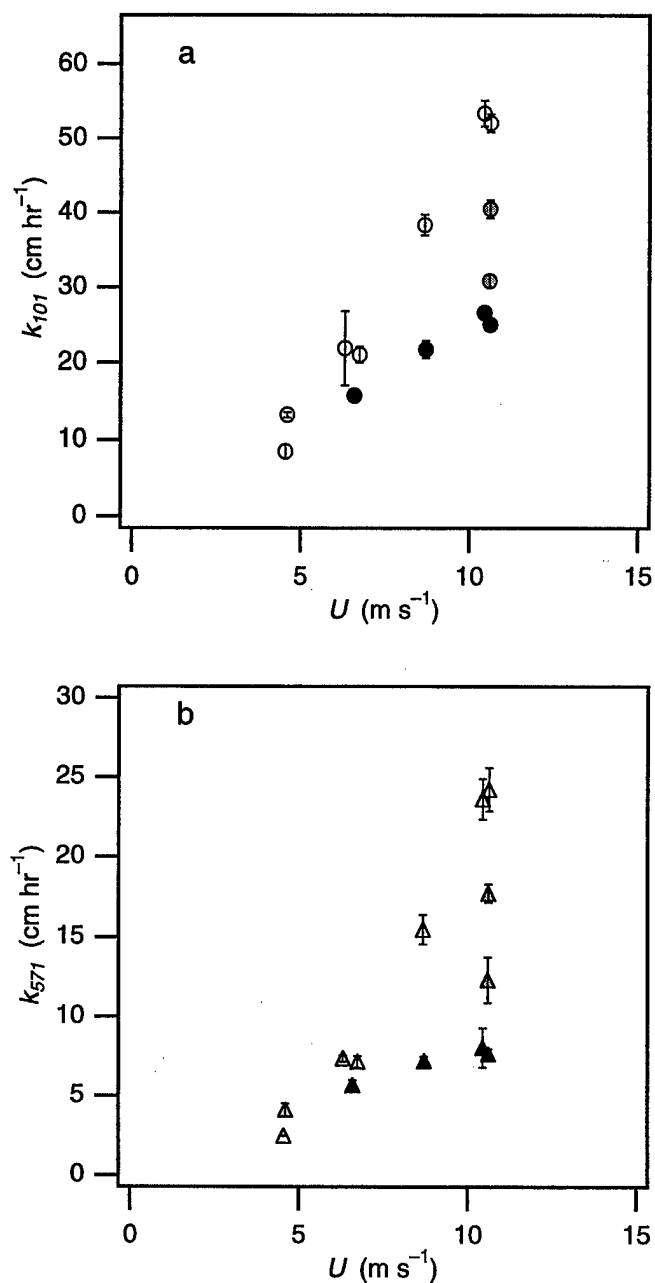


Figure 4.1. Bulk gas transfer velocity, k , plotted against wind speed, U , for (a) He (k_{101} for $Sc = 101$ at 30°C) and (b) SF_6 (k_{571} for $Sc = 571$ at 30°C). Open markers correspond to data for a cleaned surface, shaded markers to data for a surface affected by biological activity, and solid markers to data for a surfactant-influenced surface. The error bars for k represent the standard error of the fit from the linear regression $-\ln[c(t)/c(0)]$ versus time.

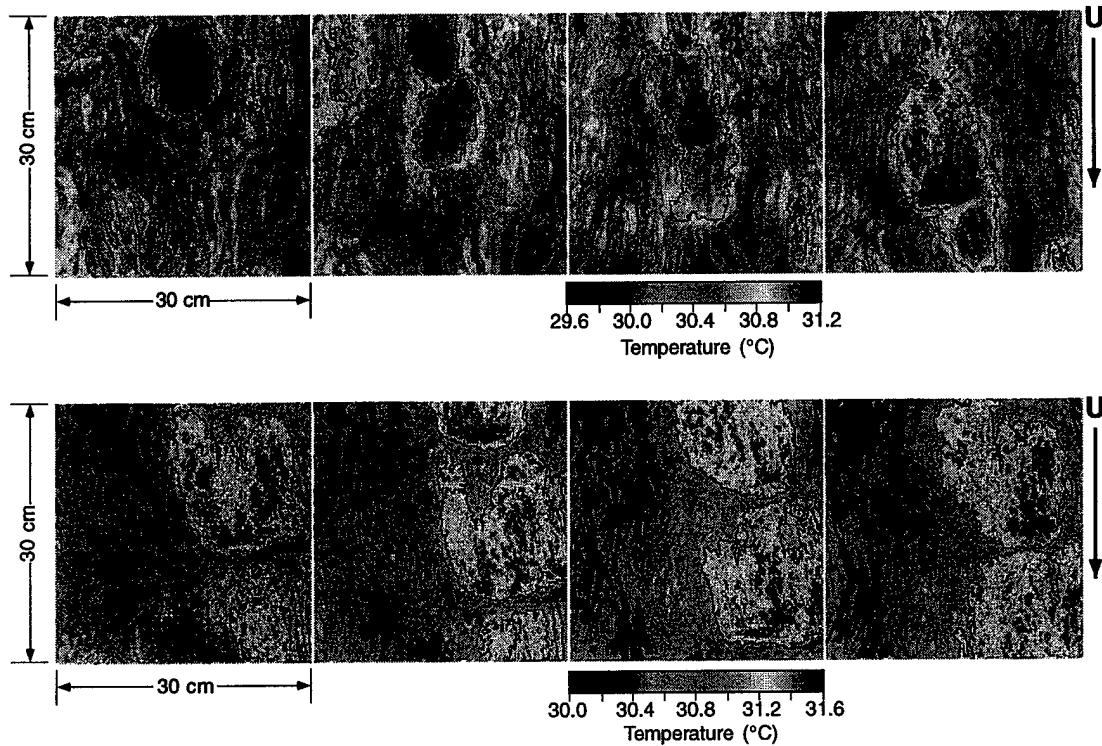


Figure 4.2. Fractional area coverage of microscale wave breaking, A_B , measured at a fetch of 5.5 m plotted versus wind speed. Open markers correspond to data for a cleaned surface, shaded markers to data for a surface affected by biological activity, and solid markers to data for a surfactant-influenced surface. Each data point represents the average of five runs performed during one Harris I experiment that lasted between 80 and 334 minutes, depending on the wind speed. Error bars for A_B represent the standard deviation of the means calculated for each run.

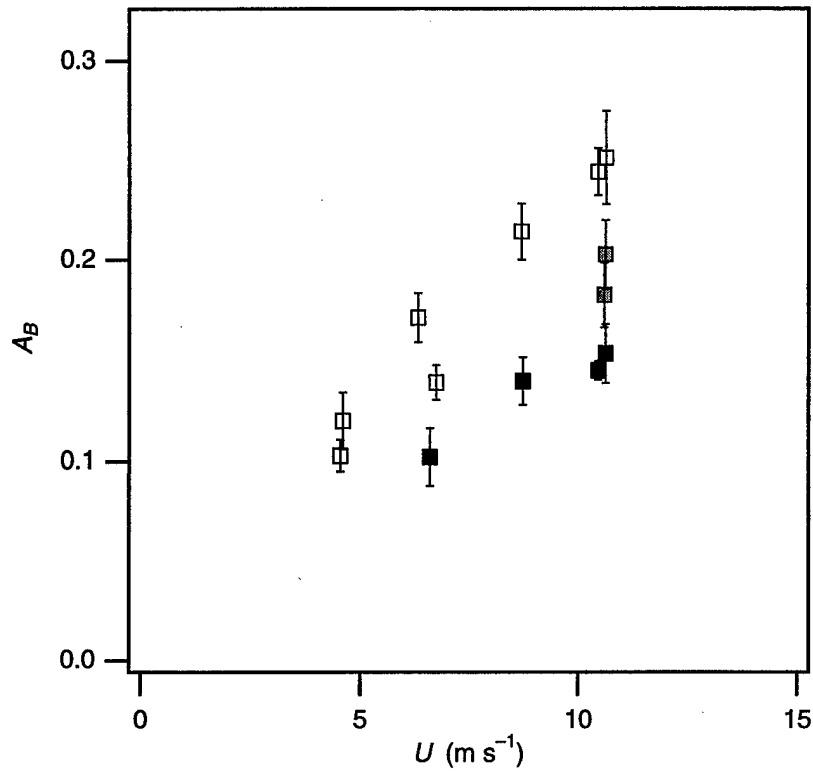


Figure 4.3. Fractional area coverage of microscale wave breaking, A_B , measured at a fetch of 5.5 m plotted versus wind speed. Open markers correspond to data for a cleaned surface, shaded markers to data for a surface affected by biological activity, and solid markers to data for a surfactant-influenced surface. Each data point represents the average of five runs performed during one Harris I experiment that lasted between 80 and 334 minutes, depending on the wind speed. Error bars for A_B represent the standard deviation of the means calculated for each run.

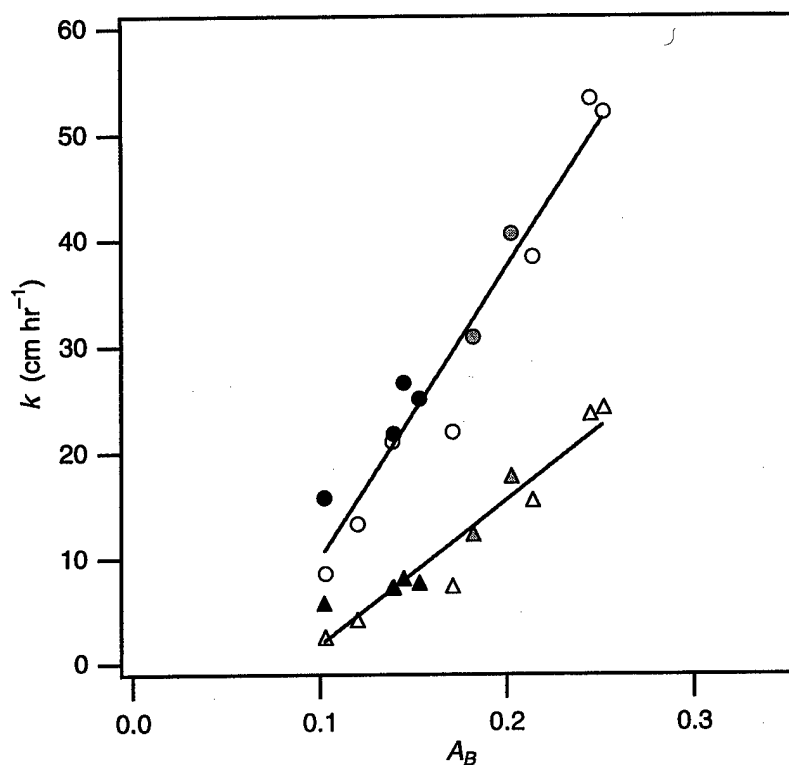


Figure 4.4. The bulk gas transfer velocity, k , versus the fractional area coverage of microscale wave breaking, A_B , for He (circles; k_{101} for $Sc = 101$ at 30°C) and SF_6 (triangles; k_{571} for $Sc = 571$ at 30°C). Open markers correspond to data for a cleaned surface, shaded markers to data for a surface affected by biological activity, and solid markers to data for a surfactant-influenced surface. The correlation between k and A_B is independent of surface cleanliness and implies that microscale wave breaking is the dominant physical process that regulates the flux of gas across the air–water interface at low to moderate wind speeds.

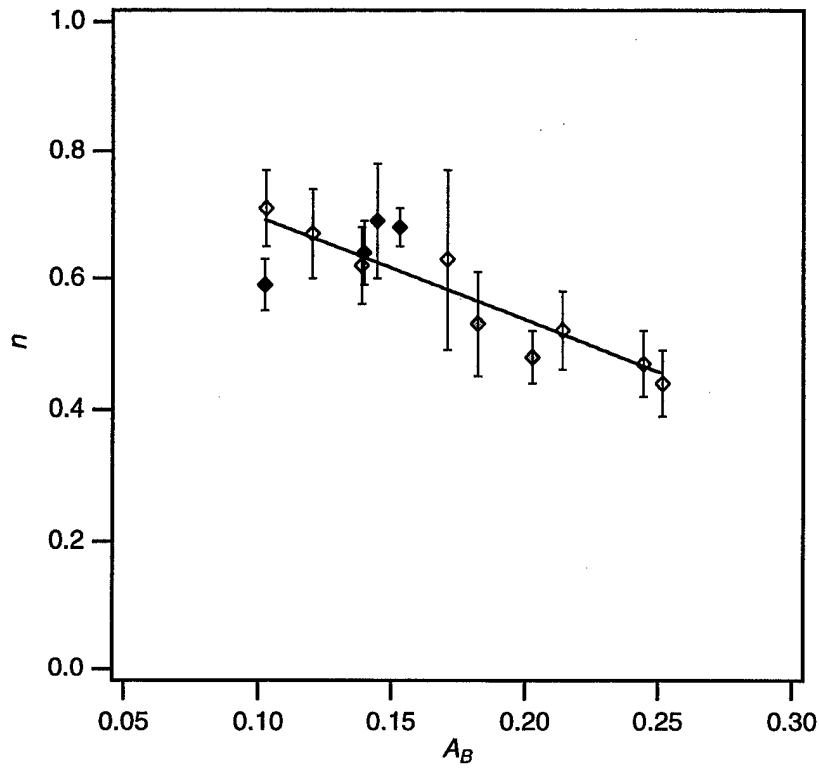


Figure 4.5. The Schmidt number exponent, n , versus the fractional area coverage of microscale wave breaking, A_B . Open markers correspond to data for a cleaned surface, shaded markers to data for a surface affected by biological activity, and solid markers to data for a surfactant-influenced surface. The linear regression shown is $n = 0.855 - 1.591A_B$ with a linear coefficient of determination of 0.86.

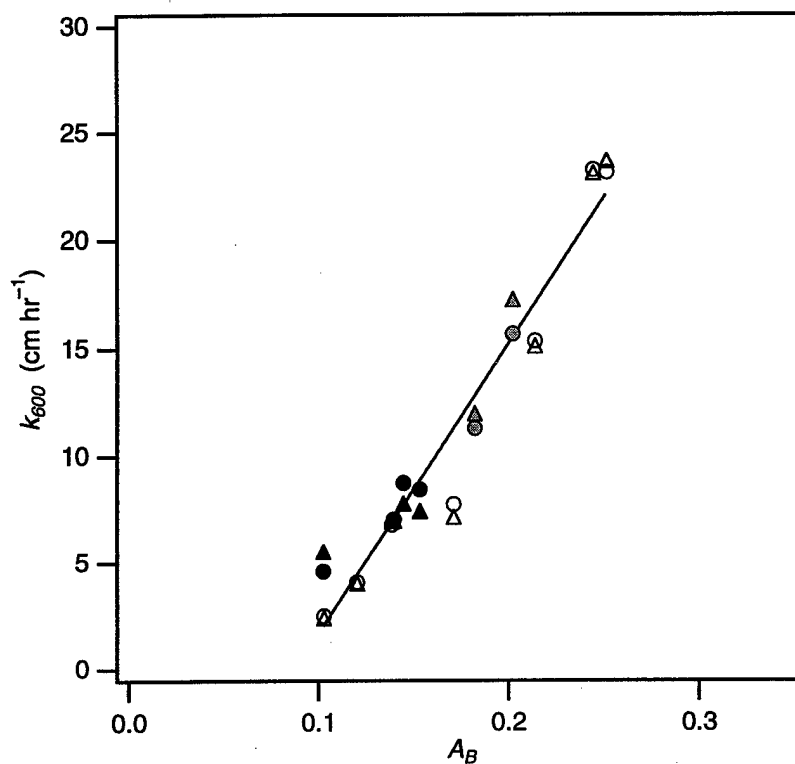


Figure 4.6. The bulk gas transfer velocity, k_{600} , referenced to $Sc = 600$ (CO_2 at 20°C) versus the fractional area coverage of microscale wave breaking, A_B . The gas transfer velocity referenced to CO_2 was calculated from k for He (circles) and SF_6 (triangles) using n as predicted at a particular A_B from the linear regression of the data in Figure 4.5. Open markers correspond to data for a cleaned surface, shaded markers to data for a surface affected by biological activity, and solid markers to data for a surfactant-influenced surface.

Table 4.1. Environmental conditions for the Harris I study. Wind speed (U), bulk-skin temperature difference (T), air-water temperature difference (T_{aw}), water temperature (T_w), relative humidity (RH), peak wave frequency (f_p), and root-mean-square surface displacement (RMS η) have been averaged for the duration of each experiment. Experiment numbers increase in chronological order and were performed over a two-month time period. The large air-water temperature differences were used to ensure a measurable infrared signal and did not affect the determination of k . Asterisks represent experiments with the surfactant Triton X-100 and daggers represent experiments with unsterilized water.

U (m s ⁻¹)	T (°C)	T_{aw} (°C)	T_w (°C)	RH (%)	f_p (Hz)	RMS η (cm)	Duration (minutes)	Experiment No.
4.6	1.8	-12.0	30.2	59.1	5.0	0.11	166	H2
4.6	2.1	-12.7	30.2	47.4	4.8	0.13	334	H8
6.3	1.6	-11.0	30.1	61.9	3.9	0.23	145	H1
6.6	1.8	-12.3	30.3	40.6	3.8	0.18	149	H10*
6.8	2.0	-12.2	29.5	43.3	3.7	0.27	210	H6
8.7	1.7	-12.4	30.4	43.0	3.3	0.31	175	H4
8.7	1.6	-9.2	29.8	34.3	3.4	0.30	132	H12*
10.5	1.4	-11.9	30.0	47.5	2.9	0.58	100	H9
10.5	1.7	-10.5	30.5	40.6	2.9	0.30	101	H11*
10.6	1.4	-7.9	29.4	43.5	3.0	0.37	150	H3†
10.6	1.7	-10.0	29.4	37.4	2.9	0.54	150	H7†
10.6	1.4	-7.1	28.7	29.9	3.0	0.30	80	H13*
10.7	1.0	-6.9	28.5	36.1	2.9	0.58	158	H5

CHAPTER 5: QUANTIFYING THE DIRECT EFFECT OF MICROSCALE WAVE BREAKING ON GAS TRANSFER

5.1 INTRODUCTION

The results described in Chapter 4 (and also by Zappa *et al.* [1999]) have shown that k is linearly correlated with A_B and that this correlation is insensitive to the presence of surfactants. This correlation is strong evidence for a causal link between microscale wave breaking and gas transfer. In order to provide definitive proof that microscale wave breaking is the physical process that regulates k at low to moderate wind speeds, experiments were performed in the wind-wave flume at the Air-Sea Interaction Research Facility at NASA Goddard Space Flight Center/Wallops Flight Facility in October–December 1998. By using this facility, it was possible to make fetch-dependent, concurrent, and collocated measurements of the relevant physical processes associated with air-water transfer. The measurements of infrared and wave slope imagery during the experiments at this Wallops facility have been discussed in Chapter 3 and showed that the skin-layer disruptions observed in the infrared were indeed caused by microscale wave breaking. As in the Harris I experiment of Chapter 4, measurements were made of A_B and of tank-averaged gas transfer using He and SF₆. Additionally, it was possible to measure k_B and k_{NB} , the local transfer velocities in and out of the wakes of microscale breaking waves, respectively, using the controlled flux technique (CFT). Measurements of air-side friction velocity, u_{*a} , were provided by W. R. McGillis of Woods Hole Oceanographic Institution (WHOI) using the gradient method applied to wind profiles measured from pitot tubes. S. Long of the Air-Sea Interaction Research Facility provided facilities support as well as measurements of surface displacement and wind speed.

5.2 EXPERIMENTAL SETUP

Figure 5.1 shows the wind-wave flume at the Air-Sea Interaction Research Facility at NASA GSFC/Wallops Flight Facility. The flume is 18.29 m long, 1.22 m high, and 0.91 m wide, the water depth is 0.76 m, and the air headspace is 0.46 m. The facility is capable of wind speeds up to 25 m s^{-1} and currents up to 0.5 m s^{-1} . The tank is equipped with a water heating/circulation system and a 10-cm thick water-wave-absorbing "beach" made of plastic honeycomb. The facility is instrumented to measure wind speed, friction velocity and surface displacement. For this study, measurements of bulk gas transfer, bulk water temperature, air temperature, relative humidity, and wind speed were made. Gas concentrations were measured by gas chromatography using a Carle model 1100 thermal electron capture detector (Chandler Engineering Company, Tulsa, OK) for He and a Hewlett Packard model 5790 electron capture detector (Hewlett Packard Company, Palo Alto, CA) for SF_6 . Both chromatography measurements of gas concentration had an analytical experimental accuracy within 4%. R.M. Young model 41342 slow-response thermistors (R.M. Young Company, Traverse City, MI) measured the air and water temperature with an accuracy of 0.3°C and a sensitivity of $\pm 0.1^\circ\text{C}$. A Rotronic model 41367 probe (Rotronic Instrument Corp., Huntington, NY) monitored the relative humidity with an accuracy of 3% and a sensitivity of $\pm 0.1\%$. A redundant measurement of air velocity was made with an Omega model FMA-905 (Omega Engineering Inc., Stamford, CT) with an accuracy of 1.5% of the free stream velocity, complementing the measurements by pitot tubes. Table 5.1 summarizes the conditions during the 21 experiments conducted for the Wallops study. The duration of each experiment was determined by the gas transfer measurement of He and SF_6 by inventory method and lasted between 1.5 and 3.5 hours, similar to the duration of each experiment during the Harris I study. The environmental conditions were continuously monitored throughout the experiment. Two simultaneous sequences of infrared and wave slope imagery, as well as infrared and PIV imagery, were taken at three equal intervals during the course of the experiment, for a total of six runs for each pair of techniques.

In order to investigate the dependence of gas transfer and microscale wave breaking on fetch, measurements were made at two fetches of 5.6 m and 11.1 m (u_{*a} was only measured during experiments at 5.6 m). Figure 5.2 shows the experimental setup used at the fetches of 5.6 m and 11.1 m. Furthermore, the influence of surfactants was also investigated by purposely adding surfactant to the water for a portion of the experiments at both fetches. The water used in the tank was filtered tapwater, and the surface was skimmed before each experiment to remove accumulated surface contaminants. Biological activity was minimized by continuous bromination to 5 ppm levels using dissolving pellets of 1-bromo-3-chloro-5, 5-dimethylhydantoin (Bio-Lab Inc., Decatur, GA). As a further precaution, the tank was drained, cleaned, and refilled between the groups of experiments performed at the two fetches. For experiments with a purposely contaminated water surface, 1 g m^{-3} of the soluble surfactant Triton X-100 (polyoxyethylene isooctylphenyl ether, Aldrich Chemical Co., Milwaukee, WI) was added to the water. While transferring the equipment between the groups of experiments made at the 5.6 m and 11.1 m fetches, the light box used for the image slope system was re-sealed using Terostat MS939 putty (Sahlberg, Feldkirchen bei München, Germany) that bled an oily surfactant slowly into the water. The water for these experiments immediately following the change in fetch (W14 through W17) was not treated with Triton X-100, but the presence of this adventitious surfactant made these experiments into surfactant-influenced cases. After observing the lower transfer velocities and an n of $\frac{2}{3}$ characteristic of surfactant contamination, the tank was drained, the oily sealant was removed, and the tank was cleaned and refilled. The surface conditions for Experiments W14 through W17, therefore, have been denoted as adventitious surfactant cases.

5.3 MEASUREMENTS OF TRANSFER VELOCITY AND A_b

Tank-averaged bulk transfer velocities were calculated for He ($Sc = 94$ at 31.5°C) and SF_6 ($Sc = 510$ at 31.5°C) and Schmidt number exponents, n , were deduced from these data in

the manner discussed in Chapter 4 for the Harris I experiment. Figure 5.3 shows the gas transfer velocity for He, k_{600-G} , referenced to a $Sc = 600$ as a function of wind speed for both fetches, and as a function of u_{*a} for the fetch of 5.6 m. The plot of k_{600-G} in Figure 5.3a shows that for a given wind speed, the transfer velocity is multi-valued depending on surface cleanliness. Since k_{600-G} is tank-averaged, no fetch dependence of this quantity was observed. Rather, the variation in k_{600-G} at a given wind speed is the consequence of a variation in the degree of surface contamination. The result in Figure 5.3 confirms the result shown in Figure 4.1 from the Harris I experiment. As expected, k was lower for a given wind speed for the controlled and adventitious surfactant-influenced experiments compared to the cleaned surface cases, consistent with previous results in wind-wave flumes [Frew, 1997].

Infrared imagery was used to detect and quantify the fractional coverage of microscale wave breaking and to implement the CFT. The infrared measurements were made using an Amber model Radiance HS infrared imager (Amber Engineering, Goleta, CA). At a range of 1.4 m and an incidence angle of 30° , the imager viewed a surface area with a vertical scale of 52 cm and a horizontal scale of 51 cm at the top of the image and 47 cm at the bottom. A non-uniformity correction of the focal-plane array was performed before each run during the experiment using a Santa Barbara Infrared (SBIR) model 2004S blackbody (Santa Barbara Infrared Inc., Santa Barbara, CA) (see Appendix A) and care was taken to minimize reflection effects. Laboratory tests of the imager show a noise-equivalent temperature difference of less than 0.025°C (see Appendix A). In addition, the imager was calibrated before each run during the experiment, such that the skin temperature could be inferred from the measured infrared radiance (see Appendix A). A_B was computed by applying a thresholding technique to the infrared images coupled with standard morphological processing operations (see Appendix A). The threshold is based upon the mean skin temperature represented by the minimum temperature, $\langle T_{min} \rangle$, within each image and a measure of the bulk-skin temperature difference, T ,

represented by the standard deviation of the image temperature, σ_T . Here, $\langle T_{min} \rangle$ was calculated as the average temperature of 1% of the pixels (655) in each image with the lowest temperature. The threshold of $3.5\sigma_T$ above $\langle T_{min} \rangle$ was chosen to detect the features processed as A_B . For the runs used to detect A_B , 1536 frames of infrared imagery ^{were} digitized at a frequency of 15 Hz for a record of 100 s in duration. Figure 5.4 shows A_B as a function of wind speed for both fetches, and as a function of u_{*a} for the 5.6 m fetch. For the cleaned surface cases, A_B increased from 0.25 to 0.40 as the wind speed increased from 4.2 to 8.3 m s⁻¹. With the addition of the surfactant Triton X-100 and for the adventitious surfactant cases observed at the 11.1 m fetch, A_B was significantly lower at a given wind speed, consistent with the results in Figure 4.1 for the Harris I study. These measurements of A_B are the first to cover a wide range of conditions at two fetches, and the values determined here are comparable to previous estimates [Csanady, 1990] and measurements [Jessup *et al.*, 1997b; Zappa *et al.*, 1999].

The plot of the Schmidt number exponent, n , versus A_B in Figure 5.5 shows that n decreases smoothly from $\frac{2}{3}$ to $\frac{1}{2}$ as A_B increases from 0.10 to 0.40. This result is consistent with that from the Harris I study shown in Figure 4.5. Together, Figure 4.5 and Figure 5.5 show that a cleaned surface does not necessarily result in an n of $\frac{1}{2}$ and likewise that a surfactant-influenced surface does not necessarily result in an n of $\frac{2}{3}$.

Figure 5.6 shows k_{600-G} from He versus A_B . The data appear to fall into two groups, distinguished as the cleaned and as the surfactant-influenced surfaces, and each is linearly correlated. The correlation coefficient is 0.93 for the cleaned case and 0.94 for the surfactant-influenced case. The linear fit for the cleaned case does not pass through the origin, while that for the surfactant-influenced data nearly does. These results differ from the Harris I study shown in Figure 4.4 where the data showed a linear correlation coefficient of 0.98 that was independent of surface contamination. One possible explanation for this difference is that k_{600-G} is a tank-

averaged quantity and A_B is measured locally. In order to correlate with the k_{600-G} measurement, A_B would need to be averaged at every location down the long Wallops tank. Rather than make measurements of A_B at all fetches, the controlled flux technique was used to measure k at the same fetch as A_B . This avoided problems associated with correlating a tank-averaged value for k with a local estimate of A_B .

5.4 CONTROLLED FLUX TECHNIQUE

The controlled flux technique (CFT) outlined in section 2.2 uses heat as a proxy tracer for gas to infer the local k with fast response times and high spatial resolution. Here, the controlled flux technique was used to determine the direct effect of microscale wave breaking on gas transfer. A Synrad model G48-2-28(W) continuous-wave 25-W CO₂ laser (Synrad Inc., Mulkinleto, WA) operating at 10.6 μm was directed at the water surface from above the tank using a series of mirrors, as depicted in Figure 5.2, and was pulsed for 40 ms with a gating frequency of roughly 1 Hz. The laser beam generated heated spots on the water surface in the field of view of the infrared imager roughly 2–3 cm in diameter. For the runs used to determine the decay time from the CFT, the infrared imagery was digitized at a frequency of 120 Hz. Figure 5.7 is a sequence of infrared images taken for a wind speed of 6.9 m s⁻¹ showing a heated patch produced by the CO₂ laser as it decays over time.

The spot was tracked in the infrared imagery to determine τ for the decay method outlined in *Haußecker et al.* [1995]. The technique fits the tracked decay curve time series data to the analytical solution of the one-dimensional unsteady diffusion equation that incorporates a turbulent transport term characterized by a statistical renewal of the surface layer by large eddies. In this technique, the transfer is assumed to be controlled by water-side processes and the heat flux across the air–water interface is assumed to be minimal [*Jähne et al.*, 1989]. Following from

Danckwerts [1951], the non-steady surface renewal transport boundary layer model (assuming surface renewal can be modeled as a chemical reaction) for temperature T is

$$\frac{\partial T(z,t)}{\partial t} = \alpha \frac{\partial^2 T(z,t)}{\partial z^2} - \lambda T(z,t), \quad (5.1)$$

where α is the thermal diffusivity and $\lambda = 1/\tau$ is the statistical surface renewal rate as determined from this model. For a given initial concentration distribution within the boundary layer, the temporal solution is given by

$$T(z,t) = \frac{1}{2\sqrt{\pi\alpha t}} e^{-\lambda t} \int_{-\infty}^{\infty} T(\xi,t) e^{-\frac{(z-\xi)^2}{4\alpha t}} d\xi. \quad (5.2)$$

Assuming a near-surface Gaussian profile is applied as the initial condition, $T(z,0) = T_o e^{-z^2/h^2}$, where T_o is the temperature of the decay curve at any time chosen as the starting point and $h/2$ is the penetration depth, and assuming a semi-infinite fluid ($- \infty < z < 0$), the temperature at $z = 0$ is

$$\frac{T(0,t)}{T_o} = \frac{h}{\sqrt{h^2 + 4\alpha t}} e^{-\lambda t}. \quad (5.3)$$

The experimentally determined decay curves for $T(0,t)/T_o$ can be fit to the functional form of (5.3) to determine h and λ .

The tracking algorithm implemented here for following the heated spot uses the initial location of the patch and calculates the center of mass of the spot. This algorithm will be referred to as the Center of Mass (CM) tracking algorithm. Since the initial location of the patch is known, an image subregion surrounding the patch is thresholded by three standard deviations

above the background surface temperature to determine the spatial extent of the patch. The average temperature of this thresholded area was used as the mean patch temperature, T_p . The center of mass of the patch within the image subregion is used in subsequent timesteps as the reference location for the subregion. Roughly 25–30 individual patch decay time series were averaged to produce a mean decay time series, \bar{T}_p , for each run within the given experiment. \bar{T}_p was normalized as $T_N = (\bar{T}_p - T_{mean}) / (T_o - T_{mean})$, where T_{mean} is the spatial and temporal mean background image temperature of the water surface just prior to and during the decay process. The values for λ were determined by fitting T_N to (5.3) using a Levenberg-Marquardt optimization algorithm [Press *et al.*, 1992]. The standard error in the fitted parameter λ for the six runs was averaged to determine the total error in the measurement for a given experiment. A total of 150–180 individual patches was analyzed within an experiment. The local transfer velocity for heat as determined from the CFT, k_H , is calculated according to (1.15) as

$$k_H = \sqrt{\alpha \lambda}. \quad (5.4)$$

The CFT-modeled surface-renewal rate, λ , characterizes the inverse timescale of the turbulent flow and increases with turbulent intensity.

The mean normalized surface temperature, T_N , of the patches tracked by the CFT is shown in Figure 5.8 as a function of wind speed ranging from 4.2 m s⁻¹ to 8.3 m s⁻¹. Assuming the surface cleanliness is constant, the transfer should increase as the wind speed increases. As the wind speed increased, T_N decayed more quickly, and λ increased with wind speed from 2.0 to 7.6 s⁻¹. Since from (5.4) k_H increases with λ , Figure 5.8 implies that k_H increased with increasing wind speed for the cleaned surface experiments.

The CM tracking method used here was compared to the 3D Structure Tensor (3D-ST) tracking algorithm developed by *Haußecker and Jähne* [1997]. Starting at the initial known patch location, the 3D-ST algorithm calculates the displacement vector field within a local spatio-temporal neighborhood of the CFT patch. At each timestep, the 3D-ST algorithm computes T_p as the average temperature over a square surface area that is roughly double the actual patch area. The mean surface temperature tracked by the 3D-ST algorithm, then, is a combination of the surface water heated by the CO_2 laser as well as surface water with a temperature equal to the background. Figure 5.9 shows that values of λ calculated from the 3D-ST technique and the CM technique differ by less than 5%. The difference in the tails of the decay curves demonstrates the operational difference in the algorithms. For the CM algorithm, T_N does not return to zero, while for the 3D-ST algorithm, T_N returns to zero. The reason is that the CM algorithm tracks the patch itself only until it reaches the threshold level while the 3D-ST algorithm tracks the region/feature back to the mean. Since the CM algorithm tracks the patch itself, the CM algorithm was chosen for the analysis.

Since heat and gas are both scalar tracers, *Jähne et al.* [1987, 1989] have asserted that the transfer velocity of heat should scale directly to gases using (2.1). Therefore, k_{600} determined from He and SF_6 , k_{600-G} , should equal k_{600} determined by the CFT, k_{600-H} . Figure 5.10 compares k_{600-H} and k_{600-G} . The result shows that for this experiment k_{600-H} overestimates k_{600-G} by a factor of roughly 2.5. This significant difference between k_{600-H} and k_{600-G} has not been observed in previous comparisons of CFT- with bulk-determined k [*Jähne et al.*, 1987; *Jähne et al.*, 1989; *Haußecker et al.*, 1995]. The difference cannot be explained by the choice of n , since n was determined independently from (4.2) using He and SF_6 and the values are consistent with previous wind-tunnel results [*Jähne and Haußecker*, 1998]. Furthermore, the discrepancy is too large to be explained by the fetch dependence of k . The measurements of k_{600-H} at fetches of 5.6 m and 11.1 m both show values at least double those of k_{600-G} . Since k_{600-G} is tank-averaged, fetch

as an explanation would require the local transfer for a significant portion of the tank to be less than half that of k_{600-G} . Since these measurements of k_{600-H} extend over a significant portion of the tank and the local transfer increases with fetch, it is unlikely that the contributions at short fetch would be small enough to force a 1:1 correlation between k_{600-H} and k_{600-G} .

The higher values of k_{600-H} are most likely the result of heat flux from the patch dominated by the air-side fluxes of water vapor and sensible heat. These fluxes of heat from the laser-heated patch to the atmosphere may significantly contribute to the overall temperature decay rate. This increase in the decay rate will directly affect the k_{600-H} and its relationship with k_{600-G} if the assumption that all transfer into the bulk water is not valid. A supplemental experiment (Harris II) was performed at the Harris Hydraulics Laboratory at the University of Washington to investigate the dependence of k_H on the heat flux, Q (see Appendix B). The results from Wallops and Harris II together show that k_H depends on Q . Although this finding is new and significant, it does not affect the use of CFT for the comparison of local transfer measurements inside and outside of the wakes of microscale breaking waves during Wallops. Therefore, the details of the dependence of k_H on Q are given in Appendix B.

The data in Figure 5.10 show that $0.377k_{600-H} = k_{600-G}$, where the scale factor of 0.377 was determined by minimizing the root mean square error to 1.05 cm hr^{-1} for the difference between k_{600-H} and k_{600-G} . Therefore, by applying this factor, k_H can be scaled to match k_G for He and SF_6 . Figure 5.11 shows the scaled k_H , k_{600-SH} , referenced to a Sc of 600 compared with k_{600-G} . The scaling was found to produce a 1:1 correlation between k_{600-H} and k_{600-G} for the entire data set. Since k_{600-H} varied relatively little compared to the variation of total net heat flux during the experiment, the scaling is assumed to be appropriate for this data set. However, throughout the remainder of this thesis, the unscaled k_{600-H} will be used for consistency instead of the scaled

k_{600-SH} , since k_H does not extrapolate directly to a gas without the use of a scale factor, which may change for different experiments.

Figure 5.12 shows the local heat transfer velocity, k_{600-H} , (a) as a function of wind speed, U , for both fetches and (b) as a function of the air-side friction velocity, u_{*a} , at a fetch of 5.6 m. Consistent with the results in Figure 4.1 and Figure 5.3, k_{600-H} was lower at a given U or u_{*a} for the Triton X-100 surfactant-influenced experiments. Experiments performed with the adventitious oily surfactant also showed a decrease in k_{600-H} . Figure 5.12 demonstrates the difficulty of using wind speed or friction velocity to parameterize gas transfer since k can be a multi-valued function of U or u_{*a} , depending on the surface cleanliness.

Figure 5.13 shows that the local transfer velocity for heat, k_{600-H} , determined from the CFT referenced to a Sc of 600 is linearly correlated with the fractional area coverage of microscale wave breaking and this correlation is independent of surfactant. The correlation coefficient is 0.94 and the linear fit passes through the origin. As mentioned previously, the results of k_{600-G} versus A_B for the Harris I study in Figure 4.4 and for the Wallops study in Figure 5.6 compare a tank-averaged to a local quantity. Since k_{600-H} and A_B are both local measurements, a single correlation is expected that is independent of surface cleanliness.

5.5 LOCALIZED GAS TRANSFER WITHIN MICROSCALE BREAKING WAVES

The correlation between k and A_B observed in the Harris I experiment and duplicated in the Wallops experiment suggests that microscale wave breaking is the underlying mechanism controlling the gas transfer velocity. However, a correlation does not necessarily indicate a causal relation. If microscale breaking waves are the source of near-surface turbulence responsible for the correlation, the transfer velocity inside the wake of microscale breaking waves should be enhanced. Thus, a model for the transfer velocity given in (4.1) has been suggested

based upon the partitioning of k into two separate transfer velocities, one within the skin-layer disruptions in the wakes of microscale breaking waves and one outside the wakes in the background. The CFT allows us to look locally at the fine-scale processes at the air–water interface that regulate gas transfer. While implementing the CFT, the individual decay rates of the actively heated patches produced by the CO_2 laser were observed to vary substantially in the infrared imagery, and these decay rates were dependent on the influence of microscale wave breaking.

The objective of implementing the CFT is to quantify k_B and k_{NB} in order to determine the effect that microscale breaking has on the overall gas transfer. However, the patch decay will depend on the stage of breaking that affects the patch. CFT patches that occur in the background may never be affected by a microscale breaking wave since not all waves that propagate past a particular point in the image are breaking. These CFT patches unaffected by microscale breaking decay slowly and are termed Background examples. Many microscale breaking waves affect the heated patches only partially. In essence, a patch may decay in the background for some time before a microscale breaker propagates over the patch and mixes it completely into the bulk as demonstrated in Figure 5.14. The decay for these events varies significantly since the microscale breaking wave may affect it at any time and is termed a Delayed Microbreaker example. Finally, patches laid immediately in the actively breaking wave crest decay abruptly and are termed Microbreakers. Patches that occur in the wakes of microscale breaking waves also decay quickly and are also deemed Microbreakers.

Figure 5.14 shows infrared sequences illustrating the three types of decay of the actively heated CFT patches observed, which have been designated Background, Delayed Microbreaker, and Microbreaker. The top sequence shows the background decay in which the patch is unaffected by microscale breaking. The middle sequence shows the delayed decay when a microscale breaker affects the patch after the patch has decayed in the background for a period

of time. The bottom sequence shows microbreaking decay, when a patch is laid directly in the actively breaking wave crest of a microscale breaker. Comparing these sequences, the patches directly affected by microscale wave breaking decay faster than those patches in the background. These observations are quantified by the normalized decay curve time series, T_N , shown in Figure 5.15. The comparison of the Microbreaker and Background examples will be used to determine the direct effect of microscale wave breaking on the gas transfer velocity.

Distinguishing microbreaker patches from background patches has been achieved by using A_B in the vicinity of the patch. Those patches that were coincident with an active microscale breaking wave were classified as Microbreakers and used to determine the transfer velocity due to microscale wave breaking, k_B . Specifically, if at the moment the patch reaches its peak T_N and it is completely within an area of the image designated by A_B , it was classified as a Microbreaker. Those patches that were unaffected by microscale wave breaking were classified as Background and used to compute k_{NB} , the transfer velocity that is unaffected by microscale breaking waves. If throughout the whole decay process, the patch is never completely within an area of the image defined by A_B , the patch is classified as Background. Typically, approximately 2 to 12 events from each experiment were determined to be included in k_B and roughly 7 to 12 time series were determined to be included in k_{NB} . The incidence of microbreaking events tended to rise with A_B and the incidence of background events tended to fall with A_B . This observation suggests that the frequency of microscale breaking might be estimated by classifying the CFT patches directly affected by microscale breaking. However, a statistically significant result would require many more decay time series than available here.

Figure 5.16 shows k_B and k_{NB} as a function of A_B . Both k_B and k_{NB} increase with A_B , but k_B is significantly greater than k_{NB} . Figure 5.17 shows the ratio of k_B to k_{NB} , $R_{enh} = k_B/k_{NB}$, versus A_B . The ratio R_{enh} serves as an estimate of the enhancement of the transfer

velocity due to microscale wave breaking. The turbulence generated by the actively breaking microscale wave crest consistently enhances the local transfer velocity by a factor of 3, with a mean enhancement factor of nearly 3.5 for all experiments. Therefore, microscale wave breaking has a significant effect on the increased transfer of gas across the air–water interface observed in the presence of waves.

Figure 5.18 shows the ratio $R_{eff} = A_B k_B / k_m$ versus A_B , where $k_m = A_B k_B + (1 - A_B) k_{NB}$ according to (4.1). The ratio R_{eff} serves as an estimate of the effect of microscale wave breaking on the overall transfer velocity. At low A_B , the contribution of microscale wave breaking to gas transfer is 25%. As A_B increases the effect of microscale wave breaking on the total transfer velocity approaches nearly 75% and is significantly greater than the contribution of the background. A check on the partitioned model in (4.1) for k based on k_B and k_{NB} is the plot of k_m against k_{600-H} in Figure 5.19. The comparison of k_m to k_{600-H} demonstrated in Figure 5.19 shows that the model describes the overall transfer velocity k_{600-H} very well.

5.6 DISCUSSION

The surface boundary condition should be determined by its dynamical effect on the near-surface velocity field and not by its cleanliness alone, as discussed in Chapter 1. Since waves are strongly affected by the presence of surfactants [Lucassen, 1982; Frew, 1997] and near-surface turbulence has been linked with the presence of microscale breaking waves [Jähne *et al.*, 1987], the change in n with A_B in Figure 5.5 reveals a change in the interaction of turbulence with the air–water interface. The near-surface turbulence due to microscale wave breaking should increase with A_B . Disruptions of the diffusive boundary layer by microscale wave breaking observed in the infrared imply that the near-surface turbulence generated by these events was strong enough to produce convergence or divergence as stipulated by continuity in (1.22).

This suggests that locally the air–water interface behaves as free surface. Thus, as A_B increases, the cumulative effect of these areas of convergence and divergence should force n to approach $\frac{1}{2}$. Since waves were always present during these measurements, the flow regime was always rough. Therefore, the transition of n from $\frac{2}{3}$ to $\frac{1}{2}$ can be seen as a transition from a rigid surface to a free surface boundary condition, rather than a smooth to a rough regime.

As mentioned previously, the observed dependence of k_{600-G} versus A_B on surface contamination shown in Figure 5.6 for the Wallops study may be the result of fetch effects when comparing a tank-averaged quantity to a locally measured quantity. The tank-averaged bulk transfer velocity can be described as the average of all local transfer velocities down the tank

$$k = \frac{1}{m} \int_0^m k' \{f(V, \ell), \Omega, \text{surfactant}\} d\Omega, \quad (5.5)$$

where k' is the local transfer velocity, $f(V, \ell)$ represents the near-surface hydrodynamics, Ω is the fetch, and m is the total length of the tank. The data of Jähne *et al.* [1989] shown in Figure 1.7 demonstrate that for a cleaned surface the local transfer velocity increased significantly with fetch (2 m – 8 m) as a function of wind speed. The fetch dependence was greatest at low wind speeds but insignificant at wind speeds of 7.7 m s^{-1} , and the behavior of $\langle S^2 \rangle$ with fetch was shown to be similar to the behavior of k . Surfactants may also affect k_{600-G} by damping both the evolving wave field and near-surface turbulence. Surfactants will damp waves to varying degrees depending upon the wavelength of the wave and the amount of surfactant present at the water surface. Since the dominant wavelength and spectral wave energy increase with fetch, surfactants will have less effect on the total energy of the wave field as fetch increases [Lucassen, 1982; Frew, 1997]. For a cleaned surface, the dominant wavelength and spectral wave energy will also increase with fetch, but at each fetch, the total wave energy will be greater than for a surfactant-

influenced surface. The average statistics of the wave field, in general, are not uniform as a function of fetch, and this non-uniformity is further affected by surfactants.

The two distinct linear relationships in Figure 5.6 for cleaned and surfactant-influenced surfaces may result from a combination of the coupled effects described in (5.5) and outlined above. At low k_{600-G} , A_B is significantly greater for the cleaned surface case than for the surfactant-influenced case for a given k_{600-G} . These low k_{600-G} values correspond to low wind speeds comparable to those reported by Jähne *et al.* [1989] where the fetch dependence of gas transfer and slope was significant. The addition of surfactant may further accentuate the fetch effect observed for low wind speeds and short fetch by Jähne *et al.* [1989]. With the addition of surfactant, the point at which transfer becomes fetch-independent may increase for both wind speed and fetch. If this is valid, the location where k becomes fetch-independent is crucial to the comparison of k_{600-G} with A_B . Measurements of A_B were made at fetches of 5.6 m and 11.1 m, where the results of Jähne and co-workers [Jähne *et al.*, 1985; Jähne *et al.*, 1987; Jähne *et al.*, 1989] suggest that minimal fetch dependence exists for k and $\langle S^2 \rangle$ for cleaned water surfaces. If A_B is measured in the fetch-dependent region for surfactant influenced cases and in the fetch-independent region for the cleaned case, two distinct linear relationships would be expected. The evolution of microscale breaking waves, which directly enhances gas transfer, will be mitigated in the presence of surfactant and leads to less breaking as shown in Figure 5.4. At shorter fetch, waves will be suppressed to an even greater extent, and less turbulence will be generated by wave breaking to promote gas transfer. Furthermore, surfactants damp turbulence at the free surface, and diminished near-surface turbulence leads to diminished transfer as shown in Figure 5.12 where k_{600-H} decreased locally for the surfactant-influenced cases. All these contributing factors highlight the difficulty in interpretation of the results of correlating the tank-averaged k_{600-G} with the local single-fetch measurement of A_B for conditions of varying surface contamination.

Though conclusive evidence is beyond the scope of this study, the observation that k_{600-G} versus A_B shows two groupings with respect to surface condition in Figure 5.6 can be explained to be related to the dependence of k on fetch as described by (5.5). The implication is that it is crucial to compare measurements locally since the processes affecting transfer may vary significantly with fetch. Because transfer is affected directly at the air-water interface by the near-surface turbulence, the local transfer velocity was measured by the controlled flux technique and correlated with A_B . Measurements of k_{600-H} using the CFT showed that the local heat transfer velocity increased with the timescale for surface renewal that is directly related to turbulence. Since k_{600-H} and A_B are co-located measurements and always made concurrently, the single linear correlation for k_{600-H} versus A_B is independent of fetch and surface contamination and provides further evidence that microscale breaking waves regulate gas transfer.

The transfer velocity within the wake of a microscale breaking wave should be greater than k in the background because of the increased turbulence generated by the breaking process. The skin-layer disruptions associated with microscale wave breaking events can be viewed as regions where the replacement of fluid, or surface renewal, within the concentration boundary layer is enhanced. It is this area of enhanced surface renewal generated in the wake of a microscale breaking wave that regulates the transfer of gas across the air-water interface. The local measurements of k_B and k_{NB} from CFT are directly estimated from the surface-renewal properties at the air-water interface. Therefore, the model in (4.1) suggests that if k_B is much greater than k_{NB} , k will correlate with A_B , and surface renewal due to microbreaking will contribute significantly to gas transfer. The results in Figure 5.16 indeed show that $k_B \gg k_{NB}$, and surface renewal in the wakes of microscale breaking waves was shown to enhance gas transfer by a factor of 3.5 over that in the background. PIV measurements showed enhanced vorticity beneath the crests and in the wakes of breaking waves, confirming the idea that turbulence is driving the enhanced transfer observed from the local heat transfer velocity results. Furthermore,

microscale breaking was shown to directly contribute up to 75% of the transfer across the air–water interface under moderate wind speed conditions. These results show conclusively that microscale wave breaking is an underlying mechanism that explains the observation of enhanced gas transfer in the presence of waves and may indeed govern air–water gas transfer at low to moderate wind speeds.

The model for k_m in (4.1) compares well with k_{600-H} , suggesting that the analysis is consistent with the results and that the model properly describes the surface-renewal processes that affect gas transfer. Surface renewal due to microscale wave breaking and to shear- or convectively driven turbulence in the background are both accounted for in the model. Only at low k_{600-H} does the modeled k_m underestimate k_{600-H} . At these low k_{600-H} values and correspondingly low A_B values, a secondary mechanism not detected as a microscale breaking wave, such as small-scale Langmuir circulation, may begin to be of import to the mixing processes near the free surface. Small-scale Langmuir circulation has been observed in laboratory wind-wave initiation studies by *Melville et al.* [1998] and was shown to be both persistent and energetic. The comparison of k_m to k_{600-H} and the results in Figure 5.18 demonstrate that the potential for microscale wave breaking to dominate gas transfer is of significant importance when considering the processes that affect air–sea exchanges of heat and mass.

The success of the model in (4.1) in describing k cannot go without comment on its weaknesses. First, the model assumes that the measured k_B is constant when applied over the region A_B . This causes some error since k_B is an average of the complete distribution of the transfer velocities detected within A_B . Some breaking events may be actively breaking while others may be decaying turbulent wakes. The intensity of the individual breaking events may vary as well. Therefore, a representative distribution of all stages, scales, and strengths of

breaking must be included in the average k_B . The model also assumes that A_B is detected correctly as the effective area in breaking-induced transfer. If A_B varies, the contribution due to breaking may be expected to vary. But consider that as A_B becomes smaller, k_B should increase since fewer heated patches would be determined to be affected by breaking, and vice-versa. Future experiments should measure a larger distribution of events than sampled here in order to estimate k_B properly and to investigate the effect of varying A_B and on both k_B and k_m .

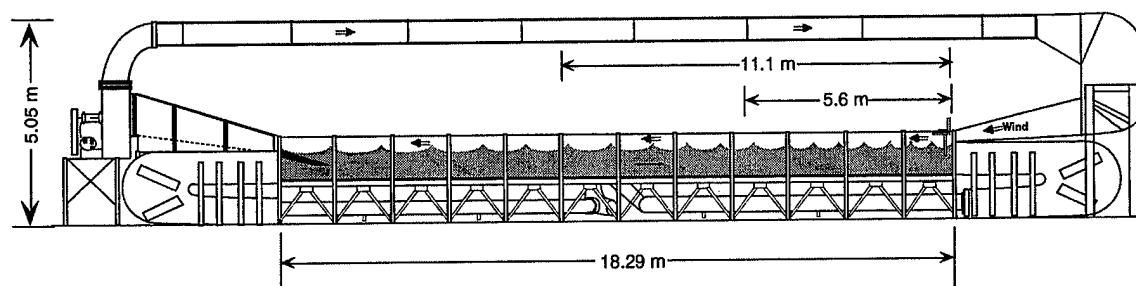


Figure 5.1. Wind wave flume at the Air-Sea Interaction Research Facility at NASA GSFC, Wallops Flight Facility.

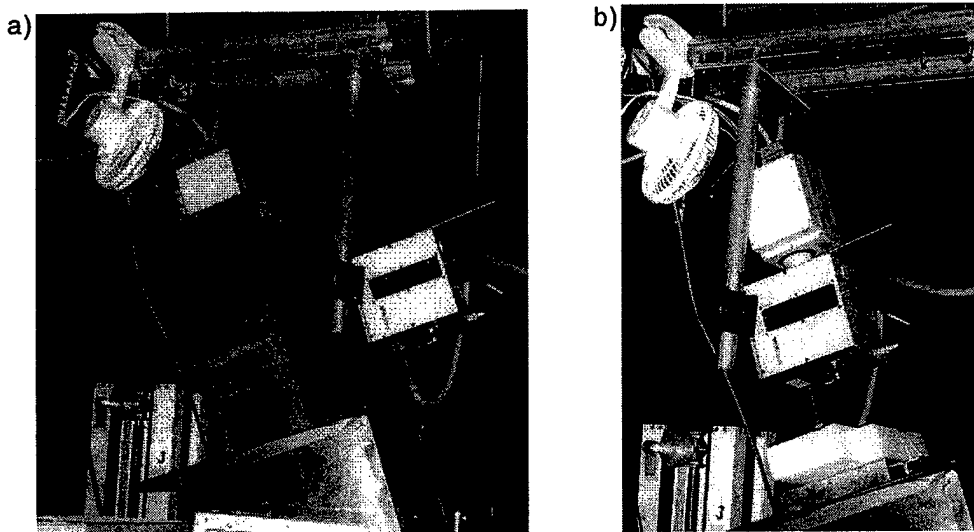
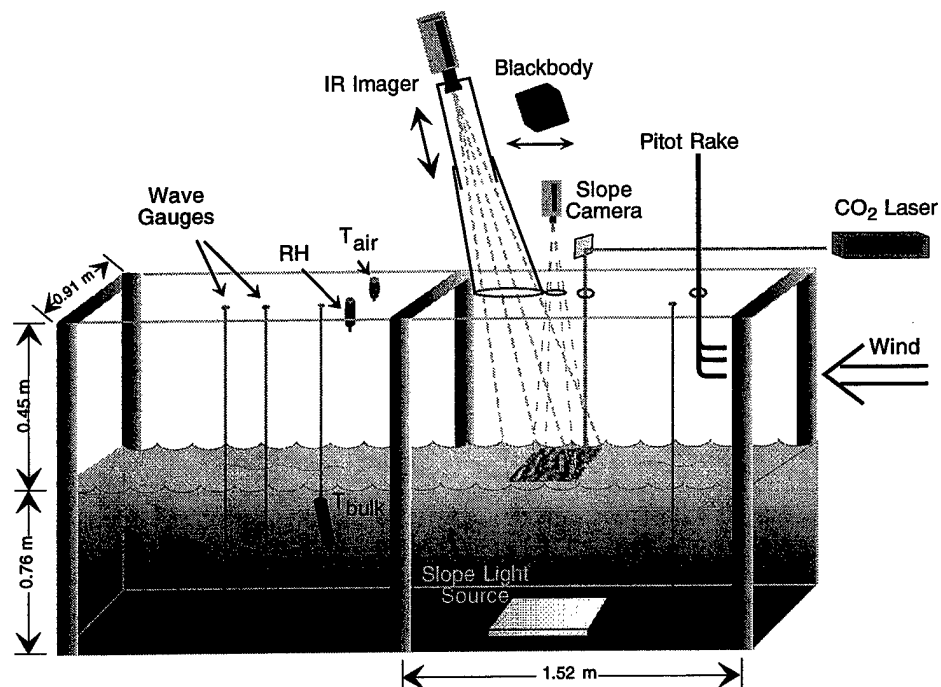


Figure 5.2. Top: Experimental setup for a given fetch during the Wallops study. Bottom: Photographs showing the Amber model Radiance HS infrared camera (a) imaging the water surface with the reflection guard in place and (b) observing the SBIR model 2004S blackbody during the calibration/NUC mode. The reflection guard ducting slides along the imager line of sight to allow the blackbody carriage to move into position for calibrating the imager and correcting the non-uniformity (NUC) of the detector (see Appendix A).

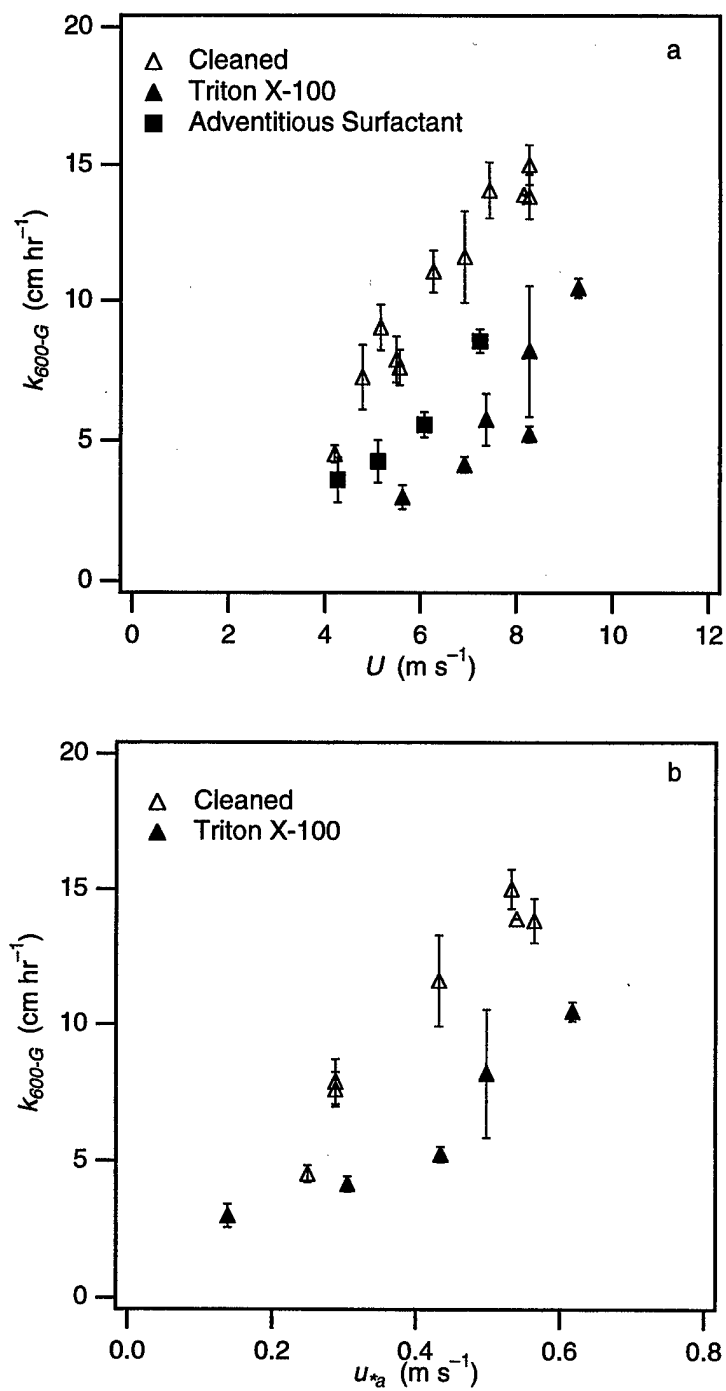


Figure 5.3. Bulk gas transfer velocity, k_{600-G} , for He referenced to a $Sc = 600$ as a function of (a) wind speed, U , and (b) air-side friction velocity, u_{*a} .

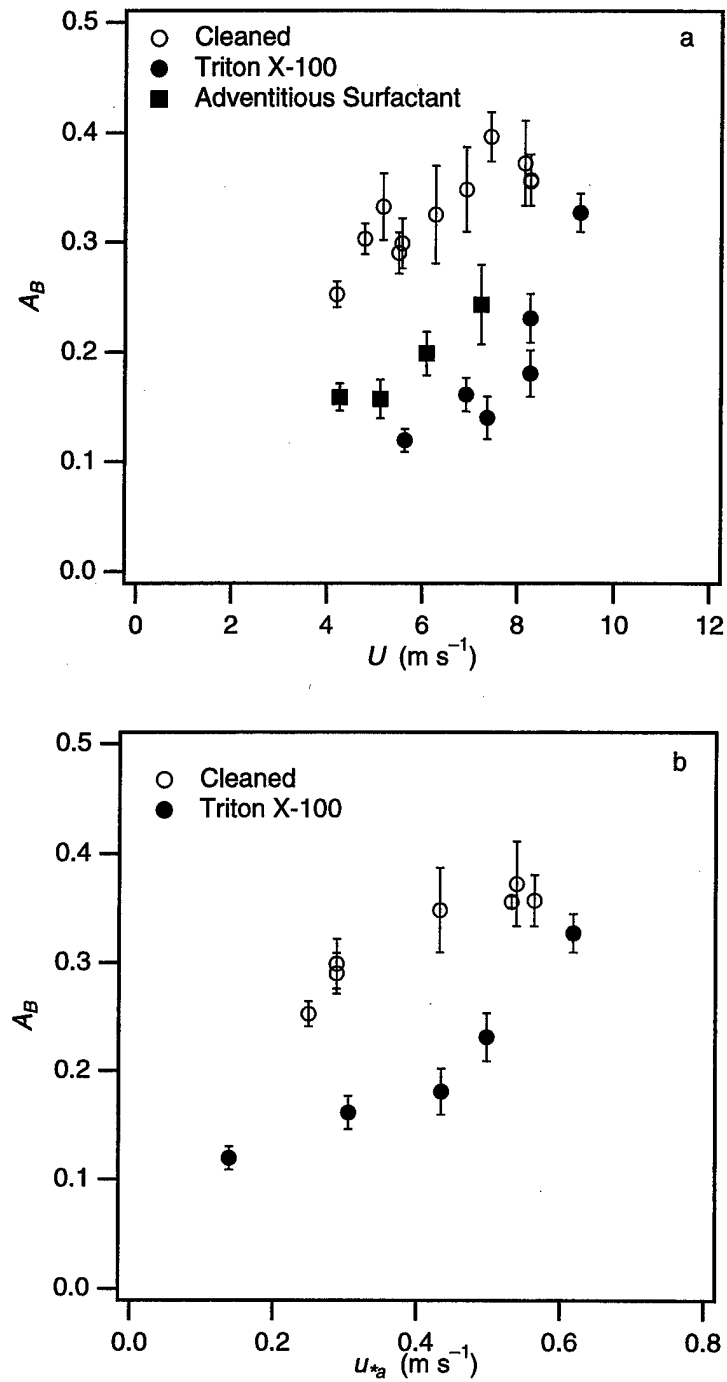


Figure 5.4. Fractional area coverage of microscale wave breaking, A_B , as a function of (a) wind speed, U , and (b) air-side friction velocity, u_{*a} .

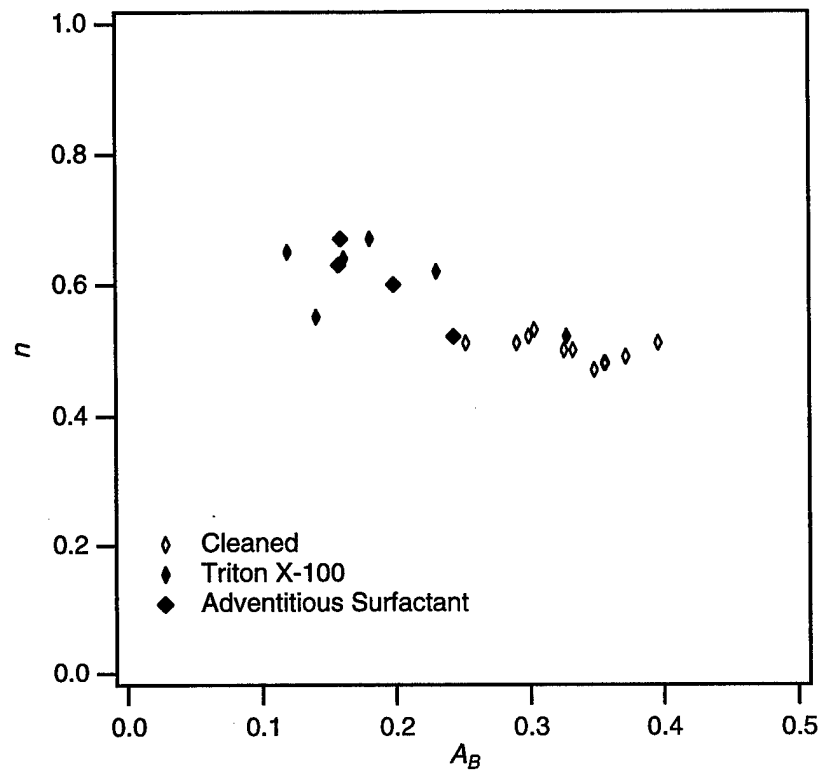


Figure 5.5. Schmidt number exponent, n , as a function of the fractional area coverage of microscale wave breaking, A_B .

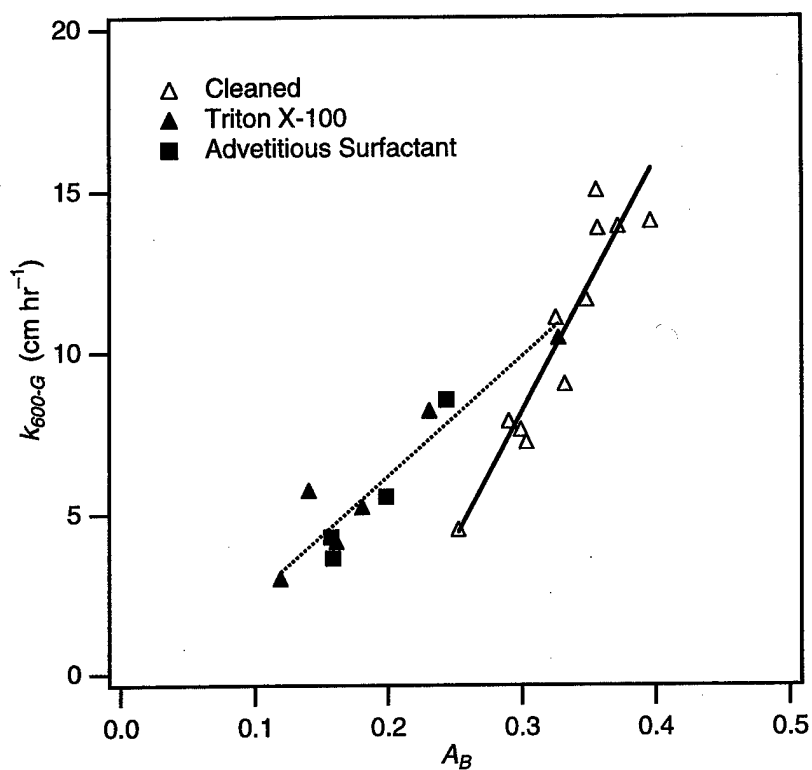


Figure 5.6. Bulk gas transfer velocity, k_{600-G} , for He referenced to a $Sc = 600$ versus the fractional area coverage of microscale wave breaking, A_B .

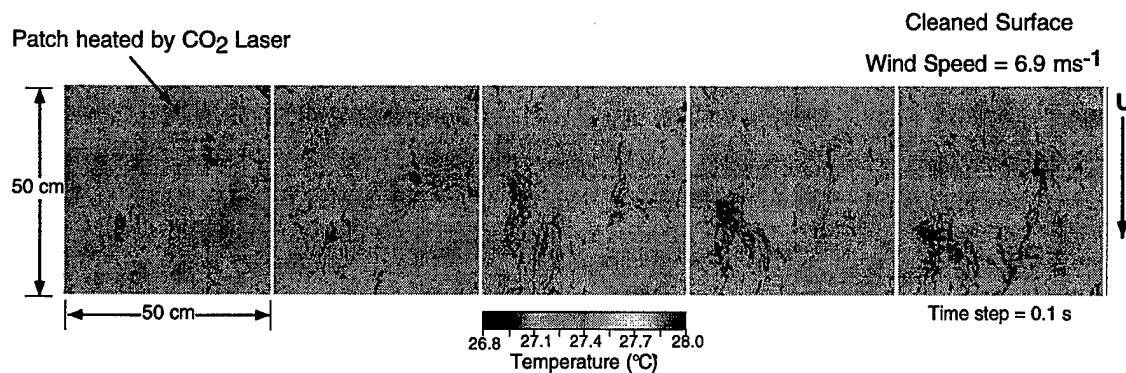


Figure 5.7. Sequence of infrared images of the water surface heated by the CO_2 laser. The patch is tracked and used to determine the characteristic timescale for transfer across the air–water interface. Time increases from left to right in 0.1 s increments and the wind direction in the images is from top to bottom. The experiment number was W5 and the wind speed was 6.9 m s^{-1} ; $T_w = 28.2^\circ\text{C}$, $T_{aw} = -5.2^\circ\text{C}$, $RH = 42.4\%$, and $f_p = 3.17 \text{ Hz}$.

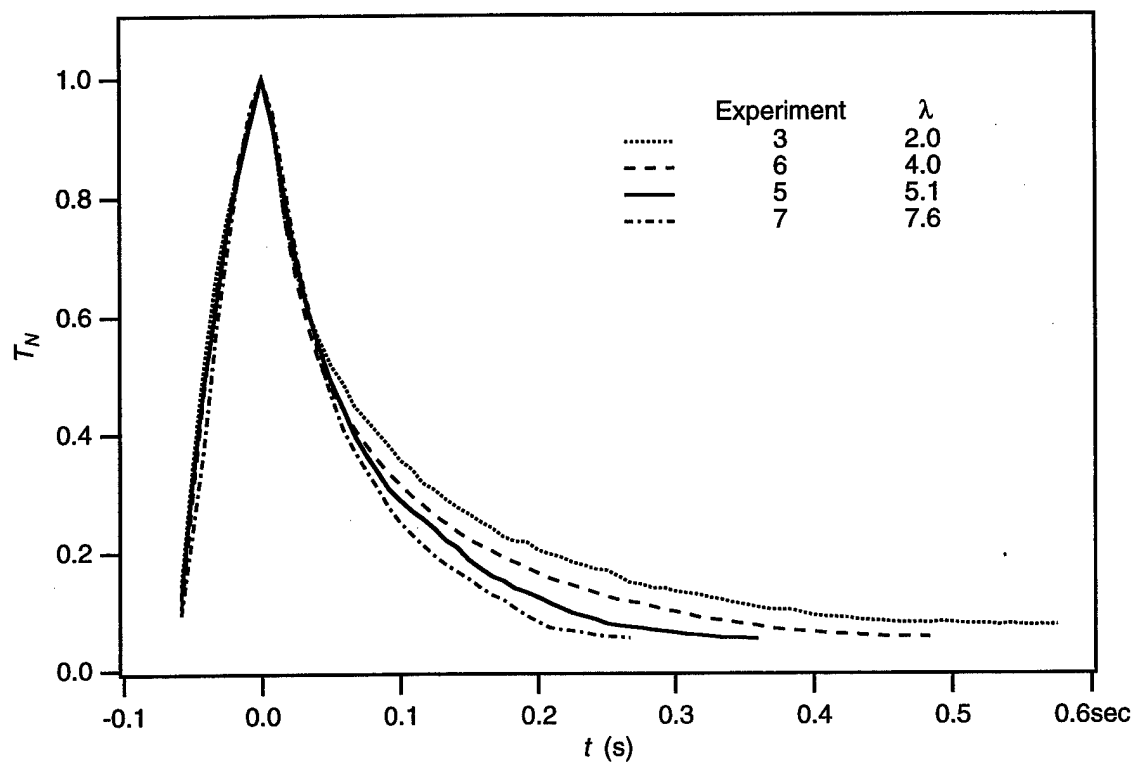


Figure 5.8. Time series of the normalized surface temperature, T_N , of the tracked CFT patch varying as a function of wind speed.

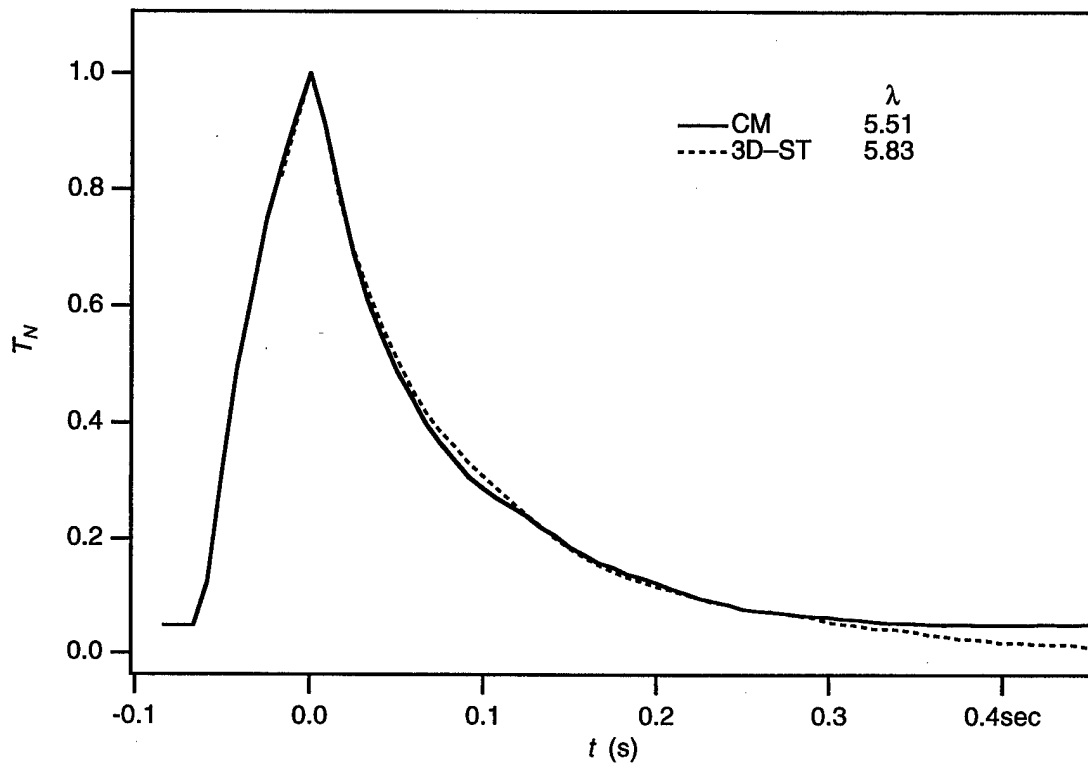


Figure 5.9. Comparison of decay curve time series determined by the CM and 3D-ST tracking algorithms.

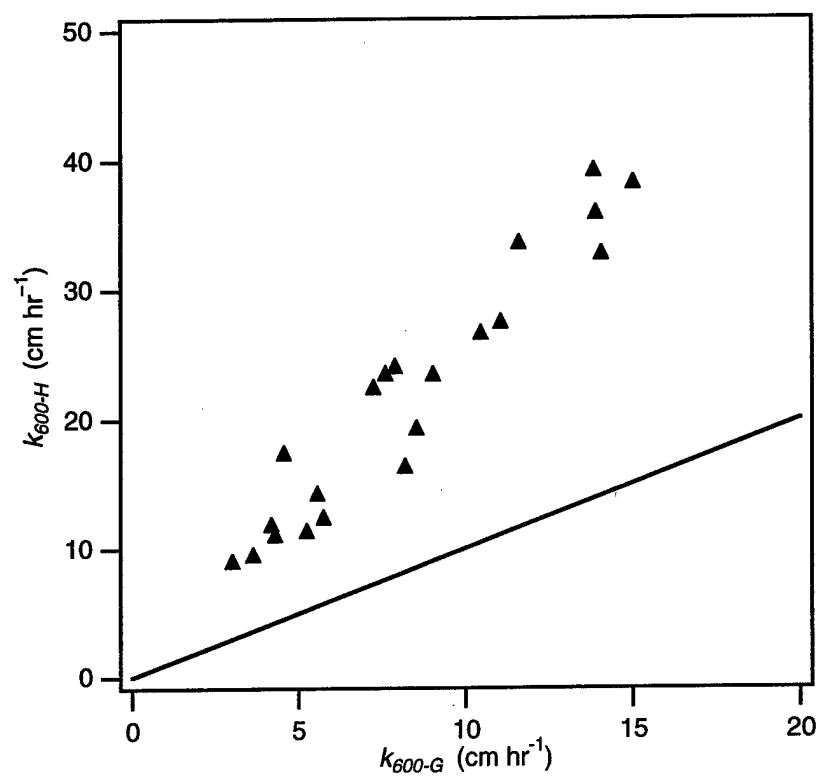


Figure 5.10. Direct comparison of k_{600-H} and k_{600-G} referenced to a $Sc = 600$.

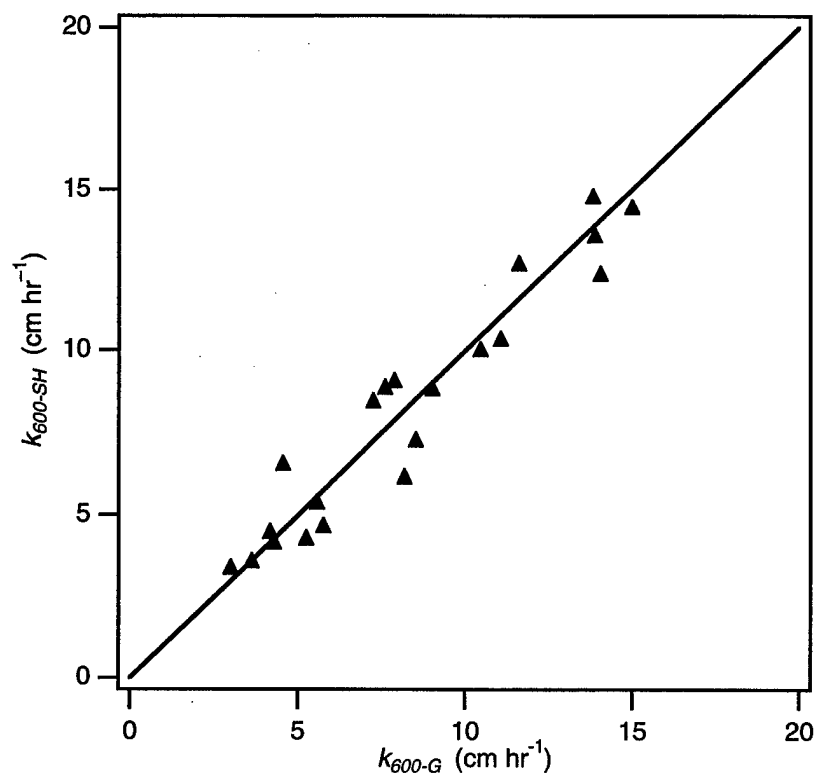


Figure 5.11. Local heat transfer velocity, k_{600-SH} , determined by the CFT referenced to a $Sc = 600$ and scaled by the factor 0.377, compared directly to the gas transfer velocity, k_{600-G} , referenced to a $Sc = 600$.

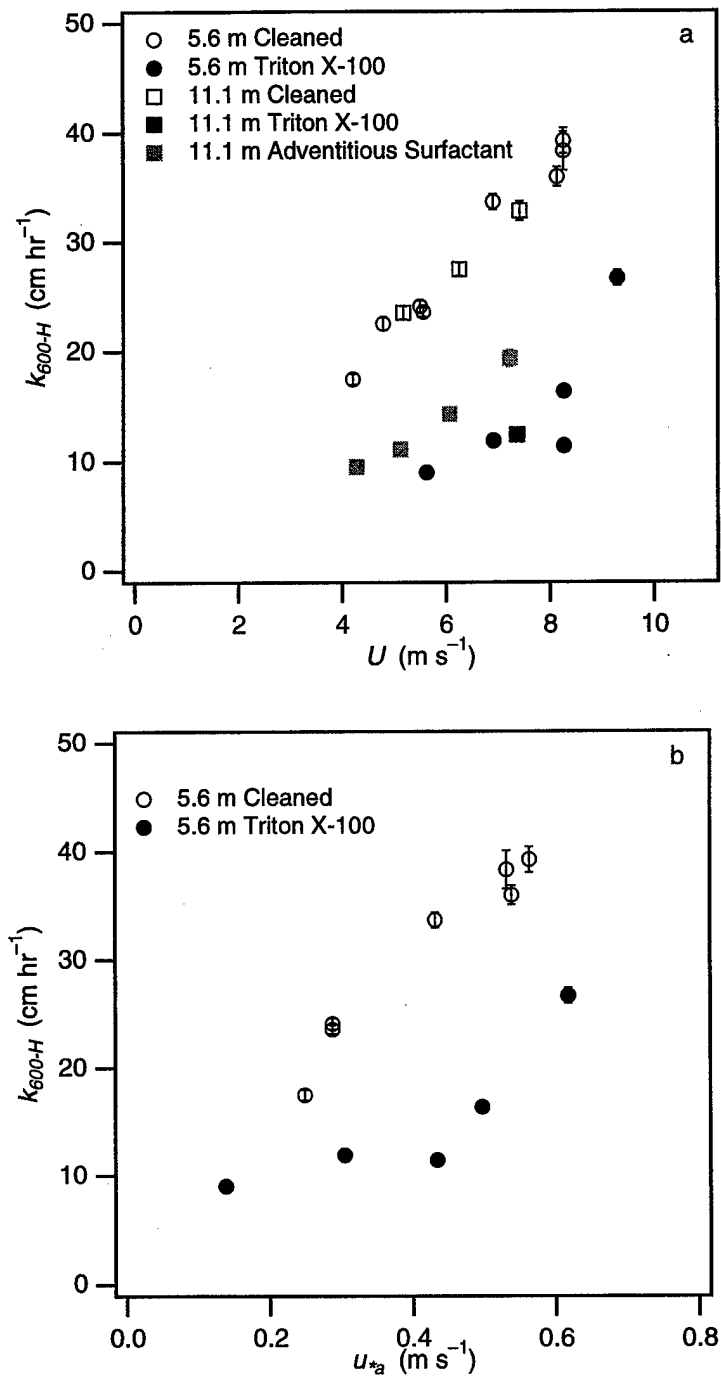


Figure 5.12. Local heat transfer velocity, k_{600-H} , for CFT referenced to a $Sc = 600$ as a function of (a) wind speed, U , and (b) air-side friction velocity, u_{*a} .

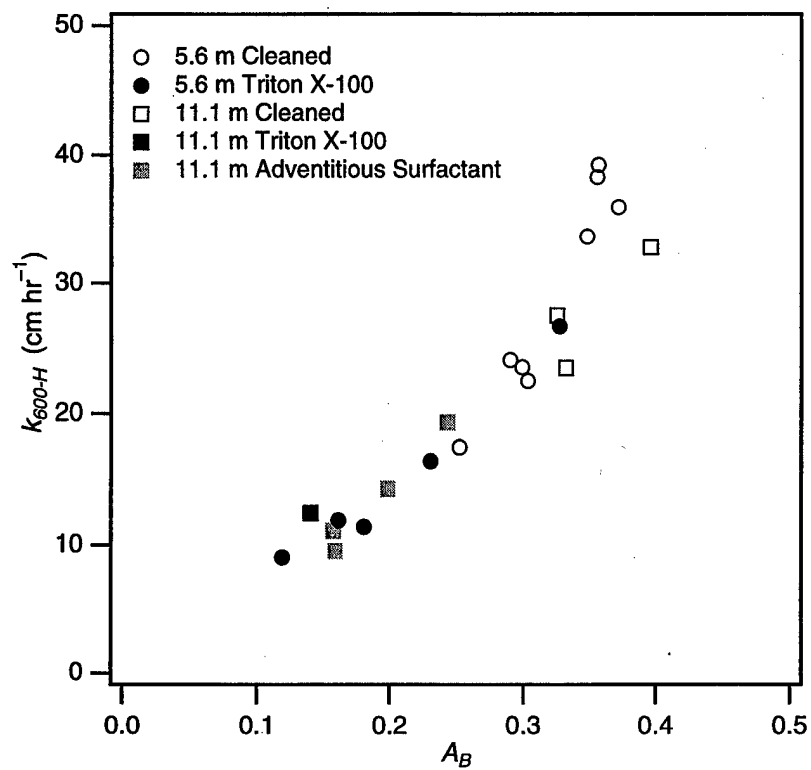


Figure 5.13. Local transfer velocity of k_{600-H} for $Sc = 600$ versus A_B .

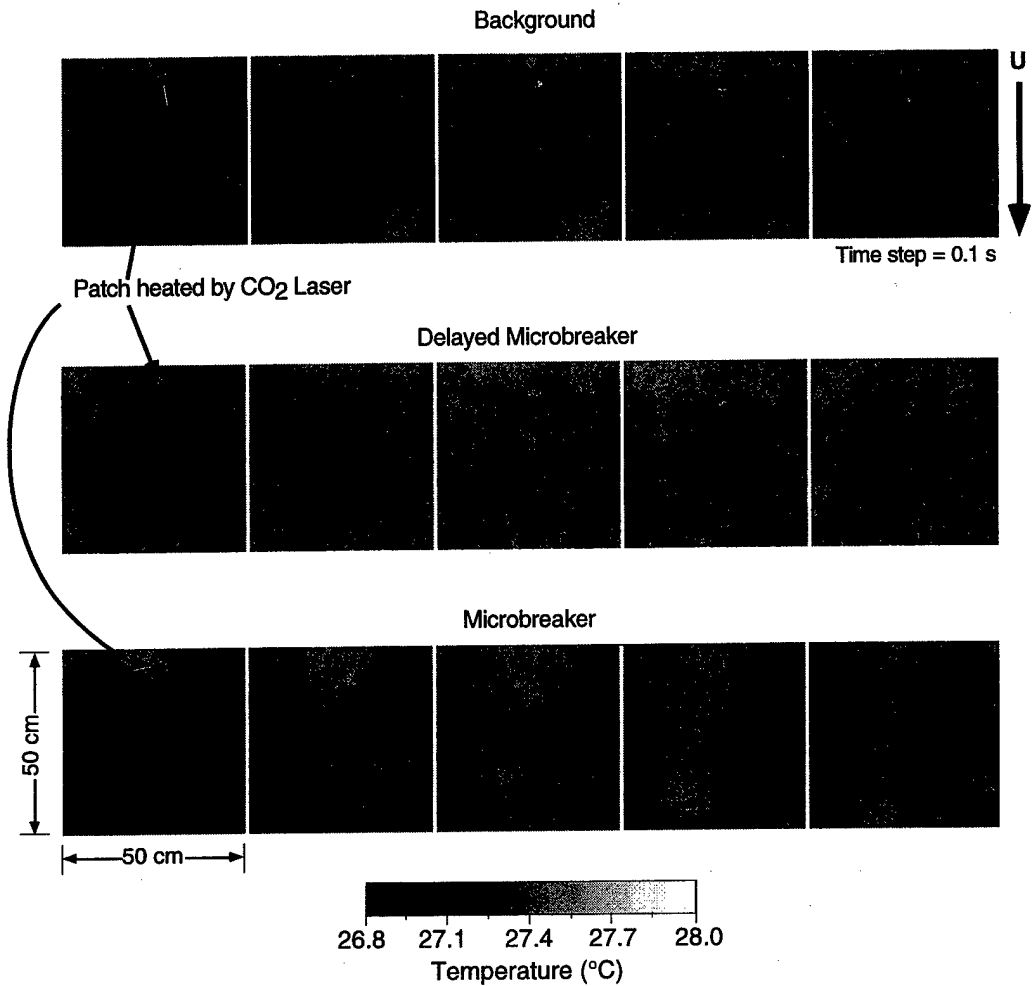


Figure 5.14. Comparison of CFT patch decay affected directly by a microscale breaking wave (Microbreaker), one that was partially affected by a microscale breaking wave (Delayed Microbreaker), and one that was not affected at all (Background). The experiment number was W5 and the wind speed was 6.9 m s^{-1} . The experimental conditions are identical to those in Figure 5.7.

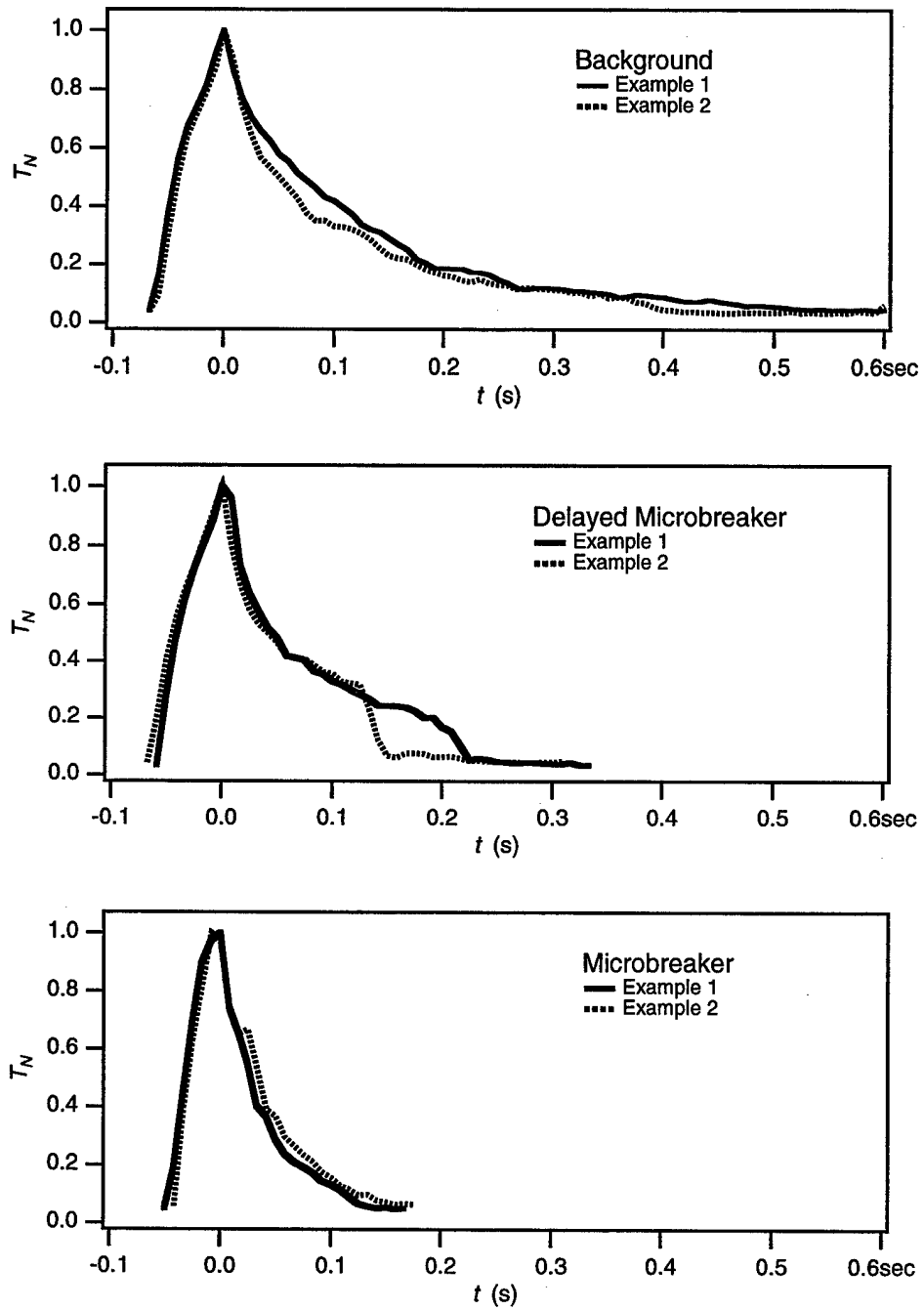


Figure 5.15. Time series of the CFT patch decay. Examples include decay affected directly by microscale breaking (Microbreaker), decay affected by microscale breaking after some time (Delayed Microbreaker), and decay not affected by microscale breaking (Background).

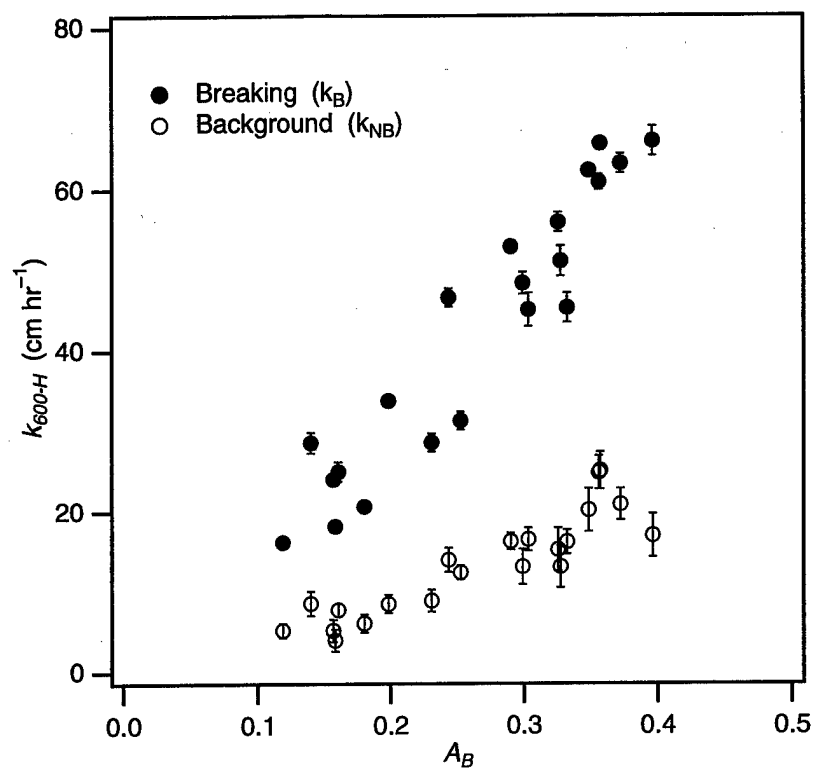


Figure 5.16. Local transfer velocities as determined by CFT referenced to $Sc = 600$ for decay patches affected directly by microscale breaking, k_B , and those in the background, k_{NB} , as a function of A_B .

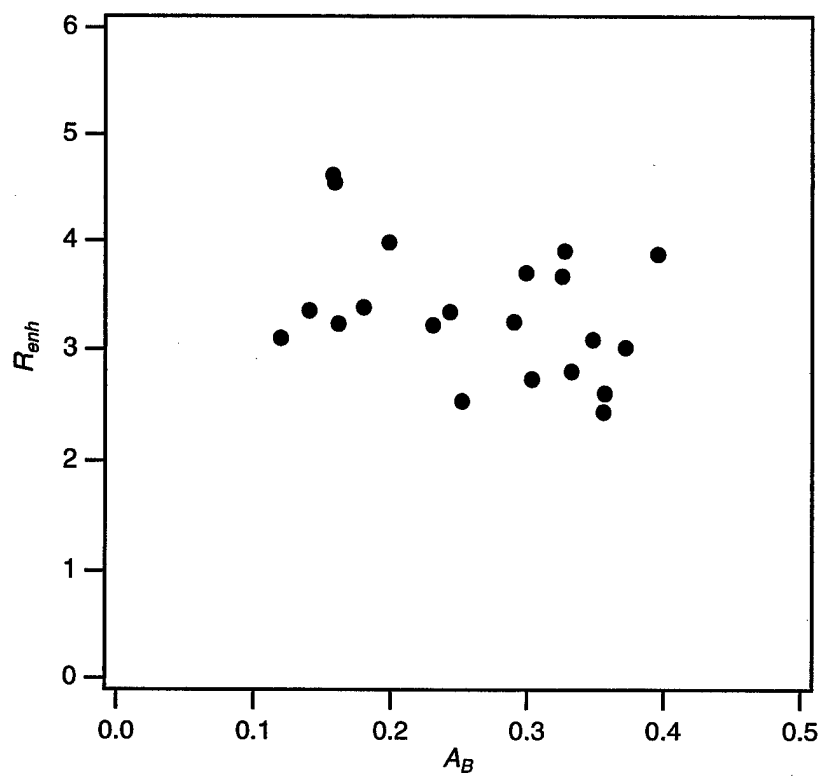


Figure 5.17. The ratio of k_B to k_{NB} , R_{enh} , as a function of A_B .

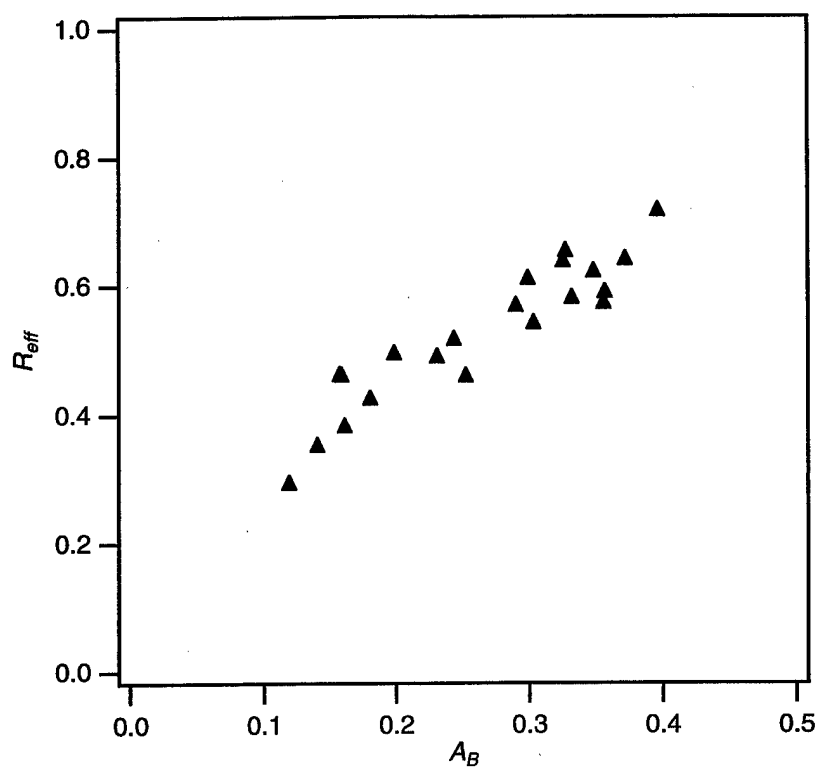


Figure 5.18. The ratio $R_{eff} = A_B k_B / k_m$ as a function of A_B , where $k_m = A_B k_B + (1 - A_B) k_{NB}$ according to (4.1).

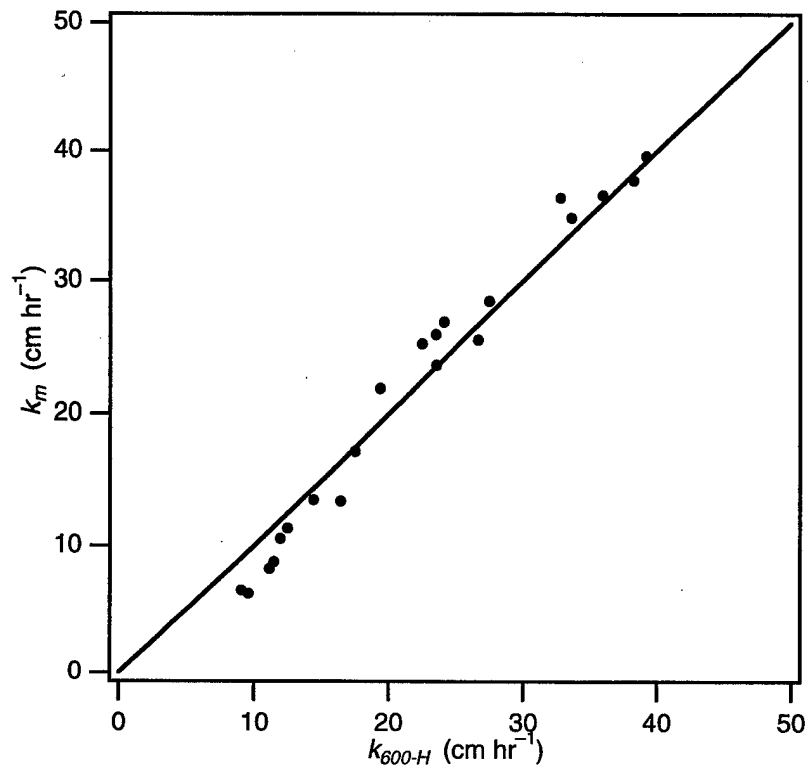


Figure 5.19. Comparison of $k_m = A_B k_B + (1 - A_B) k_{NB}$ determined from the model in (4.1) and k_{600-H} determined from CFT directly.

Table 5.1. Environmental conditions for the Wallops study. Wind speed (U), bulk-skin temperature difference (T), air-water temperature difference (T_{aw}), water temperature (T_w), relative humidity (RH), the peak wave frequency (f_p), and the root-mean-square (RMS) surface displacement (η) have been averaged for the duration of each experiment. Fetch (Ω) is measured to the top of the infrared image and experiment numbers increase in chronological order and were performed over a one-month time period. The large air-water temperature differences were used to ensure a measurable infrared signal and did not affect the determination of k . Asterisks represent experiments with the surfactant Triton X-100 and daggers represent experiments with an adventitious oily surfactant. NA denotes data that is not available.

U (m s^{-1})	T ($^{\circ}\text{C}$)	T_{aw} ($^{\circ}\text{C}$)	T_w ($^{\circ}\text{C}$)	RH (%)	f_p (Hz)	RMS η (cm)	Ω (m)	Experiment No.
4.8	0.9	-6.5	31.1	57.9	NA	NA	5.6	W1
8.3	0.8	-5.5	31.1	61.9	NA	NA	5.6	W2
4.2	0.9	-6.7	31.0	50.5	4.6	0.24	5.6	W3
8.1	0.8	-6.2	29.8	44.6	2.9	0.68	5.6	W4
6.9	0.7	-5.5	27.8	42.1	3.2	0.53	5.6	W5
5.6	0.7	-5.4	28.8	43.8	3.6	0.39	5.6	W6
8.3	0.7	-5.1	29.7	45.8	2.9	0.67	5.6	W7
5.5	0.6	-5.8	28.5	46.3	3.6	0.40	5.6	W8
8.3	0.9	-6.8	29.1	68.6	2.9	0.51	5.6	W9*
5.6	1.0	-7.4	29.9	64.4	3.7	0.32	5.6	W10*
9.3	1.0	-7.1	29.4	43.2	2.6	0.79	5.6	W11*
8.3	1.0	-6.6	27.6	41.8	2.9	0.58	5.6	W12*
6.9	0.8	-5.6	27.7	47.2	3.2	0.43	5.6	W13*
7.2	1.0	-7.7	30.9	69.2	2.5	0.80	11.1	W14†
6.1	0.9	-7.0	30.9	76.0	2.7	0.63	11.1	W15†
5.1	1.1	-8.3	29.7	40.8	2.9	0.52	11.1	W16†
4.3	1.1	-8.1	29.5	41.6	3.4	0.37	11.1	W17†
5.2	0.7	-5.0	27.0	39.0	2.9	0.55	11.1	W18
6.3	0.7	-5.6	28.2	51.9	2.6	0.71	11.1	W19
7.4	1.0	-8.9	30.5	44.4	2.4	0.91	11.1	W20
7.4	1.0	-6.6	27.7	45.2	2.5	0.68	11.1	W21*

CHAPTER 6: RELATIONSHIP BETWEEN MICROSCALE WAVE BREAKING, WAVE SLOPE, AND GAS TRANSFER

6.1 INTRODUCTION

The gas transfer velocity has been shown to correlate with the fractional area coverage of microscale wave breaking. Local measurements of k_{600-H} show that this correlation is independent of fetch and of contamination of the air–water interface by surfactant. Furthermore, microscale breaking has been shown to directly enhance the transfer velocity by a factor of 3.5 compared to k in the background. The correlation of k with wave slope has shown results similar to k with A_B . Jähne *et al.* [1987] observed a correlation of k with $\langle S^2 \rangle$ for both fetch-limited and unlimited fetch cases and Frew [1997] showed the correlation was independent of surfactant. As mentioned in section 1.3.2, Bock *et al.* [1999] confirmed that $\langle S^2 \rangle$ showed the best overall correlation for the unlimited fetch case, but also demonstrated that $\langle S^2 \rangle_{200}$ showed the best correlation for k over ranges of wavenumber components and suggested that small-scale waves are important to gas transfer. While $\langle S^2 \rangle_{200}$ is highly sensitive to surfactants, the scales associated with microscale wave breaking are most closely related to the dominant wavelength, and therefore $\langle S^2 \rangle$. The question remains, however, as to why k is correlated with $\langle S^2 \rangle$ and $\langle S^2 \rangle_{200}$. The simple explanation is that microscale wave breaking enhances slope. Each local packet of capillary-gravity waves will continue to grow until it can no longer support energy input from the wind. Eventually, the capillary-gravity wave packet will reach its limiting steepness, break, and dissipate energy into near-surface turbulence that enhances k . In this chapter, the simultaneous and co-located infrared and wave slope imagery presented in Chapter 3 are used to investigate this hypothesis.

Wave slope characterizes the stability of water waves (e.g., *Longuet-Higgins and Cleaver* [1994]) and certain limiting values of slope are typically used to detect and define wave breaking (e.g., *Xu et al.* [1986]; *Banner* [1990]). Therefore, *Jähne et al.* [1987] have argued that wave slope is representative of the near-surface turbulence produced by wave breaking. Mean square slope describes the characteristic overall stability of the wave system and the propensity of the wave field to produce turbulence via wave breaking. Since k also correlates with A_B and microscale wave breaking has been shown to directly enhance k , it is possible that microscale wave breaking may serve as a link between the observed correlation of k with $\langle S^2 \rangle$ and $\langle S^2 \rangle_{200}$. Microscale breaking waves are observed to develop from a bore-like crest accompanied by parasitic capillary waves on its forward face. If the features associated with microscale wave breaking prove to contribute significantly to mean square slope, then microscale wave breaking may explain the correlation of k with $\langle S^2 \rangle$ and $\langle S^2 \rangle_{200}$.

6.2 CORRELATING GAS TRANSFER AND A_B WITH $\langle S^2 \rangle$

Both *Jähne et al.* [1987] and *Bock et al.* [1999] have shown that $\langle S^2 \rangle$ is the best overall slope correlate with gas transfer. Figure 6.1 shows a plot of the heat transfer velocity, k_{600-H} , versus $\langle S^2 \rangle$ from the Wallops experiment (J. Klinke of Scripps Institution of Oceanography (SIO) provided wave slope measurements using a one-dimensional image slope system discussed in Chapter 3). The correlation is comparable to those observed by *Jähne et al.* [1987] and *Bock et al.* [1999] with a linear coefficient of determination of 0.90, which is less than the value of 0.94 for the correlation of k_{600-H} with A_B . For a given $\langle S^2 \rangle$, the heat transfer velocity for cleaned cases is greater than that for the surfactant-influenced cases. The difference between a cleaned and surfactant-influenced surface lies in the boundary condition at the air-water interface. Near-surface turbulence at a clean surface, whether generated by microscale wave breaking, velocity shear, or buoyancy, penetrates into the diffusive boundary layers, and

thereby enhances transfer. However, a surface contaminated by surfactants will dampen the turbulence near the air–water interface. The fact that both the small-scale waves and turbulence are damped in the presence of surfactants may not be coincidental. Regardless, the diminished turbulence directly leads to diminished transfer. This increase in transfer velocity at a particular $\langle S^2 \rangle$ for the cleaned versus surfactant-influenced cases is not surprising especially since microscale breaking waves occur whether the surface is contaminated or not. Microscale wave breaking is a direct mechanism that produces near-surface turbulence, which directly enhances air–water heat and mass transfer.

The microscale breaking process is the culminating event in the development of capillary-gravity wave packets. Throughout the evolution of a wave packet, the full spectrum of scales of slope from capillary waves through gravity wavelengths will contribute to $\langle S^2 \rangle$. *Jähne et al.* [1987] suggest that $\langle S^2 \rangle$ serves as a parameter to correlate with k as a measure of the stability of the waves and near-surface turbulence, and *Frew* [1997] suggests that $\langle S^2 \rangle$ incorporates the effect of surfactants on the wave field. Therefore, it is likely that A_B will correlate with $\langle S^2 \rangle$ since k correlates with both A_B and $\langle S^2 \rangle$. Figure 6.2 shows A_B plotted versus $\langle S^2 \rangle$. The correlation suggests that microscale wave breaking may be the process that links the observed correlation of gas transfer to wave slope. Specifically, the steep slope at the front of the microscale breaking wave and the dimpled roughness features of the bore-like crest and its wake may provide a significant contribution to $\langle S^2 \rangle$.

6.3 ANALYSIS OF INFRARED AND WAVE SLOPE IMAGERY

In order to explore if these roughness features associated with microscale wave breaking provide the link between k and $\langle S^2 \rangle$, the magnitude of the contribution by microscale wave breaking to $\langle S^2 \rangle$ must be determined. The analysis of the data set was limited to the examples (one run each for three experiments) of simultaneous and co-located infrared and wave

slope imagery discussed in Chapter 3. In a manner similar to discriminating between CFT patches affected and unaffected by microscale breaking waves, the combination of infrared and wave slope imagery has been utilized to investigate the direct effect of microscale wave breaking on $\langle S^2 \rangle$. Using the thresholded outline of the disruption of the thermal boundary layer by microscale breaking from the infrared imagery as a mask, the slope is calculated for the region within A_B as Breaking and for the region $(1 - A_B)$ as the Background. Figure 6.3 shows short time series of the mean square slope within A_B , $\langle S^2 \rangle_B$, the mean square slope in the background, $\langle S^2 \rangle_{NB}$, and the total mean square slope of the area overlapping infrared and slope images, $\langle S^2 \rangle_{ov}$, as well as the corresponding time series of A_B . The time series in Figure 6.3 includes the sequences shown in Figure 3.6, Figure 3.7 and Figure 3.8 during Experiment W5 ($U = 7.0 \text{ m s}^{-1}$; cleaned surface). The sequences shown in Figure 3.6 and Figure 3.7 are labeled A and B respectively, and the sequence in Figure 3.8 is C. Two additional breaking events occur within the time series and are labeled D and E, but are not shown in Figure 3.6 or Figure 3.7. The time series shows strong enhancement of slope due to microscale wave breaking signified by large spikes in $\langle S^2 \rangle_B$. As the microscale breaking Event A appears within the infrared and slope imagery in Figure 3.6, $\langle S^2 \rangle_B$ spikes to roughly twice $\langle S^2 \rangle_{ov}$ just as the wave begins to break. As the microscale breaker propagates through the image, the extent of the wake left behind by the breaking wave increases, and $\langle S^2 \rangle_B$ decreases. The concentrated, steep slopes during the initiation of breaking contribute significantly to $\langle S^2 \rangle_B$. Subsequently, the slope decreases simultaneous with the increase in A_B . Event D shows the same characteristics of initial increase in $\langle S^2 \rangle_B$ to double that of $\langle S^2 \rangle_{ov}$, and the subsequent rapid decrease with the increase in A_B . Note that no significant $\langle S^2 \rangle_B$ is observed during C and that, when observed, the values for $\langle S^2 \rangle_B$ are half that of $\langle S^2 \rangle_{ov}$. Events E and B, corresponding to Figure 3.7, show strong spikes in $\langle S^2 \rangle_B$ to 100% and 50% more than $\langle S^2 \rangle_{ov}$ respectively, in conjunction with the

steady increase in A_B . The average $\langle S^2 \rangle_B$ for the run was 11% greater than $\langle S^2 \rangle_{NB}$, suggesting that $\langle S^2 \rangle_B$ has the potential to contribute significantly to $\langle S^2 \rangle$.

Also plotted in Figure 6.3 are the effective contribution to mean square slope due to breaking, defined as $R_{SB} = A_B \langle S^2 \rangle_B / \langle S^2 \rangle_{ov}$, and the effective contribution to mean square slope in the background, defined as $R_{SNB} = (1 - A_B) \langle S^2 \rangle_{NB} / \langle S^2 \rangle_{ov}$. For Events A and D, R_{SB} reached 0.4 and 0.2 respectively, and R_{SB} for the successive Events E and B were 0.4 and 0.6 respectively. These successive events show that the effect of breaking can contribute significantly to $\langle S^2 \rangle$. For the non-breaking region C, $R_{SB} = 0$ since no slope contribution of consequence exists that is due to microscale wave breaking. The average R_{SB} for the record was 0.23, suggesting that a substantial contribution to $\langle S^2 \rangle$ was due to actively breaking waves.

Figure 6.4 shows time series of the same parameters as in Figure 6.3 that include the sequences shown in Figure 3.9 and Figure 3.10 for Experiment W8 ($U = 5.5 \text{ m s}^{-1}$; cleaned surface). The results are similar to those found at the higher wind speed case in Figure 6.3. The sequences shown in Figure 3.9 and Figure 3.10 are labeled F and G respectively. The four additional events that occur in the middle and at the end of the time series are denoted as Events H, I, J, and K. The Events H, I, and J appeared smaller and less intense than Events F, G, and K, consistent with the difference in the magnitude of A_B values. Events H, I, and J showed the initial stages of microscale breaking, and propagated out of the field of view of the slope imagery before completing the wave breaking process, which was observed in the infrared. Significant increases in $\langle S^2 \rangle_B$ occur during the inception of each individual breaking event. These values of $\langle S^2 \rangle_B$ were consistently 50% greater than $\langle S^2 \rangle_{ov}$, with some reaching twice that of $\langle S^2 \rangle_{ov}$, and the average $\langle S^2 \rangle_B$ for the run was 20% greater than $\langle S^2 \rangle_{NB}$, slightly greater than the result in the previous example. During Events H, I, and J, R_{SB} is shown to be small. The larger and more intense Event F forced R_{SB} up to 0.4 and the successive Events G and K drive R_{SB} up to 0.6,

suggesting that microscale wave breaking contributed substantially to $\langle S^2 \rangle$. Similar to the result in the previous example, the average R_{SB} for the run was 0.29, suggesting again that a significant contribution to $\langle S^2 \rangle$ is due to waves associated with actively breaking crests.

Figure 6.5 shows similar time series that include the sequence of a surfactant-influenced water surface shown in Figure 3.11 for Experiment W13 ($U = 7.0 \text{ m s}^{-1}$; Triton X-100). The sequence shown in Figure 3.11 is labeled L. Other microscale breaking events continuously propagated through the sequence and are not specifically labeled. While the steep slopes associated with the actively breaking crest are noticeably absent in Figure 3.11, the dimpled features were observed in the actively breaking crest and serve to contribute consistently to $\langle S^2 \rangle_B$. Therefore, no distinct spike in $\langle S^2 \rangle_B$ was observed in Figure 6.5 at any time during the run. Instead, both $\langle S^2 \rangle_B$ and $\langle S^2 \rangle_{NB}$ rose steadily throughout the run from 0.02 to 0.04 as A_B increased from 0.10 to 0.35. Contrary to the previous cleaned surface experiments, the average $\langle S^2 \rangle_B$ for the run was 6% less than $\langle S^2 \rangle_{NB}$, most likely due to the damping of steep-sloped, small-scale disturbances within the actively breaking crest, although the faint dimpled features were still observed. Values for R_{SB} also steadily increase during the run from 0.1 to 0.5. The average R_{SB} for the run was 0.32, higher than both the cleaned surface experiments discussed previously and likely due to the damping of capillary waves that would contribute significantly to $\langle S^2 \rangle_{ov}$ for a cleaned surface.

6.4 DISCUSSION

The infrared and slope measurements presented in section 3.3 may serve to elucidate the relationship between microscale wave breaking and the correlation of gas transfer with $\langle S^2 \rangle$ and $\langle S^2 \rangle_{200}$. Substantial increases in slope due to short-crested, or three-dimensional, roughness features have been observed in the actively breaking bore-like crest of a

microscale breaking wave and within its dimpled wake. These roughness features are observed in microscale breaking events that occur during both cleaned and surfactant-influenced cases, and both with and without capillary waves. The significant effective contribution of microscale wave breaking to $\langle S^2 \rangle_{ov}$ suggests that the observed correlation of k with $\langle S^2 \rangle$ may be greatly influenced directly by microscale wave breaking. A more detailed study of these results is necessary to explore the cumulative effect of microscale wave breaking on $\langle S^2 \rangle$ as well as the correlation of k with R_{SB} . In the present approach, R_{SB} becomes significant for short duration when either $\langle S^2 \rangle_B$ or A_B is large. This observation was demonstrated on a consistent basis for the examples analyzed during the Wallops study such that $\langle S^2 \rangle_B$ would produce a significant contribution to $\langle S^2 \rangle$. Since the bore-like crest produces the signature of breaking detected as A_B in the infrared imagery, only the steep slopes associated with the actively breaking crest and the wake of a microscale breaker have been included in the estimate of the influence of $\langle S^2 \rangle_B$ on $\langle S^2 \rangle$. Capillary waves that have been shown to contribute significantly to $\langle S^2 \rangle$ [Bock *et al.*, 1999] and that are observed to be transient during the microscale breaking process, however, have been neglected in the present approach. The fact that capillary waves are damped by surfactants, coupled with the fact that $\langle S^2 \rangle_{200}$ has been shown to correlate with k , suggests that capillary waves play a significant role in gas transfer. The potential for capillary waves as a mechanism for gas transfer has been demonstrated both experimentally [Saylor and Handler, 1997] and theoretically [Witting, 1971; Coantic, 1986; Szeri, 1997]. The existence, near disappearance and re-emergence of capillary waves as microscale breaking waves evolve may be directly attributable to the phenomenon and related to a possible link between A_B and $\langle S^2 \rangle$.

From the observations in Figure 3.6 through Figure 3.11, the density of capillary waves present during the microscale wave breaking process is less than that present for non-breaking waves. Specifically, the capillary waves on the forward face of the bore-like crest become extremely short and nearly disappear during the most intense initiation of microscale

breaking when steep slopes occupy the bore-like crest itself. As the microscale breaking wave continues to dissipate energy while propagating through the images, short steeper parasitic capillary waves begin to emerge on the forward face of the bore-like crest. *Longuet-Higgins* [1963] suggested that capillary waves are highly dissipative and ride on the forward faces of gravity waves as they extract energy from them. The parasitic capillary waves most likely are generated before the breaking process during the evolution of the wave train as described by *Longuet-Higgins and Cleaver* [1994]. These capillary waves have been theorized to assist in the eventual breaking process [*Longuet-Higgins*, 1992] by producing vorticity that is shed into the crest. This shed vorticity could give rise to an unstable shear layer [*Longuet-Higgins*, 1994], leading to the “dimpled” features of the turbulent bore-like crest of the microscale breakers and similar to the observations of wave-following surface displacement profiles by *Duncan et al.* [1999]. During the microscale breaking event, the parasitic capillary waves are observed to become extremely short and nearly disappear. The energy that the parasitic capillary waves would normally extract from the gravity wave crest may be dissipated by the microscale breaking process into near-surface turbulence. With the conduit for energy dissipation shifted away from the capillary waves, the capillary waves quickly diminish. The near disappearance and extreme shortening of capillary waves may suggest that the breaking crest speed itself is too fast to support the phase speed of even the shortest parasitic capillary wave. This hypothesis is supported by the observation that the bore-like crest surges forward from an initially linear wave crest to form the scalloped frontal feature, suggesting that the actively breaking wave crest gains speed as it breaks and subsequently slows to the phase speed of the dominant wave. The short capillary waves that nearly disappear are of $O(10^{-3} \text{ m})$ in wavelength, corresponding to phase speeds of roughly 60 to 70 cm s^{-1} which is in the same range as the measured phase speed of the breaking steep-sloped front. As the breaking process continued, the wavelengths of capillary waves increased by at least a factor of two corresponding to a decrease in the phase speeds to roughly 40 to 50 cm s^{-1} , which is in the same range as the dominant wave. As the energy

dissipation due to breaking process diminishes, the parasitic capillary waves can again begin to extract energy from the larger gravity wave as the wind inputs energy into the gravity wave.

The conceptual illustration in Figure 6.6 depicts the evolution of a capillary-gravity wave packet that eventually culminates in microscale wave breaking. Capillary waves are generated initially and grow to form capillary-gravity wave packets due to the continued momentum energy transfer from the air to the water, as well as the effects of nonlinear wave-wave interaction and dispersion. These packets will eventually break, dissipate energy to turbulence, and produce the signatures of microscale wave breaking observed in the infrared imagery. Following breaking, the cycle is repeated continuously as long as the wind forcing is present. From the time that capillary waves are formed to the moment that microscale wave breaking occurs, the wave slope characteristics are constantly evolving throughout the growth process of wave packet. The evolutionary history leading up to a microscale breaker depicted in Figure 6.6 incorporates contributions of slope from waves of all scale and distinction. Microscale wave breaking is merely one component of this wind-wave cycle and of short duration. Therefore, another method to quantify the contribution of microscale wave breaking to $\langle S^2 \rangle$ would be to measure the mean square slope over one complete dominant wavelength about a propagating crest, including the slope contribution from the parasitic capillary waves.

The relevance to gas exchange for the contribution of microscale breaking to $\langle S^2 \rangle$, however, is the relationship between the roughness features of and the turbulence generated by the microscale breaking waves. Microscale breaking waves appear to directly and significantly contribute to $\langle S^2 \rangle$. The roughness features of the bore-like crest and in the wake of microscale breakers may also be indicative of the scales of turbulence produced by microscale breaking waves as shown in the comparison of infrared, slope, and PIV imagery in section 3.5. Therefore, the detected events of microscale breaking quantified as A_b represent turbulent

disruptions of the diffusive boundary layer that directly enhance gas transfer and produce surface roughness elements that contribute directly to $\langle S^2 \rangle$.

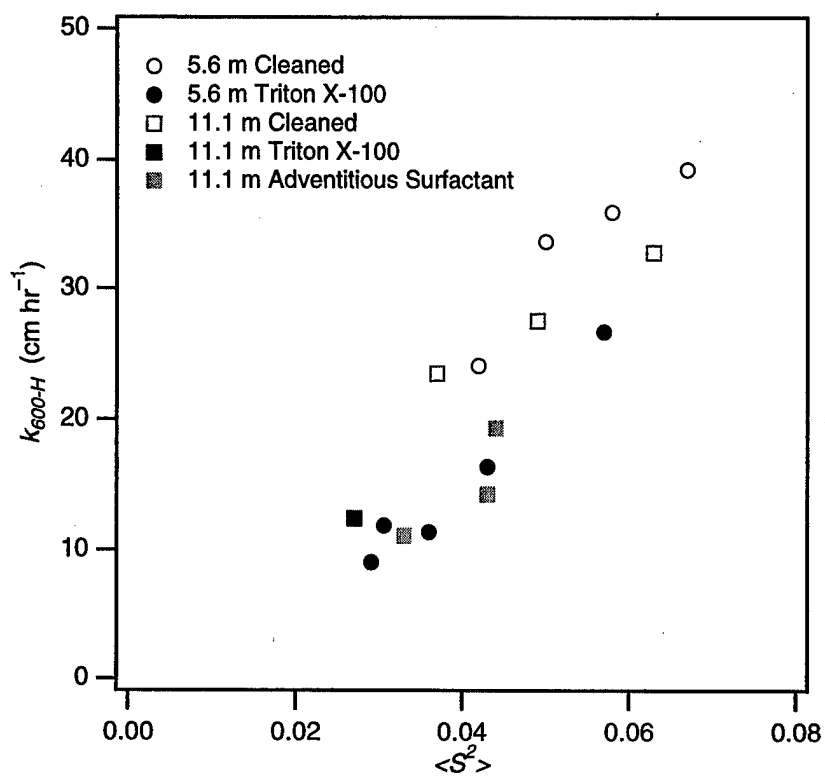


Figure 6.1. The local heat transfer velocity, k_{600-H} , versus the total mean square slope, $\langle S^2 \rangle$.

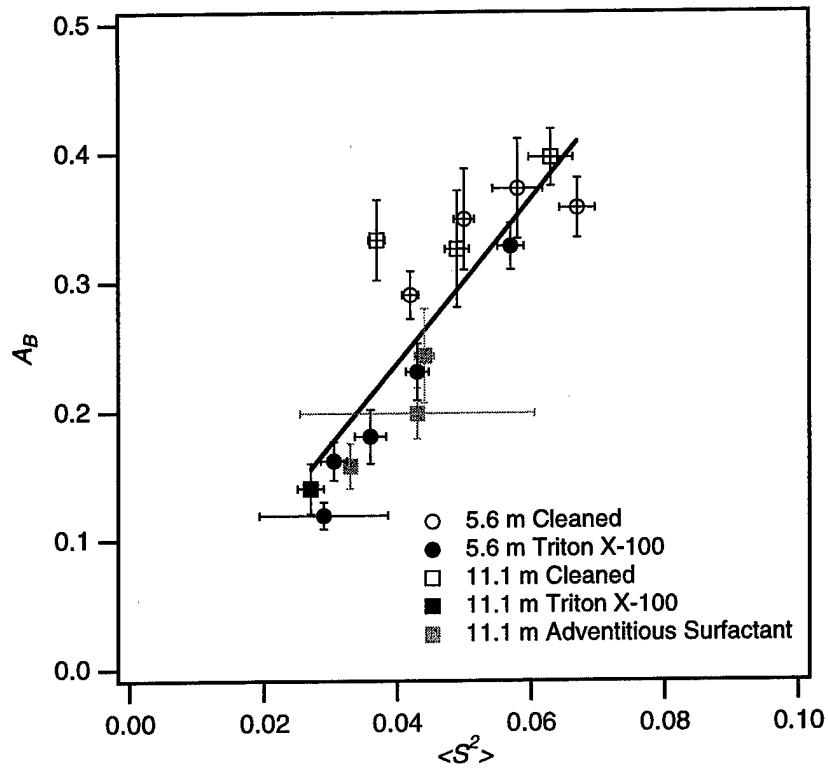


Figure 6.2. The fractional area coverage of microscale wave breaking, A_B , versus the total mean square slope, $\langle S^2 \rangle$.

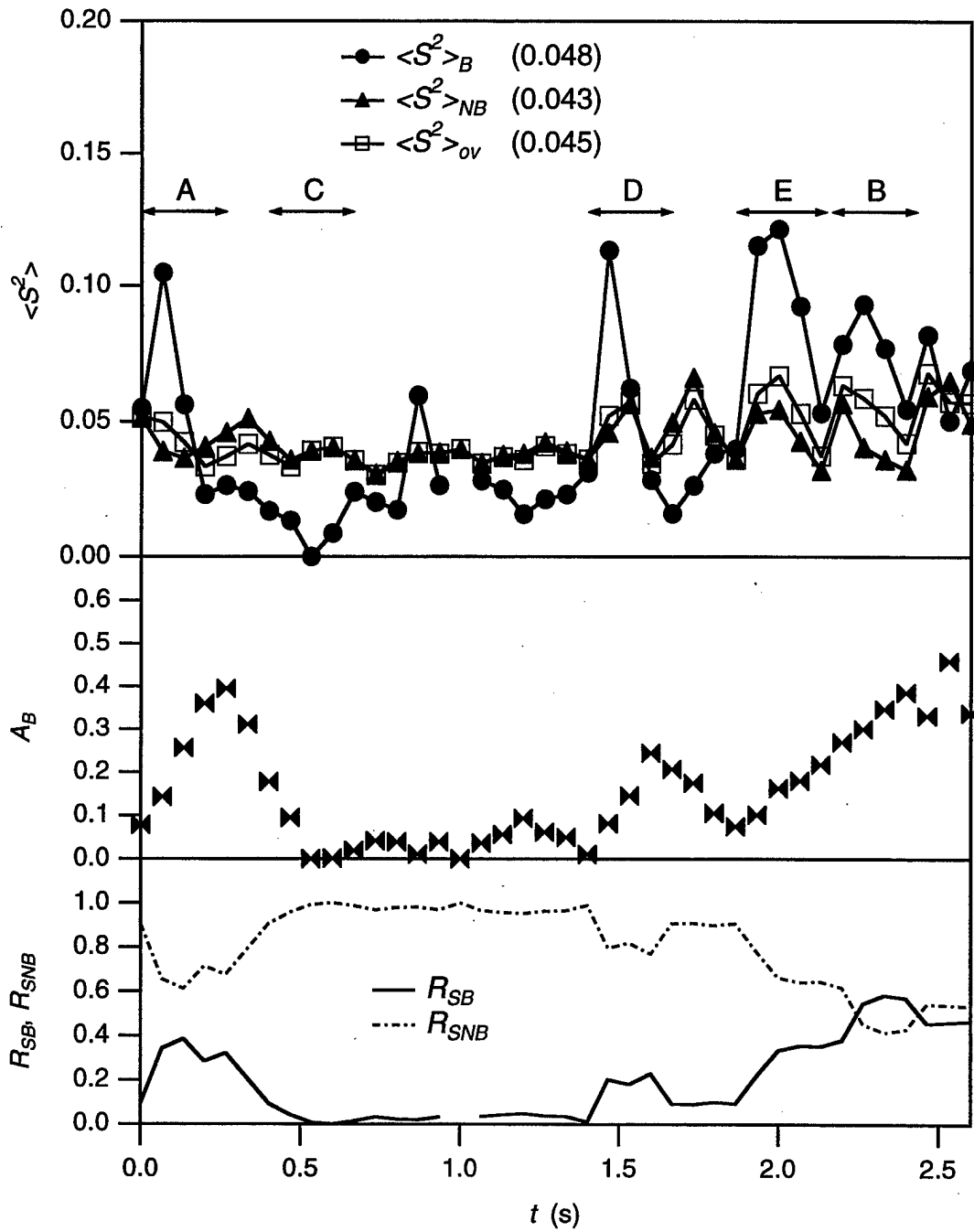


Figure 6.3. Time series of $\langle S^2 \rangle_B$, $\langle S^2 \rangle_{NB}$, $\langle S^2 \rangle_{ov}$, A_B , R_{SB} , and R_{SNB} during Experiment Number W5 and including data determined from Figure 3.6, Figure 3.7 and Figure 3.8.

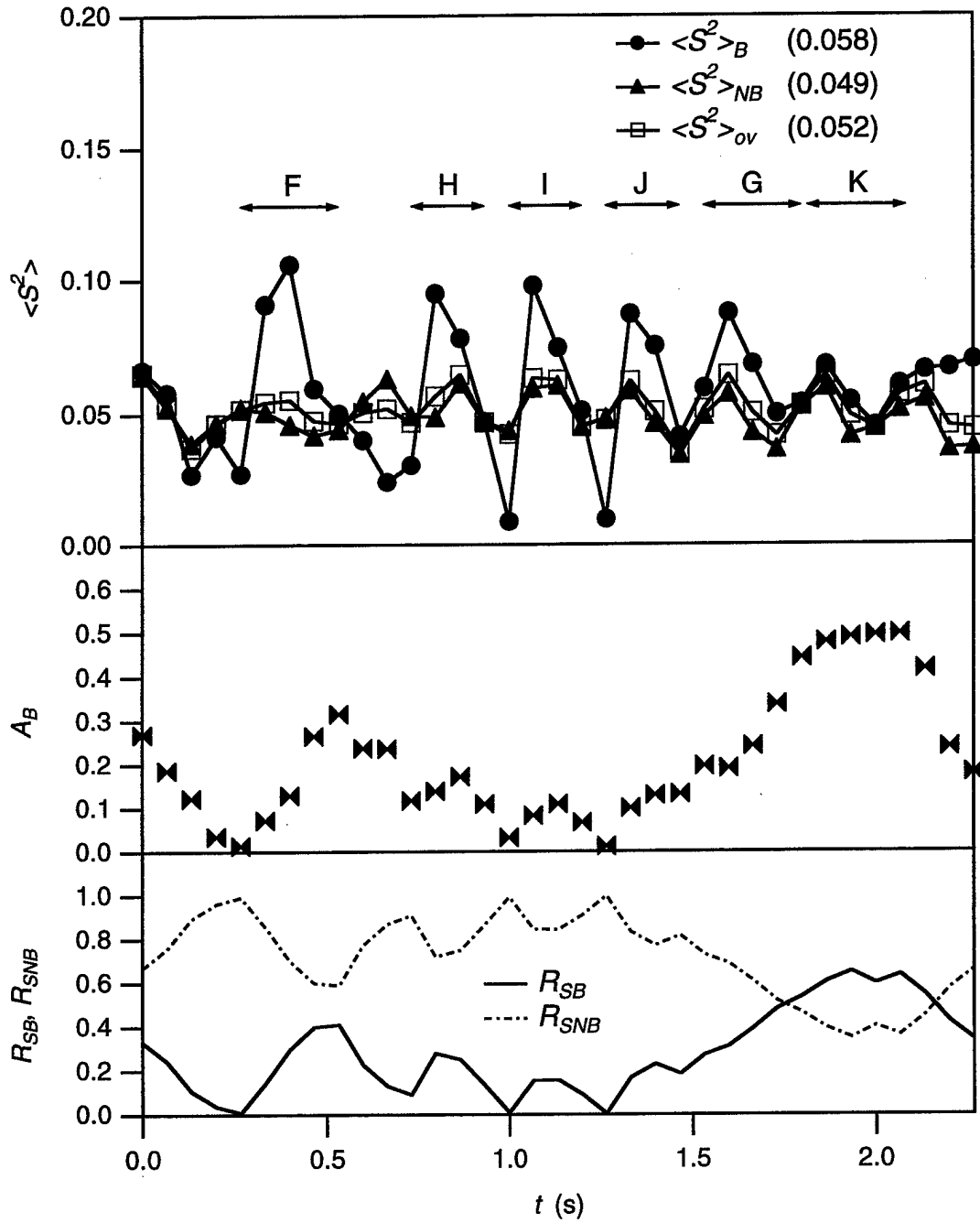


Figure 6.4. Time series of $\langle S^2 \rangle_B$, $\langle S^2 \rangle_{NB}$, $\langle S^2 \rangle_{ov}$, A_B , R_{SB} , and R_{SNB} during Experiment Number W8 and including data determined from Figure 3.9 and Figure 3.10.

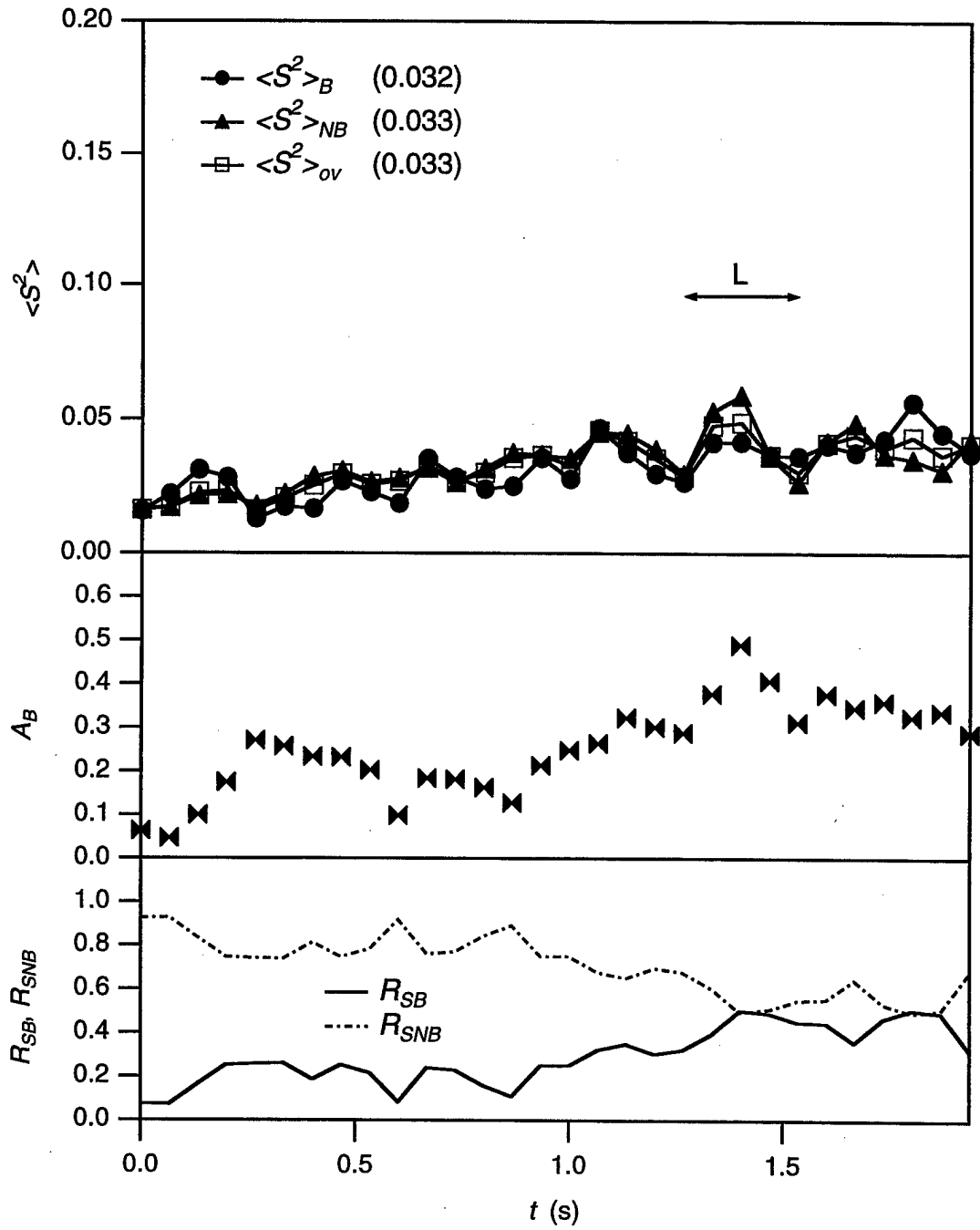


Figure 6.5. Time series of $\langle S^2 \rangle_B$, $\langle S^2 \rangle_{NB}$, $\langle S^2 \rangle_{ov}$, A_B , R_{SB} , and R_{SNB} during Experiment Number W13 and including data determined from Figure 3.11.

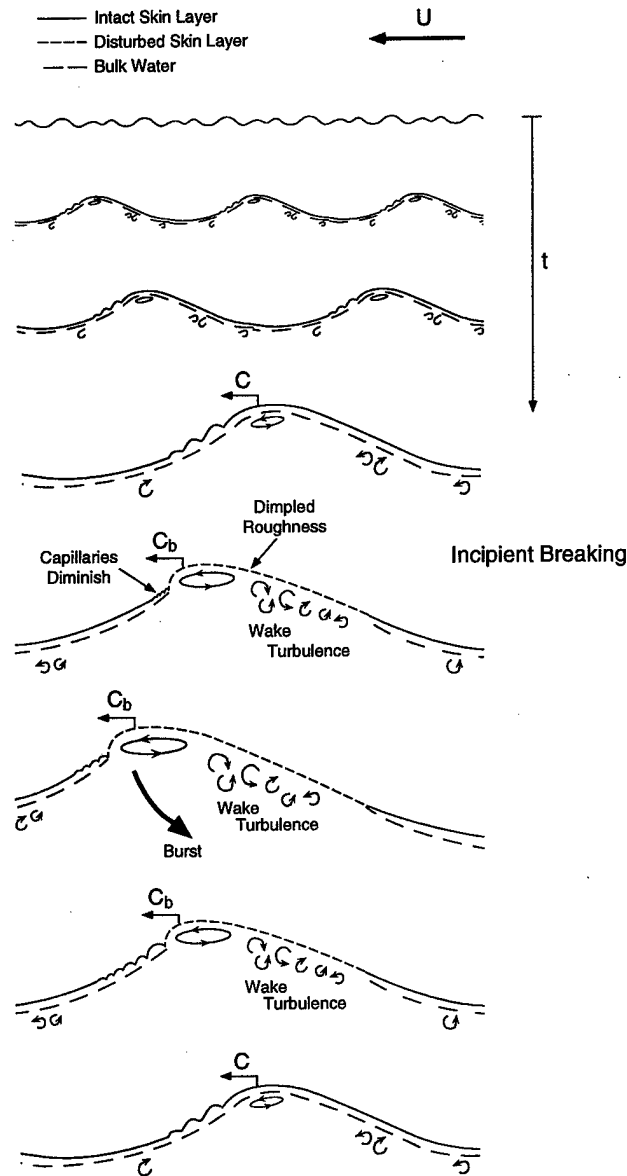


Figure 6.6. Conceptual illustration of the evolution of a capillary-gravity wave packet that eventually culminates in microscale wave breaking. The wind is from right to left and time increases down the page. The observer is moving with the waves at the phase speed, C .

CHAPTER 7: SUMMARY AND CONCLUSIONS

This thesis investigated the detection and quantification of microscale wave breaking using infrared imagery and examined the role that microscale wave breaking plays in gas transfer. The source and characteristics of the surface thermal signature of microscale wave breaking were investigated using simultaneous infrared and visual imagery of laboratory wind waves. These measurements were used to show that the infrared signature of microscale wave breaking can be used to define and quantify this visually ambiguous process. Measurements of the gas transfer velocity, k , were used to determine if k scales with the fractional area coverage of microscale breaking, A_B , as suggested by previous models. The role that a surfactant-influenced water surface—known to affect the hydrodynamics of waves and turbulence—plays in gas transfer was also investigated. The controlled flux technique was implemented to quantify the direct effect of microscale wave breaking on the transfer velocity. Finally, the contribution of surface roughness features associated with microscale wave breaking to mean square wave slope was investigated.

In the course of this thesis work, four groups of experiments were undertaken. Experiments during the Preliminary CCIW/Harris study of infrared and video measurements of the water surface under the influence of moderate wind were performed at the Canada Centre for Inland Waters (CCIW) in Burlington, Ontario, and the Harris Hydraulics Laboratory (Harris) at the University of Washington. During these initial experiments, the infrared signature of microscale wave breaking was first observed, and infrared techniques were developed to determine the area extent of microscale breaking. Subsequently, infrared measurements of microscale wave breaking at a single fetch and tank-averaged gas transfer using He and SF₆ were made during the Harris I study at the Harris wind-wave tank. Extensive measurements were

made during the Wallops study in the wind-wave flume at the Air-Sea Interaction Research Facility at NASA GSFC/Wallops Flight Facility. This facility provided an opportunity to make fetch-dependent, concurrent, and collocated measurements of the relevant physical processes associated with air-water transfer. Measurements were made of A_b using infrared imagery, of tank-averaged gas transfer using He and SF_6 , of wave slope using a 1-D image slope system, and of near-surface water velocities using particle image velocimetry (PIV). Additionally, the local transfer velocities inside and outside the wakes of microscale breaking waves were measured using the controlled flux technique (CFT). Finally, a small study at the Harris tank measured k using the CFT for various heat fluxes during the Harris II study.

The characteristic signature of microscale wave breaking in the infrared imagery consisted of an abrupt front of increased temperature that propagated through the image in the direction of the wind at roughly the phase speed of the dominant wave. This distinct propagating front disrupted the thermal boundary layer leaving behind a decaying turbulent wake of warm water. These surface thermal signatures were quantified by infrared image processing techniques. Simultaneous and co-located infrared and wave slope imagery of laboratory wind waves showed that distinct areas of the water surface where the thermal boundary layer is disrupted occur coincidentally with waves that have a steep forward face. The visually dominant features of the microscale breaking wave were a "dimpled" bore-like crest, with short-crested, or three-dimensional, roughness features left in the wake. These features were observed for both the cleaned and surfactant-influenced cases. Waves that did not produce the characteristic infrared signature did not exhibit these surface roughness features. Capillary waves may or may not be present during breaking depending on the level of surfactant. Ripples, forward of the crest, nearly disappear then re-emerge during the breaking process. As the wave breaks and dissipates its energy, the parasitic capillary waves are left with no dominant wave upon which to ride and therefore quickly diminish. Concentrated regions of high sub-surface vorticity measured by

particle image velocimetry were coincident with the crests of the steep, breaking waves. The small-scale renewal structure within the wake of the infrared signature of microscale wave breaking, the scale of the dimpled roughness features observed in the wave slope imagery, and the scale of the eddies in the PIV were all of $O(0.01 \text{ m})$. The measurements showed that these wave-related areas of enhanced surface renewal are the turbulent wakes of microscale breaking waves.

The infrared techniques outlined here provide a new and objective measurement method for identifying and quantifying microscale breaking waves despite their low visual contrast and small scale. Furthermore, the observations suggest that the surface disruption visible in the infrared images may serve as a practical means of defining microscale wave breaking. The infrared thresholding technique reliably quantified the fractional area coverage, A_B , of the surface affected by the renewal features of microscale breaking. A_B can be substantial, ranging from 0.25 to 0.40 under a moderately forced laboratory wind-wave field, and is significantly reduced in the presence of surfactant. Examples of ocean measurements demonstrated that these infrared techniques may also be applied in the field.

Tank-averaged bulk measurements of k in a wind-wave flume during Harris I showed that k was linearly correlated with the fractional area coverage, A_B , of microscale wave breaking (see Figure 4.4 and Figure 4.6). Furthermore, this correlation was insensitive to the presence of surfactant. This correlation supports the hypothesis that microscale wave breaking is the underlying physical process that determines the air–water gas transfer velocity, k , at low to moderate wind speeds. The results are consistent with modeling efforts that suggest k should scale with A_B since the majority of gas transfer occurs within the region A_B . The correlation of k and A_B at Wallops showed two distinct linear relationships characterized by cleaned and surfactant-influenced water surfaces (see Figure 5.6). The difference between the Harris I and Wallops results may be explained by fetch effects on the tank-averaged k when compared to the

local measurements of A_B . Measurements of the local transfer velocity, k_H , were made using the controlled flux technique during the Wallops study and confirmed the correlation observed during Harris I (see Figure 5.13). Moreover, the correlation between k_H and A_B at Wallops was independent of both fetch and surface cleanliness.

A model was presented to quantify the effect of microscale wave breaking on gas transfer. The model given in (4.1), $k_m = A_B k_B + (1 - A_B) k_{NB}$, partitions the contribution to k from the transfer velocity inside (k_B) and outside (k_{NB}) the wakes of microscale wave breaking. The validity of this model was determined by the direct measurement of k_B , the transfer velocity due to microscale breaking, and k_{NB} , the transfer velocity in the background, using the controlled flux technique. The results showed that k_B is significantly greater than k_{NB} , and that surface renewal in the wakes of microscale wave breaking enhanced gas transfer by a factor of 3.5 over the background (see Figure 5.16 and Figure 5.17). Furthermore, microscale wave breaking was shown to directly contribute up to 75% of the transfer across the air-water interface under moderate wind speeds (see Figure 5.18). This is the first direct evidence that microscale wave breaking enhances the gas transfer velocity. The k_B and k_{NB} results were supported by PIV measurements showing enhanced vorticity beneath the crests and in the wakes of breaking waves, confirming the idea that turbulence is driving the enhanced transfer observed from the local heat transfer velocity results (see Figure 3.12). The results show conclusively that microscale wave breaking is the process that explains the observation of enhanced gas transfer in the presence of waves and that the turbulence generated by microscale wave breaking is the underlying mechanism governing air-water gas transfer at low to moderate wind speeds.

Since k correlates well with A_B , the correlation of A_B with $\langle S^2 \rangle$ suggests that microscale wave breaking may explain the correlation of k with $\langle S^2 \rangle$ and $\langle S^2 \rangle_{200}$. In support of this, time series of slope within A_B and outside A_B show that the roughness features associated

with microscale wave breaking consistently produced mean square slope values nearly double those in the background. The dimpled, short-crested roughness features of microscale breaking contribute up to 60% to $\langle S^2 \rangle$. However, the transient nature of the slope features during the breaking events suggests that no one dominant feature of microscale breaking persists throughout the whole process except the infrared signature of the disruption of the thermal boundary layer. Wave slope itself cannot be used to track microscale wave breaking.

Previous CFT measurements by Jähne and co-workers have given reliable estimates of k in the laboratory under conditions of minimal heat flux across the air–water interface. However, in an unanticipated result, the Wallops laboratory data for conditions of high heat flux show that, when referenced to a common Schmidt number, the CFT estimates of k are roughly 2.5 times greater than k determined from He and SF₆ (see Figure 5.10). A basic assumption of the controlled flux technique is minimal heat loss to the atmosphere and, thus, transfer is dominated by water-side processes. Previous laboratory and field results of the skin-layer recovery rate of free surface wakes and breaking waves have shown a strong dependence on the net heat flux. In the Harris II laboratory experiments, the thermal decay of the CFT patch shows a similar dependence on the net heat flux across the air–water interface (see Appendix B). Therefore, k_H is a function of the net heat flux and may not be appropriate as a tracer for individual species of gas under conditions of highly varying heat flux, since it is dependent on both air- and water-side controlled processes.

The laboratory experiments presented here examined the signature of microscale wave breaking under conditions of moderate wind speed ($U = 4 - 10 \text{ m s}^{-1}$) and high heat flux ($RH < 70\%$; $T_{aw} < -5^\circ\text{C}$) that forced a high bulk–skin temperature difference, T . Future measurements of microscale wave breaking should look to improve the detection limits for the cases of low and high wind speeds as well as the effects of surfactants on these limits. Once the limits of detection are determined, further studies should investigate the relative importance of

mixing due to microscale wave breaking and Langmuir circulation under low wind speed conditions and the relative importance of transport due to microscale wave breaking and bubbles at higher wind speeds. Furthermore, future experiments are warranted to investigate the effect of buoyancy-driven turbulence on the induction of microscale wave breaking under conditions of high heat flux. The detection of microscale wave breaking using infrared imagery under the conditions of minimal heat flux will be difficult since T approaches zero. Active heating of an extensive water surface area should force a uniform T and a known undisturbed surface temperature. Future measurements employing active-heating techniques would allow for the detection of microscale wave breaking independent of the background heat flux and possibly lead to a more robust thresholding scheme based on the known constant flux source.

Infrared techniques provide the quantitative measurements necessary to incorporate microscale wave breaking into models of heat and gas flux at the air-sea interface. In addition to A_B , one might expect k to depend on other parameters measured by infrared imagery that characterize microscale breaking, such as the duration and frequency of events, the rate of recovery of the affected area, and the size and intensity distribution of surface disruptions produced by breaking-generated turbulence. Further studies involving the classification of CFT patches are warranted to determine the feasibility of extracting the statistics of microscale wave breaking using alternative active-heating techniques. Further analysis of the temporal and spatial scales observed in the PIV is necessary for a comprehensive understanding of the transport mechanisms associated with microscale wave breaking.

Whether the capillary waves are generated by the breaking process itself or are merely a by-product of the varying breaking crest speed remains to be answered. Furthermore, the modulation of capillary waves during microbreaking has yet to be completely understood. A comprehensive examination of the data set should clarify the relationship between A_B and $\langle S^2 \rangle$. Careful future wave-following measurements will provide an experimental examination of the

complete evolution of the wave train, and will give details on the wave characteristics from initial wave growth through the microscale wave breaking process.

The heat flux dependence of the local heat transfer velocity suggests that dependable measurements of k inferred from CFT during field experiments will require the determination of the surface-renewal rate from the thermal decay of the heated patch that appropriately accounts for the heat loss to the atmosphere. Specifically, the heat flux dependence of k_H will require models that incorporate boundary conditions of the Robin type or two-phase models that account for the enhanced decay of the CFT patch due to net upward heat flux.

The results presented in this thesis are the first quantitative laboratory evidence that microscale wave breaking is the wave-related mechanism that regulates the gas transfer velocity at low to moderate wind speeds. The widespread occurrence of microscale wave breaking in nature suggests that its cumulative effect on the flux of gas across the air-sea interface will also prove to be dominant. Using the infrared signature of microscale wave breaking to parameterize gas transfer offers advantages over using wave statistics, such as slope, because the infrared technique measures a physical process related directly to the turbulence governing the gas flux. Laboratory wave conditions for the wind speed range studied in these experiments may not be directly comparable to field conditions at similar wind speeds. Field applications of the remote detection of microscale wave breaking in conjunction with dual-tracer studies should provide a better experimental constraint on k , which is necessary for modeling both the ocean carbon cycle and ocean general circulation. If the results presented here extend to the ocean, estimating the transfer velocity from infrared measurements of microscale wave breaking would obviate the difficult task of determining the surface cleanliness. More generally, the promise of infrared imaging was demonstrated to reveal and quantify the small-scale processes that govern fluxes across the air-sea interface.

In conclusion, this thesis has demonstrated that the infrared signature of microscale wave breaking can be used to define and quantify this visually ambiguous process. Simultaneous infrared and wave slope imagery of laboratory wind waves shows that the source of the propagating surface thermal signature is indeed the bore-like crest of a microscale breaking wave. These measurements were used to show that the gas transfer velocity, k , scales with the fractional area coverage of the turbulent wakes of microscale breaking, A_B , as suggested by previous models. Surfactant-influenced water surfaces did not affect the correlation between k and A_B . Microscale wave breaking was shown to substantially enhance gas transfer and this enhancement is directly linked to the near-surface turbulence generated by the breaking process. Furthermore, the surface roughness features associated with microscale wave breaking contribute significantly to the mean square wave slope. This is the first compelling evidence that microscale wave breaking directly enhances the gas transfer velocity. The results show conclusively that microscale wave breaking is the underlying process that regulates air–water gas transfer at low to moderate wind speeds.

BIBLIOGRAPHY

- Agrawal, Y. C., E. A. Terray, M. A. Donelan, P. A. Hwang, Williams-A-J-III, W. M. Drennan, K. K. Kahma, and S. A. Kitaigorodskii, Enhanced dissipation of kinetic energy beneath surface waves, *Nature*, 359, 219-20, 1992.
- Alpers, W., and H. Hühnerfuss, The damping of ocean waves by surface films: A new look at an old problem, *J. Geophys. Res.*, 94, 6251-6265, 1989.
- Asher, W., and R. Wanninkhof, Transient tracers and air-sea gas transfer, *J. Geophys. Res.*, 103, 15939-15958, 1998.
- Asher, W. E., L. M. Karle, B. J. Higgins, P. J. Farley, E. C. Monahan, and I. S. Leifer, The influence of bubble plumes on air-seawater gas transfer velocities, *J. Geophys. Res.*, 101, 12027-12041, 1996.
- Asher, W. E., and J. F. Pankow, The interaction of mechanically generated turbulence and interfacial films with a liquid phase controlled gas/liquid transport process, *Tellus, Series B*, 38, 305-18, 1986.
- Back, D. D., and M. J. McCreedy, Effect of small-wavelength waves on gas transfer across the ocean surface, *J. Geophys. Res.*, 93, 5143-52, 1988.
- Banner, M. L., The influence of wave breaking on the surface pressure distribution in wind-wave interactions, *J. Fluid Mech.*, 211, 463-495, 1990.
- Banner, M. L., and W. L. Peirson, Tangential stress beneath wind-driven air-water interfaces, *J. Fluid Mech.*, 364, 115-45, 1998.
- Banner, M. L., and D. H. Peregrine, Wave breaking in deep water, *Ann. Rev. Fluid Mech.*, 25, 373-397, 1993.
- Banner, M. L., and O. M. Phillips, On the incipient breaking of small scale waves, *J. Fluid Mech.*, 65, 647-656, 1974.
- Bock, E. J., T. Hara, N. M. Frew, and W. R. McGillis, Relationship between air-sea gas transfer and short wind waves, *J. Geophys. Res.*, in press, 1999.

- Broecker, W. S., and T. H. Peng, The vertical distribution of radon in the BOMEX area, *Earth Planet. Sci. Lett.*, *11*, 99-108, 1971.
- Broecker, W. S., T. H. Peng, G. Östlund, and M. Stuiver, The distribution of bomb radiocarbon in the ocean, *J. Geophys. Res.*, *90*, 6953-6970, 1985.
- Brumley, B. H., and G. H. Jirka, Air-water transfer of slightly soluble gases: Turbulence, interfacial processes and conceptual models, *PHC PhysicoChemical Hydrodynamics*, *10*, 295-319, 1988.
- Cember, R., Bomb radiocarbon in the Red Sea: A medium scale gas exchange experiment, *J. Geophys. Res.*, *94*, 2111-2123, 1989.
- Coantic, M., A model of gas transfer across air-water interfaces with capillary waves, *J. Geophys. Res.*, *91*, 3925-43, 1986.
- Csanady, G. T., The role of breaking wavelets in air-sea gas transfer, *J. Geophys. Res.*, *95*, 749-759, 1990.
- Danckwerts, P. V., Significance of liquid-film coefficients in gas absorption, *Ind. Eng. Chem.*, *43*, 1460-1467, 1951.
- Deacon, E. L., Gas transfer to and across an air-water interface, *Tellus*, *29*, 363-74, 1977.
- Donelan, M., M. S. Longuet-Higgins, and J. S. Turner, Periodicity in whitecaps, *Nature*, *239*, 449-451, 1972.
- Donelan, M. A., Air-water exchange processes. Proceedings of the IUTAM Symposium on Physical Limnology, Broome, Australia, 1995.
- Dudzic, M. C., Ed. *Electro-Optical Systems Design, Analysis, and Testing*. The Infrared and Electro-Optical Systems Handbook. Bellingham, WA, SPIE Optical Engineering Press, 1993.
- Duncan, J. H., V. Philomin, M. Behres, and J. Kimmel, The formation of spilling breaking water waves, *Phys. Fluids*, *6*, 2558-2560, 1994.
- Duncan, J. H., H. Qiao, V. Philomin, and A. Wenz, Gentle spilling breakers: crest profile evolution, *J. Fluid Mech.*, *379*, 191-222, 1999.
- Ebuchi, N., H. Kawamura, and Y. Toba, Fine structure of laboratory wind-wave surfaces studied using an optical method, *Bound.-Layer Meteor.*, *39*, 133-151, 1987.

- Eisner, L., E. E. Bell, J. Young, and R. A. Oetjen, Spectral radiance of sky and terrain at wavelengths between 1 and 20 microns. III. Terrain measurements, *J. Optic. Soc. Am.*, 52, 201-209, 1962.
- England, M. H., V. Garcon, and J. F. Minster, Chlorofluorocarbon uptake in a world ocean model. 1. Sensitivity to the surface gas forcing, *J. Geophys. Res.*, 99, 25215-25233, 1994.
- Ewing, G., and E. D. McAlister, On the thermal boundary layer of the ocean, *Science*, 131, 1374-1376, 1960.
- Fairall, C. W., E. F. Bradley, D. P. Rogers, J. B. Edson, and G. S. Young, Bulk parameterization of air-sea fluxes for Tropical Ocean Global Atmosphere Coupled Ocean Atmosphere Response Experiment, *J. Geophys. Res.*, 101, 3747-3764, 1996.
- Farmer, D. M., C. L. McNeil, and B. D. Johnson, Evidence for the importance of bubbles in increasing air-sea gas flux, *Nature*, 361, 620-3, 1993.
- Fortescue, G. E., and J. R. A. Pearson, On gas absorption into a turbulent fluid, *Chem. Eng. Sci.*, 22, 1163-1176, 1967.
- Foster, T. D., Intermittent convection, *Geophys. Fluid Dyn.*, 2, 201-217, 1971.
- Frew, N. M., The role of organic films in air-sea exchange, *The Sea Surface and Global Change*, Eds. P. S. Liss and R. A. Duce, Cambridge, Cambridge University Press, 121-172, 1997.
- Frew, N. M., E. J. Bock, W. R. McGillis, A. V. Karachintsev, T. Hara, T. Münsterer, and B. Jähne, Variation of air-water gas transfer with wind stress and surface viscoelasticity, *Air-Water Gas Transfer*, Eds. B. Jähne and E. C. Monahan, Hanau, AEON Verlag & Studio, 529-541, 1995.
- Gasparovic, R. F., G. H. Emmons, and L. D. Tubbs, Two wavelength measurements of the ocean surface radiometric clutter, *Proceedings of IRIS*, 19, 85-100, 1974.
- Gemmrich, J., and L. Hasse, Small-scale surface streaming under natural conditions as effective in air-sea gas exchange, *Tellus*, 44B, 150-159, 1992.
- Gulliver, J. S., Introduction to air-water mass transfer, *Air-Water Mass Transfer*, Eds. S. C. Wilhelms and J. S. Gulliver, New York, NY, American Society of Civil Engineers, 1-7, 1991.
- Harriott, P., A random eddy modification of the penetration theory, *Chemical Engineering Science*, 17, 149-154, 1962.

- Hasse, L., On the mechanism of gas exchange at the air-sea interface, *Tellus*, 42B, 250-3, 1990.
- Haußecker, H., Messung und simulation von kleinskaligen austauschvorgängen an der ozeanoberfläche mittels thermographie, Ph.D. Thesis, University of Heidelberg, 1996.
- Haußecker, H., and B. Jähne, In situ measurements of the air-sea gas transfer rate during the MBL/CoOP West Coast Experiment, *Air-Water Gas Transfer*, Eds. B. Jähne and E. C. Monahan, Hanau, AEON Verlag & Studio, 775-784, 1995.
- Haußecker, H., and B. Jähne, A tensor approach for precise computation of dense displacement vector fields, *Informatik aktuell*, Eds. E. Paulus and F. M. Wahl, Berlin, Heidelberg, Springer-Verlag, 199-208, 1997.
- Haußecker, H., S. Reinelt, and B. Jähne, Heat a proxy tracer for gas exchange measurements in the field: Principles and technical realization, *Air-Water Gas Transfer*, Eds. B. Jähne and E. C. Monahan, Hanau, AEON Verlag & Studio, 405-413, 1995.
- Higbie, R., The rate of absorption of a pure gas into a still liquid during short periods of exposure, *Trans. A.I.C.E.*, 31, 365-389, 1935.
- Hill, R. H., Laboratory measurement of heat transfer and thermal structure near an air-water interface, *J. Phys. Oceanogr.*, 2, 190-198, 1972.
- Hirsa, A., and W. W. Willmarth, Measurements of vortex pair interaction with a clean or contaminated free surface, *J. Fluid Mech.*, 259, 25-45, 1994.
- Jähne, B., and H. Haußecker, Air-water gas exchange, *Ann. Rev. Fluid Mech.*, 14, 321-350, 1998.
- Jähne, B., W. Huber, A. Dutzi, T. Wais, and J. Ilmberger, Wind/wave-tunnel experiment on the Schmidt number — and wave field dependence of air/water gas exchange, *Gas Transfer at Water Surfaces*, Eds. W. Brutsaert and G. H. Jirka, Norwell, MA, D. Reidel, 303-309, 1984.
- Jähne, B., J. Klinke, and S. Waas, Imaging of short ocean wind waves: a critical theoretical review, *J. Opt. Soc. Am. A*, 11, 2197-2209, 1994.
- Jähne, B., P. Libner, R. Fischer, T. Billen, and E. J. Plate, Investigating the transfer processes across the free aqueous viscous boundary layer by the controlled flux method, *Tellus*, 41B, 177-95, 1989.
- Jähne, B., K. O. Munnich, R. Bosinger, A. Dutzi, W. Huber, and P. Libner, On the parameters influencing air-water gas exchange, *J. Geophys. Res.*, 92, 1937-1949, 1987.

- Jähne, B., K. O. Münnich, and U. Siegenthaler, Measurements of gas exchange and momentum transfer in a circular wind tunnel, *Tellus*, 31, 321-9, 1979.
- Jähne, B., T. Wais, L. Memery, G. Caulliez, L. Merlivat, K. O. Münnich, and M. Coantic, He and Rn gas exchange experiments in the large wind-wave facility of IMST, *J. Geophys. Res.*, 90, 11989-97, 1985.
- Jessup, A. T., and V. Hesany, Modulation of ocean skin temperature by swell waves, *J. Geophys. Res.*, 101, 6501-6511, 1996.
- Jessup, A. T., C. J. Zappa, V. Hesany, M. R. Loewen, and M. G. Skafel, Dependence of the skin layer recovery rate on heat flux and turbulence, *Air-Water Gas Transfer*, Eds. B. Jähne and E. C. Monahan, Hanau, AEON Verlag & Studio, 601-610, 1995.
- Jessup, A. T., C. J. Zappa, M. R. Loewen, and V. Hesany, Infrared remote sensing of breaking waves, *Nature*, 385, 52-55, 1997a.
- Jessup, A. T., C. J. Zappa, and H. Yeh, Defining and quantifying microscale wave breaking with infrared imagery, *J. Geophys. Res.*, 102, 23145-23154, 1997b.
- Kanwisher, J., On the exchange of gases between the atmosphere and the sea, *Deep-Sea Research*, 10, 195-207, 1963.
- Katsaros, K. B., The sea surface temperature deviation at very low wind speeds; Is there a limit?, *Tellus*, 29, 229-239, 1977.
- Katsaros, K. B., The aqueous thermal boundary layer, *Bound.-Layer Meteor.*, 18, 107-127, 1980.
- Kawamura, H., and Y. Toba, Ordered motion in the turbulent boundary layer over wind waves, *J. Fluid Mech.*, 197, 105-138, 1988.
- Keller, W. C., and B. L. Gotwols, Two-dimensional optical measurement of wave slope, *Applied Optics*, 22, 3476-8, 1983.
- Kitaigorodskii, S. A., On the fluid dynamical theory of turbulent gas transfer across an air-sea interface in the presence of breaking wind-waves, *J. Phys. Oceanogr.*, 14, 960-972, 1984.
- Kitaigorodskii, S. A., M. A. Donelan, J. L. Lumely, and E. A. Terray, Wave-turbulence interactions in the upper ocean. II. Statistical characteristics of wave and turbulent components of the random velocity field in the marine surface layer, *J. Phys. Oceanogr.*, 13, 1988-99, 1983.

- Komori, S., Y. Murakami, and H. Ueda, The relationship between surface-renewal and bursting motions in an open-channel flow, *J. Fluid Mech.*, 203, 103-23, 1989.
- Komori, S., R. Nagaosa, and Y. Murakami, Turbulence structure and mass transfer across a sheared air-water interface in wind-driven turbulence, *J. Fluid Mech.*, 249, 161-183, 1993.
- Kromer, B., and W. Roether, Field measurements of air-sea exchange by the radon deficit method during JASIN (1978) and FGGE (1979), *Meteor Forsch.-Ergebnisse, Reihe A/B*, 24, 55-75, 1983.
- Kudryavtsev, V. N., and G. L. Luchnik, On thermal state of the cool skin, *Proc. Mar. Hydrophys. Inst.*, 3, 105-112, 1979.
- Lamont, J. C., and D. S. Scott, An eddy cell model of mass transfer into the surface of a turbulent liquid, *A.I.Ch.E. J.*, 16, 512-519, 1970.
- Ledwell, J. J., The variation of the gas transfer coefficient with molecular diffusivity, *Gas Transfer at Water Surfaces*, Eds. W. Brutsaert and G. H. Jirka, Norwell, MA, D. Reidel, 293-302, 1984.
- Liss, P. S., Processes of gas exchange across an air-water interface, *Deep-Sea Research*, 20, 221-238, 1973.
- Liss, P. S., and L. Merlivat, Air-sea gas exchange rates: Introduction and synthesis, *The Role of Air-Sea Exchange in Geochemical Cycling*, Ed. P. Buat-Ménard, Dordrecht, D. Reidel, 113-127, 1986.
- Liu, W. T., and J. A. Businger, Temperature profile in the molecular sublayer near the interface of a fluid in turbulent motion, *Geophys. Res. Lett.*, 2, 403-404, 1975.
- Liu, W. T., K. B. Katsaros, and J. A. Businger, Bulk parameterization of air-sea exchanges of heat and water vapor including the molecular constraints at the interface, *J. Atmos. Sci.*, 36, 1722-35, 1979.
- Longuet-Higgins, M. S., The generation of capillary waves by steep gravity waves, *J. Fluid Mech.*, 16, 138-159, 1963.
- Longuet-Higgins, M. S., Capillary rollers and bores, *J. Fluid Mech.*, 240, 659-679, 1992.
- Longuet-Higgins, M. S., Shear instability in spilling breakers, *Proc. R. Soc. Lond. A*, 446, 399-409, 1994.

- Longuet-Higgins, M. S., and R. P. Cleaver, Crest instabilities of gravity waves. Part 1. The almost-highest wave, *J. Fluid Mech.*, 258, 115-129, 1994.
- Lucassen, J., Effect of surface-active material on the damping of gravity waves: A reappraisal, *Journal of Colloid and Interface Science*, 85, 52-58, 1982.
- McAlister, E. D., Infrared-optical techniques applied to oceanography I. Measurement of total heat flow from the sea surface, *Applied Optics*, 3, 609-612, 1964.
- McAlister, E. D., and W. McLeish, Heat transfer in the top millimeter of the ocean, *J. Geophys. Res.*, 74, 3408-3414, 1969.
- McAlister, E. D., and W. McLeish, A radiometric system for airborne measurement of the total heat flow from the sea, *Applied Optics*, 9, 2697-2705, 1970.
- McAlister, E. D., W. McLeish, and E. A. Corduan, Airborne measurements of the total heat flux from the sea during Bomex, *J. Geophys. Res.*, 76, 4172-4180, 1971.
- McAlister, E. D., and W. L. McLeish, Oceanographic measurements with airborne infrared equipment and their limitations, *Oceanography From Space*, Ed. G. C. Ewing, Woods Hole, MA, Woods Hole Oceanographic Inst. Rep. No. 65-10, 189-215, 1965.
- McKeown, W., and R. Leighton, Mapping heat flux, *Journal of Atmospheric and Oceanic Technology*, 16, 80-91, 1999.
- Melville, W. K., The role of surface-wave breaking in air-sea interaction, *Ann. Rev. Fluid Mech.*, 28, 279-321, 1996.
- Melville, W. K., R. Shear, and F. Veron, Laboratory measurements of the generation and evolution of Langmuir circulations, *J. Fluid Mech.*, 364, 31-58, 1998.
- Okuda, K., Internal flow structure of short wind waves. Part I. On the internal vorticity structure., *J. Oceanogr. Soc. Japan.*, 38, 28-42, 1982.
- Peirson, W. L., Measurement of surface velocities and shears at a wavy air-water interface using particle image velocimetry, *Experiments in Fluids*, 23, 427-37, 1997.
- Peng, T. H., W. S. Broecker, G. G. Mathieu, Y. H. Li, and A. E. Bainbridge, Radon evasion rates in the Atlantic and Pacific Oceans as determined during the GEOSECS program, *J. Geophys. Res.*, 84, 2471-2486, 1979.

- Peng, T. H., T. Takahashi, and W. S. Broecker, Surface radon measurements in the North Pacific Ocean station PAPA, *J. Geophys. Res.*, 79, 1772-1780, 1974.
- Phillips, O. M., and M. L. Banner, Wave breaking in the presence of wind drift and swell, *J. Fluid Mech.*, 66, 625-640, 1974.
- Plant, W. J., A model for microwave Doppler sea return at high incidence angles: Bragg scattering from bound, tilted waves, *Journal of Geophysical Research-Oceans*, 109, 21131-21146, 1997.
- Plant, W. J., W. C. Keller, V. Hesany, T. Hara, E. Bock, and M. A. Donelan, Bound waves and Bragg scattering in a wind-wave tank, *Journal of Geophysical Research-Oceans*, 104, 3243-3263, 1999.
- Press, W. H., S. A. Teukolsky, W. T. Vetterling, and B. P. Flannery, *Numerical Recipes*, Cambridge University Press, 1992.
- Robinson, I. S., N. C. Wells, and H. Charnock, The sea surface thermal boundary layer and its relevance to the measurement of sea surface temperature by airborne and spaceborne radiometers, *Int. J. Remote Sens.*, 5, 19-45, 1984.
- Sarmiento, J. L., J. C. Orr, and U. Siegenthaler, A perturbation simulation of CO₂ uptake in an ocean general circulation model, *J. Geophys. Res.*, 97, 3621-3645, 1992.
- Sarpkaya, T., Vorticity, free surface, and surfactants, *Ann. Rev. Fluid Mech.*, 28, 83-128, 1996.
- Saunders, P. M., The temperature at the ocean-air interface, *J. Atmos. Sci.*, 24, 269-273, 1967.
- Saylor, J. R., and R. A. Handler, Gas transport across an air/water interface populated with capillary waves, *Phys. Fluids*, 9, 2529-41, 1997.
- Schiff, R. K., Calibrated field measurements of the effect of wind-induced surface roughness on infrared sea surface temperature (SST), M. S. Thesis, University of Washington, 1996.
- Schwarzenbach, R., P. H. Gshwend, and D. M. Omboden, *Environmental Organic Chemistry*, John Wiley & Sons, Inc., 1993.
- Siddiqui, M., M. R. Loewen, C. Richardson, C. J. Zappa, A. T. Jessup, and W. E. Asher, Simultaneous infrared imagery and particle image velocimetry of microscale breaking waves. 2000 Ocean Sciences Meeting of the American Geophysical Union, San Antonio, TX, to appear.

- Simpson, J. J., and C. A. Paulson, Small-scale sea surface temperature structure, *J. Phys. Oceanogr.*, 10, 399-410, 1980.
- Soloviev, A. V., and P. Schlüssel, Parameterization of the cool skin of the ocean and of the air-ocean gas transfer on the basis of modeling surface renewal, *J. Phys. Oceanogr.*, 24, 1339-46, 1994.
- Szeri, A. J., Capillary waves and air-sea gas transfer, *J. Fluid Mech.*, 332, 341-58, 1997.
- Terray, E. A., M. A. Donelan, Y. C. Agrawal, W. M. Drennan, K. K. Kahma, I. A. J. Williams, P. A. Hwang, and S. A. Kitaigorodskii, Estimates of kinetic energy dissipation under surface waves, *J. Phys. Oceanogr.*, 26, 792-807, 1996.
- Thorpe, S. A., On the clouds of bubbles formed by breaking wind-waves in deep water, and their role in air-sea gas transfer, *Phil. Trans. R. Soc. Lond. A*, 304, 155-210, 1982.
- Thorpe, S. A., Dynamical processes of transfer at the sea surface, *Prog. Oceanogr.*, 35, 315-352, 1995.
- Toba, Y., M. Tokuda, K. Okuda, and S. Kawai, Forced convection accompanying wind waves, *J. Oceanogr. Soc. Japan*, 31, 192-198, 1975.
- Trizna, D. B., and D. J. Carlson, Studies of dual polarized low grazing angle radar sea scatter in nearshore regions, *IEEE Transactions on Geoscience and Remote Sensing*, 34, 747-757, 1996.
- Wallace, D. W. R., and C. D. Wirrick, Large air-sea fluxes associated with breaking waves, *Nature*, 356, 694-696, 1992.
- Wanninkhof, R., Relationship between wind speed and gas exchange over the ocean, *J. Geophys. Res.*, 97, 7373-7382, 1992.
- Wanninkhof, R., W. Asher, R. Weppernig, H. Chen, P. Schlosser, C. Langdon, and R. Sambrotto, Gas transfer experiment on Georges Bank using two volatile deliberate tracers, *J. Geophys. Res.*, 98, 20237-20248, 1993.
- Wanninkhof, R., G. Hitchcock, W. Wiseman, P. Ortner, W. Asher, D. Ho, P. Schlosser, M. L. Dickson, M. Anderson, R. Masserini, K. Fanning, and J. K. Zhang, Gas exchange, dispersion, and biological productivity on the west Florida shelf: Results from a Lagrangian tracer study, *Geophys. Res. Lett.*, 24, 1767-1770, 1997.

- Wanninkhof, R., and W. McGillis, A cubic relationship between air-sea CO₂ exchange and wind speed, *Geophys. Res. Lett.*, 26, 1999.
- Watson, A. J., R. C. Upstill-Goddard, and P. S. Liss, Air-sea gas exchange in rough and stormy seas measured by a dual-tracer technique, *Nature*, 349, 145-147, 1991.
- Weaver, A. J., The oceans and global warming, *Nature*, 364, 192-193, 1993.
- Wick, G. A., W. J. Emery, L. H. Kantha, and P. Schlüssel, The behavior of the bulk-skin sea surface temperature difference under varying wind speed and heat flux, *J. Phys. Oceanogr.*, 26, 1969-1988, 1996.
- Wick, G. A., and A. T. Jessup, Simulation of ocean skin temperature modulation by swell waves, *J. Geophys. Res.*, 103, 3149-3161, 1998.
- Witting, J., Effects of plane progressive irrotational waves on thermal boundary layers, *J. Fluid Mech.*, 50, 321-334, 1971.
- Wu, J., An estimation of oceanic thermal-sublayer thickness, *J. Phys. Oceanogr.*, 1, 284-286, 1971.
- Xu, D., P. A. Hwang, and J. Wu, Breaking of wind-generated waves, *J. Phys. Oceanogr.*, 16, 2172-8, 1986.
- Yeh, H. H., Vorticity generation at a fluid interface, *Breaking Waves*, Eds. M. L. Banner and R. H. J. Grimshaw, Berlin, Springer-Verlag, 257-265, 1992.
- Yeh, H. H., Free-surface dynamics, *Advances in Coastal Engineering*, Ed. P. L.-F. Liu, World Scientific, 1-74, 1995.
- Yoshikawa, I., H. Kawamura, K. Okuda, and Y. Toba, Turbulent structure in water under laboratory wind waves, *J. Oceanogr. Soc. Japan*, 44, 143-156, 1988.
- Zappa, C. J., Infrared field measurements of sea surface temperature: Analysis of wake signatures and comparison of skin layer models, M. S. Thesis, University of Washington, 1994.
- Zappa, C. J., W. E. Asher, and A. T. Jessup, Microscale wave breaking and air-water gas transfer, *Geophys. Res. Lett.*, submitted, 1999.

Zappa, C. J., A. T. Jessup, and H. H. Yeh, Skin-layer recovery of free-surface wakes:
Relationship to surface renewal and dependence on heat flux and background turbulence, *J. Geophys. Res.*, *103*, 21711–21722, 1998.

APPENDIX A: DETERMINATION OF A_B FROM INFRARED IMAGERY

The determination of A_B requires the implementation of a thresholding scheme coupled with a reliable morphological image-processing algorithm. Observations have indicated that when the air–water interface is disturbed by a turbulent event, the skin temperature, T_s , measured by a radiometric device is approximately equal to the bulk water temperature, T_w [Ewing and McAlister, 1960; Katsaros, 1977; Zappa, 1994; Haußecker *et al.*, 1995; Schiff, 1996; Jessup *et al.*, 1997a; Zappa *et al.*, 1998]. The knowledge of T_s previous to and following the disruption allows one to estimate the bulk–skin temperature difference, $\Delta T = T_w - T_s$. Therefore, since microscale wave breaking is a turbulent event that causes the disruption of the thermal boundary layer, a threshold based upon T is an appropriate choice. Furthermore, according to surface renewal theory, water at the surface is continually and randomly renewed with water from the bulk. Thus, the surface is continually being disrupted on a scale comparable to the eddy size, and the variation in the temperature with an infrared image should also give an estimate of T . The threshold has the form

$$T_{thresh} = T_{base} + j\Delta T_{md}, \quad (\text{A.1})$$

where T_{thresh} is the threshold temperature level, T_{base} is the measure of the skin temperature, T_{md} is the basis for estimation of T , and j is the arbitrary threshold parameter. Specific values for T_{thresh} will be discussed later for each experiment.

Once an image has been thresholded using T_{thresh} , a series of morphological operations is performed on the thresholded binary image to remove smaller disturbances, to

produce distinct detected events of microscale wave breaking, and to quantify the fractional coverage of these events within an image to produce A_B . A schematic of the image-processing algorithm used to determine A_B is diagrammed in Figure A.1. The first step is to expand the original grayscale image, A, for use in the subsequent processing. The second step is to apply the defined threshold to the expanded image, B, to produce a binary thresholded image, denoted as C in Figure A.1, upon which the morphological operations will be performed. At this stage, it may be difficult to identify the microscale breaking events as the image is filled with thresholded regions (particles) of varying size as demonstrated in image C of Figure A.1. Since the ultimate goal is to determine microscale wave breaking events, the third step consists of removing thresholded particles due to disturbances that are small compared to the breaking events, i.e., particles of $O(10^{-2} \text{ m})$ or less. A series of binary erosion operations is applied to a duplicated image, C'. The number of erosions applied is set by the user, and here was chosen to be 2 so as to remove only the particles smaller than $O(10^{-2} \text{ m})$. All particles that are remaining in the image after the erosions are performed are then set back to their original sizes in C for further processing, resulting in the image denoted as D. The fourth step consists of filling the holes within the particles. This is accomplished by duplicating D to create D', inverting image D', removing all particles that touch the border of the inverted image D', inverting this image once again, and then performing a logical "OR" operation with the original image D to produce image E. Image E is then quantified to determine the fractional area coverage of particles within the image. This serves as the measure of A_B . Application of a gradient operator to image E produces an outline of the detected microscale wave-breaking event, F, that can be used as an overlay on the original equalized grayscale infrared image, B, as shown in Figure A.1.

When available, co-located visual observations of the wave field are used in conjunction with the algorithm in order to verify independently that the appropriate threshold was chosen. Three studies have been performed, each implementing a different experimental setup

and slightly different instrumentation. Over the course of developing this technique, the choice of threshold has evolved as each experiment has added new information. Many T_{thresh} have been applied to the infrared imagery, tested for correct identification of microscale breaking events, and verified through the visual manifestation of breaking. Table A.1 highlights the differences between the three studies and serves as a reference for the subsequent discussion.

Two types of infrared imagers were used during these studies—an Agema model 880 LW scanner (Agema Infrared Systems, Danderyd, Sweden) and an Amber model Radiance HS staring camera (Amber Engineering, Goleta, CA). The Agema model 880 LW scanner implements a single liquid-nitrogen cooled Mercury-Cadmium-Telluride (HgCdTe) detector. The lens focuses the radiation from the target area onto a vertically oscillating primary mirror. As this primary mirror oscillates vertically, the radiation is reflected through a series of fixed mirrors and directed to a single horizontally rotating polygonal mirror. The rotating polygonal mirror effectively scans through each line of the image on the primary mirror as the primary mirror oscillates. A final set of relay optics focuses the radiation onto the HgCdTe detector. Synchronization of the vertically oscillating primary mirror and the rotating polygonal mirror produces a complete frame at a rate of 25 Hz. The mean sensor response of the Agema model 880 LW scanner is 93% between the wavelengths of 8–11 μm . The sensitivity of the complete optical system is represented by the ratio of the measured signal intensity to the thermal noise produced within the system. This signal to noise ratio is given by

$$SNR = \int \frac{\Phi_{in}(\lambda')}{\Phi_{noise}(\lambda')} d\lambda', \quad (A.2)$$

where λ' is the wavelength of light, Φ_{in} is the spectral radiant flux incident on the detector and Φ_{noise} is the noise equivalent power defined as the incident power at a detector's surface that

produces a unity ratio of the RMS signal to RMS noise in the detector output. For thermal imaging systems, the *SNR* is typically quantified as the noise equivalent temperature difference defined as

$$NETD = \frac{\sigma_{vn}}{\Re} = \frac{\sigma_{vn}}{\Delta V_s / \Delta T_s}, \quad (\text{A.3})$$

where σ_{vn} is the standard deviation of the voltage noise, $\Re = \Delta V_s / \Delta T_s$ is the responsivity of the detector, and ΔV_s is the change in signal voltage corresponding to a change in target temperature, ΔT_s . The manufacturer's specification of *NETD* for the Agema model 880 LW scanner is 0.05 °C. In the three-dimensional noise model, the *NETD* accounts for both temporal and spatial thermal noise. In scanning systems, significant residual internal heating will cause fixed pattern noise (FPN), or spatial inhomogeneity in an image that is constant over the measurement time period. The fixed pattern noise is easily subtracted out of the imagery during the image processing using a reference image of a target of uniform temperature, T_T , that was regularly placed in the imager field-of-view.

The development of the focal-plane-array (FPA) infrared imager has led to the elimination of fixed pattern noise, the capability to sample at rates up to 120 Hz, and better performance in the form of lower *NETD*. The Amber model Radiance HS staring camera implements an Indium Antimonide (InSb) focal plane array enclosed in an all metal dewar and cooled to cryogenic temperatures using a closed-cycle Split Stirling refrigerator. The focal plane array consists of a 256 x 256 detector hybridized onto a two-dimensional CMOS integrated circuit with one sample and hold amplifier for each element that allows for snapshot operation. The Amber camera detects radiation in the wavelength range of 3–5 μm . The Amber imager has a digital output with 12-bit resolution and an internal calibration flag assembly to correct for any

residual fixed pattern noise (non-uniformity) existing in the focal plane array. Two-point corrections of element-to-element non-uniformity were accomplished by using the internal flag or an external calibration source. For these studies, the Santa Barbara Infrared (SBIR) model 2004S blackbody (Santa Barbara Infrared Inc., Santa Barbara, CA) was used as the external calibration source and is accurate to 0.01°C and stable to within $\pm 0.003^{\circ}\text{C}$. Non-uniformity corrections (NUC) are performed regularly and the coefficients are stored in non-volatile memory. The camera does not have the ability to change the output range (gain control) and the saturation level of the detector array is adjusted by the integration time of the focal-plane array. For the surface water temperature range observed in these studies, an integration time of 1.2 ms was adequate to detect a range of temperatures that spanned roughly from 10°C to 40°C , while the range of T_s observed within a single image is roughly 1°C to 2°C . The manufacturer's specification of *NETD* for the Amber model Radiance HS staring camera is 0.025°C . As a check on this specification, laboratory tests using the SBIR model 2004S blackbody were performed to estimate *NETD* for the temperature range and integration time specified above. The *NETD* is determined using (A.3) where σ_{vn} is defined operationally as the standard deviation of the random three-dimensional noise (x , y , and t dimensions) over 150 frames digitized at a 15 Hz sample rate. Figure A.2 shows the *NETD* for the laboratory tests and the results demonstrate that the focal plane array performed within or near the manufacturer's specification for the entire observed target temperature range.

During the Preliminary CCIW/Harris study discussed in Chapter 3, T_s was not measured directly using a radiometer and therefore an adequate independent measure of T was not available. Instead, infrared measurement T_{base} was taken to be the mean temperature in the image, $\langle T \rangle$, and T_{md} was defined as the mean difference between the maximum, T_{max} , and mean, $\langle T \rangle$, temperatures within an image over the course of the run. To the casual observer of an infrared sequence, a microscale breaking wave will appear to disrupt the cool skin layer, producing a striking warm feature that propagates through the image. Once an event was

identified from studying these images, the operator applied different thresholds and ran the detection algorithm to determine the T_{thresh} that located the microscale breaking events reliably. The distinctive propagating front of warm temperature was the main feature used to identify the microscale breaking waves as well as the chosen threshold level. Thresholds for $j = 0.20$ and $j = 0.33$ show that the outlined features in Figure 3.1 produced by the algorithm are indeed the features observed as microscale wave breaking in Figure 2.3. The co-located infrared and visual measurements shown in Figure 2.3 demonstrate that the features highlighted with the image processing detection algorithm correspond directly with the visual observations of the dimpled wave crests. Therefore, the subjective choice of threshold is verified with visual observation. The lower threshold ($j = 0.20$) detects one large event, whereas the higher threshold ($j = 0.33$) successfully separates three events identified with the three individual crests in Figure 2.3. Although this simple definition of fractional area averages out the effect of multiple events in various stages of development within a single image, A_B nonetheless provides a measure of the area extent of microscale breaking. However, the threshold level was not tested for a variety of conditions, as measurements were made at only one wind speed in each facility.

Consistent with the Preliminary CCIW/Harris study, the Harris I study discussed in Chapter 4 used a similar approach for determining the threshold. Here, however, T_{md} was determined directly and independently using calibrated Heimann KT-19 radiometers and a bulk water thermometer. A new T_{thresh} needed to be determined since T_{md} was measured in a manner different from the Preliminary CCIW/Harris study. Also, the Amber model Radiance HS infrared imager was used, with much better spatial and thermal resolution that required a more refined T_{thresh} than during the Preliminary CCIW/Harris study. The Amber model Radiance HS was calibrated in the laboratory at the beginning and the end of the study using the SBIR model 2004S blackbody, and the spatial non-uniformity in the detector was corrected using the internal flag during the experiments before each run. Again, T_{base} was taken as the mean temperature within

the images. Studying the images and testing different values for j in the same manner as before revealed that $j = 0.10$ produced the most reasonable result for the outlined features as shown in Figure 4.2. This single T_{thresh} was then applied to the complete suite of runs during Harris I that cover a range of low to moderate wind speeds and varying surface conditions as outlined in Table 4.1. The results were favorable in that A_B increased with wind speed for the same surface condition and decreased for increasing surfactant at given wind speed. However, co-located visual observations were not recorded and the threshold could not be independently verified.

During the Wallops study, an independent measurement of T_s using the Heimann KT-19 radiometer was not attempted. Instead, the Amber model Radiance HS camera was used to determine T_s , and was calibrated and corrected for spatial non-uniformity in the detector using the SBIR model 2004S blackbody. The manufacturer of the Radiance HS stipulates that the measurement of absolute temperature requires extremely well controlled environmental conditions during the calibration and measurement period. A three-point calibration spanning $\pm 3^\circ\text{C}$ about the surface water temperature was performed every hour. A summary of all the calibrations in Figure A.3 shows the values for the 12-bit digital dynamic range, DU , plotted against the blackbody target temperature, T_T . The calibration varied significantly about the mean experimental calibration curve considering the measured responsivity \mathfrak{R} of the InSb FPA increased from 50 to 75 counts/ $^\circ\text{C}$ for this temperature range (methods to determine \mathfrak{R} are found in Dudzik [1993]). Furthermore, these deviations from the mean experimental calibration occurred on short time scales. Figure A.4 shows a time series of the mean standard deviation of surface temperature, $\sigma_{T'}$, from an image for a given run and the mean $\Delta T'$ as determined using the mean calibrated image temperature as T_s and T_w measured by the aforementioned bulk water thermometer. Each group of three points in time corresponds to a different imager calibration. This measure of T_{md} was shown to vary depending on the calibration in a manner not related to any real change in surface temperature. $\Delta T'$ starts at a level of roughly 0.71°C during the first

calibration set of runs, then drops to 0.46°C during the second calibration set before coming back up to a level of 0.64°C during the third calibration set. Realistically, the surface temperature and bulk temperature should cool similarly. Since T_w is shown to slowly decrease over the course of these calibrations, the mean surface temperature determined from the imager is the cause of this discrepancy. This suggests that the calibration is inconsistent and, in this study, the imager should not be used to measure absolute surface temperature for use in the detection of skin-layer disruptions. The standard deviation of temperature in the image, σ_T , however, remains relatively constant throughout the three calibrations because it is independent of any external measurement of temperature, with an expected small decrease in σ_T over time. Anything affecting the overall absolute temperature measured by the imager does not affect the variation in temperature within the image. The imager retains its non-uniformity correction, even though the measurement of absolute temperature may vary significantly.

Since the calibration appears to follow the standard deviation for the first and third calibrations, but deviates for the middle calibration, the calibration of the imager is the source of the problem. The air temperature in Figure A.4 is shown to decrease by 2°C between the first and second calibration, coincident with the relative deviation between standard deviation and $\Delta T'$. Since the conditions changed, the absolute measure of T_s from the imager drifted between the time the second calibration was performed and the measurements were made. This would suggest that small changes in the ambient conditions caused the imager to drift over time, potentially leading to significant errors in $\Delta T'$. During the whole experiment, the drift that occurred over the course of three runs performed during each calibration cycle had a root mean square value of nearly 11 counts, and many times as high as 20 or 30 counts. Because of this inconsistency in the absolute measurement of temperature by the imager due to its drift with changing environmental conditions, an alternative measure of T_{md} was sought.

According to classical surface renewal, the average standard deviation in temperature within an infrared image should represent a measure of the bulk-skin temperature difference. The mean value of $T(t)$ from (2.2) at a fixed location between two surface renewal events is given by

$$\overline{\Delta T(\theta)} = \frac{1}{\theta} \int_0^{\theta} \Delta T(t) dt. \quad (\text{A.4})$$

Following from *Kudryavtsev and Lichnic* [1979], the average bulk-skin temperature difference is given by the expected value of $\overline{\Delta T(\theta)}$ as

$$E\{\Delta T\} = \int_0^{\infty} \overline{\Delta T(\theta)} \Theta(\theta) d\theta. \quad (\text{A.5})$$

Following *Haußecker* [1996], the variance of T_s can now be defined as

$$\sigma_T^2 = \int_0^{\infty} \left[\frac{1}{\theta} \int_0^{\theta} T_s^2(t) dt \right] \Theta(\theta) d\theta - E\{\Delta T\}^2, \quad (\text{A.6})$$

and the standard deviation, σ_T , is shown to be a function of T . As discussed in section 2.2, *Haußecker* [1996] argued that the ratio $R_T = E\{\Delta T\}/\sigma_T$ is constant and can be used to determine k_H from (2.3). Here the ratio is determined experimentally and σ_T is used as a measure of T_{md} for use in determining the appropriate T_{thresh} . Figure A.5 shows the correlation between (a) T and σ_T measured during the Harris I study and between (b) $\Delta T'$ and σ_T measured during the Wallops study. For both experiments, σ_T was roughly of $O(10\%)$ of T and $\Delta T'$. Therefore, the standard deviation within the infrared imagery taken at Wallops may be used to represent T_{md} .

T_{base} was defined as the mean minimum temperature within an image, $\langle T_{min} \rangle$. $\langle T_{min} \rangle$ is defined as the average temperature of 1% of the pixels in the image with the lowest temperature and represents T_s that is closest to the undisturbed state.

Following the model for determining the appropriate j described above for the Preliminary CCIW/Harris and the Harris I studies, microscale breaking events at different wind speeds and surface conditions for the Wallops study were first identified in the infrared sequences by the operator. The threshold chosen to detect these regions of disruption by microscale wave breaking most reliably for all conditions was for $j = 3.5$. Here, co-located slope imagery was available to verify the threshold level and detection of microscale breaking events. Figure A.6 shows the infrared imagery also shown in Figure 3.9b, with outlines of the detected A_B at varying thresholds for $j = 3.5, 4.0$, and 4.5 . Figure A.7 shows the corresponding wave slope imagery accompanied by overlays of the detected A_B for the three thresholds. The high threshold serves only to detect the actively breaking crest, while the lower thresholds detect both the front of the bore-like crest and the turbulent wake left behind. All microscale breaking events should be characterized by the propagating front of sharp temperature contrast corresponding to the bore-like crest, as well as the warm region left behind the propagating front corresponding to the decaying turbulent wake. The threshold for $j = 3.5$ produced the most reliable detection of microscale wave breaking events covering all wind speeds and surface conditions. The comparison of the detected A_B with the slope imagery provides the independent verification to substantiate the choice of threshold.

While the magnitude of A_B may change for these varying thresholds, the correlation between A_B and k_{600-G} does not diminish. Figure A.8 shows k_{600-G} versus A_B for (a) a comparison of three thresholds $j = 0.100, 0.075, 0.050$ for the Harris I study and (b) a comparison of two thresholds defined by $j = 3.5$ and 4.0 for the Wallops study. In the Harris I comparison, the linear coefficient of determination is improved slightly from the original 0.97 to 0.99 for both

$j = 0.075$ and 0.050 , yet only the offset of the linear fit changes while the slope remains similar. In the Wallops comparison, the linear coefficient of determination remained constant at 0.89 , yet both the offset (-3.3 for $j = 3.5$ and -1.5 for $j = 4.0$) and slope (54.6 for $j = 3.5$ and 43.3 for $j = 4.0$) of the linear fit changes only slightly. This is further evidence that the implementation and verification of the algorithm are sound. While the threshold was chosen to match the appearance of the microscale wave breaking in the slope images (i.e., the scale of the wave), the quality of the correlation of k_{600-G} and A_B is retained and is independent of the choice of reasonable values for j . However, since the different threshold was used because of the differing operating conditions, a direct comparison between the studies at Harris and Wallops is not appropriate. Each threshold scheme will give a unique relationship, and the results show the need for consistent experimental setup and instrumentation if a robust parameterization is to be developed.

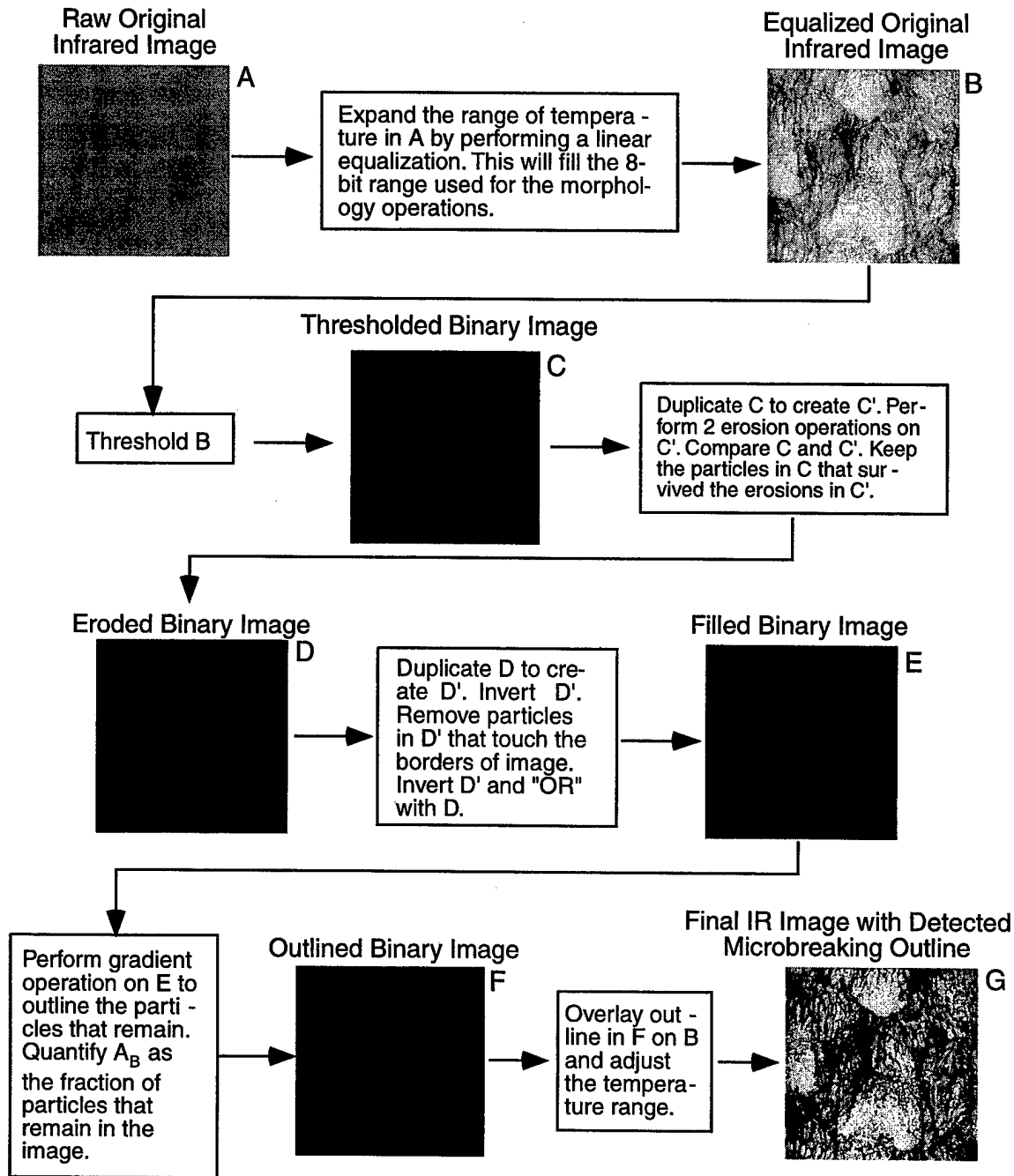


Figure A.1. Schematic diagram of the image processing algorithm used to determine A_B .

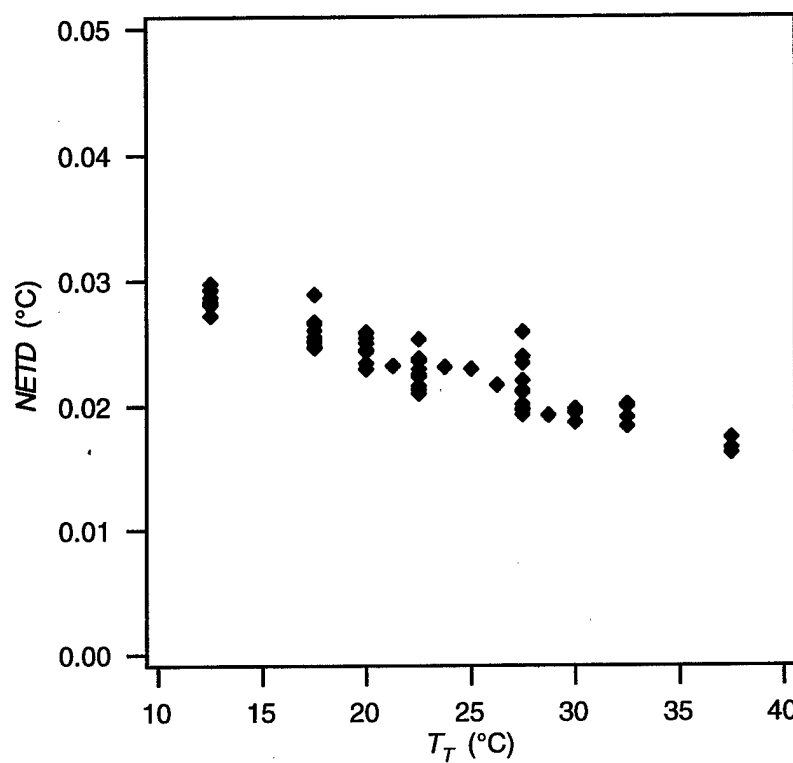


Figure A.2. Noise equivalent temperature difference, $NETD$, for the Amber model Radiance HS camera determined using the SBIR model 2004S blackbody as a function of the target temperature, T_T .

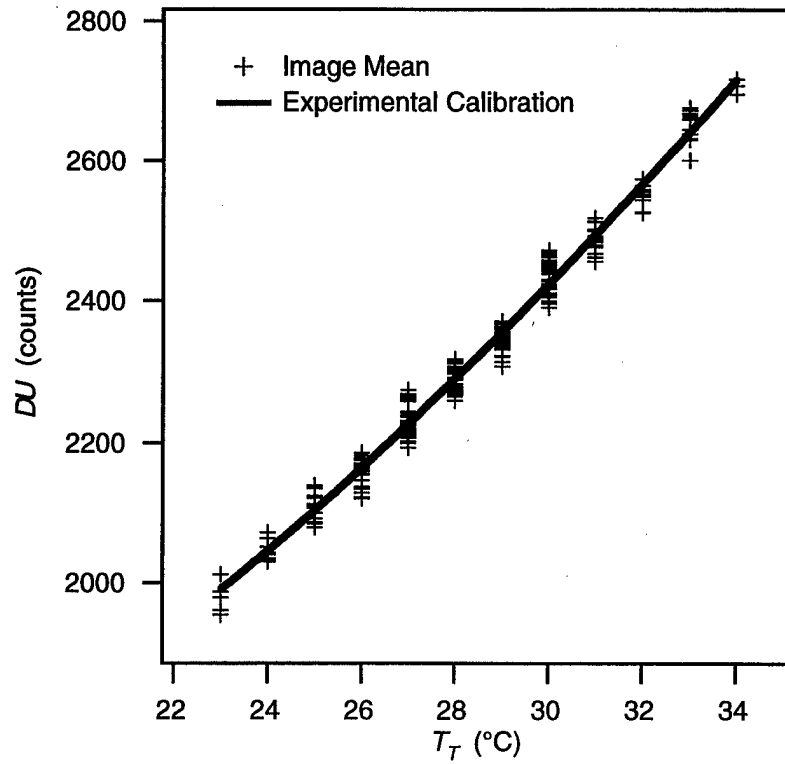


Figure A.3. Summary of all calibrations of the Amber model Radiance HS camera performed using the SBIR model 2004S blackbody during the Wallops study. DU is the 12-bit digital dynamic range and T_T is the blackbody target temperature. The line is a polynomial fit through the data and serves as the overall calibration for this study.

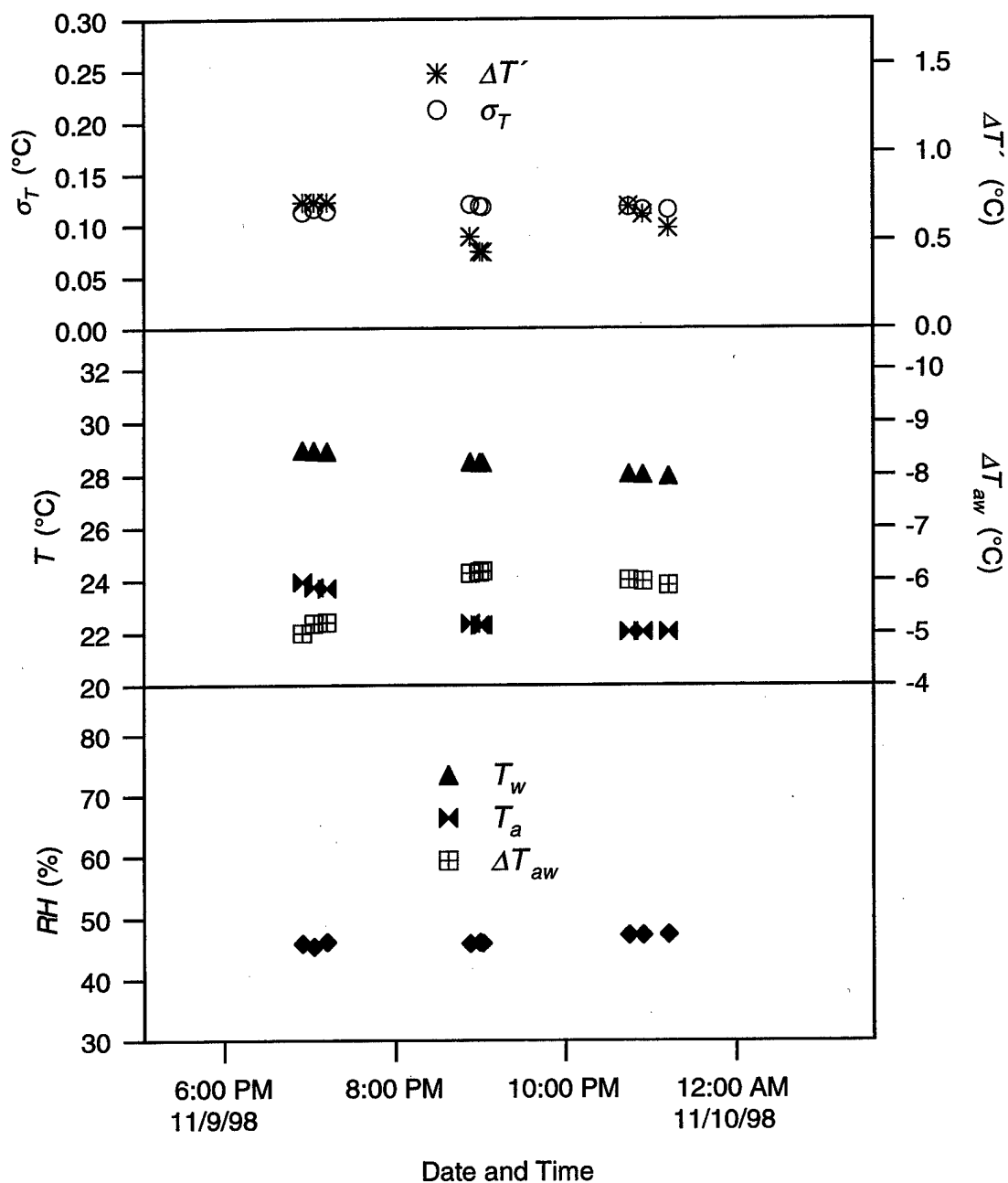


Figure A.4. Time series of the mean standard deviation of surface temperature, σ_T , from an image for a given run and the mean $\Delta T'$ as determined using the mean calibrated image temperature as T_s and T_w measured by the aforementioned bulk water thermometer. Also shown are time series of T_a , T_w , T_{aw} , and RH. Each group corresponds to different imager calibration.

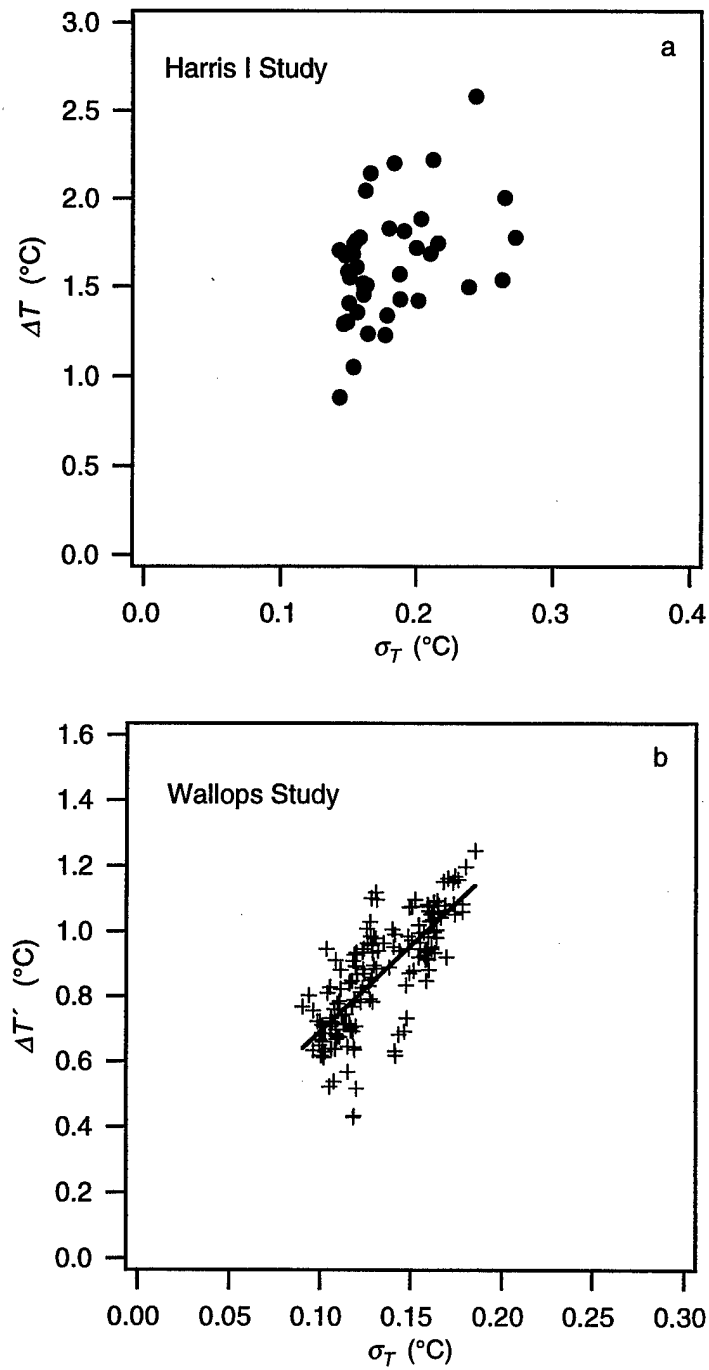


Figure A.5. (a) The bulk-skin temperature difference, ΔT , measured during the Harris I study and (b) $\Delta T'$ measured during the Wallops study versus the standard deviation in surface temperature, σ_T , from the infrared imagery.

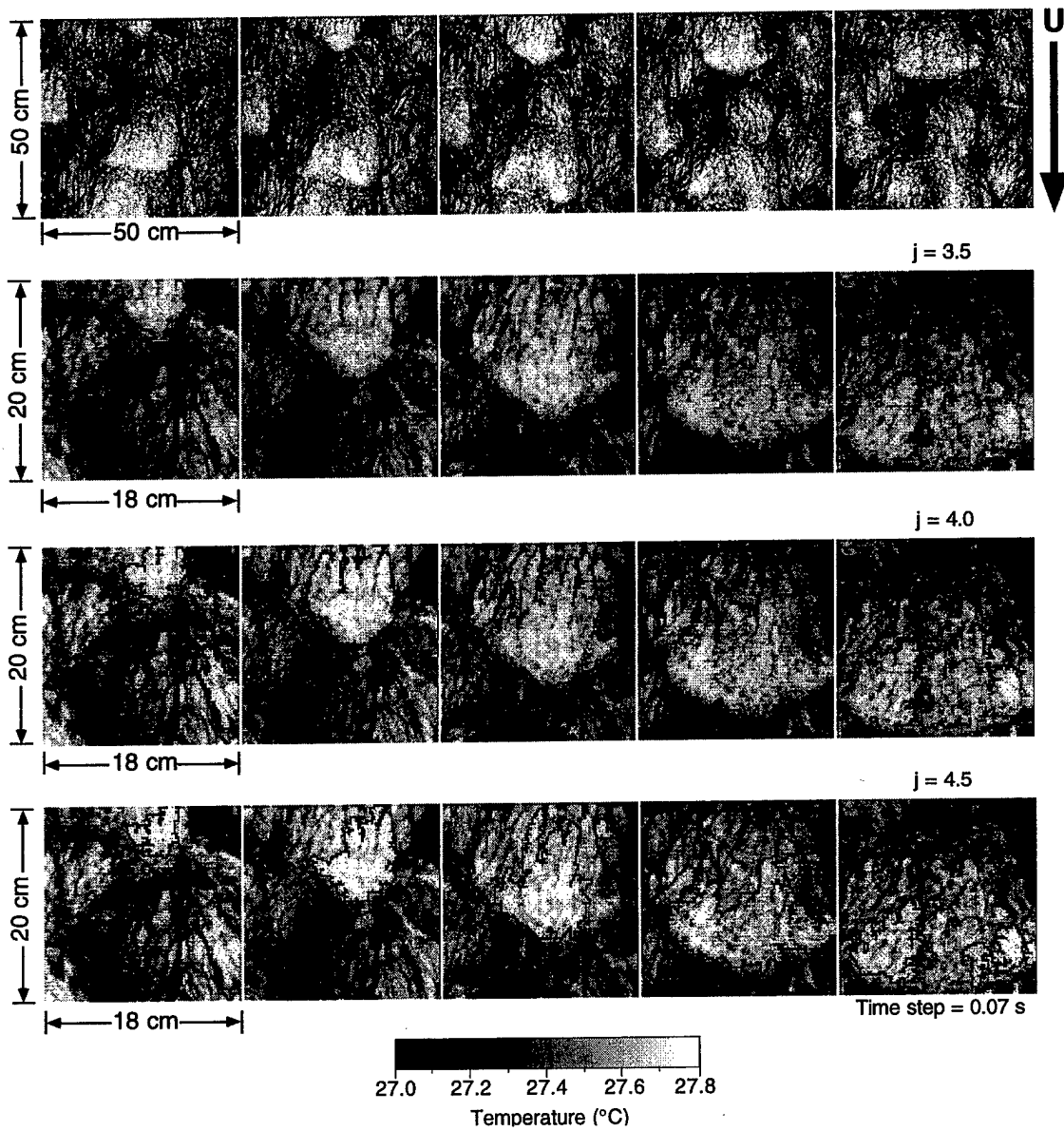


Figure A.6. Sequence of infrared imagery with outlines of the detected regions of skin-layer disruption due to microscale wave breaking, A_B , that shows the difference between the various thresholds for $j = 3.5, 4.0$, and 4.5 . Example is taken from Figure 3.9.

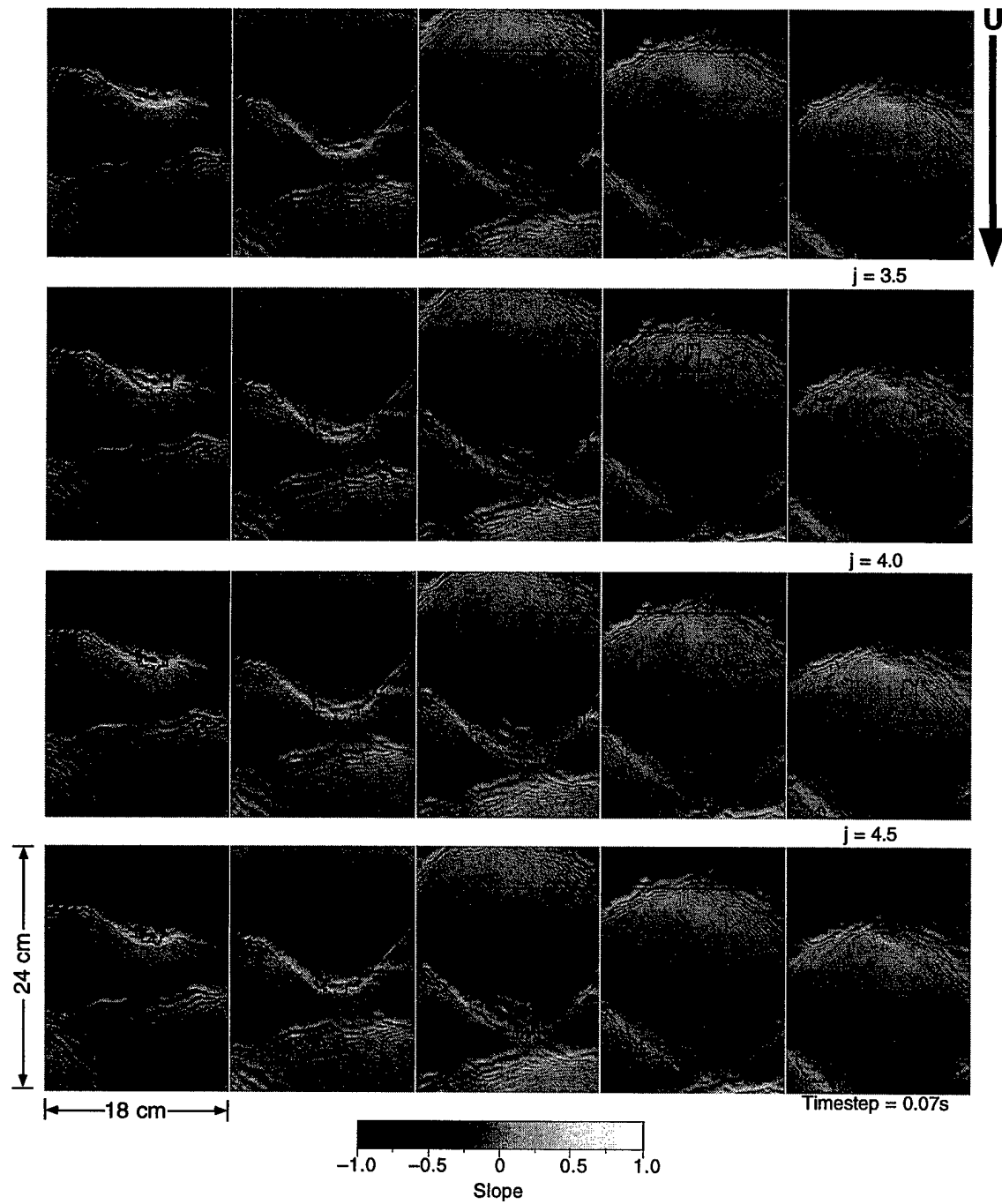


Figure A.7. Sequence of wave slope imagery with overlays of the detected A_B in Figure A.6.

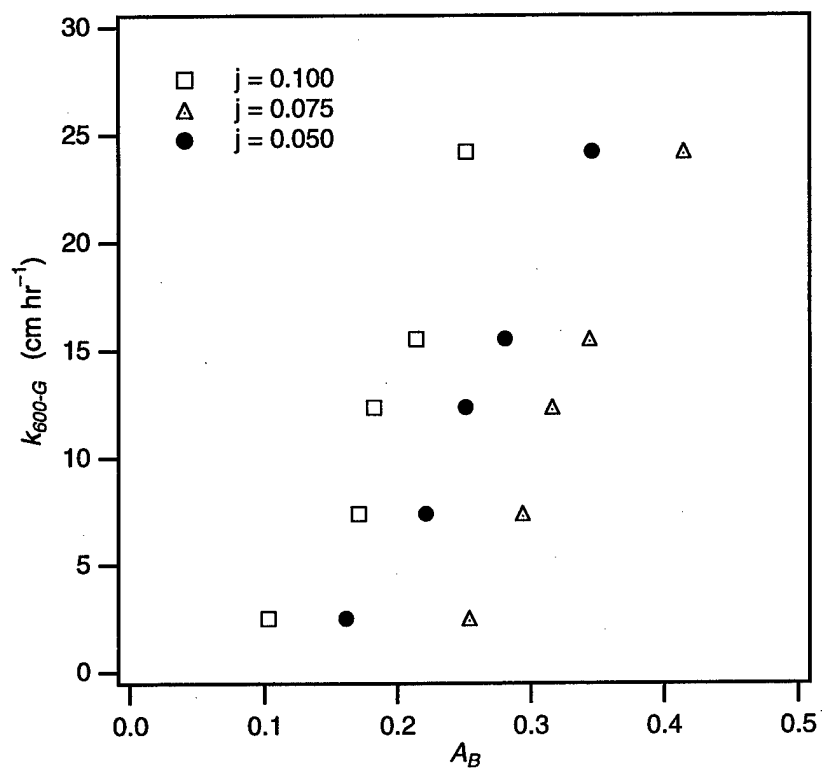


Figure A.8. The gas transfer velocity, k_{600-G} , referenced to a $Sc = 600$ versus A_B for a comparison of three thresholds $j = 0.100, 0.075, 0.050$ for the Harris I study.

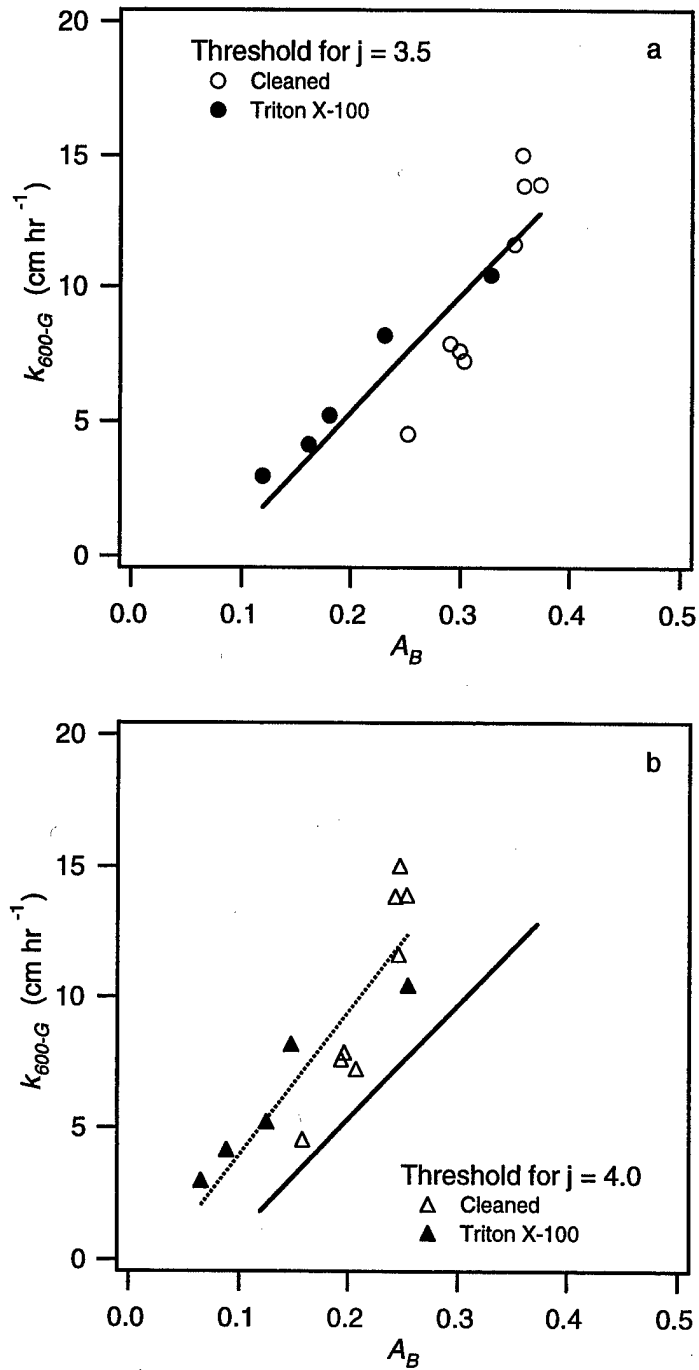


Figure A.9. The gas transfer velocity, k_{600-G} , referenced to a $Sc = 600$ versus A_B for a comparison of two thresholds defined by (a) $j = 3.5$ and (b) $j = 4.0$ for the Wallops study. Also shown are the linear fits to the data for $j = 3.5$ (solid line) and $j = 4.0$ (dashed line).

Table A.1. Comparison of experimental differences between the Preliminary CCIW/Harris, the Harris I, and the Wallops studies.

Experiment	Preliminary CCIW/Harris	Harris I	Wallops
Imager	Agema model 880 LW scanner	Amber model Radiance HS camera	Amber model Radiance HS camera
NUC	1-point (lens cap served as the target to remove fixed pattern noise)	2-point (built in flag calculated gain and offset for each pixel every hour, valid between the two end point temperatures of 30°C and 40°C)	2-point (external blackbody set to $\pm 3^\circ\text{C}$ about T_s and performed every hour)
Calibration	factory	pre- and post-experiment blackbody calibration for a full range of temperatures 20–40°C	3-point (external blackbody set to $\pm 3^\circ\text{C}$ about T_s and performed every hour)
Infrared Setup Comments	fixed location	fixed location	shroud was slid out of the way to allow for the SBIR blackbody to perform the NUC and the calibration; caused varying shadows and different bias in image that affects the absolute measure of T_s ; moved setup for two fetches
T_{base}	Imager (mean image temperature, $\langle T \rangle$)	Imager (mean image temperature, $\langle T \rangle$)	Imager (1% of the pixels with the lowest temperature in the image, $\langle T_{min} \rangle$)
T_{md}	mean difference between the maximum temperature in the image, T_{max} , and $\langle T \rangle$ over the course of a run	T measured directly from a bulk water thermometer and a calibrated Heimann KT-19 radiometer	σ_T in the image; calibrated T_s showed excessive variation
j	0.20 and 0.33	0.1	3.5

APPENDIX B: HEAT FLUX DEPENDENCE OF THE CONTROLLED FLUX TECHNIQUE

The controlled flux technique (CFT) [Jähne and Haußecker, 1998] uses heat as a proxy tracer for gas to obtain the remote measurement of the local transfer velocity with high spatial resolution and short response times. In the CFT, the water surface is heated with a CO₂ laser to produce a spot with a measurable temperature difference that can be tracked within a sequence of infrared images. The heat transfer velocity, k_H , is determined from the surface renewal rate, which is estimated from the thermal decay of the heated spot as predicted from a simple surface renewal model. Since both heat and gas are scalars, k_H is assumed to scale directly to the gas transfer velocity, k . Previous CFT measurements by Jähne and co-workers [Jähne *et al.*, 1989; Haußecker *et al.*, 1995; Jähne and Haußecker, 1998] have given reliable estimates of k in the laboratory under conditions of minimal heat flux across the air–water interface. However, our recent laboratory data for conditions of high heat flux show that, when referenced to a common Schmidt number, the CFT estimates of k are roughly 2.5 times greater than k determined from He and SF₆.

A basic assumption of the controlled flux technique is minimal heat loss to the atmosphere and, thus, transfer is dominated by water-side processes. Previous laboratory and field results of the skin-layer recovery rate of free surface wakes and breaking waves have shown a strong dependence on the net heat flux [Zappa *et al.*, 1998]. Here, in laboratory experiments, the thermal decay of the CFT patch shows a similar dependence on the net heat flux across the air–water interface.

Direct measurements of the sensible heat flux, Q_S , and latent heat flux, Q_L , were not made during the Wallops study. Estimates of these heat fluxes were made according to

$$Q_S = k_S \rho C_p \Delta T_{aw} \quad (\text{B.1})$$

and

$$Q_L = k_L \left(c_a - \frac{c_w}{\phi} \right) L = k_L \frac{c_w}{\phi} (RH - 1) L, \quad (\text{B.2})$$

where k_L is the transfer velocity for water vapor as determined from the data of *Liss* [1973] as summarized in *Schwarzenbach et al.* [1993] ($k_L = 0.005 + 0.32U$), k_S is the transfer velocity for sensible heat as scaled from k_L using (2.1), ϕ is the solubility of water in water and is a strong function of temperature, and L is the latent heat of vaporization. The heat fluxes present during Wallops averaged -115 W m^{-2} for Q_S and -630 W m^{-2} for Q_L . Calculations of the effect of Q_S and Q_L on the thermal decay rate of the CO_2 -laser-heated patch performed at Wallops result in timescales comparable to $\tau = 1/\lambda$ as determined from the fit of T_N to (5.3). The net heat flux, $Q_N = Q_S + Q_L$, was roughly -745 W m^{-2} and will cause a change in temperature over time according to $Q_N = \rho C_p (\partial T / \partial t) \delta_T$. For the given rise in surface temperature caused by the CO_2 -laser of 5°C and the absorption depth of roughly $20 \mu\text{m}$ for the infrared radiation by the CO_2 -laser, the timescale for decay by the background heat flux is of $O(10^{-1} \text{ s})$ and comparable to $\tau = 1/\lambda$. Therefore, the major effect of the heat flux on CFT is in the form of a sink for heat to the atmosphere that will decrease the decay time of the patch.

In order to investigate further the heat flux dependence of the controlled flux technique, additional experiments were performed in the Harris tank (Harris II) for two cases at different net heat fluxes. In Case 1, Q_N was -186 W m^{-2} and, in Case 2, Q_N was -536 W m^{-2} . For these cases summarized in Table B.1, the RH and T_{aw} remained relatively constant and the variation in Q_L and Q_S is due to k_L and k_S , which vary with U . Figure B.1 shows a comparison of

k_{600-H} measured during the Harris II study and k_{600-G} data for cleaned surfaces from Figure 4.1 of the Harris I experiments, both referenced to a Sc of 600 versus U . When the net heat flux was low in Case 1, the data show that k_{600-H} during Harris II was comparable to k_{600-G} during Harris I. However, k_{600-H} is shown to increase at a given wind speed with the net heat flux, Q_N . The agreement between k_{600-H} and k_{600-G} is good at high wind speeds, but the net heat flux dependence becomes pronounced at low wind speeds, with k_{600-H} increasing with Q_N . These data support the hypothesis that k_H is affected by the heat flux from the water to the air.

Both the heat flux and k_{600-H} were much larger during the Wallops Island study than during the Harris II study for comparable wind speeds. Figure B.2 shows k_H versus Q_N , Figure B.3 shows k_H versus Q_L , and Figure B.4 shows k_H versus Q_S for both the Wallops and Harris II studies. The results show that k_H increases with Q_N and specifically as a smoothly varying function of Q_L . Because the values for Q_S in both studies were comparable yet small relative to the Q_L , the data in Figure B.4 showed no significant correlation between k_H and Q_S . Figure B.1 through Figure B.4 demonstrate that the measurement of k_H using the CFT is indeed affected by the transfer of heat from the water to the atmosphere. The CFT-measured k_H , then, is one that incorporates not only the downward transfer of sensible heat into the bulk water, but upward transfer of sensible and latent heat fluxes into the air. Also, the portion of k_H due to Q_L will not scale with the water-side processes, since the exchange of water vapor is an air-phase rate controlled process [Liss, 1973], i.e., turbulence on the water side will have no effect on the latent heat transfer. Therefore, k_H is a function of the net heat flux and may not be appropriate as a tracer for individual species of gas under conditions of highly varying heat flux, since it is dependent on both air- and water-side controlled processes. These results suggest that dependable measurements of k inferred from CFT during field experiments will require the

determination of the surface-renewal rate from the thermal decay of the heated patch that appropriately accounts for the heat loss to the atmosphere.

A fundamental problem exists with the boundary layer equation posed by *Jähne et al.* [1989] and *Haußecker et al.* [1995] that was applied to the controlled flux technique. The unsteady diffusion equation (5.1) assumes that surface renewal can be modeled as a first order chemical reaction, i.e., the decay of temperature through the sink term, $-\lambda T(z, t)$. This assumption is problematic for two reasons. First, this sink term incorporates the effect of upward transfer of heat, therefore biasing high the measured values of λ and k_H . Second, incorporating a sink term is inherently inappropriate for classical surface renewal modeling as originally proposed by *Danckwerts* [1951]. Here, an alternative approach is proposed to analytically determine λ from the CFT data.

The new approach is based on classical surface renewal models that assume a distribution of eddy lifetimes, θ , is defined by (1.13), where s is the surface renewal rate, and the governing equation is

$$\frac{\partial T(z, t)}{\partial t} = \alpha \frac{\partial^2 T(z, t)}{\partial z^2}. \quad (\text{B.3})$$

Following from the boundary conditions as previously outlined by *Haußecker et al.* [1995], the solution to (B.3) is

$$\frac{T(0, t)}{T_o} = \frac{h}{\sqrt{h^2 + 4\alpha t}}. \quad (\text{B.4})$$

Surface renewal is incorporated into this alternative approach using the distribution (1.13) as the eddy lifetimes observed within the CFT patch. At each timestep of the algorithm, the patch is divided into i small areas corresponding to a parcel of water at the surface with a lifetime θ_i . The CFT patch will decay according to (B.4) as long as the surface is not renewed, i.e., $t < \theta_i$. Once renewed, $t > \theta_i$, and the water surface returns to the initial mean surface temperature. The algorithm calculates the normalized predicted patch temperature, T_{NP} , at each timestep for all θ_i while enforcing the following conditions: for $t < \theta_i$, solve (B.4); for $t > \theta_i$, $T_{NP} = 0$, or the normalized initial patch temperature. Averaging all realizations of T_{NP} within the patch for all θ_i produces the predicted T_{NP} at that timestep. Accordingly, the surface renewal rate will be determined by fitting the normalized data, T_N , to the predicted decay curve, T_{NP} , within a Levenberg-Marquardt optimization. The values of s determined using this surface renewal model were identical to the values of λ determined from optimization of (5.3) with the data. This is not surprising since $e^{-\lambda t}$ in (5.3) is identical to the integrated effect of (1.13). Therefore, this new method is in the spirit of traditional surface renewal modeling and provides a viable alternative approach for future analytical models that are needed to improve the controlled flux technique. Specifically, the heat flux dependence of k_H will require models that incorporate boundary conditions of the Robin type (a linear combination of Dirichlet and Neumann conditions used to describe heat flux at boundaries) or two-phase models that account for the enhanced decay of the CFT patch due to net upward heat flux.

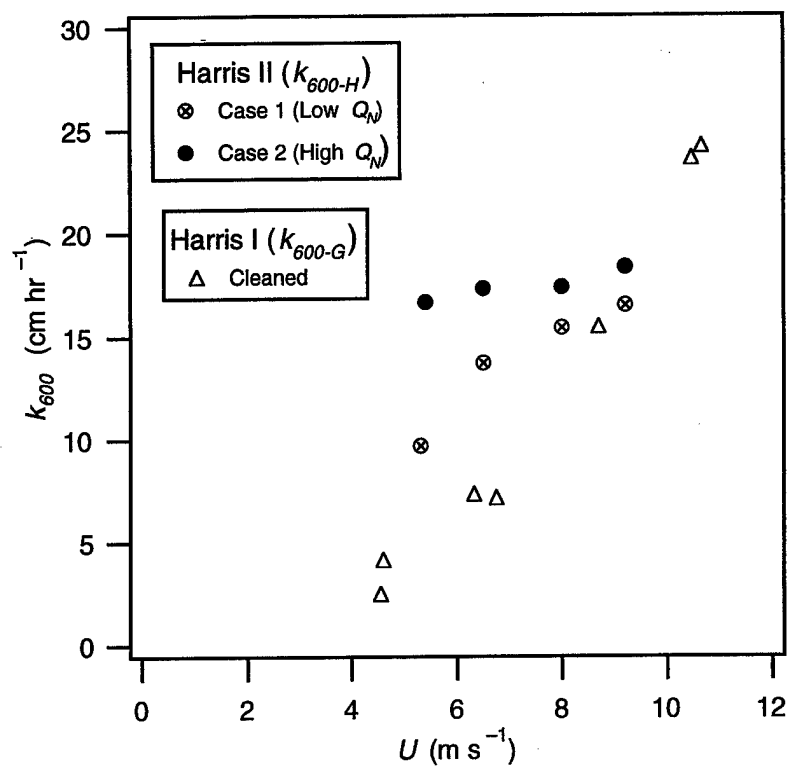


Figure B.1. Comparison of k_{600-H} from the Harris II study and k_{600-G} from the Harris I study discussed in Chapter 4.

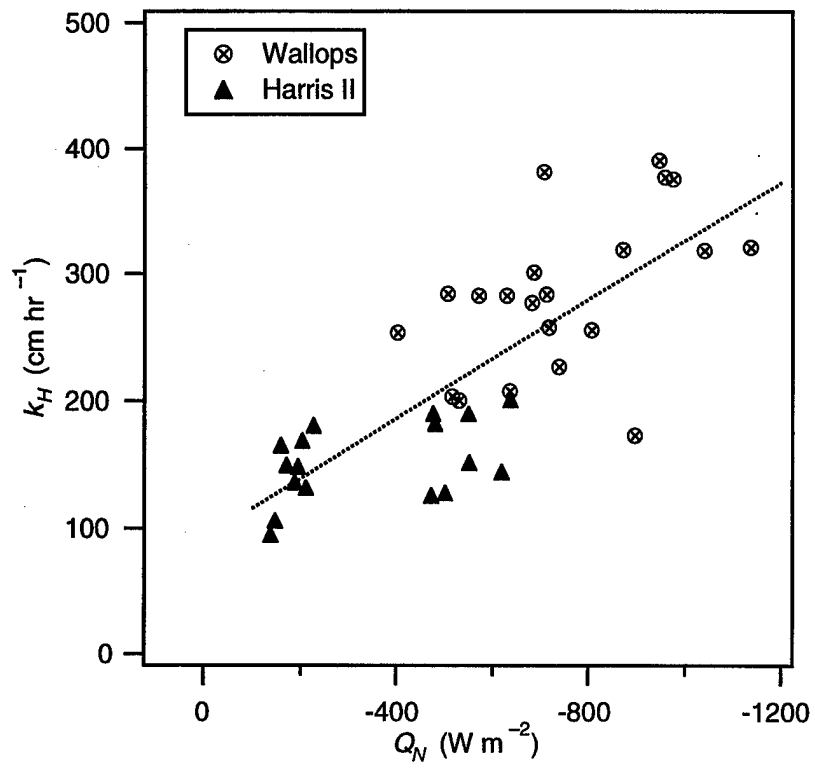


Figure B.2. Dependence of k_H on Q_N during the Wallops and the Harris II experiments.

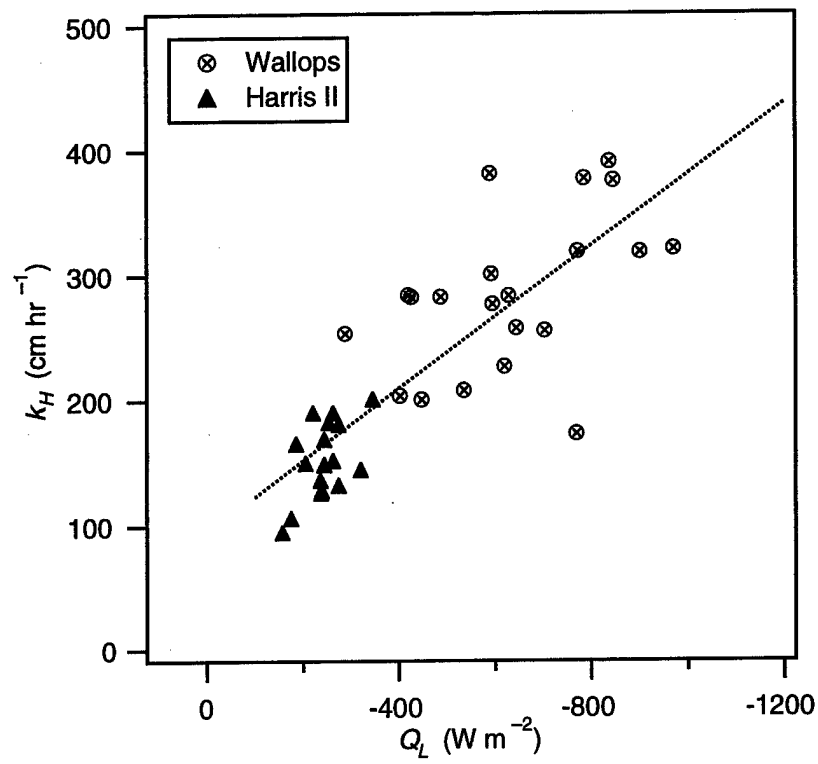


Figure B.3. Dependence of k_H on Q_L during the Wallops and the Harris II experiments.

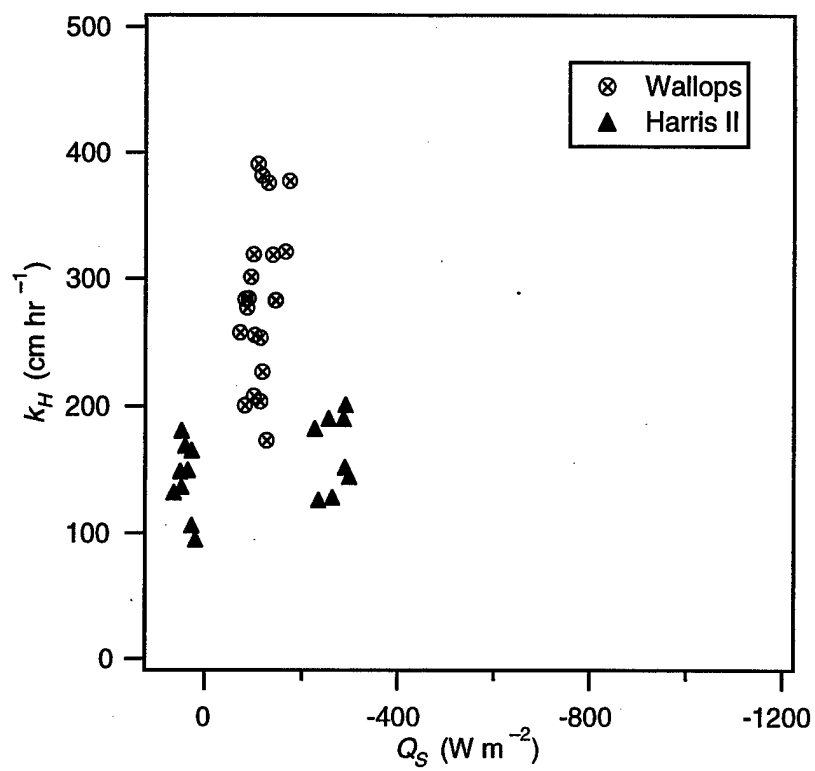


Figure B.4. Dependence of k_H on Q_S during the Wallops and the Harris II experiments.

Table B.1. Comparison of Cases 1 and 2 during the Harris II study.

Case No.	U (m s ⁻¹)	T_{aw} (°C)	T_w (°C)	RH (%)	Q_L (W m ⁻²)	Q_s (W m ⁻²)	Q_N (W m ⁻²)
1	5.3	1.9	19.7	70.0	-175.1	27.9	-147.2
1	6.5	2.1	19.4	70.0	-206.1	36.3	-169.7
1	8.0	2.0	19.4	70.0	-244.7	41.1	-203.6
1	9.2	2.1	19.5	70.0	-275.6	48.6	-227.0
2	5.4	-15.2	37.7	84.0	-254.6	-226.7	-481.3
2	6.5	-14.8	37.8	88.0	-221.4	-255.9	-477.3
2	8.0	-14.0	37.5	88.0	-262.9	-287.5	-550.4
2	9.2	-12.6	37.0	86.0	-345.4	-291.4	-636.8

VITA

CHRISTOPHER J. ZAPPA

University of Washington

1999

EDUCATION

University of Washington, Seattle, WA

Ph.D. in Civil and Environmental Engineering - Autumn, 1999

University of Washington, Seattle, WA

M.S. in Engineering - August, 1994

Columbia University, New York, NY

B.S. in Mechanical Engineering - May, 1992

HONORS

American Defense Preparedness Association Fellowship, 1997

Geophysical Fluid Dynamics Fellowship, University of Cambridge, 1996

Applied Physics Laboratory Graduate Fellowship, 1992-3

Tau Beta Pi and Chi Epsilon Honor Societies

PUBLICATIONS

Zappa, C. J., W. E. Asher, and A. T. Jessup, Microscale wave breaking and air-water gas transfer, *Geophysical Research Letters*, submitted, 1999.

Zappa, C. J., A. T. Jessup, and H. Yeh, Skin-layer recovery of free-surface wakes: Relationship to surface renewal and dependence on heat flux and background turbulence, *J. Geophys. Res.*, 103, 21711-21722, 1998.

Jessup, A. T., C. J. Zappa, and H. Yeh, Defining and quantifying microscale wave breaking with infrared imagery, *J. Geophys. Res.*, 102, 23145–23154, 1997.

Jessup, A. T., C. J. Zappa, M. R. Loewen, and V. Hesany, Infrared remote sensing of breaking waves, *Nature*, 385, 52–55, 1997.

Jessup, A. T., C. J. Zappa, V. Hesany, M. R. Loewen, and M. G. Skafel, Dependence of the skin layer recovery rate on heat flux and turbulence, *Air–Water Gas Transfer*, edited by B. Jähne, and E. C. Monahan, AEON Verlag & Studio, Hanau, pp. 601–610, 1995.

Zappa, C. J., Infrared field measurements of sea surface temperature: Analysis of wake signatures and comparison of skin layer models, M. S. Thesis, University of Washington, 1994.

PRESENTATIONS

Zappa, C. J., W. E. Asher, and A.T. Jessup, Microscale wave breaking as the mechanism controlling air–water gas transfer. Spring Meeting of the American Geophysical Union, Boston, MA, June, 1999.

Zappa, C. J., W. E. Asher, and A.T. Jessup, Correlating microscale wave breaking with gas transfer for cleaned and surfactant-influenced water surfaces. Air–Sea Interface Symposium, Sydney, Australia, January, 1999.

Zappa, C. J., A.T. Jessup, and W. E. Asher, Influence of microscale wave breaking on gas transfer. Johns Hopkins Conference in Environmental Fluid Mechanics, Baltimore, MD, April, 1998.

Zappa, C. J., Evaluation of the well-stirred bath technique for calibration of infrared radiometers. CASOTS Workshop, Milan, Italy, October, 1997.

Jessup, A. T., and C. J. Zappa, Quantifying surface fluxes due to wave breaking using infrared imagery. Ocean Interfaces Meeting of The Oceanography Society, Seattle, WA, April, 1997.

- Zappa, C. J., A. T. Jessup, and H. H. Yeh, Quantifying microscale wave breaking using infrared imagery. Ocean Sciences Meeting of the American Geophysical Union, San Diego, CA, February, 1996.
- Plant, W. J., W. C. Keller, A. T. Jessup, K. A. Hayes, C. J. Zappa, K. W. Hoppel, and E. A. Uliana, Microwave backscatter, surface fluxes and infrared imagery measured from a blimp over the ocean. International Geoscience and Remote Sensing Symposium, Pasadena, CA, August, 1994.
- Jessup, A. T., H. H. Yeh, and C. J. Zappa, The infrared signature of free-surface wakes. Twelfth U.S. National Congress of Applied Mechanics, Seattle, WA, June, 1994.

REPORT DOCUMENTATION PAGE

Form Approved
OPM No. 0704-0188

Public reporting burden for this collection of information is estimated to average 1 hour per response, including the time for reviewing instructions, searching existing data sources, gathering and maintaining the data needed, and reviewing the collection of information. Send comments regarding this burden estimate or any other aspect of this collection of information, including suggestions for reducing this burden, to Washington Headquarters Services, Directorate for Information Operations and Reports, 1215 Jefferson Davis Highway, Suite 1204, Arlington, VA 22202-4302, and to the Office of Information and Regulatory Affairs, Office of Management and Budget, Washington, DC 20503.

1. AGENCY USE ONLY (Leave blank)		2. REPORT DATE December 1999		3. REPORT TYPE AND DATES COVERED Technical	
4. TITLE AND SUBTITLE Microscale Wave Breaking and Its Effect on Air-Water Gas Transfer Using Infrared Imagery				5. FUNDING NUMBERS N00014-93-1-1326 NSF 9633423	
6. AUTHOR(S) Christopher J. Zappa					
7. PERFORMING ORGANIZATION NAME(S) AND ADDRESS(ES) Applied Physics Laboratory University of Washington 1013 NE 40th Street Seattle, WA 98105-6698				8. PERFORMING ORGANIZATION REPORT NUMBER APL-UW TR 9904	
9. SPONSORING / MONITORING AGENCY NAME(S) AND ADDRESS(ES) Office of Naval Research Space and Remote Sensing Program Code 321SR 800 N. Quincy Street Arlington, VA 22217-5660 National Science Foundation Division of Ocean Sciences Arlington, VA 22230				10. SPONSORING / MONITORING AGENCY REPORT NUMBER	
11. SUPPLEMENTARY NOTES					
12a. DISTRIBUTION / AVAILABILITY STATEMENT Approved for public release; distribution is unlimited.				12b. DISTRIBUTION CODE	
13. ABSTRACT (Maximum 200 words) Air-sea gas exchange plays a crucial role in geochemical cycling, and a robust parameterization of the gas transfer velocity, k , is needed to improve models of global fluxes. However, the dependence of k on wind speed or wind stress has been shown to be a function of the concentration of surfactants, which are ubiquitous in nature. Laboratory measurements indicate that a wave-related mechanism regulates gas transfer because the correlation of k with wave slope is unaffected by the presence of surfactants. Microscale wave breaking has been proposed as the underlying physical process that determines k at low to moderate wind speeds. However, quantifying the effects of microscale wave breaking has been difficult because the phenomenon lacks the visible manifestation of whitecapping. Measurements here show that microscale breaking waves produce thermal surface signatures that can be quantified by infrared imaging techniques. Simultaneous and co-located infrared and wave slope imagery of laboratory wind waves show that distinct areas of the water surface where the thermal boundary layer is disrupted occur coincidentally with waves that have a steep forward face and a dimpled bore-like crest. The measurements show that these wave-related areas of enhanced surface renewal are the turbulent wakes of microscale breaking waves. The local k within the wakes, measured using the controlled flux technique, is on average 3.5 times greater than k outside the wakes. The fractional area coverage, A_B , of the surface affected by these renewal features is significant (0.25 - 0.40) and found to be linearly correlated with both k and the mean square wave slope, $\langle S^2 \rangle$. Microscale wave breaking is shown to directly contribute up to 75% of the transfer across the air-water interface under moderate wind speeds. The roughness features associated with microscale breaking waves are shown to contribute significantly to $\langle S^2 \rangle$ and may explain the observed correlation between k and $\langle S^2 \rangle$. The correlation between k and A_B that is insensitive to the presence of surfactants, combined with the local k and wave slope results, provides the first quantitative laboratory evidence that microscale wave breaking is the underlying physical mechanism that governs gas transfer at low to moderate wind speeds.					
14. SUBJECT TERMS Free-surface turbulence, air-sea interaction, bulk-skin temperature difference, infrared imagery, air-water gas transfer, surface renewal				15. NUMBER OF PAGES 246	
				16. PRICE CODE	
17. SECURITY CLASSIFICATION OF REPORT Unclassified	18. SECURITY CLASSIFICATION OF THIS PAGE Unclassified	19. SECURITY CLASSIFICATION OF ABSTRACT Unclassified	20. LIMITATION OF ABSTRACT SAR		